UNIVERSITY OF CALIFORNIA

Santa Barbara

Himalaya gneiss dome formation, focused radiogenic heating in southern Madagascar, and fertilization of the Neoproterozoic ocean by mantle-derived phosphorus

A dissertation submitted in partial satisfaction of the

requirements for the degree Doctor of Philosophy

in Geological Sciences

by

Forrest Miller Horton

Committee in charge:

Professor Bradley Hacker, Chair

Professor John Cottle

Professor Frank Spera

Professor Matthew Jackson

June 2015

The dissertation of Forrest Miller Horton is approved.

_____

Matthew Jackson

_____

Frank Spera

_____

John Cottle

_____

Bradley Hacker, Committee Chair

June 2015

Himalaya gneiss dome formation, focused radiogenic heating in southern Madagascar, and fertilization of the Neoproterozoic ocean by mantle-derived phosphorus

ACKNOWLEDGEMENTS

I thank my advisor Brad Hacker for his invariably constructive advice, and for encouraging me to pursue a diverse range of research topics; working with him has been an inspiring and fulfilling experience. Professors John Cottle, Matthew Jackson, and Frank Spera also provided helpful guidance as committee members. Professor Jeffery Lee (Central Washington University), Meilani Bowman-Kamaha'o (Central Washington University), and Michael Cosca (USGS, Denver) contributed to Chapter I of this dissertation. Professor Michel Rakatondrazafy (University of Antananarivo), Jeremia Ramarijaona, Laurent Rakotondramanana, Robert Holder, Professor Chris Clark (Curtin University), Andrew Kylander-Clark, and Gareth Seward contributed to Chapter II. Comments from Professor Cin-Ty Lee (Rice University) and Professor Noah Planavsky (Yale University), and discussion with numerous University of California Santa Barbara Department of Earth Science faculty members provided the impetus for—and drastically improved—Chapter III.

VITA OF FORREST MILLER HORTON

June 2015

EDUCATION

Bachelor of Arts in Geology and Environmental Studies, Bowdoin College, May 2008.

Master of Science in Geology, San Francisco State University, May, 2011.

Doctor of Philosophy in Geology, University of California, Santa Barbara, June 2015.

PEER-REVIEWED PUBLICATIONS

Horton, F., 2015, Did phosphorus derived from the weathering of large igneous provinces fertilize the Neoproterozoic ocean? *Geochemistry, Geophysics, Geosystems*, DOI 10.1002/2015GC005792.

Horton, F., Lee, J., Hacker, B., Bowman-Kamaha'o, M., Cosca, M., 2014, Himalaya gneiss dome formation in the middle crust and exhumation by normal faulting: New geochronology of Gianbul dome, northwestern India, *GSA Bulletin*, v. 126, B31005.1.

Horton, F., Leech, M.L., 2013, Age and origin of granites in the Karakoram shear zone and Greater Himalaya Sequence, NW India, *Lithosphere*, v. 5, p. 300–320.

Tucker, R.D., Belkin, H.E., Schulz, K.J., Peters, S.G., **Horton, F.**, Buttleman, K., Scott, E.R., 2012, A major rare-earth element (LREE) resource in the Khanneshin carbonatite complex, Southern Afghanistan, *Economic Geology*, v. 107, no. 2, 197-208.

THESES

Horton, F., 2008. EBSD and HRxCT analysis of elongated garnets of the Spring Point Formation, Casco Bay, ME. *Bowdoin College Archives*, Thesis 2008 H6, p. 1–45, CD-ROMs 1–2.

Horton, F., 2011, Geochronology and zircon geochemistry of Greater Himalaya leucogranites in Zanskar, NW India, *San Francisco State University Archives*, p. 1–104.

PROFESSIONAL EXPERIENCE

University of California Santa Barbara, Department of Earth Science. Teaching assistant for field and introductory Earth science courses, 2012–2015.

Department of Defense Task Force for Business and Stability Operations. Mineral exploration geologist in Afghanistan, 2010–2011.

Avalon Development Corporation. Mineral exploration geologist at Donlin Creek gold deposit in Alaska, 2008.

DJ&A Engineers. Land surveying in Montana, 2004, 2006.

GRANTS AND AWARDS

Caltech Division of Geologic and Planetary Sciences Geochemistry Postdoctoral Fellowship, 2015.

University of California Santa Barbara Department of Earth Science G.K. Gilbert Award, 2015.

University of California Santa Barbara Department of Earth Science, Alumni Graduate Award for Research Excellence, 2015.

University of California Santa Barbara Department of Earth Science Migues Field Research Prize, 2013.

University of California Santa Barbara Doctoral Fellowship, 2011.

National Science Foundation Graduate Research Fellowship, 2010.

Geological Society of America Graduate Research Grant, 2010.

Global War on Terror Civilian Service Medal, 2010.

Bowdoin College Arthur M. Hussey Geology Award, 2008.

Maine Space Grant Consortium Fellowship, 2007.

Frank Hervey Cook Scholarship, 2000.

FIELD RESEARCH LOCALITIES

India. Ladakh Himalayas, 2009. Kerala Khondalite belt, 2014.

Afghanistan. Helmand, Herat, Ghazni, Kunar, and Kabul provices. 2010–2011.

Madagascar. Ihosy to Fort Dauphin, 2012 and 2014.

Antarctica. Ross Orogen, 2012–2013.

Alaska. Donlin Creek, Kuskokwim mountains, 2008.

Maine. Casco Bay, 2007.

LABORATORY EXPERIENCE

Laser ablation split stream (LASS) ICPMS. Petrochronology of zircon, monazite, and rutile via excimer laser, multicollector, single collector, and quadrupole.

USGS-Stanford SHRIMP. U/Th-Pb geochronology of monazite and zircon.

Scanning electron microscopy. Secondary electron, X-ray spectrometry, and cathodoluminescence mapping of minerals in thin sections.

High-resolution X-ray computed tomography. 3D scanning of elongate garnets to evaluate mineral growth conditions and deformation mechanisms at UT Austin.

Electron backscatter diffraction. Analysis of garnet and zircon deformation microstructures using Oxford Instruments and HKL Channel 5 software.

ABSTRACT

Himalaya gneiss dome formation, focused radiogenic heating in southern Madagascar, and fertilization of the Neoproterozoic ocean by mantle-derived phosphorus

by

Forrest Miller Horton

(I) Geochronology, thermochronology, and structural observations across Gianbul gneiss dome provide insight about the exhumation of middle crust in the India-Asia collision zone: Doming (1) initiated during the early stages of extension; (2) was driven by a positive feedback among dehydration melting, buoyancy, and decompression; and (3) culminated with the injection of anatectic melts into the upper levels of the dome. The dome was subsequently exhumed as part of a footwall block beneath a brittle normal fault.

(II) Focused internal heating led to melting, metamorphism, and crustal weakening during the Neoproterozoic continent-continent collision between East and West Gondwana. Numerical models based on chronologic and thermal constraints across southern Madagascar indicate that radioactive decay of thorium was the principal heat source responsible for regional metamorphism at temperatures >900° C in the middle to lower crust.

(III) The Neoproterozoic era was punctuated by profound tectonic, evolutionary, and environmental change. Biologic and climatic conditions may have been especially sensitive to fluxes of phosphorus (P) from the weathering of continental crust. Large igneous

provinces—containing abundant P and highly susceptible to chemical weathering—occurred regularly during the breakup of the Rodinia supercontinent. An estimated bioavailable P flux to the ocean from the weathering of basalt peaked at ~720 Ma, immediately prior to rapid biologic diversification and the Sturtian glaciation; I postulate that the burial of organic carbon that resulted from this unprecedented P flux helped facilitate glaciation and triggered the oxidation of the ocean-atmosphere system.

TABLE OF CONTENTS

I. Himalayan gneiss dome formation in the middle crust and exhumation by normal faulting: New geochronology of Gianbul dome, northwestern India

1. Introduction

In the predominantly contractional India–Asia collision zone, Himalayan gneiss domes are prevalent—yet seemingly paradoxical—extensional structures that have been attributed to a surprising number of different processes. Three mechanisms were proposed by early researchers to explain the North Himalayan gneiss domes in the eastern portion of the orogen: i) thrust duplex formation as a result of north–south contractional folding (Burg et al., 1984; Hauck et al., 1998; Makovsky et al., 1999), ii) diapiric rise of anatectic melts (Le Fort, 1986; Le Fort et al., 1987), and iii) Cordilleran-style metamorphic core-complex formation (Chen et al., 1990). Subsequent research has highlighted the complexity of Himalayan gneiss dome formation and led to doming models that involve feedback among multiple mechanisms. For example, dome formation has been explained by shear heating-induced melting and diapirism (Harrison et al., 1997), antiformal doming within the hanging wall of a thrust fault superseding diapirism (Lee et al., 2004), and granitic magmas advecting heat that caused extension and anatexis (Aoya et al., 2005).

Himalayan gneiss domes have also been interpreted in the context of the middle crust channel-flow model (e.g. Nelson et al., 1996; Beaumont et al., 2001; Grujic et al., 2002; Langille et al., 2010) that predicts partial melting and foreland-directed extrusion of Indian crust sandwiched between the South Tibetan detachment system above and the Main Central thrust below. Exhumation of the Greater Himalayan sequence (GHS) of gneisses and

anatectic leucogranites between these structures can be explained by low viscosity in the middle crust, a horizontal gravitational potential energy gradient, and high denudation rates along the range front (Beaumont et al., 2001, 2004). In this context, plugging of the mid-crustal channel due to inefficient surface denudation—coupled with localized extension in overthickened upper crust—could favor exhumation of middle crust in hinterland domes rather than in a channel (Beaumont et al., 2004; Jamieson et al., 2006). The parallel tectonic histories for the GHS and the North Himalayan gneiss domes imply that southward flow of ductile middle crust and doming were coeval and related processes (Lee et al., 2006). Whereas the majority of Himalaya gneiss domes are associated with north-south extension, a subset of younger (and possibly unrelated) domes formed during orogen-parallel extension (e.g. Hintersberger et al., 2010).

Unlike the eastern part of the Himalayan orogen where gneiss domes form a distinct belt north of the east-west striking South Tibetan detachment system (Le Fort, 1986), gneiss domes in the western Himalaya are exposed south of and in the footwall of the western continuation of the South Tibetan detachment system (Herren, 1987; Kündig, 1989). Noting that the westernmost gneiss domes commonly have Paleozoic orthogneiss cores, Kündig (1989) proposed that lithologic heterogeneities contributed to preferential exhumation of low-density orthogneiss relative to the surrounding metasedimentary rocks, and that heat transfer by granites caused localized anatexis along their margins. Dèzes et al. (1999), however, attributed regional doming to late-stage isostatic uplift in the footwall of a low-angle normal fault (analogous to Cordilleran-style metamorphic core complex formation). Recent interpretations of Gianbul dome reflect polarized views of northwestern Himalayan tectonic evolution: Gianbul dome is either framed in the context of i) a thermo-mechanical channel-flow model (Beaumont et al., 2004; Searle et al., 2007) or ii) a structural tectonic

wedge model (Yin, 2006; Webb et al., 2007, 2013), in which the GHS thrust wedge propagates southward below the alternating motion of a roof fault. Based on channel flow models, Robyr et al. (2002) proposed that inefficient surface denudation and a weak upper crust caused doming. Elaborating upon this hypothesis, Robyr et al. (2006) suggested that the overlying metasedimentary rocks acted as a backstop for the ductile exhumation of the GHS gneisses and migmatites and that decompression led to a positive feedback with partial melting and enhanced exhumation. In the tectonic wedge model, however, Gianbul dome represents the southeastern extent of a regional GHS antiform that inherited irregular topography of the thrust ramp or underwent bending during underthrusting (Yin, 2006).

To address the lack of consensus about gneiss domes in general, and to reevaluate doming mechanisms in the western Himalaya, I present new structural observations, monazite U/Th-Pb geochronology, and $^{40}Ar/^{39}Ar$ mica thermochronology for Gianbul dome. My data suggest that doming (1) occurred in the middle crust during upper-crustal extension, (2) was driven by positive feedback between decompression melting of metasedimentary rocks and buoyancy-driven exhumation, and (3) ceased prior to brittle exhumation in the footwall of a normal fault. These results have implications for the tectonic evolution of the Himalaya and improve our understanding gneiss dome formation in continental collision zones worldwide.

2. Geologic Setting

2.1. Regional Setting

In the western Himalaya, high-grade metamorphic rocks from the middle crust are exposed as the GHS (also referred to as the High Himalayan crystalline sequence), bounded by the northeast-dipping Main Central thrust to the southwest, and separated from overlying

Tethyan Himalayan sediments by the 150 km-long Zanskar shear zone (ZSZ), the western extent of the South Tibetan detachment system, to the northeast (Figure 1). In the Zanskar region of northwest India, the GHS consists of Precambrian fine-grained biotite paragneisses and Precambrian–Early Cambrian Phe metapelites (Herren, 1987), Cambrian–Ordovician K-feldspar augen gneiss (Frank et al., 1977; Mehta, 1977; Stutz and Thöni, 1987; Pognante et al., 1990; Noble and Searle, 1995; Walker et al., 1999; this study), and several Mississippian–Permian orthogneiss bodies (Honegger et al., 1982; Spring et al., 1993; Noble et al., 2001; Horton and Leech, 2013). Peak Barrovian, M1, metamorphism related to crustal thickening reached 550–680° C and 0.8–1.0 GPa (Dèzes et al., 1999; Searle et al., 1999; Walker et al., 2001; Robyr et al., 2002) at ~35–30 Ma (Vance and Harris, 1999; Walker et al., 1999); the M1 metamorphic isograds (chlorite to kyanite) define domes (Herren, 1987; Kündig, 1989; Stäubli, 1989). The isograds are telescoped in the footwall of the ZSZ (Herren, 1987; Searle and Rex, 1989; Dèzes et al., 1999; Walker et al., 2001; Robyr et al., 2002) and overprinted by a sillimanite-grade, M2, metamorphism and anatexis at 650–770° C and 0.45–0.7 GPa (Searle et al., 1999; Robyr et al., 2002). Cenozoic migmatites, leucogranite dikes, and small plutons are prevalent (Honegger et al., 1982; Searle and Fryer, 1986; Noble and Searle, 1995), especially near Paleozoic orthogneisses (Kündig, 1989).

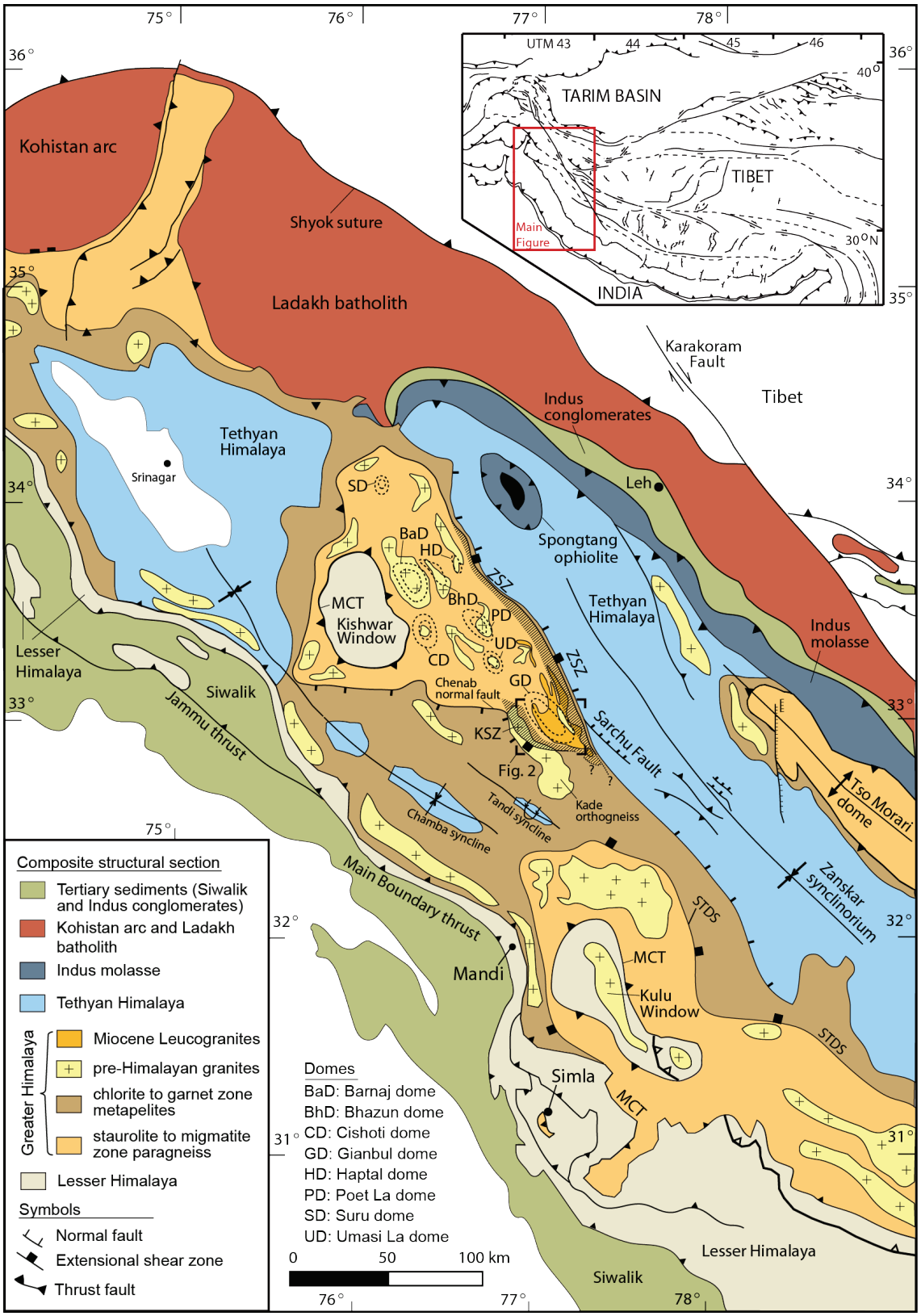

Figure 1. Regional geology map the northwestern Himalaya, modified from Thakur (1998) and Yin (2006). Gianbul dome is exposed in the footwall of Zanskar normal fault, which separates low-grade Tethyan sediments from underlying Greater Himalayan metamorphic rocks.

2.2. Gianbul Dome Geology

Gianbul dome is bounded by the northeast dipping ZSZ in Gianbul Valley and the southwest dipping Khanjar shear zone (KSZ) in Miyar Valley (Figs. 2, 3). The core of Gianbul dome is composed of migmatitic paragneiss (Figure 4a) mantled by metasedimentary rocks (Figure 4b) and orthogneiss (Figure 4c) that are cut by multiple generations of leucogranite dikes (Dèzes et al., 1999; Robyr et al., 2002, 2006, 2014; this study) (Figure 4d). The Precambrian to Cambrian Phe paragneiss includes aluminosilicates + garnet + biotite + muscovite. The Paleozoic Kade orthogneiss in the Miyar Valley contains metamorphic garnet and foliated biotite-rich melanosomes that indicate local migmatization (Pognante et al., 1990; Dèzes, 1999). Textures demonstrate that Cenozoic leucogranites and pegmatites were derived from the migmatites: leucogranites intermingle with leucosomes in the core of the dome, cut gneisses as a stockwork of dikes, and form sill-like bodies concordant to the gneissic foliation.

Migmatites, metasedimentary rocks, and orthogneiss record two primary Cenozoic ductile deformation events (earlier pre-Himalayan deformation is manifested elsewhere by Cambro–Ordovician granites that cut structures in metasedimentary rocks: Gehrels et al., 2003). The oldest Cenozoic deformation, D1, is characterized by contractional structures related to NE–SW shortening and vertical thickening. Regional contraction produced the largely brittle nappe system in the Tethyan Himalayan sequence north of Gianbul dome, and the underlying ductile “Crystalline” or “Shikar Beh” nappe that makes up the GHS (Steck et al., 1993; Epard and Steck, 2004). Extensional deformation, D2, that largely overprints D1 is associated with orogen-scale extensional slip along the ZSZ and doming (Dèzes et al., 1999; Robyr et al., 2002).

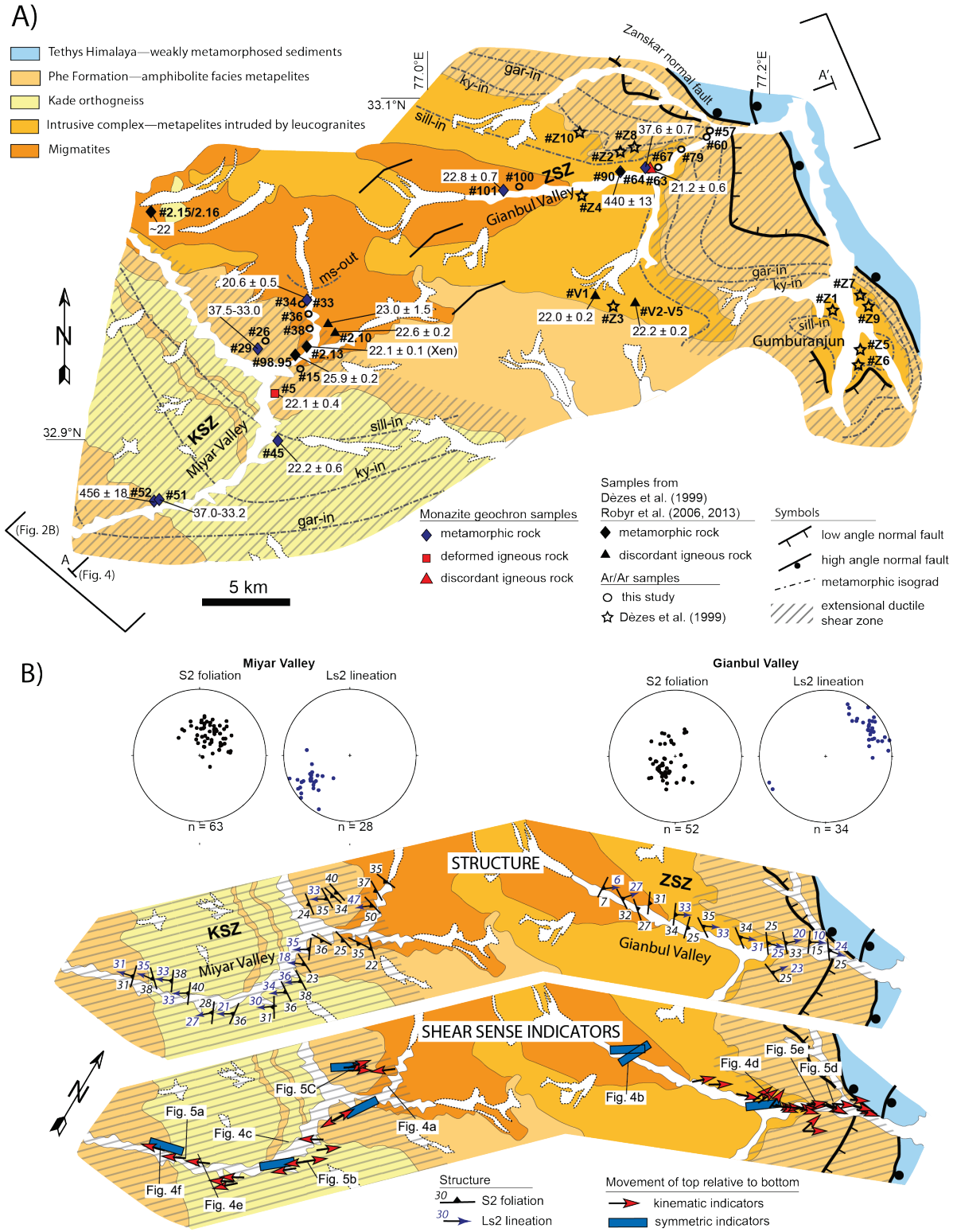

Figure 2. (A) A geologic map of the Gianbul study area (from Dèzes, 1999, Robyr et al., 2006; this study) shows major lithologic units, Barrovian metamorphic isograds, shear zones, and sample locations. Monazite U/Th-Pb ages from this study (color) and literature (black) are reported in Ma (Xen, Xenotime). (B) Structural data and kinematic shear-sense indicators along a NE-SW transect of Gianbul dome, as well as lower-hemisphere projection stereonets for S2 foliation and Ls2 lineation measurements.

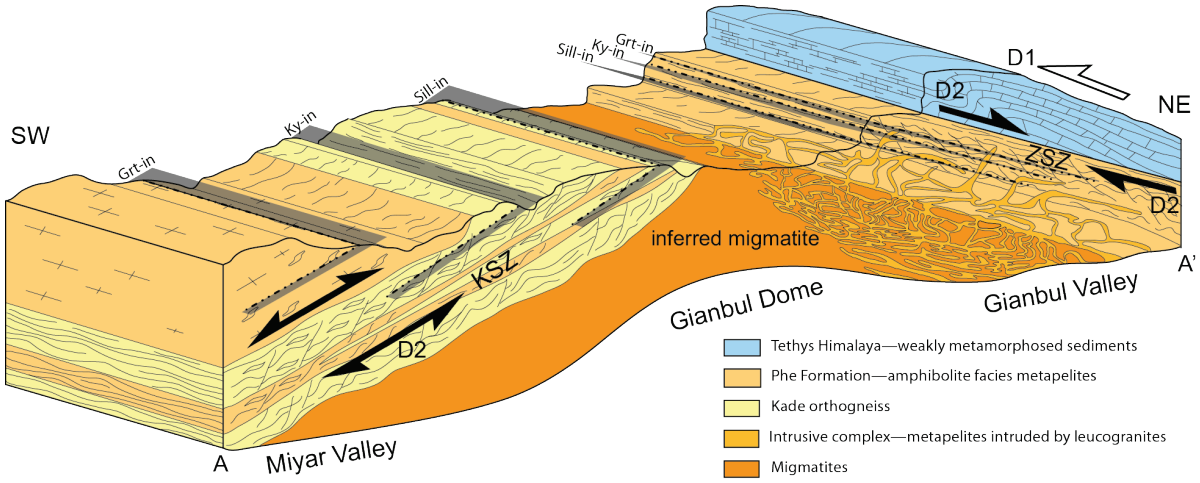

Figure 3. A generalized synthetic block diagram for Gianbul dome along the Miyar Valley–Gianbul Valley transect (modified from Robyr et al., 2006). Migmatite, metasediment, and orthogneiss record two ductile deformation events: D1 contractional related to NE-SW shortening and vertical thickening and D2 ductile NE-SW extension that overprints D1 structures. The ZSZ and KSZ were most likely segments of the same planar top-NE extensional shear zone before doming transposed the KSZ into its present-day orientation (see text for explanation). Leucogranites from migmatite zones in the Gianbul valley intrude metasediments during late D2 deformation and after doming ended.

Ductile deformation within Gianbul dome is concentrated within two prominent shear zones: 1) the ~15 km wide ZSZ on the northeastern flank of the dome and (2) the ~16 km wide KSZ on the southwestern flank (Figure 2b). Both shear zones have complex multistage deformation histories. In the ZSZ, syntectonic garnets and sigma clasts are thought to represent D1 top-to-the SW thrusting along the boundary between the Tethyan and crystalline nappe systems (Dèzes et al., 1999). In the KSZ, top-to-the NE syntectonic garnets, C-S fabrics, and sigmoidal K-feldspar clasts (e.g., Figure 4e) have also been attributed to D1 thrusting (Robyr et al., 2002, 2014), but some or all of these fabrics could alternatively represent early D2 extension later transposed during doming. If contractional features on both limbs are relics of D1 burial, it remains unclear whether the opposing D1 contractional shear zones were parallel prior to doming or intersected in the now-eroded upper levels of the dome. Extensional D2 deformation is better understood: both shear zones clearly exhibit a well-developed, high-strain S2 foliation that dips moderately to the

northeast within the ZSZ and moderately to the southwest in the KSZ, and is associated with a NE-trending stretching lineation (Figures 2b, 4f). As noted by Robyr et al. (2006), the absence of a thrust structure between the ZSZ and the KSZ suggests coeval extension along both shear zones.

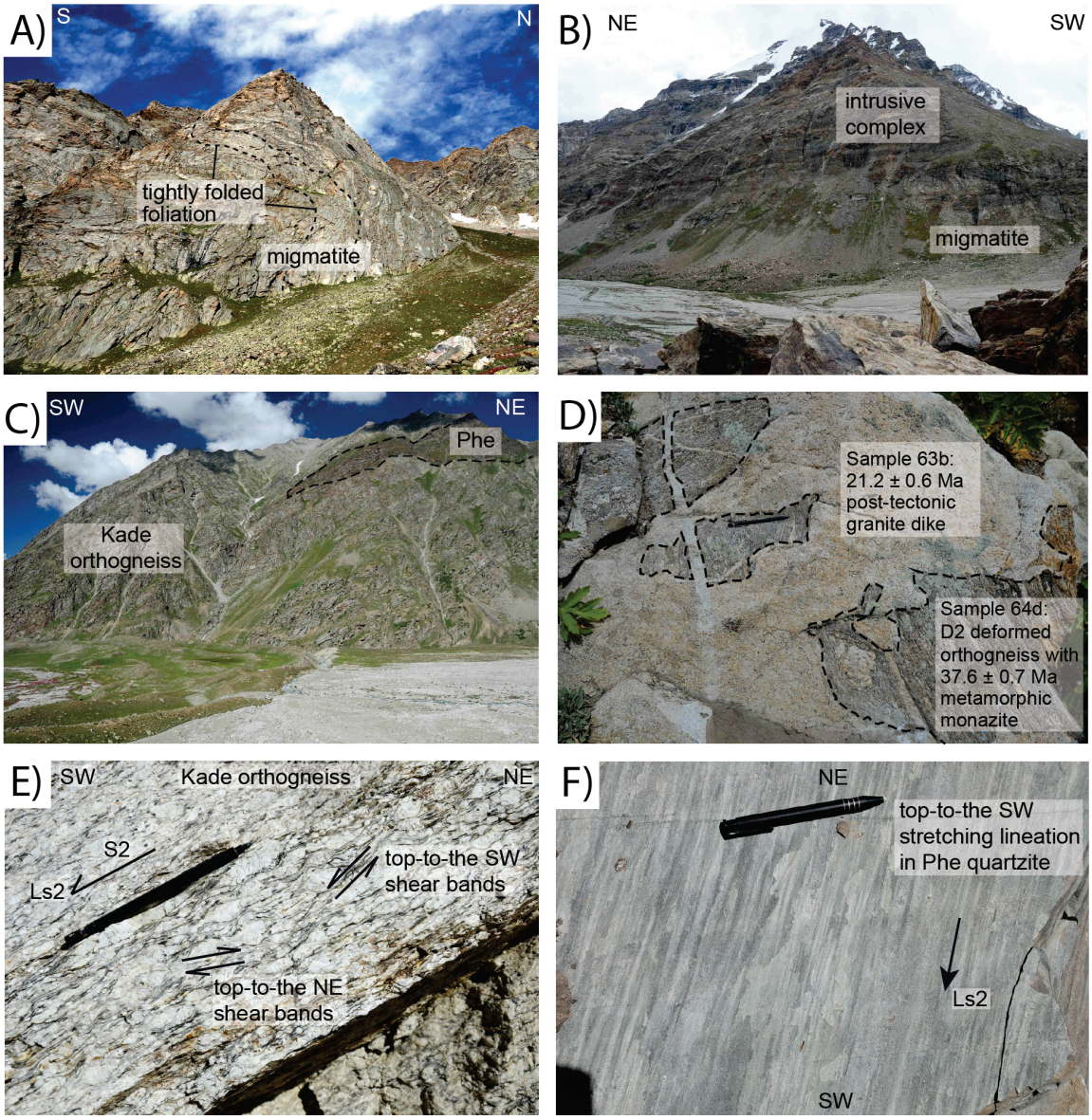

Figure 4. Photographs illustrating mesoscopic and microscopic field relations and textures (see Figure 2b for locations). (A) Tightly folded migmatite in the core of the dome exposed in Miyar valley. (B) Intrusive complex overlying migmatite core in Gianbul Valley with well-developed compositional banding (S2 foliation) dipping to the northeast. (C) Kade orthogneiss intruding Phe metapelite in Miyar Valley with well-developed S2 foliation dipping to the southwest. (D) Deformed orthogneiss in Gianbul Valley with K-feldspar megacrysts crosscut by a nondeformed dike. (E) K-feldspar sigma-clasts in Kade orthogneiss showing top-to-the NE and top-to-the-SW shear bands. Outcrop face is approximately perpendicular to the S2 foliation and parallel to the Ls2 stretching lineation. (F) Top-to-the SW stretching lineations in Phe quartzite in Miyar Valley.

Mesoscopic and microscopic structures within both shear zones, including asymmetric boudins of leucocratic dikes and quartz veins, shear bands, S-C fabrics, asymmetric tails on K-feldspar porphyroclasts, asymmetric grain shape foliations, and asymmetric crystallographic preferred orientations (CPOs) of quartz record the senses of shear associated with the development of the S2 foliation (Dèzes et al., 1999; Robyr et al., 2006; this study) (Figures 5, 6). Kinematic structures exposed across the KSZ are dominated by top-down to the southwest senses of shear (Figures 2b, 5a, 5b, 6), but top-up to the northeast shear indicators are exposed locally (Figures 4e, 5c). Kinematic fabrics exposed across the ZSZ in Gianbul Valley are almost exclusively characterized by top-down to the northeast senses of shear (Figures 2b, 5d, 5e, 6).

There has been considerable debate as to whether the ZSZ and KSZ are part of the same detachment fault system. Thakur (1998) and Dèzes (1999) infer that the ZSZ bends southward around Gianbul dome and joins the KSZ and Chenab normal fault. This view suggests that the entire GHS exposure in the northwestern Himalaya forms an antiformal window surrounded by normal faults (Thakur, 1998; Yin, 2006). Because no equivalent of the ZSZ-KSZ fault exists south of Gianbul dome and the Chenab normal fault, Yin (2006) postulated that the ZSZ and Main Central thrust merge at depth. The counterview that the KSZ and ZSZ are discrete structures is based on two lines of reasoning. First, syntectonic garnets in the KSZ suggest that top-to-the NE shearing occurred during burial and, therefore, before top-to-the NE extensional shearing in the ZSZ (Robyr et al., 2002, 2014). Second, mapping by Epard and Steck (2004) shows that the ZSZ bends southward around Gianbul dome—but not entirely—and can be followed eastward into a series of low-angle brittle normal faults that presumably connect with eastern segments of the South Tibetan detachment system. These early extensional faults are cut by steeper brittle faults (Epard and

Steck, 2004) associated with the northeast-dipping Zanskar normal fault that caps the ZSZ (Inger, 1998). Steep conjugate normal faults also cut the ZSZ hanging wall and splay into the Tethyan metasedimentary rocks (Dèzes et al., 1999; Searle et al., 2007). No equivalent brittle extensional structures have been observed above the KSZ.

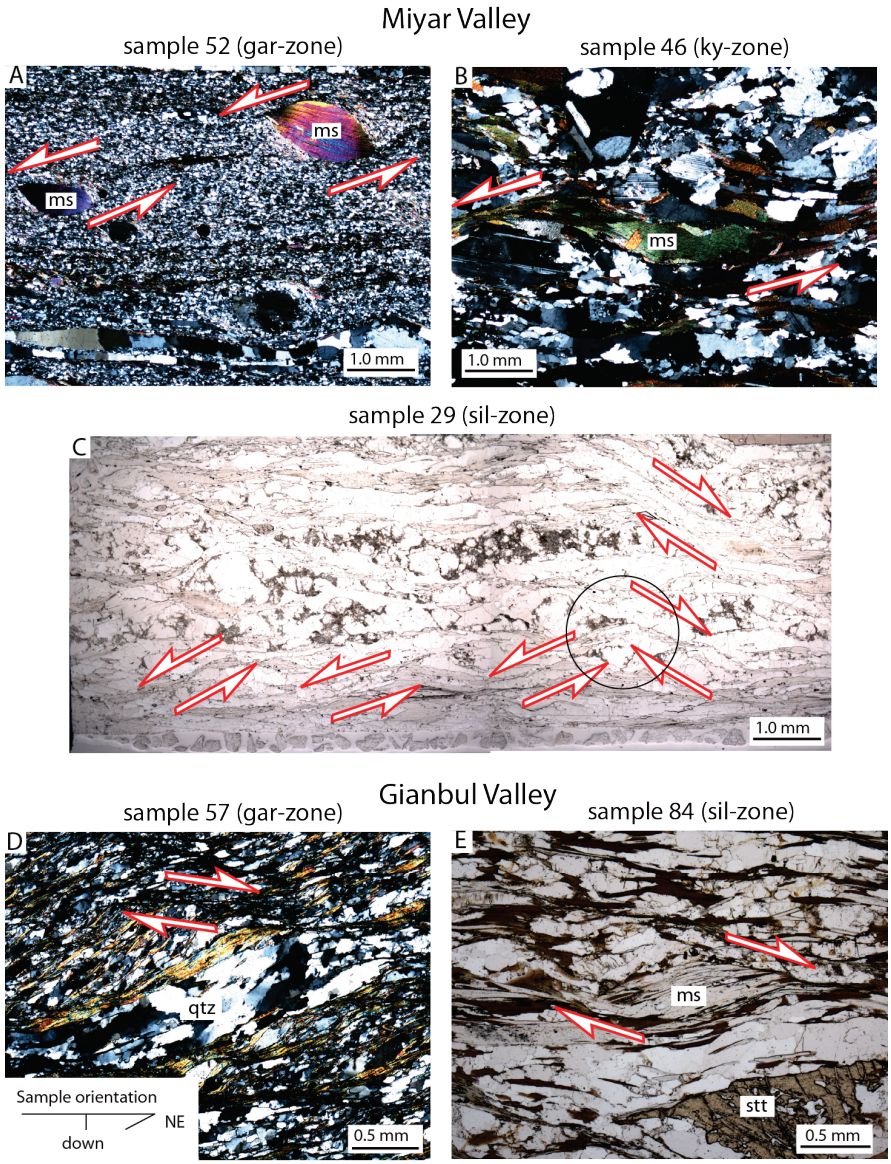

Figure 5. Photomicrographs of shear sense indicators. (A) Mica fish in Kade orthogneiss indicating top-southwest sense of shear. (B) C′-type shear bands in Kade orthogneiss indicating top-southwest sense of shear. (C) C′-type shear bands in Kade orthogneiss indicating both top-southwest and top-northeast senses of shear. Circle shows where, in this photomicrograph, top-northeast C′-type shear band cross-cuts top-southwest C′-type shear band. (D) Oblique quartz grain shear foliation and shear bands indicating top-northeast sense of shear. (E) C′-type shear bands indicating top-northeast sense of shear. All photomicrographs are from samples cut parallel to the stretching lineation and perpendicular to the foliation and are cross-polars except (c) which is plane light. Sample orientation shown; arrow pairs indicate sense of shear. Abbreviations: gar, garnet; ky, kyanite; ms, muscovite; qtz, quartz; sil, sillimanite; stt; staurolite.

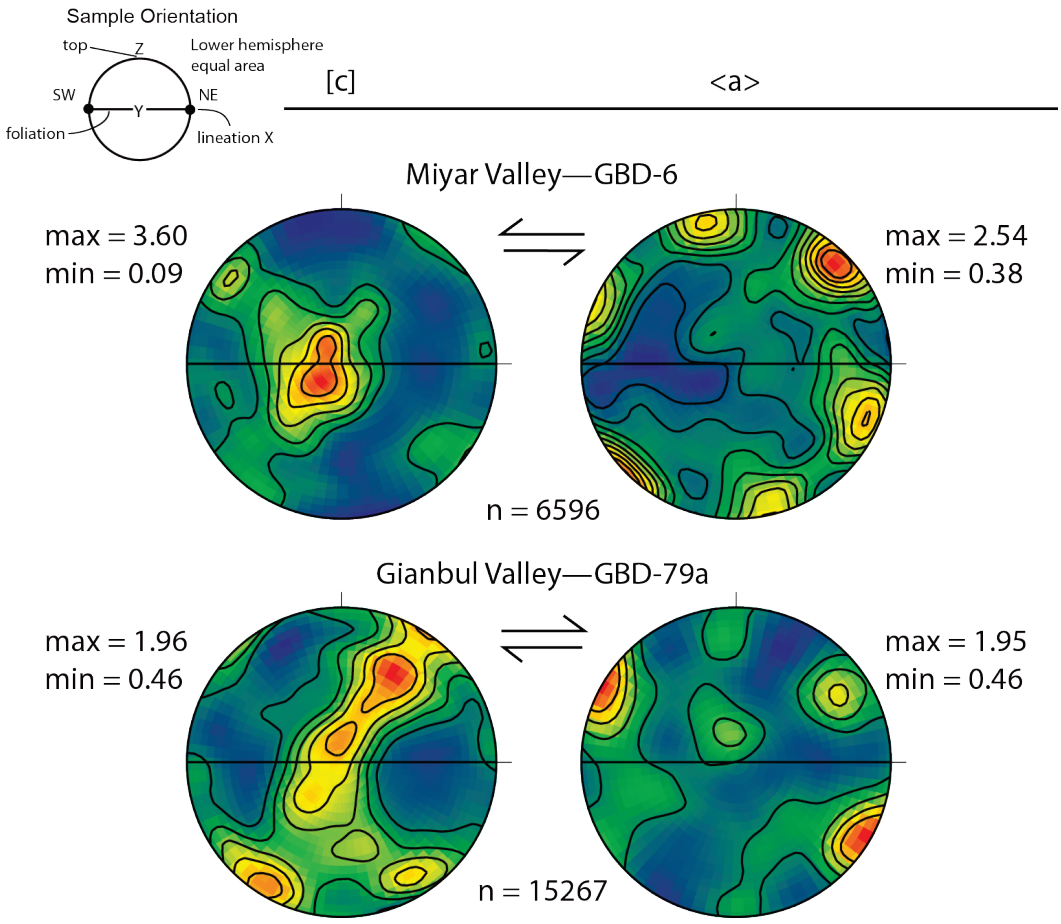

Figure 6. Representative interpretable EBSD-generated quartz CPOs from sillimanite-zone paragneiss samples from Miyar and Gianbul valleys cut perpendicular to foliation and parallel to lineation. Lower hemisphere (c) and <a> axis stereonet plots shown and oriented as indicated in the sample orientation. Data are point-per grain; contours are mean uniform density (m.u.d.) within indicated maximum (max) and minimum (min) values; number (n) of quartz grains measured noted. EBSD methods are described by Langille et al. (2010).

Minimum displacement along the ZSZ, based on the distance between metamorphic isograds (Herren, 1987), telescoped thermobarometric estimates of peak pressure in the garnet and kyanite zones (Dèzes et al., 1999), telescoped deformation temperatures (Stahr, 2013), and orientation of sheared dikes (Finch et al., 2014), is estimated at between 15 and 40 km. Considering that quartz microstructures in the ZSZ record a pure-shear component of deformation (Hasalova and Weinberg, 2011), this may be an overestimate of ductile displacement because of the assumption of 100% simple shear in these calculations. Also, a significant fraction of the net slip—60 km is required to exhume the migmatite core from

>30 km depth at a dip of 20°—may have occurred during late-stage brittle faulting. If the ZSZ originally had a gentler dip (<10° for example), the offset could have been >100 km (Dèzes, 1999); similarly high estimates of net slip have been proposed for the South Tibetan detachment in the eastern Himalaya based on mineral assemblage pressure estimates (Searle et al., 2003), telescoped isotherms (Law et al., 2011), and INDEPTH seismic-reflection profiles and the restoration of Tethyan sedimentary sequences (Hauck et al., 1998). Overall displacement along the ZSZ in Gianbul dome should be viewed as a maximum for the western Himalaya because the apparent total shear along the ZSZ decreases to the northwest (Inger, 1998). Beyond the eastern terminus of the ductile ZSZ, poor exposure precludes estimations of total offset along brittle normal faults (Epard and Steck, 2004), making it difficult to estimate the tectonic significance of these structures.

The grade of M1 Barrovian metamorphism increases from garnet-zone on the flanks of Gianbul dome to migmatites in the core. Textural evidence indicates that this metamorphism occurred during D1, and thermobarometry suggests peak conditions of ~800° C and 1.2 GPa (Pognante and Lombardo, 1989; Dèzes et al., 1999; Robyr et al., 2002). Near-isothermal decompression led to a second metamorphism, M2, that was synchronous with the D2 extension and characterized by growth of fibrolite, garnet, cordierite, and retrograde andalusite (Dèzes et al., 1999; Robyr et al., 2002; this study). The stability of biotite during both metamorphic events suggests that muscovite breakdown was principally responsible for melt generation, which constrains peak temperatures to <850° C (Dèzes et al., 1999). Temperatures were probably highest in the core of the dome, but thermometry based on Fe–Mg exchange and oxygen isotopes uniformly indicates ~800° C across melted and unmelted metasedimentary units (Robyr et al., 2002).

3. Geochronology and Thermometry

3.1. U/Th-Pb Geochronology Results

To constrain the timing of ductile deformation, LASS (laser ablation split-stream inductively coupled mass spectrometry) in situ U/Th–Pb monazite geochronology and trace-element geochemistry was conducted on monazites and zircons in 10 metamorphic and igneous thin sections. (Table 1; see Appendix 1 for analytical data, Appendix 2 for LASS methods, and Appendix 3 for petrologic sample descriptions). Samples were collected along a northeast–southwest transect across Gianbul dome, subparallel to the D2 stretching lineation (Figure 2). Metamorphic samples were analyzed to place temporal constraints on the P-T evolution of the dome; orthogneisses proved most useful because they i) are the dominant lithology in Miyar Valley, ii) contain abundant monazite, and iii) preserve both D1 contraction and D2 extension. Several samples, however, yielded igneous protolith dates rather Cenozoic metamorphic dates. Deformed and nondeformed Miocene granites were analyzed to constrain the late stages and termination of ductile extension.

3.1.1. Paleozoic dates

Most of the metamorphic rocks analyzed have Cenozoic monazite dates, but two samples preserve Paleozoic igneous protolith crystallization dates. Sample 52b is from the top of the main megacrystic Kade orthogneiss body in Miyar Valley that intrudes overlying Phe metasediments within the garnet zone. At this outcrop, top-to-the NE shear fabrics are overprinted by dominant D2 top-to-the SW shear fabrics (Figure 5a). Textures common to all orthogneiss samples—equant to elongate quartz grains with equant subgrains and bent, twinned, and cracked feldspar—are compatible with strong deformation at amphibolite-facies conditions. Monazites in sample 52b occur primarily in porphyroclastic garnets; some

have been partially replaced by allanite, apatite, and zircon. Eleven concordant analyzes of 52b monazites yield an igneous emplacement concordia date of 466 ± 10 Ma (Figure 7a). To avert potential effects of minor Pb-loss, this date was calculated using the maximum number of spot analyses consistent with a single population.

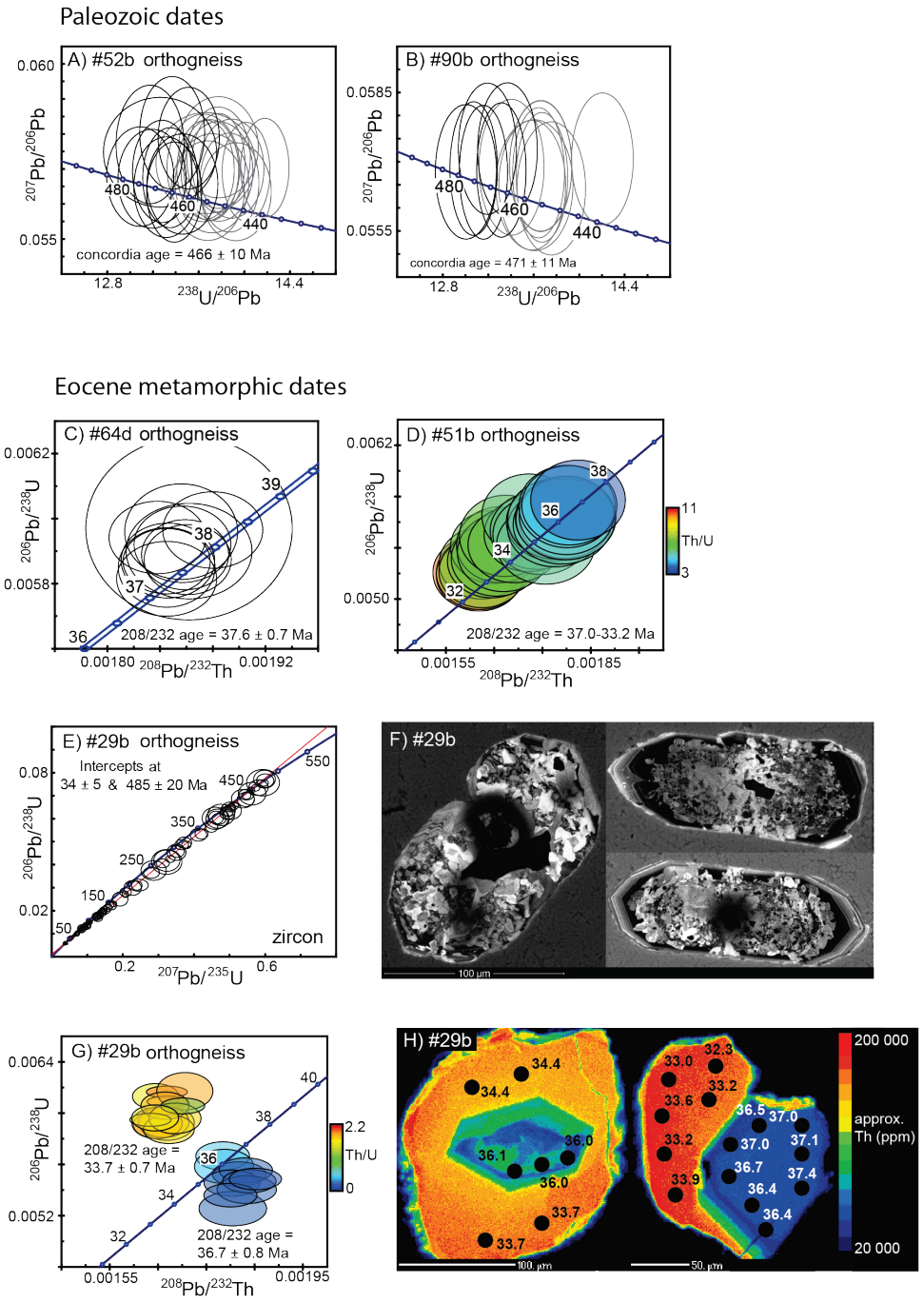

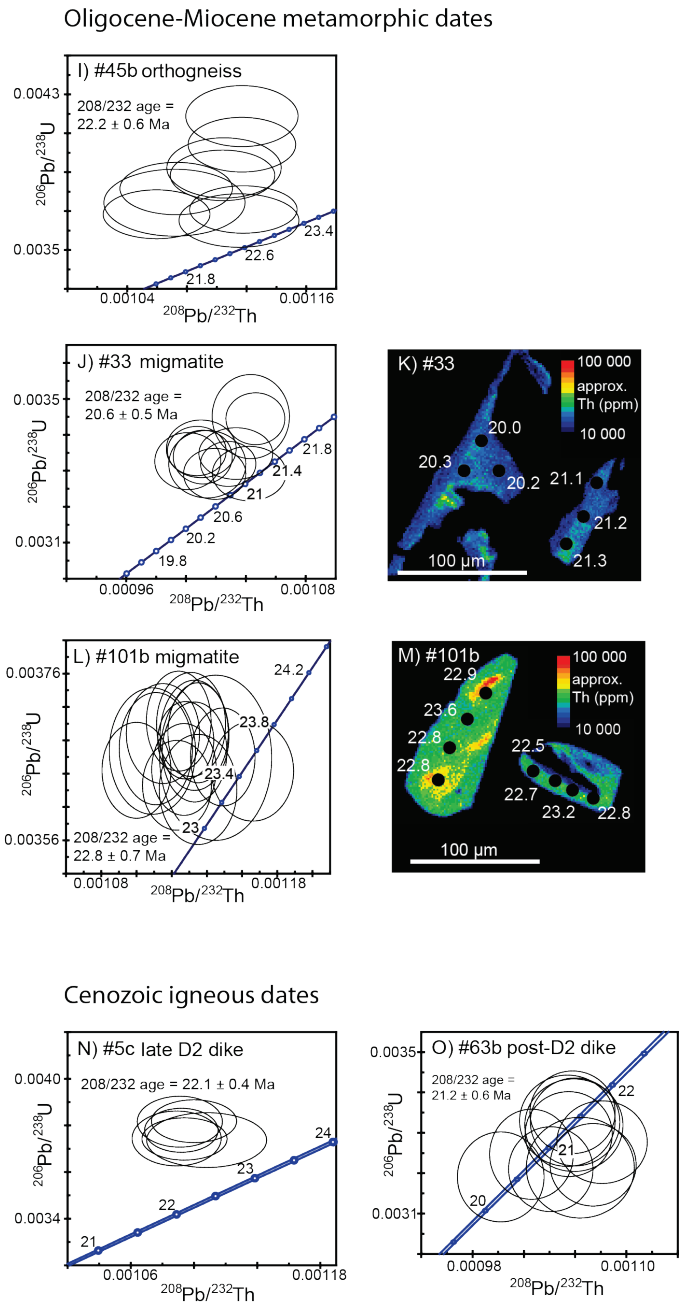

Figure 7. U/Th-Pb geochronology concordia diagrams and relevant mineral textures. Paleozoic emplacement ages of the Kade orthogneiss are recorded for samples 52b (A) and 90b (B); black ellipses were used to calculate U-Pb concordia ages and discarded grey ellipses may have undergone Pb-loss or mixing with Cenozoic rims. Samples 64d (C), 51b (D), and 29b (E and G) have M1 metamorphic monazite dates from ~37–33 Ma. Cathodoluminescence images (F) of inherited Paleozoic zircons in sample 29b have annealing textures that suggest recrystallization during Cenozoic metamorphism. Electron microprobe images (H) illustrate intragrain monazite textures for sample 29b, showing oscillatory zoning in metamorphic monazite indicative of crystallization in the presence of fluids. Monazite from samples 45b (I), 33 (J and K), and 101b (L and M) record late M2 metamorphism. Samples 5c (N) and 63b (O) (late- and post-tectonic leucogranite dikes, respectively) constrain the end of ductile deformation. For Cenozoic monazite, mean ^{232}Th–^{208}Pb dates and ±2 σ error are reported.

TABLE 1. U/TH-Pb GEOCHRONOLOGY AND ARGON THERMOCHRONOLOGY RESULTS

Sample No.	Latitude	Longitude	Lithology		monazite	±2σ	zircon	±2σ	muscovite	±1σ	biotite
Miyar Valley						σ					
GBD-5c	32.93034	76.90175	pegmatite dike	deformed	22.1	0.4	N.D.		20.7	0.1	21.3*
GBD-15	32.94436	76.90836	pegmatite dike	deformed	N.D.		N.D.		20.7	0.2	N.D.
GBD-26c	32.95797	76.88536	aplite dike	deformed	N.D.		N.D.		20.7	0.1	21.4
GBD-29b	32.96137	76.88853	pegmatite dike	deformed	36.7-33.7	0.8	485	20	20.7	0.2	N.D.
GBD-33	32.98282	76.91902	biotite migmatite	deformed	20.6	0.5	N.D.		N.D.		22.0*
GBD-34	32.98130	76.91970	migmatic gneiss	deformed	N.D.		N.D.		N.D.		23.0*
GBD-36b	32.97470	76.91834	pegmatite dike	deformed	N.D.		N.D.		20.8	0.1	22.6*
GBD-38	32.96735	76.91959	dike	deformed	N.D.		N.D.		21.1	0.2	N.D.
GBD-45b	32.90104	76.89998	orthogneiss	deformed	22.2	0.6	N.D.		N.D.		21.8
GBD- 51b	32.86728	76.83001	orthogneiss	deformed	37.0-33.2	0.8	N.D.		N.D.		25.9*
GBD-52b	32.86730	76.83075	orthogneiss	deformed	466.0	10.0	N.D.		21.4	0.1	25.1
Gianbul Valley											
GBD-57a	33.07651	77.15437	schist	deformed	N.D.		N.D.		20.2	0.2	20.4*
GBD-60b	33.07519	77.15351	biotite schist	deformed	N.D.		N.D.		21.4*	0.3	21.4
GBD- 63b	33.05773	77.11447	pegmatite dike	nondeformed	21.2	0.6	N.D.		19.7	0.1	19.8
GBD-64c	33.05815	77.11371	granite dike	nondeformed	N.D.		N.D.		19.8	0.2	19.6*
GBD- 64d	33.05815	77.11371	orthogneiss	deformed	37.6	0.7	N.D.		20.1	0.2	19.9
GBD-67a	33.05863	77.11839	pegmatite dike	deformed	N.D.		N.D.		19.9	0.2	N.D.
GBD-79c	33.06576	77.13253	biotite schist	deformed	N.D.		N.D.		20.4	0.2	22.7
GBD-90b	33.05584	77.09758	orthogneiss	deformed	471.0	11.0	N.D.		20.2	0.2	21.6
GBD-100b	33.04867	77.03239	biotite pegmatite	deformed	N.D.		N.D.		21.1*	0.2	20.9*
GBD-101b	33.04776	77.02861	migmatite	deformed	22.8	0.7	N.D.		N.D.		22.5*

Ages from Dezes et al. (1999)

Sample No.	Lithology	monazite†	95% conf.	Muscovite	±2σ
Z1§	deformed dike	N.D.		22.0	0.1
Z2	deformed dike	N.D.		20.9	0.1
Z3§	leucogranite	N.D.		20.3	0.1
Z4	leucogranite	N.D.		20.3	0.1
Z5§	leucogranite	N.D.		19.6	0.1
Z6§	leucogranite	N.D.		19.5	0.1
Z7§	nondeformed dike	N.D.		19.7	0.1
Z8	nondeformed dike	N.D.		19.6#	0.2
Z9§	nondeformed dike	N.D.		19.4	0.1
Z10	nondeformed dike	N.D.		19.3	0.1
V1-V5§	leucogranite	22.2	0.2	N.D.	

Ages from Robyr et al. (2006)

Sample No.	Lithology	monazite†	±2σ	xenotime†	±2σ	monazite**	95% conf.
02-10	nondeformed dike	22.6	0.2	N.D.		N.D.	
02-13	migmatite	N.D.		22.1	0.1	N.D.	
02-15§	migmatite	N.D.		N.D.		22.6	0.9
02-16§	migmatite	N.D.		N.D.		23.3	0.9
98-95	migmatite	25.9	0.2	N.D.		26.6	0.2

Ages from Robyr et al. (in press)

Sample No.	Lithology	monazite**	95% conf.
98-65	nondeformed dike	23.0	1.5

* Preferred age

† $^{207}Pb/^{235}U$ dates collected using thermal ionization mass spectrometry

§ Sampling location outside Gianbul and Miyar valleys

Isochron age

** Mean $^{208}Pb/^{232}Th$ ages

N.D. = not determined

Sample 90b is from an orthogneiss intruding Phe metasediments in the sillimanite zone of Gianbul Valley. This orthogneiss has a well-developed D2 structural fabric including top-NE shear indicators, and is crosscut by multiple generations of stockwork dikes that extend from the migmatites below to the intrusion complex above, where sills are concordant with the host metapelite S2 foliation. Euhedral to subhedral monazite grains in sample 90b have igneous oscillatory zoning textures and surface embayments indicative of partial dissolution. The oldest six analyses have an igneous emplacement concordia date of 471 ± 11 Ma (Figure 7b). The abundance of monazite in orthogneisses—as well as differing degrees of monazite dissolution/precipitation during Cenozoic orogenesis—seems independent of metamorphic grade, suggesting that a range in bulk composition may account for the variability.

3.1.2. Cenozoic metamorphic dates

Eocene to early Oligocene metamorphic dates that span Gianbul dome are broadly attributed to D1 burial-related deformation and M1 prograde metamorphism. Sample 64d is from a minor megacrystic orthogneiss body in the upper portion of the intrusive complex in Gianbul Valley, amid sillimanite zone Phe metapelites and leucogranite sills. Sigma shaped K-feldspar clasts preserve top-to-the NE shear fabrics and are cut by nondeformed post-tectonic leucogranite dikes (Figure 4d). Subhedral monazites are found in a quartz and feldspar matrix and have Y-rich cores with subtle oscillatory zoning, as well as embayments indicative of partial dissolution. Analyses of sample 64d form a single population of $^{232}Th/^{208}Pb$ dates at 37.6 ± 0.7 Ma (Figure 7c).

On the far side of the dome, orthogneiss sample 51b from Miyar Valley was collected from the uppermost Kade orthogneiss near overlying Phe metasediments. 51b is in the garnet

zone and exhibits discrete greenschist-facies shear bands. Monazites occur in biotite pressure shadows and some have been partially replaced by allanite, apatite, and zircon. Subhedral monazites in 51b with compositionally mottled textures have a range of dates from 37.0–33.2 Ma (Figure 7d); a corresponding decrease in Th/U may represent a transition from fluid-assisted growth to crystallization in the presence of silicate melt.

Sample 29b is from a tourmaline-bearing orthogneiss dike amid migmatites in the sillimanite zone in Miyar Valley; transposed into the D2 foliation, this dike possesses a well-developed S2 foliation, NE-SW trending mineral elongation, and both top-to-the NE and top-to-the SW kinematic indicators (Figure 5c). Whereas all other U/Th-Pb analyses were done *in situ* on thin sections, monazite and zircon mineral separates from sample 29b were mounted and analyzed in an epoxy mount. U-Pb zircon analyses for 29b fall on a mixing line between ~485 and ~35 Ma (Figure 7e), recording Paleozoic protolith emplacement and Cenozoic metamorphism that caused rim growth and the annealing of radiation-damaged cores (Figure 7f). Large (>100 μm) anhedral monazites exhibit oscillatory zoned cores and high-Th/low-Y rims; euhedral core zones have a $^{232}Th/^{208}Pb$ date of 36.7 ± 0.8 Ma and rims have a date of 33.7 ± 0.7 Ma (Figs 7g, 7f). Incorporation of ^{230}Th during the growth of the extremely Th-rich rims (~20 wt.%) explains excess ^{206}Pb and positive discordance of the younger population. As with sample 51b, Th-rich rims of 29b monazites are attributed to the presence of silicate melt. Unlike sample 51b, however, distinct core and rim zones are suggestive of two distinct crystallization events.

Several metamorphic samples yielded distinctly younger dates. In the kyanite-zone of Miyar Valley, sample 45b is from the middle portion of the main Kade orthogneiss body. The orthogneiss has dominant D2 top-to-the SW shear fabrics overprinting top-to-the NE shear fabrics. Small (<100 μm) subhedral monazites have patchy compositional variations

and are spatially associated with D2 foliation-parallel biotite; these presumably metamorphic monazites have a date of 22.2 ± 0.6 Ma (Figure 7i). To the northeast, sample 33 is from the migmatite core of the dome in the sillimanite zone of Miyar Valley and has a well-developed S2 gneissic foliation with symmetrical fabrics suggesting bulk pure shear. Sample 33 monazites are elongate, highly anhedral, have patchy compositional zoning, and yield a rather young date of 20.6 ± 0.5 Ma (Figure 7j, 7k), perhaps related to late-stage fluid-related growth. From the northern core of the dome, sample 101b from the sillimanite zone in Gianbul valley also possesses S2 gneissic foliation suggestive of bulk pure shear. Sample 101b has microstructures indicative of hypersolidus deformation with little subsequent strain and well-developed NE-SW trending mineral stretching lineation, Ls_2. Subhedral 101b monazites that are located mostly in a coarse quartz and feldspar matrix have a date of 22.8 ± 0.7 Ma (Figure 7l, 7m).

3.1.3. Cenozoic igneous dates

Sample 5c is part of a weakly deformed late D2 leucogranite dike swarm in the Miyar Valley sillimanite zone that cuts the migmatites, orthogneisses, and metasediments. The S2 foliation feathers a few mm into the rims of thick (>1 m) dikes, whereas cm-scale dikes are isoclinally folded with an axial plane parallel to the S2 foliation. Small (<100 μm) euhedral monazites in sample 5c have Y-rich cores and an average date of 22.1 ± 0.4 Ma (Figure 7n) that overlaps with the metamorphic samples. Although cores and rims could not be analyzed separately, the cluster of nearly-concordant analyses most likely represents emplacement of the dike prior to the cessation of ductile shearing. Sample 63b is from a nondeformed dike in the upper levels of the intrusion complex in Gianbul Valley that crosscuts metapelites, minor Paleozoic orthogneiss bodies (sample 64d) (Figure 4d), and prior generations of leucogranite

dikes. Small (<100 μm) euhedral monazites have Y-rich cores with oscillatory zoning, thin rims, and an average date of 21.2 ± 0.6 Ma (Figure 7o).

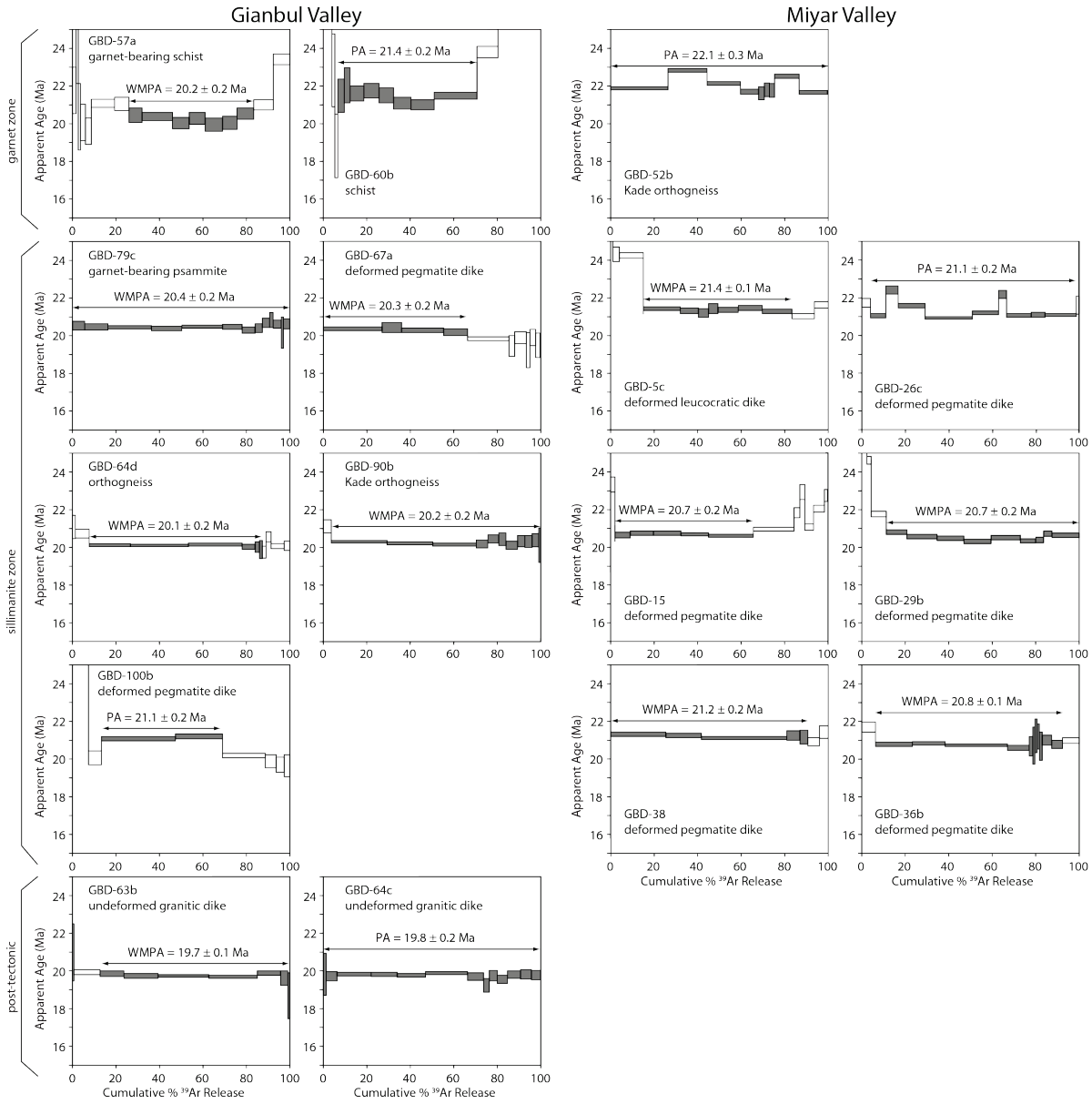

Figure 8. Muscovite $^{40}Ar/^{39}Ar$ age spectra for Miyar and Gianbul valleys. The shaded steps are those used to determine the weighted mean plateau age or preferred age (*); errors are reported to ±1 σ.

3.2. $^{40}Ar/^{39}Ar$ thermochronology

$^{40}Ar/^{39}Ar$ thermochronology was conducted on mica separations from rocks across Gianbul dome to evaluate the timing and style of moderate temperature cooling and exhumation (Table 1; see Appendix 4 for analytical data and Appendix 5 for $^{40}Ar/^{39}Ar$ methods). Twenty-one samples were analyzed from D2 deformed metapelites, orthogneisses, migmatites, and dikes across the dome along a transect subparallel to the NE–SW-trending Ls_2 stretching lineation (Figure 2). I report a weighted mean plateau age (WMPA) for those samples in which three or more consecutive steps yield ages within 1σ and comprise more than 50% of the total gas released. In the absence of a WMPA, a preferred age (PA) is reported for consecutive steps that yield a nearly flat spectrum. Errors are reported to 1σ for all ages. The estimated Ar closure temperatures for muscovite are ~415–460°C (for grain sizes from 100 to 500 μm at cooling rates of ~10 K/Myr and 0.5 GPa: Kirschner et al., 1996; Harrison et al., 2009) and for biotite are ~320 ± 50°C (for 150 μm grains at cooling rates of ~10 K/Myr: Grove and Harrison, 1996).

Sixteen muscovite samples were analyzed from D2 deformed metapelites, orthogneisses, and dikes, and post-tectonic dikes spanning garnet through sillimanite zones. Fourteen of the samples yield well-defined plateau ages and two yield disturbed age spectra (samples 60b and 100b), for which I calculate preferred ages (Figure 8, Table 1). The age for sample 100b is considered reliable because the analyzed muscovites were mostly inclusion free, whereas sample 60b muscovites contained small inclusions of biotite and, perhaps, tourmaline or graphite. Excluding sample 60b, and accounting for variable sample elevation, muscovite ages for D2 deformed samples decrease northeastward across the dome from 21.4 ± 0.1 Ma in the garnet zone of Miyar Valley to 20.2 ± 0.2 Ma in the garnet zone in Gianbul Valley. The two post-D2 granite dikes from Gianbul Valley yield ages of ~19.8 Ma.

Seventeen biotite samples were analyzed from D2 deformed metapelites, orthogneisses, migmatites, and dikes, and post-tectonic dikes spanning garnet- through sillimanite-zone rocks. Ten of the samples yield well-defined plateau ages and seven yield disturbed age spectra with preferred ages (Appendix 6). Approximately 40% of the biotite ages are older than co-existing muscovite ages regardless of structural depth, suggesting that many of the biotite ages are unreliable. Many biotites contained minor degrees of alteration to chlorite and some contain muscovite inclusions; they likely incorporated extraneous argon thus yielding ages older than the co-existing muscovite. The two post-D2 granite dikes from Gianbul Valley yield biotite ages of ~19.7 Ma.

3.3. Interpretation of results

The U/Th-Pb results record three distinct (re)crystallization events: 1) Paleozoic emplacement of the Kade orthogneiss and associated granite dikes, 2) metamorphic monazite crystallization in the presence of melt/fluid (evident from oscillatory zoning) from ~37 to 33 Ma, and 3) metamorphic monazite growth preceding the emplacement of late- to post-tectonic leucogranite dikes from 22–21 Ma. These results are broadly consistent with previous geochronology of Gianbul dome by Dèzes et al. (1999) and Robyr et al. (2006, 2014). Metamorphic xenotime from migmatite in the Miyar Valley preserving NE shear sense overprinted by SW-directed shear sense (Robyr sample 2-13) gave a TIMS $^{207}Pb/^{235}U$ date of 22.1 ± 0.1 Ma, and a monazite from a nearby migmatite (sample 98-95) has a TIMS $^{207}Pb/^{235}U$ date of 25.9 ± 0.2 Ma (Robyr et al., 2006) (Table 1); a single population of ion-microprobe $^{208}Pb/^{232}Th$ dates of ~26 Ma from the latter sample indicate that the TIMS date is an accurate age of monazite crystallization. At the base of the KSZ, post-tectonic granite dikes have a TIMS date of 22.6 ± 0.2 Ma (sample 2-10: Robyr et al., 2006) and a mean laser

ablation ICPMS $^{232}Th/^{208}Pb$ date of 23.0 ± 1.5 Ma (for sample 98-65 excluding two analyses affected by common-Pb: Robyr et al., 2006), suggesting that ductile deformation, at least in the lower part of the shear zone, ceased by this time. Two other deformed metasedimentary migmatites in Miyar Valley (samples 2-15 and 2-16) gave ion-microprobe dates with a range of ~3 Myr (Robyr et al., 2006), suggesting inheritance or prolonged recrystallization, so I interpret the youngest spot dates as the end of metamorphic (re)crystallization at ~22.5–22.0 Ma. My new leucogranite dates are in accord with seven U-Pb TIMS monazite analyses from a deformed Cenozoic granite in the sillimanite zone of Gianbul Valley that yielded a range of $^{207}Pb/^{235}U$ dates from 29 to 22 Ma (Dèzes et al., 1999). The combined geochronology results indicate that waning stages of ductile shearing continued until ~22.1 Ma and had ceased by ~21 Ma.

My thermochronology results from across the dome are consistent with muscovite $^{40}Ar/^{39}Ar$ dates for deformed granites (~22–21 Ma) and nondeformed dikes (19.8–19.3 Ma) exposed in Gianbul Valley reported by Dèzes et al. (1999). Nondeformed dike $^{40}Ar/^{39}Ar$ dates are ~1 Myr younger than nearby metamorphic sample dates; one explanation is that nondeformed dikes were emplaced after the country rocks cooled below muscovite Ar closure temperatures. However, $^{232}Th/^{208}Pb$ monazite dates for nondeformed dike sample 63 are ~2 Myr older than coexisting muscovite $^{40}Ar/^{39}Ar$ dates, and a granite dike intruded into country rock with temperatures <500° C would cool in much less than 1 Myr (e.g., Harris et al., 2000). If monazites in nondeformed dikes are inherited as xenocrysts or antecrysts (e.g., Lederer et al., 2013), $^{232}Th/^{208}Pb$ monazite dates may reflect protracted melting processes rather than dike emplacement. Different Ar closure temperatures for nondeformed dikes and country rock could also explain the younger $^{40}Ar/^{39}Ar$ muscovite dates observed for nondeformed dikes. Although 500 μm grains can undergo muscovite Ar closure at >50° C

higher than 100 μm grains (Harrison et al., 2009), finer muscovite grains were not observed in nondeformed samples. Other factors that affect Ar closure in muscovite—such as composition—may warrant further investigation.

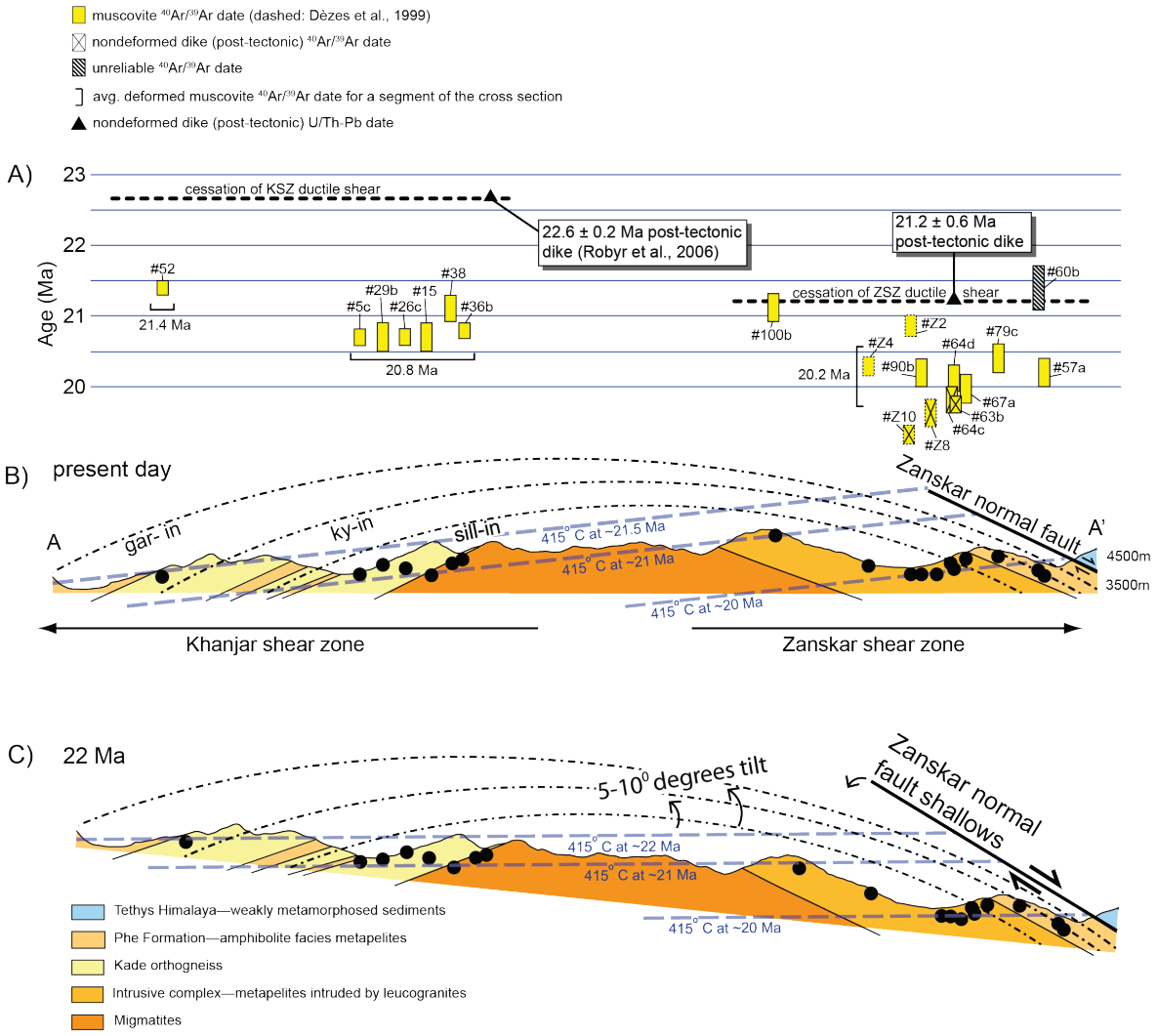

Figure 9. Summary of muscovite $^{40}Ar/^{39}Ar$ thermochronology across Gianbul dome showing exhumation in the footwall of the brittle Zanskar normal fault. (A) $^{40}Ar/^{39}Ar$ ages (rectangle heights represents 1σ uncertainties) along the Miyar–Gianbul valley transect do not define a domal geometry. (B) Unlike domed metamorphic isograds, estimated ~415° C chrontours (assumed to represent Ar muscovite closure) based on muscovite $^{40}Ar/^{39}Ar$ ages across the dome are tilted to the southwest. (C) Assuming isotherms relaxed to horizontal prior to passing through muscovite Ar closure, reconstruction of a horizontal geotherm suggests that Gianbul was exhumed as a brittle block in the footwall of the Zanskar normal fault and tilted 5–10° top-to-the SW after ~22 Ma.

Doming might be expected to bend isotherms upward and/or condense them in the core. $^{40}Ar/^{39}Ar$ dates do not preserve such a trend. Instead, they decrease in age northward across the dome and are youngest on the northeast flank (Figure 9a), which suggests that the observed $^{40}Ar/^{39}Ar$ trend is not due to doming. The simplest explanation is that isotherms had time to relax after doming ended and before Gianbul dome passed through muscovite Ar closure temperatures. $^{40}Ar/^{39}Ar$ dates indicate that rocks in the Miyar valley cooled below muscovite Ar closure as early as ~21.4 Ma, approximately 1.2 Myr before the northeast flank of the dome in Gianbul Valley. Making the first order assumption that isotherms relaxed to near horizontal prior to cooling past Ar muscovite closure, the inferred asymmetry is consistent with the exhumation of Gianbul dome as a southwest tilted block in the footwall of the Zanskar normal fault after ~21.2 Ma. If so, the age gradient indicates that the footwall tilted 5–10° after ~22 Ma as the ZSZ shallowed from 25–30° to the present-day orientation of ~20° (Figure 9c). Although ductile exhumation and magmatism ended by ~21.2 Ma, isotherms could have remained perturbed for at least several million years. Younger $^{40}Ar/^{39}Ar$ dates in the northeast could also be explained by the uniform exhumation of Gianbul dome before isotherms—perturbed by granite intrusions—fully relaxed. This might explain the discrepancy between monazite and muscovite dates for post-tectonic dike sample 63b, but fails to account for the age discrepancy between adjacent metamorphic and post-tectonic dikes samples.

Late-stage ductile deformation within Gianbul dome was ongoing at ~22 Ma and ceased by 21 Ma, as demonstrated by deformed and nondeformed leucogranite crystallization ages. Furthermore, granites in Gianbul Valley cooled from hydrous granite solidus temperatures to muscovite Ar closure temperatures in less than 2 Myr. Nearby $^{87}Rb–^{86}Sr$ biotite dates of ~18.5 Ma for the Gumburanjun granite body (Ferrara et al., 1991) probably represent lower

temperature closure at ~360° C (e.g., Baxter et al., 2002) and indicate that cooling decelerated after muscovite Ar closure at 20 Ma in the ZSZ. Apatite fission-track and (U-Th)/He dates (closure temperature of <200° C) reported by Deeken et al. (2011) increase systematically with elevation in Miyar Valley and exhibit no evidence of variable exhumation since 15 Ma. In contrast, apatite fission-track and (U-Th)/He dates from the footwall of the Zanskar normal fault indicate exhumation events at 14–10 and 9–6 Ma (Shurtleff et al., 2013); some of the inferred 5–10° tilting in the footwall of the Zanskar normal fault likely occurred during these younger episodes of fault slip. The proposed fit of planar isotherms to the $^{40}Ar/^{39}Ar$ data may favor a >5 Ma period of quiescence after doming and magmatism, allowing perturbed isotherms time to relax to near-horizontal before tilting of the footwall block.

4. Discussion

4.1. Geochronologic Constraints on Ductile Deformation and Metamorphism

Prograde metamorphism is recorded by monazite (re)crystallization dates from 37–33 Ma across Gianbul dome and from 37–30 Ma near Gumburanjun (Walker et al., 1999); these ages likely represent the peak Barrovian M1 metamorphism caused by crustal thickening. Oscillatory zoning—commonly inferred to result from growth in the presence of melt—in M1 monazites may indicate that limited muscovite dehydration occurred in the GHS during this phase. Northwest of Gianbul dome, where partial melting was less pervasive, Sm–Nd garnet dates from 33 to 28 Ma (Vance and Harris, 1999) record prograde burial-related metamorphism and 27 Ma metamorphic monazite in upper GHS metapelite (Horton and Leech, 2013) may reflect near-peak metamorphic conditions. Peak temperatures in the middle crust were likely attained by a combination of thermal re-equilibration, radiogenic

heat production, and mechanical heating in shear zones. Retrograde monazite growth at 26 Ma (Robyr et al., 2006) marks the transition from contractional M1 metamorphism and D1 deformation to extensional M2 metamorphism and D2 deformation. Based on U-Pb monazite ages from leucogranites that record contractional and extensional shear, Finch et al. (2014) also suggest that ~26 Ma marks the upper bound for the onset of ductile extension along the ZSZ.

The M1 Barrovian metamorphic isograds are telescoped within the ZSZ by D2 deformation, and overprinted in the core of Gianbul dome by M2 sillimanite-grade metamorphism and migmatization. As analogous structures, the KSZ and ZSZ might be expected to have similar ages. However, the ages of discordant dikes demonstrate that ductile extension ended by 22.6 Ma in the KSZ and 21.2 Ma within the ZSZ. If Miyar Valley exposes deeper portions of the Greater Himalaya sequence, the age discrepancy suggests that shear zones within the GHS propagated upward over time (Searle et al., 2007), or that distributed shear became condensed at the top of the sequence. Alternatively, longer-lived and/or higher strain within the ZSZ explains the greater degree to which isograds are collapsed within the ZSZ (Figure 9). Continued exhumation after ~22 was most likely accommodated by the overlying brittle Zanskar normal fault.

4.2. Timing of Gianbul Dome Formation

Gianbul dome probably did not form as a consequence of D1 contractional folding. Flexural flow folding within the crystalline nappe complex is a possible explanation for the proposed opposing-sense contractional deformation along limbs of the dome (e.g., Robyr et al., 2002, 2006, 2014) directed toward the fold hinge (top-to-the NE in Miyar Valley and top-to-the SW in Gianbul Valley). But finite element modeling conducted by Hudleston et al. (1996)

suggests that flexural flow folding is unlikely in crystalline rock without high anisotropic competency, unless there are alternating low and high viscosity layers. Because the Kade orthogneiss preserves a contractional fabric but has neither a high anisotropic competency nor layers with alternating viscosity, flexural flow folding is an improbable mechanism for the domal morphology. The occurrence of distinct opposing-sense D1 contraction events is a more feasible explanation for opposing-sense D1 contractional structures.

Viewing the ZSZ and KSZ as the same structure—which is compatible with both channel flow and tectonic wedge models—raises the possibility that the top-NE kinematic indicators in the KSZ are not D1 contractional structures (e.g., Robyr et al., 2002, 2006, 2014), but are instead early D2 structures coincident with early extension along the ZSZ. D1 top-SW structures have not been observed in the KSZ, except possibly for one sample that has the top-NE C' bands that cross-cut top-SW C' bands (Figure 5c). Considering that D1 top-SW structures would have been reactivated or overprinted during D2 top-SW shearing, they may be difficult to identify. If the KSZ and ZSZ were part of a bent roof fault (e.g., Yin, 2006), then the KSZ segment may have been a backthrust structure on the southern flank of the preexisting Gianbul dome. If, on the other hand, the KSZ-ZSZ was originally a planar NE-dipping extensional shear zone, subsequent doming must have transposed the KSZ segment into its current SW-dipping orientation. I favor the latter scenario for three reasons. First, the kinematic indicators are asymmetric across the dome: in the KSZ, distributed top-to-the NE shear is generally overprinted by top-to-the SW shear in the upper levels, whereas the ZSZ exhibits almost exclusively top-to-the NE shear that became concentrated in the upper levels. Second, whereas ductile shearing during passive roof faulting would have caused uniform flattening of footwall isograds, metamorphic isograds in Gianbul dome are more condensed within the ZSZ. Third, coeval opposing-sense ductile extension that ended

at different times in the KSZ and ZSZ suggests that the kinematic histories of the two faults diverged after doming.

Based on this rational, I propose that doming postdated a transition from thrust to normal-sense motion in the upper GHS (at approximately 26 Ma) and transposed early extensional features in the KSZ. Ductile extension—and thus doming—ended prior to the emplacement of post-tectonic dikes at ~22.6–21.2 Ma. This is confirmed by the $^{40}Ar/^{39}Ar$ transect that does not exhibit signs of doming after Gianbul dome cooled through Ar muscovite closure at ~22–21 Ma. Notably, the episode of ductile extension and associated doming in the middle crust from ~26 to 22 Ma coincides with syn-tectonic magmatism along the Karakoram shear zone (Valli et al., 2008), a ~1000 km strike-slip fault that has accommodated lateral extrusion in the western Himalaya. I propose that this was a period of tectonic relaxation in response to weakening of thickened crust, during which lateral extrusion along crustal-scale strike-slip faults and southward extrusion of ductile middle crust simultaneously accommodated regionally-extensive subsidence.

4.3. Doming Mechanisms

An adequate model for Gianbul dome formation must explain several key datasets: i) core of anatectic melt, ii) syn-extensional leucogranites crosscutting gneisses, iii) ductile extensional deformation, iv) coeval opposing normal-sense shear zones, v) asymmetric ductile extension, and vi) brittle normal slip along the previously-ductile ZSZ (see Table 2 for comparison of doming models). Below, I discuss three principal factors—lithologic differences, upper-crustal extension, and decompression melting—that explain the formation of Gianbul dome.

TABLE 2. SUMMARY OF DOMING MODEL PREDICTIONS

Doming Model	Structural and kinematic predictions	Chronologic predictions
1. Thrust duplexing during N-S contraction	Fault contact between core and cover	Doming during contractional shear
	Duplicate structural section	Doming during crustal thickening
	Hanging wall originated at higher temperatures and greater depths than footwall	Asymmetric cooling with ages increasing up-dip
	Foliation may or may not be parallel to the fault	
	Unidirectional lineations and reverse up-dip shear sense	
5. Tectonic wedge model (purely kinematic)	Top-SW shear overprinted by top-NE shear	Both limbs record top-SW sense of shear
	Parallel kinematic histories for both limbs of the dome	Both limbs overprinted by top-NE sense of shear
3. Upper-crustal extension (i.e. core complex)	Doming in the footwall of a detachment fault	Synchronlous with localized upper-crustal extension
(including instability in upper crust after plugged channel flow)	Low grade hanging wall above high grade footwall	Magmatism may occur throughout exhumation
	Pure shear component	Coeval opposing normal-sense shear
	Asymmetric simple shear (highest near hanging wall)	Asymmetric cooling with ages decreasing down dip
	Omitted structural/metamorphic section at fault	
	Footwall strain increases towards the core-cover contact	
	Unidirectional footwall lineations	
4. Diapirism in static stress field	Core of migmatite and/or leucogranite	Simultaneous radial shearing
	Concentric foliation	Rapid ascent
	Dome-up sense of shear	Rapid cooling
	Finite strain increases towards contact	Symmetrical cooling
	Syn- to post-kinematic growth of metamorphic porphyroblasts in cover rocks	
	Core-cover contact characterized by intrusion of core into cover	
	Steep metamorphic field gradient in cover rocks	

4.3.1. Paleozoic Orthogneiss Megaboudins

With regard to gneiss dome formation, the nearly ubiquitous presence of Paleozoic orthogneiss in the cores of Himalayan gneiss domes is worth noting. In the northwest Himalaya, the Greater Himalayan sequence consists of a NE-SW trending series of domes cored by orthogneiss, including Barnaj, Bhazun, Cishoti, Chenab, Haptal, Umasi La, Poet La, and Gianbul domes (Herren, 1987; Kündig, 1989; Dèzes, 1999; Stephenson et al., 2001) (Figure 2). In the eastern part of the orogen, orthogneiss is also documented in the cores of many North Himalayan gneiss domes, including Lhagoi Kangri (Watts et al., 2005), Mabja (Lee et al., 2004; Watts et al., 2005), Kampa (Quigley et al., 2006), and Kangmar (Lee et al., 2000) domes. Migmatitic textures in the Kade orthogneiss suggest that melting of ortho- and paragneiss generated Miocene magmas (Pognante et al., 1990; Pognante, 1992). Furthermore, bimodal $^{87}Sr/^{86}Sr$ ratios suggest that Miocene leucogranites in the western Himalaya had two source components: low initial $^{87}Sr/^{86}Sr$ (<0.76) from metawacke or metapelite and high $^{87}Sr/^{86}Sr$ (>0.76) from Paleozoic orthogneiss (Ferrara et al., 1991). The orthogneisses presumably formed during thin-skinned Paleozoic thrusting (Gehrels et al., 2003).

Field observations suggest that migmatization in Gianbul dome was most prevalent in paragneisses. Paleozoic orthogneiss protoliths probably contained less muscovite than surrounding metapelites because existing muscovite formed during the retrogression of biotite and sillimanite (Pognante, 1992). Consequently, they would have produced less muscovite-dehydration melt and may have been more resistant to D2 deformation, undergoing less vertical thinning. If the Kade orthogneiss was more competent than the surrounding metasedimentary rocks, it may be a dome-scale megaboudin around which strain concentrated during vertical thinning. This could help explain the high strain fabrics

preserved in the uppermost Kade orthogneiss and overlying Phe metapelites (Figures 4e, f). These observations suggest that strain and melt localization in the GHS may be related to the distribution of Paleozoic granites. But vertical thinning around orthogneiss bodies neither accounts for decompression melting nor the magnitude of ductile shear accommodated by the ZSZ and KSZ.

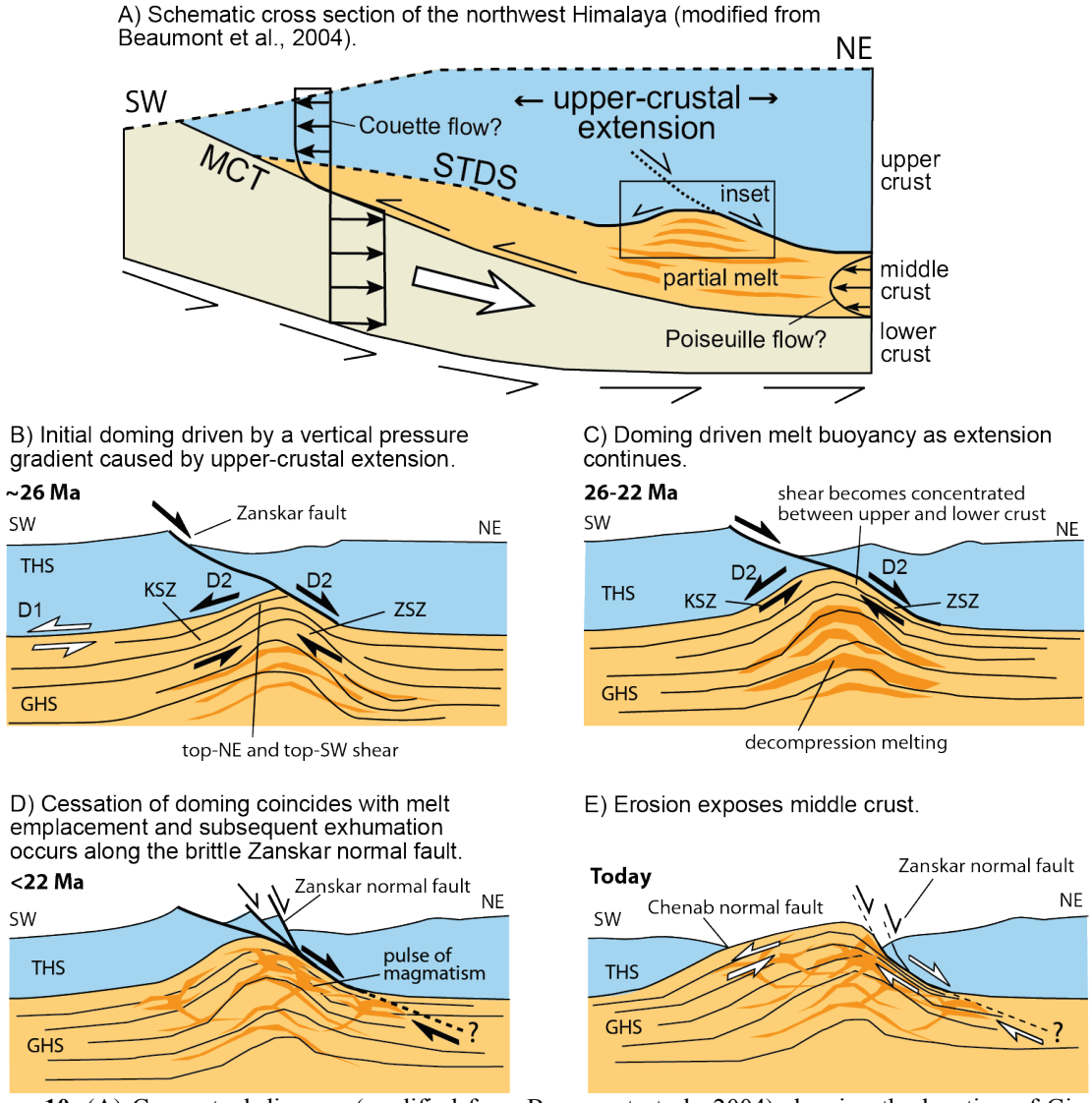

Figure 10. (A) Conceptual diagram (modified from Beaumont et al., 2004) showing the location of Gianbul dome formation in the middle crust. Colors correspond to Figure 1: the Tethys Himalaya in the upper crust is blue, the GHS in the middle crust is orange, and the subducting Indian plate is tan. (B-E) Conceptual diagrams for of Gianbul dome (see inset location in A) modified from Rey et al. (2011). Initial doming is driven by vertical pressure gradients below a thinning upper crust (B), after which decompression melting causes buoyancy-driven ascent of the dome (C). Melt emplacement marks the end of doming at ~22 Ma as normal-sense displacement in the Zanskar shear zone was transferred to the brittle Zanskar normal fault (D). Subsequent surface erosion has exposed the core of Gianbul dome at the surface (E).

4.3.2. Upper-crustal Extension

My results indicate that the formation of Gianbul dome occurred between depths of approximately 40 km and 15 km during a period of extensional deformation and decompression melting in the upper GHS that lasted from ~26 to 22 Ma (Figure 10a). These constraints rule out doming mechanisms associated with D1 contraction such as flexural folding and early thrust duplexing (Table 2). Also, my $^{40}Ar/^{39}Ar$ results suggest that Gianbul dome was exhumed as a coherent, rigid block in the footwall of the Zanskar normal fault (Figure 9). Thus, upper-crustal exhumation-related processes since ~22 Ma cannot explain doming either.

I interpret the SW-dipping top-to-the NE shear fabrics preserved in the KSZ to the transposition of initially NE-dipping extensional deformation fabrics. Thus, doming occurred after considerable extensional offset had been accommodated by the ZSZ-KSZ. Ductile exhumation (e.g., Lee et al., 2000; Beaumont et al., 2004; Jamieson et al., 2006) or thrusting (e.g., Yin, 2006) of the GHS above a steepened segment of the footwall ramp could explain early domal morphology, but fails to explain decompression melting. More likely, as shown in two-dimensional thermal-mechanical models by Rey et al. (2011), reactivation of the previously contractional ZSZ (Dèzes et al., 1999; Finch et al., 2014) and thinning of the upper crust created footwall pressure gradients that drove initial doming (Figure 10b). This model accounts for near-isothermal decompression, asymmetric metamorphic isograds, and kinematics on either limb of Gianbul dome (Table 2).

A vertical pressure gradient below the thinning Tethyan Himalaya sequence may have initiated upward flow of GHS crust that was sufficiently ductile ($\geq$7% melt fraction: Rosenberg and Handy, 2005) but not yet highly buoyant. Destabilization of—and consequent extension in—upper crust above Gianbul dome could have been caused by southward

channel tunneling of the GHS and/or foreland-directed gravitational sliding of upper crust above ductile middle crust (e.g., Beaumont et al., 2004). Focused surface denudation along major rivers may also cause localized vertical pressure gradients in middle crust (e.g., Vannay et al., 2004; Montgomery and Stolar, 2006), but the fact that doming occurred during widespread orogen-perpendicular extension along the ZSZ suggests that doming was not driven by erosional processes. I conclude that Gianbul dome formation in the footwall of the ZSZ required upper-crustal extension; ductile flow driven by a vertical pressure gradient in the footwall of the ZSZ fits all of my observations, except the apparent link between decompression melting, ductile extension, and the cessation of doming.

4.3.3. Effects of Partial Melting

The high Th monazite rims indicate that some silicate melt may have been present as early as 33 Ma (Figure 7h), but there is no evidence that shear heating (which would have been severely moderated by partial melting) or advection of mantle heat via magmas (of which there are no signs) caused high percentages of melting. The near-isothermal decompression of Gianbul dome (Dèzes et al., 1999) and the resulting high-T/low-P metamorphism suggests that muscovite dehydration melting during decompression accounts for most of the melting observed in Gianbul Valley (Robyr et al., 2006). Because at least 10% of melt—and more likely ~30% melt—is required for positive buoyancy to drive doming (Teyssier and Whitney, 2002), sufficient melt for density-driven doming was probably not produced until decompression began.

Stockwork dikes, sills, and the voluminous Gumburanjun granite demonstrate that partial melt percentages were sufficient for ductile extrusion and eventually reached the 10–40% necessary for a >0.2 g/cm^3 density contrast between leucocratic melt and garnet-biotite

gneiss (Teyssier and Whitney, 2002). Thus, the positive buoyancy of partial melts may have driven later stages of dome formation (e.g., Robyr et al., 2006). After exhumation began, and once sufficient melt was generated, a positive feedback among decompression, partial melting, and the positive buoyancy of partially melted rock (e.g. Teyssier and Whitney, 2002), could have driven doming (Figure 10c). In this sense, Gianbul dome may be similar to other Himalayan gneiss domes including Malashan dome (Aoya et al., 2005) and Renbu dome (Guo et al., 2008) that have also been attributed to diapiric rise of partially molten crust. Density-driven doming in a static stress field will yield a dome cored by plutons and/or migmatites with concentric foliation and radial and tangential stretching lineations (e.g. Schwerdtner et al., 1978; Brun and Pons, 1981; Dixon and Summers, 1983; Van Den Eeckhout et al., 1986; Jelsma et al., 1993) (Table 2). This set of geologic relationships is generally not observed in the northwestern Himalaya (Kündig, 1989; Vanney and Steck, 1995; Steck, 2003; Yin, 2006). In an extensional tectonic environment (e.g., Rey et al., 2011) or when crustal flow involves a lateral component (e.g., Whitney et al., 2004), buoyancy-driven doming can cause elongate domes with dominant unidirectional stretching lineations. Gianbul dome exhibits characteristics consistent with the latter scenarios: an elongate geometry, steeper dipping orogen-parallel limbs, a dominant orogen-perpendicular stretching lineation, and normal-sense shear.

Positive feedback between melting and exhumation best explains the existence of a single magmatic pulse at ~22 Ma, rather than a protracted period of generation and emplacement of leucogranites. The low viscosity and density of partially melted regions can only be sustained if the melt does not migrate. Furthermore, once emplaced in colder rock, leucogranite dikes and sills may crystallize rapidly (probably in less than 10 ka in the upper crust: Harris et al., 2000) and strengthen the host rock. The fact that leucogranites in Gianbul

dome are exclusively late-D2 to post-tectonic and have a narrow age range from 22 to 21 Ma is consistent with accelerated doming immediately prior to a final pulse of magma migration (Figure 10d). Leucogranite emplacement also coincided with the end of extensional shearing within the KSZ at ~22.6 Ma, after which telescoping of the Barrovian metamorphic isograds continued within the ZSZ until ~21.2 Ma.

4.4. Implications for Tectonic Models

Because ductile extension within the ZSZ only lasted from ~26 to 21 Ma, mid-crustal channel flow (e.g. Nelson et al., 1996; Beaumont et al., 2001; Grujic et al., 2002; Langille et al., 2010) would have been restricted to this relatively brief period of orogenesis in the northwestern Himalayan. Nevertheless, the predictions of the channel flow model are useful for evaluating the orogen-scale forces that affected dome formation. According to the model, a low viscosity layer in the middle crust (i.e. the GHS) can begin tunneling if there is a horizontal gravitational potential energy gradient, but active channel flow extrusion—driven by surface denudation—only commences once the channel penetrates the surface (Beaumont et al., 2004). Continued contraction after arrested channel tunneling, or plugged channel flow, could cause hinterland antiforms and crustal-scale folds. The presence of Tethyan sediments south of the GHS (Thakur, 1998; Yin, 2006), the regional antiformal structure the GHS, and the occurrence of gneiss domes are consistent with channel tunneling in the northwest Himalaya that was arrested prior to reaching the surface. A transient phase of southward GHS tunneling could partially explain the development of domal structures in the northwest Himalaya. For Gianbul dome, however, the temporal link between the cessation of doming and the pulse of granite emplacement suggests that doming was influenced by the positive buoyancy of high melt percentages. Instead of ductile exhumation of a channel

below a passive hanging wall, thinning of the upper crust probably facilitated decompression melting that gave way to buoyancy-driven ascent of middle crust.

The tectonic wedge model (Yin, 2006; Webb et al., 2007, 2013) provides an alternative explanation for the southward extrusion of the GHS. This model suggests that, while GHS and overlying Tethyan Himalaya sequence were both thrust southward along the Main Central thrust, a change in the relative motion of the two thrust sheets caused a shift from top-to-the N to top-to-the S shear between them (in this case, along the ZSZ-KSZ roof fault) (Table 2). This explains the kinematics of deformation observed in the ZSZ, but fails to explain i) coeval opposing-sense extensional shear within the ZSZ and KSZ; ii) top-to-the NE shear overprinted by top-to-the SW shear in the KSZ; iii) the asymmetry of the condensed metamorphic isograds in Gianbul dome; and iv) the temporal and spatial link between penetrative D2 deformation, generation and emplacement of melts, and doming. Thus, neither channel flow nor tectonic wedging models independently explain the formation of Gianbul dome. However, localized vertical pressure gradients caused by upper-crustal extension, coupled with melt buoyancy, could explain Gianbul dome formation in the regional context of either model.

5. Conclusions

Gianbul dome exposes GHS migmatite, Paleozoic orthogneiss, and metasedimentary rock cross-cut by multiple generations of leucogranite dikes. These rocks expose a D2 penetrative deformation event characterized by a domed high-strain foliation and NE-SW trending stretching lineation within the top-to-the SW KSZ on the southwest flank and the top-to-the NE ZSZ on the northeast flank. Monazite U/Th-Pb geochronology and mica $^{40}Ar/^{39}Ar$ thermochronology across Gianbul dome record three distinct tectonometamorphic episodes:

1) Paleozoic intrusion of the Kade orthogneiss and associated granite dikes at ~470 Ma; 2) prograde M1 Barrovian metamorphism from 37 to 33 Ma during contractional D1 deformation; and 3) formation and exhumation of Gianbul dome between 26 and 22 Ma during high-T/low-P metamorphism, partial melting, and extensional D2 deformation. The late stages of the D2 ductile shearing persisted through 22 Ma, but subsequent exhumation was accommodated by ridged block tilting in the footwall of the Zanskar normal fault. Assuming isotherms relaxed to near horizontal prior to cooling through muscovite Ar closure, $^{40}Ar/^{39}Ar$ dates and low-temperature thermochronology suggest that the footwall was tilted approximately 5–10° top-to-the SW after 22 Ma.

My interpretation of Gianbul dome formation in the middle crust—driven first by upper-crustal extension and later by the positive buoyancy of partial melts—is neither entirely consistent with surface denudation-driven channel flow, nor tectonic wedge propagation. I favor a model in which localized upper-crustal extension after ~26 created vertical pressure gradients (e.g., Rey et al., 2011) in the upper GHS and initiated upward flow of ductile crust. My results are consistent with subsequent doming that was driven by a positive feedback among dehydration melting, buoyancy, exhumation, and decompression. Doming culminated with the injection of anatectic melts into the upper levels of the dome at ~22 Ma, neutralizing the effects of melt buoyancy and potentially adding strength to the host rock as leucogranites crystallized. Despite these new constraints on dome formation, our inadequate understanding of the complex feedbacks among partial melting, buoyancy, and shearing—the forces driving rapid exhumation of middle crust—continues to inhibit the development of coherent models for gneiss doming in orogenic settings.

II. Focused radiogenic heating of middle crust to ultrahigh temperature in southern Madagascar

1. Introduction

As zones of focused metamorphism, melting, and ductile deformation, hot crustal sections are especially important for understanding the evolution of the middle and lower crust in convergent orogens. Extreme regional metamorphism at ≥900° C is referred to as ultrahigh-temperature metamorphism (UHTM). Such temperatures are increasingly recognized in continental collision zones worldwide (Kelsey, 2008; Kelsey and Hand, 2014; and references therein), and geophysical evidence of melt (Unsworth et al., 2005) and UHT granulite xenoliths (Hacker et al., 2000) suggest that UHTM may be occurring beneath the Tibetan plateau. In many UHT orogens, the extreme temperatures appear to have been sustained for >40 Myr (Kelsey and Hand, 2014), despite the fact that prograde (e.g., Lyubetskaya and Ague, 2009) and melting reactions (e.g., Thompson and Connolly, 1995) are endothermic and buffer temperature increases.

Ultrahigh temperatures in continental crust that exceed the conductive geotherm require heat advection and/or heat production, yet such heating mechanisms remain difficult to detect and poorly quantified. Heat from the mantle can advect in several ways. For example, high seismic velocities at the base of continental crust have been interpreted as underplated basalt (e.g., Rudnick and Jackson, 1995), which can cause melting (Dufek and Bergantz, 2005) and UHTM (Annen et al., 2006; Dewey et al., 2006) in the lowermost crust. Alternatively, amagmatic mantle heat advection can occur in subduction-to-collision orogens when hot backarcs contract (Currie and Hyndman, 2006; Brown, 2008).

Endogenous continental heat can be produced by mechanical heating and radioactive decay. Mechanical heating (also referred to as shear heating or viscous dissipation) of strong lithologies in continental collision zones may be significant (e.g., Kincaid and Silver, 1996; Stüwe, 1998; Burg and Gerya, 2005), especially in shear zones (Nabelek et al., 2010). However, mechanical heat production is probably most effective below 600° C due to the negative feedback between mechanical heating and thermal weakening (Stüwe, 2007). The dominant heat-producing elements (HPEs) are U, Th, and K. Natural abundances of HPEs in rocks are variable, and they strongly influence crustal temperature and therefore rheology (e.g., England and Thompson, 1984; Le Pichon et al., 1997). Given sufficient time, radiogenic heat production (RHP) can lead to UHTM (McKenzie and Priestley, 2008; Clark et al., 2011; Clark et al., 2014). Because HPEs are generally incompatible during melting of the crust and mantle, magmatic processes tend to concentrate HPEs in the upper continental crust (Bea, 2012). Despite this, the vertical distribution of HPEs in deep boreholes and exposed crustal sections does not correlate with depth (e.g., Furlong and Chapman, 2013), and some mid–deep crustal granulites contain abundant U, Th, and K (Behn et al., 2011). Recent evaluations of seismic wavespeed and heat-flow data have even suggested that the lower crust could be quite radiogenic (Hacker et al., 2011, 2015). But the role of RHP remains controversial because heat-production rates for the middle and lower crust are difficult to quantify (Hacker et al., 2011, 2015) and because the removal of HPEs during the migration of melts may limit the importance of RHP at hypersolidus temperatures (e.g., Sandiford and McLaren, 2002; Bea, 2012).

The objective of this study is to evaluate the role of RHP in contractional tectonic settings—and with respect to UHTM in particular—by studying the Neoproterozoic–Cambrian continent–continent collision zone exposed in southern Madagascar. First, I

evaluate and supplement the previous U/Th-Pb geochronology across southern Madagascar to assess the duration of orogenesis and high temperatures. Second, I apply 4+ cation thermometry to constrain peak temperatures and isotherms geographically. Third, I employ two-dimensional numerical modeling based on (i) geochronology, (ii) thermometry, and (iii) whole-rock compositions across southern Madagascar to appraise heterogeneous crustal heat production during orogenesis. This modeling approach differs from other studies (e.g., England and Thompson, 1984; Beaumont et al., 2004, 2010; Jamieson et al., 2004, 2006; Sizova et al., 2014; etc.) by calculating spatially varying heat production from U, Th, and K concentrations in rocks rather than assuming a uniform lateral distribution; my results highlight some of the problems associated with such assumptions. After assessing the effects of RHP during the assembly of Gondwana, I address broader questions that apply to orogens worldwide: Why do some metamorphic protoliths contain especially high concentrations of HPEs? How mobile are HPEs during metamorphism and melting? And to what extent can RHP cause thermal anomalies in thickened crust?

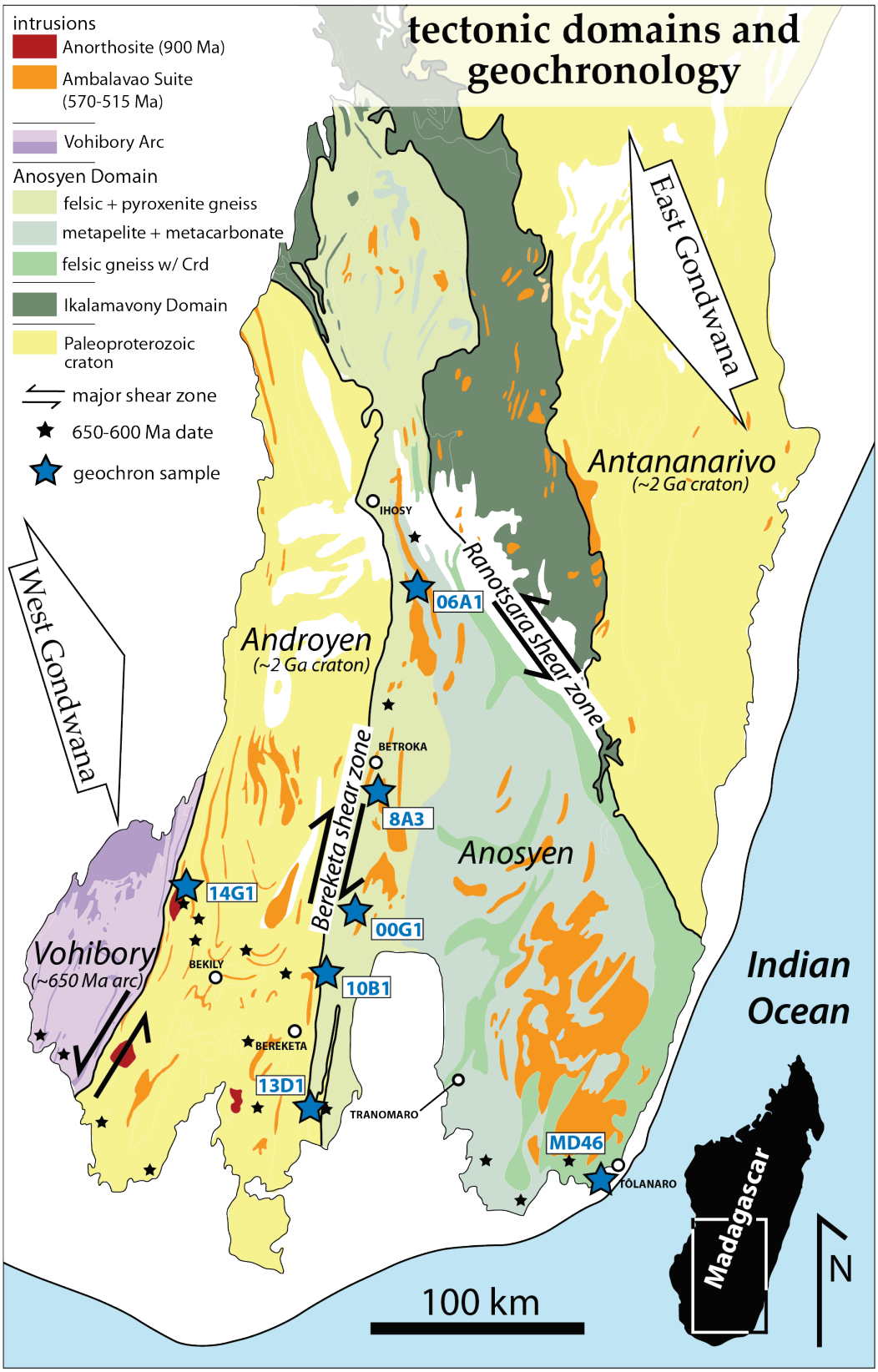

Figure 11. Lithotectonic map of southern Madagascar based on GAF-BGR (2008) showing geochronology sample locations.

2. Geologic Background

Southern Madagascar exposes a lower crustal section of the Gondwanan collisional orogen that formed during the late Neoproterozoic–early Cambrian collision of East and West Gondwana (Stern, 1994; Collins and Pisarevsky, 2005; Tucker et al., 2014). It is presumed to be analogous to the present-day India–Eurasia collision because of its great extent from the Middle East through East Africa, Madagascar, Southern India, Sri Lanka, and Antarctica (Collins and Windley, 2002).

Extensive metamorphism, melting, and ductile shearing during the assembly of Gondwana obfuscated the pre-collision geologic record such that the ages of protoliths and locations of major sutures remain uncertain. Prior to collision, the Archean Dharwar and Congo/Tanzania cratons of East and West Gondwana, respectively, were separated by the Neoarchean–Paleoproterozoic Antananarivo domain. The Antananarivo domain was either the western margin of East Gondwana (Müller et al., 2000; GAF-BGR, 2008; Tucker et al., 2011, 2014; Ichiki et al., 2015) or part of a microcontinent (Azania) that collided first with West Gondwana and later with East Gondwana (Collins and Pisarevsky, 2005; Collins et al., 2014). Prior to the final assembly of Gondwana, much of central Madagascar, including the Antananarivo Domain, was intruded by the ~850–700 Ma Imorona–Itsindro Suite that has been attributed to either intracontinental extension (Tucker et al., 2011, 2014), or a west-facing continental magmatic arc on the western margin of East Gondwana (Müller et al., 2000; GAF-BGR, 2008; Moine et al., 2014; Ichiki et al., 2015), or (c) an east-facing continental arc on the eastern margin of Azania (Collins and Pisarevsky, 2005); these plutonic rocks are notably absent in southern Madagascar. During continent–continent collision, Mesoproterozoic and Neoproterozoic sediments deposited on the Archean and

Paleoproterozoic crust became folded into and intercalated with the older crust (Tucker et al., 2014).

Lithologic domains in southern Madagascar (Figure 11) are delineated by major ductile shear zones (e.g., Windley et al., 1994). The Vohibory, Androyen, and Anosyen domains are separated by the Beraketa and Ampanihy shear zones, respectively (de Wit et al., 2001; Tucker et al., 2011). The westernmost Vohibory Domain is a mélange of ultramafic and felsic volcanic rock, terrigenous sedimentary rock, and chemical sedimentary rock (de Wit, 2003; Collins, 2006; GAF-BGR, 2008) that formed as part of an intraoceanic arc at 670–630 Ma before becoming involved in the East–West Gondwana collision (Jöns and Schenk, 2008). Immediately to the east, the Androyen Domain consists of paragneisses and felsic metavolcanic rocks, the protoliths of which are probably Paleoproterozoic (Tucker et al., 2014) and certainly predate the intrusion of ~900 Ma anorthosites (GAF-BGR, 2008). The Anosyen Domain contains aluminous metasediments, calcsilicates, and interbedded quartzofeldspathic volcanosedimentary rocks (Kröner et al., 1996, 1999; Müller, 2000; GAF-BGR, 2008) that are genetically related to the Imorona–Itsindro Suite (GAF-BGR, 2008), as well as relic Paleoproterozoic crust (Tucker et al., 2011, 2014; and references therein). Separating the southern Madagascar domains from the Antananarivo domain in the northeast is the Ranotsara shear zone and Ikalamavony Domain; the Ikalamavony which has a lower portion with Archean–Paleoproterozoic detrital zircons and an upper portion with ~1 Ga arc-related metavolcanic and metasedimentary rocks (Handke et al., 1999; Handke, 2001; Tucker et al., 2007; Tucker et al., 2011). The Anosyen Domain may have formed as a marginal sequence on West Gondwana (Müller, 2000), Azania (Collins and Pisarevsky, 2005) or East Gondwana (GAF-BGR, 2008), or in an intracontinental basin (Tucker et al., 2014). Accordingly, the suture between East and West Gondwana may be along the east or

west edges of the Antananarivo Domain (Collins and Pisarevsky, 2005), the Ranotsara shear zone (Müller, 2000), the Beraketa shear zone (GAF-BGR, 2008; Boger et al., 2014), or west of the Androyen Domain (Tucker et al., 2014). The position of the Anosyen Domain during orogenesis, however, is undisputed: initially on top of older crust, Anosyen rocks became sandwiched between (yet probably remained underlain by) older Paleoproterozoic terranes.

The earliest metamorphism associated with Gondwana assembly in southern Madagascar occurred at 630–600 Ma and is almost exclusively observed west of the Beraketa shear zone in the Vohibory and Androyen domains (GAF-BGR, 2008); this event may represent the accretion of the Vohibory Arc to either Azania (Jöns and Schenk, 2008), an exotic Androyen microcontinent of East African affinity (GAF-BGR, 2008), or the western margin of East Gondwana (Tucker et al., 2014), prior to closure of the Mozambique ocean. Peak conditions associated with this event were initially estimated to be ~800–850° C at 9–12 kbar (Nicollet, 1989; Martelat et al., 1997; Jöns and Schenk, 2008) but may be substantially lower (750–800° C at 7–8 kbar: GAF-BGR, 2008). The main stage of orogenesis that affected all of central and southern Madagascar occurred at ~585–520 Ma (Berger et al., 2006; GAF-BGR, 2008; Giese et al., 2011). UHT mineral assemblages (sapphirine + quartz, orthopyroxene + sillimanite + quartz, osumilite + garnet), Al-in-orthopyroxene thermometry, and pseudosections record the highest peak conditions of >900° C at 9–10 kbar in the southern Anosyen Domain (GAF-BGR, 2008; Jöns and Schenk, 2011; Boger et al., 2012); peak conditions in the northern Anosyen Domain were probably 50–100° C and 1 kbar lower. Modestly lower peak conditions of ~850° C at 6.5–8 kbar were also reached in the Androyen Domain (Martelat et al., 1997; Markl et al., 2000; GAF-BGR, 2008). In the Ikalamavony Domain, which was translated east over the Antananarivo Domain as a fold–thrust belt during orogenesis, temperatures peaked at ~700° C (GAF-BGR, 2008). Pre- to syn-

deformation granites intruded the Anosyen and Androyen domains from ~580–565 Ma, and post-deformation granitic plutonism—presumably corresponding to the rapid exhumation of the Anosyen Domain from 35 km to 10–20 km depth (e.g., Jöns and Schenk, 2011)—occurred throughout south and central Madagascar from ~530–510 Ma (GAF-BGR, 2008); these rocks are grouped together as the Ambalavao Suite.

The Vohibory, Androyen, and Anosyen domains have strong polyphase, granulite-facies fabrics. Early structures include ENE–WSW trending stretching lineations and fold axes (Paquette et al., 1994; de Wit et al., 2001). Large-scale remote sensing and outcrop-scale fabrics show that the intensity of this strain increases westward (Martelat et al., 2000). In the west, some or most of these fabrics may have formed when the Androyen Domain was thrust beneath the Vohibory Domain (de Wit et al., 2001). In the Anosyen Domain, however, early structures are ascribed to crustal thickening from 580–565 Ma (Nédélec et al., 1995; Paquette et al., 1994). A younger series of subvertical, ductile strike-slip shear zones (5–20 km wide) separate the intervening lower-strain domains (Windley et al., 1994); if simple shear along these zones was coeval with E–W shortening and N–S stretching, the overall deformation may have produced crustal thinning and the southward extrusion of the southern Anosyen Domain relative to the Antananarivo Domain (Martelat et al., 2000; Schreurs et al., 2010). North of Ihosy, the Anosyen Domain is highly strained, isoclinally folded, and forms a flower-like shape, suggesting that ductile flow of the Anosyen Domain under granulite-facies conditions led to northward tectonic extrusion (Tucker et al., 2014). Thus, the Antananarivo Domain probably acted as a rigid indenter, extruding the semi-rigid southern Anosyen Domain southward the ductile northern Anosyen Domain northward.

3. Geochronology

The accumulation of significant radiogenic heat requires a heat source of sufficient power and size that operates long enough in a material of low thermal diffusivity. Evaluating this in nature requires determining the 3-D distribution and abundances of HPEs, the evolution of crustal thickness crust and the timescales of metamorphism. Below, I discuss previously published geochronology of Madagascar pertaining to the collision of East and West Gondwana, and then present new U/Th-Pb geochronology that provides additional constraints.

3.1. Previous geochronology

Igneous zircon dates from rocks interlayered with Vohibory basalts suggest that most of the Vohibory Domain grew between 670 and 630 Ma (GAF-BGR, 2008; Tucker et al., 2014). Rb-Sr whole rock (Windley et al., 1994) and U-Pb/Pb-Pb magmatic zircon core dates (Emmel et al., 2008; Jöns and Schenk, 2008) suggest that parts of the Vohibory Domain may be as old as 850–700 Ma, but these older ages may be from a window into the Androyen Domain. The earliest metamorphic dates in the southwestern Androyen Domain suggest that the accretion of the Vohibory Arc to the Androyen domain may have occurred as early as 650–640 Ma (de Wit et al., 2001; Emmel et al., 2008; Jöns and Schenk, 2011), but metamorphism associated with the accretion continued through ~630–600 Ma (GAF-BGR, 2008; Jöns and Schenk, 2008). Arc-type magmatism may have continued during orogenesis because calc-alkaline igneous rocks were emplaced until ~610 Ma (Tucker et al., 2014). Although ubiquitous throughout the Androyen Domain (Paquette and Nédélec, 1998; de Wit et al., 2001; GAF-BGR, 2008; Jöns and Schenk, 2011; Boger et al., 2014), metamorphic

zircon and monazite U-Pb dates of 630–610 Ma are absent in the Anosyen Domain farther east (GAF-BGR, 2008).

Early syn-deformation plutons (576 ± 4 Ma in the Androyen Domain and 573 ± 6 Ma in the Anosyen Domain) and late- to post-deformation plutons (541 ± 2 Ma in the Androyen Domain and 521 ± 12 Ma in the Anosyen Domain) of the Ambalavao suite bracket the main stage of orogenesis in southern Madagascar (GAF-BGR, 2008). Metamorphic dates reported across both domains largely fall in the same interval (Paquette et al., 1994; Kröner et al, 1999; Martelat et al., 2000; Müller et al., 2000; de Wit et al., 2001; GAF-BGR, 2008; Collins et al., 2011; Giese et al., 2011; Tucker et al., 2011; Boger et al., 2014). The preponderance of igneous and metamorphic dates across southern Madagascar during this interval is highlighted in the detailed synopsis provided by Tucker et al. (2014) (Figure 12); metamorphism in the Antananarivo Domain to the east probably initiated later (Tucker et al., 2014) and persisted longer (until nearly 500 Ma; Giese et al., 2011). The main stage of Gondwana assembly was complete by ~520 Ma, when the nondeformed Ambalavao granites were intruded across the region and after which metamorphic dates in the Androyen and Anosyen domains are no longer observed. Dates <500 Ma obtained in major shear zones may reflect late fluid circulation (Martelat et al., 2000).

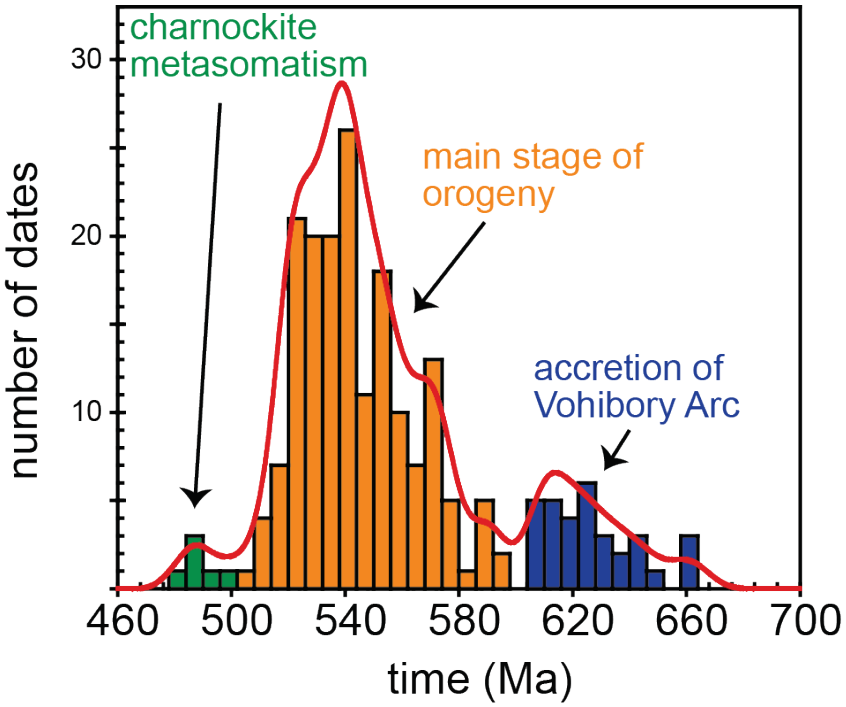

Figure 12. Probability density distribution for geochonologic dates from across Madagascar (Tucker et al., 2014).

3.2. When were southern Madagascar domains buried?

Two endmember scenarios emerge from previous southern Madagascar geochronology: (1) The accretion of the Vohibory arc may have been a tectonometamorphic event distinct from the main stage of orogenesis, affecting exclusively the Vohibory and Androyen domains and ending >20 Myr prior to the main stage of orogeny. If so, thickened crust during Gondwana collisional orogenesis may have existed for ~60 Myr (580–520 Ma). Alternatively, (2) tectonic burial, crustal thickening, and high-temperature metamorphism affected all of southern Madagascar shortly after the accretion of the Vohibory arc (~630 Ma) and persisted until ~520 Ma, when post-deformation granites signal the cessation of orogenesis. In this case, thickened crust may have persisted for >100 Myr and the dearth of 630–610 Ma metamorphic dates in the east (GAF-BGR, 2008) in the Anosyen Domain could be explained by overprinting by higher temperatures.

To distinguish between these scenarios, in situ laser-ablation split-stream (LASS) inductively coupled plasma–mass spectrometry (ICP-MS) U/Th-Pb geochronology and trace-element geochemistry analyses were conducted on monazites and zircons from across the Androyen and Anosyen domains (see Appendix 7 for LASS methods and Appendix 8 for analytical data). Most zircons in the metamorphic rocks are small (<50 μm), euhedral, have oscillatory zoning, and yield late Neoproterozoic U-Pb dates (few inherited zircons have been found), all of which suggests that, if zircon existed in the protolith, much of it dissolved into melt or rutile during peak metamorphism and reprecipitated during cooling. In contrast, monazites tend to be large (>100 μm) and preserve an inherited component and a wider range of metamorphic dates. For example, a garnet–cordierite gneiss (sample 06C1) contains large metamorphic Paleoproterozoic monazites (>1 mm) in which the U-Pb system was largely reset during the assembly of Gondwana (Figure 13).

Two samples in the Androyen Domain have monazite dates >600 Ma. A metapelite with euhedral garnet porphyroblasts (sample 14G1) from immediately west of the Ankafotra anorthosite body near the Androyen–Vohibory contact has concordant monazite dates that range from 614 ± 17 Ma to ~522 Ma (Figure 13). Discordant dates dispersed toward 2.2 Ga (not shown in figure) indicate that the highest-Y portion of the mottled monazite cores are relict Paleoproterozoic material. The cores probably underwent dissolution/reprecipitation or in situ recrystallization beginning at ~614 Ma and low-Y metamorphic rims grew from ~550–522 Ma. All spot analyses have negative Eu anomalies consistent with the presence of plagioclase, but spot dates <580 Ma have more-pronounced Eu anomalies. The Lu/Dy ratio decreases at ~600 Ma and remains low with the exception of the two youngest analyses at ~522 Ma; low Lu/Dy during this interval may be indicative of monazite (re)crystallization in the presence of garnet. A migmatitic gneiss (sample 13D1) from the southernmost portion of

the Beraketa shear zone that contains sillimanite in and around garnet porphyroblasts yields a comparable range of monazite dates from 622 ± 13 Ma to 523 ± 11 Ma, without any inheritance (Figure 13). Oscillatory zoning of the high-Y monazite cores are cut by dissolution embayments and overgrown by low-Y metamorphic rims; the sharply-delineated cores and rims suggest that analyses that yield intermediate ages are mixing between core and rim ages. The older population has less pronounced Eu anomalies and higher Lu/Dy.

Several samples in the Anosyen Domain also yielded ~600 Ma dates. Monazites in a cordierite–sillimanite gneiss collected south of Ihosy (sample 06A1) have relic high-Y Paleoproterozoic cores. These monazites retain 602 ± 12 Ma dates and a range of younger dates from ~560 Ma to 515 Ma that have more-pronounced Eu anomalies (Figure 13). Lu/Dy is anticorrelated with age. Farther south along the Beraketa shear zone, a gneissic sample (sample 00G2) contains sapphirine and large garnet porphyroblasts with cordierite symplectite overgrown by orthopyroxene–spinel symplectite. Monazites shielded in garnet have relatively homogenous trace element compositions, whereas monazites in the matrix have irregularly shaped cores with embayments consistent with dissolution, and uranium-rich rims. Cores have a weighted mean date of 593 ± 13 Ma, and the cores have an age of 524 ± 10 (Figure 13). This range is also recorded by zircon in a garnet–orthopyroxene gneiss from the south-central Anosyen Domain (sample MD46): discordant dates scatter towards ~2.2 Ga, but concordant metamorphic dates range from ~611 Ma to ~507 Ma with increasingly pronounced Eu anomalies (Figure 13).

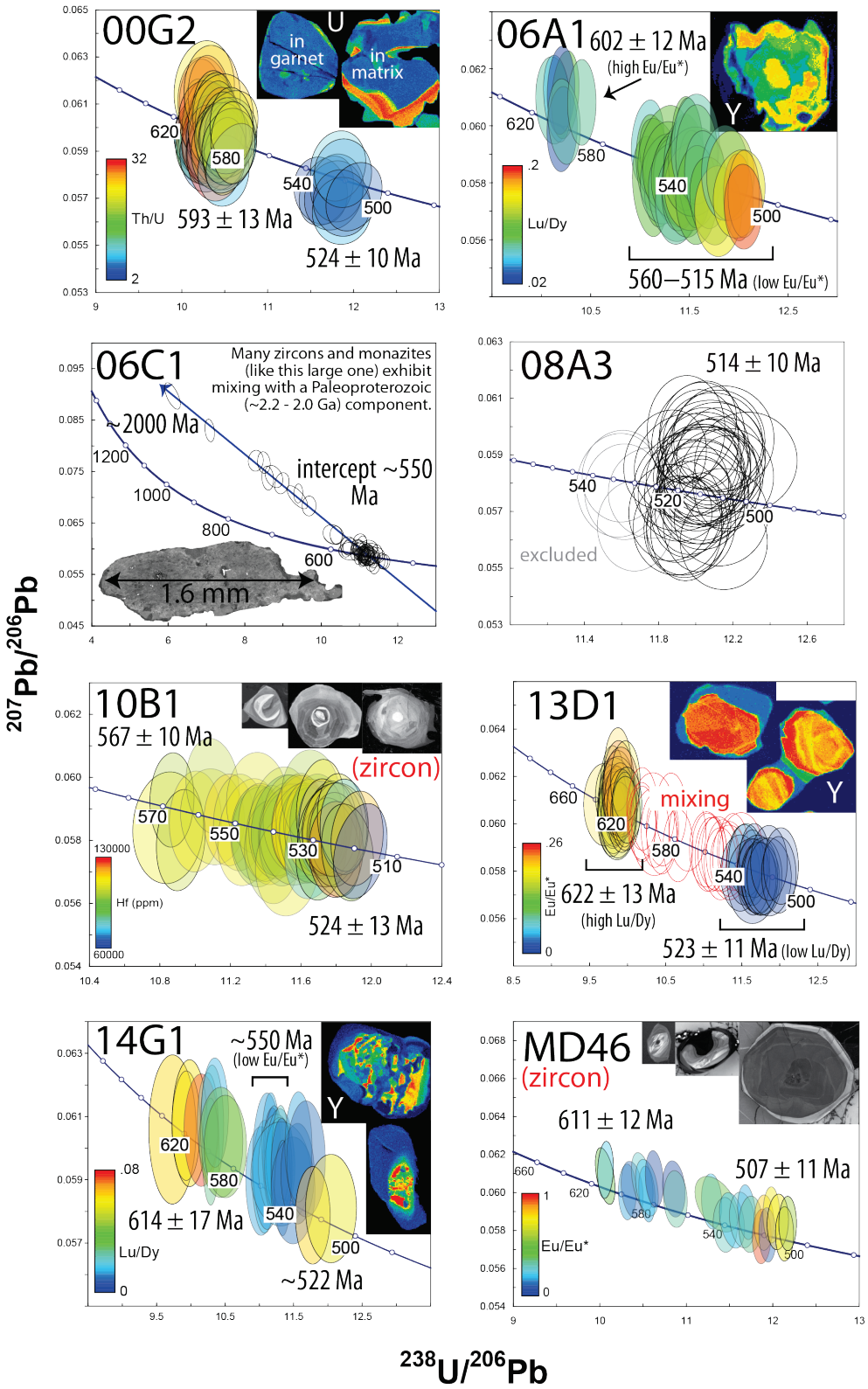

Figure 13. Concordia diagrams for LASS results. Error ellipses are 2σ are colored by trace element concentration in some cases. Ages and uncertainty for clusters of data points (bold ellipses) with MSWD <1and are reported in Ma. Red ellipses are suspected to be mixed ages. Zircon cathodoluminescence images are shown for samples 10B1 and MD46; all other grain maps were made on the electron microprobe.

3.3 Did accretion of the Vohibory arc produce thickening and accretion farther east?

The distinct trace-element signature of the >600 Ma monazite domains—high Lu/Dy, high-Y cores, and less-pronounced Eu anomalies—in samples from either edge of the Androyen Domain (13D1 and 14G1) may suggest that an early metamorphism occurred when garnet and melt were scarce or absent. Contrary to GAF-BGR (2008), I observe this early metamorphic record in the Anosyen Domain as well, revealing that this early event affected a broader area than previously recognized, and implying that the Anosyen and Androyen domains may have been joined prior to 600 Ma. Although accretion of the Vohibory arc may have initiated as early as ~650 Ma, metamorphism related to this collision occurred from ~620–600 Ma and had propagated eastward at least as far as the Anosyen Domain by this time; it remains unclear whether heat inherited from the arc system and/or crustal thickening caused metamorphism. There have been relatively few published geochronologic dates in the 600–580 Ma range (Figure 12; Tucker et al., 2014), suggesting a period of tectonic quiescence. If monazite in 06A1 and 14G1 grew in response to tectonic burial, my data suggest that parts of the Androyen and Anosyen domains were incorporated into a thickened crustal pile prior to the main stage of orogenesis that began at ~580 Ma. If so, the accretion of the Vohibory arc—although a temporally distinct tectonometamorphic event—may have been an important prelude to subsequent orogenesis, insulating heat producing crust at depth prior to continent–continent collision.

3.4. When were southern Madagascar domains exhumed?

The end of orogenesis likely coincided with the youngest metamorphic dates and the emplacement of nondeformed Ambalavao granites. Oscillatory-zone, non-cathodoluminescent zircons from a garnet–cordierite–orthopyroxene gneiss (sample 10B1)

collected within the southern Beraketa shear zone yield a range of dates from 567 ± 10 Ma to 524 ± 13 Ma (Figure 13). These zircons have oscillatory zoning indicative of crystallization from partial melt. Also within the Beraketa shear zone, monazites from a meter-scale pod (sample 08A3) of coarse cordierite with spinel and corundum—presumably formed by fluid infiltration of the shear zone during the waning stages of metamorphism—have a weighted mean age of 514 ± 10 Ma. Collectively, the youngest metamorphic spot dates I obtained in southern Madagascar (from samples 00G2, 06A1, 10B1, 13D1, 14G1, MD46) range from 525–507 Ma.

Younger dates obtained in the region are likely due to fluid circulation in shear zones in the upper crust brittle at <500 Ma (e.g., Martelat et al., 2000). Phlogopite deposits in the Beraketa shear zone yielded calcite–phlogopite two-point Rb-Sr isochrons of 491 ± 10 and 492 ± 10 Ma (Martin et al., 2013) and K-Ar ages of 491–485 Ma (Rakotondrazafy et al., 1997; in Martelat et al., 2014). A zircon-bearing calcite vein in the southern Anosyen Domain has a zircon U-Pb date of 523 ± 5 Ma. In southern India—adjacent to southern Madagascar at the time—520–510 Ma zircon rims (Whitehouse et al., 2014) and 495 Ma monazite domains (Taylor et al., 2014) have been linked to dehydration reactions (i.e., charnockitization) during CO_2-rich fluid infiltration of the crust; I interpret the coeval dates reported in southern Madagascar to this regional metasomatic event that postdates orogenesis by up to 20 Myr.

Given these constraints, the Vohibory Arc probably accreted at ~645 (de Wit et al., 2001) or 620 Ma (GAF-BGR, 2008) causing metamorphism of Androyen Domain and at least part of the Anosyen Domain from ~620–600 Ma. Heat from the arc could explain regional metamorphism at low to moderate pressure (e.g., GAF-BGR, 2008) and minimal crustal thickening. Alternatively, metamorphism could have occurred in response to burial to

greater depth (e.g., Nicollet, 1990; Martelat et al., 1997; Jöns and Schenk, 2008), in which case, thickening of the continental margin could have persisted for 40–65 Myr prior to the collision of east and west Gondwana. The formation of a broad orogenic plateau likely occurred during the main stage of orogenesis that began at ~580 Ma and lasted for ~65 Myr.

4. Thermometry

The degree of crustal heating can be broadly constrained by the areal extent of peak metamorphic isotherms. The following section summarizes previous thermal constraints based on mineral assemblages (Jöns and Schenk, 2011) and phase diagrams (GAF-BGR, 2008) and then presents new 4+ cation thermometry.

4.1. Previous thermal constraints

Mineral assemblages reported by Jöns and Schenk (2011) provide a first good measure of the area affected by UHTM (Figure 14). The UHTM-diagnostic (e.g., Harley, 2008) assemblage garnet + osumilite (inferred from pseudomorphs containing cordierite + K-feldspar + orthopyroxene or cordierite + K-feldspar + quartz + biotite) is observed in the southern Anosyen Domain west of Tôlanaro and north of Tranomaro. Osumilite pseudomorphs in garnet-absent rocks are also found north of Tranomaro; although not diagnostic, these are probable indicators of UHTM. Sapphirine + quartz and Al-rich orthopyroxene + sillimanite + quartz assemblages—also likely indicators of UHTM but stable to lower temperatures under oxidizing conditions (Harley, 2008)—exist along the southernmost Beraketa shear zone. Spinel + quartz assemblages are found across a much-larger area from Tôlanaro to Bekily in the west and Ihosy in the north. Spinel + quartz is not diagnostic of UHTM, but probably still indicative of temperatures >800° C (Harley, 2008;

and references therein). The absence of UHTM assemblages in the central and northern Anosyen Domain represents a northward decreasing metamorphic grade, and the lack of UHTM and spinel + quartz assemblages in the western part of the Androyen Domain indicates a steeper metamorphic gradient to the west (Jöns and Schenk, 2011).

GAF-BGR (2008) constructed two phase diagrams using the NCKFMASHTO model system intended to be representative of Anosyen Domain rocks. Most indicative of UHTM are the gneissic bands of cordierite-rich (cordierite was presumed to be retrograde), spinel- and magnetite-bearing Bakika formation that are only exposed in the southeastern Anosyen Domain: the peak assemblage of garnet ± orthopyroxene + magnetite + ilmenite + spinel + two feldspars + quartz constrains temperatures to >880° C. The Bakika formation contains predominantly ferric iron. The regionally extensive cordierite- and magnetite-rich Ihosy formation is also highly oxidized and has a similar composition, so the occurrence of orthopyroxene and garnet in the Ihosy gneisses also indicates that temperatures locally exceeded >880° C. Elsewhere in the Ihosy formation, the absence of garnet and orthopyroxene indicates slightly lower temperatures of ~870° C. In contrast, the garnet + biotite + sillimanite + ilmenite + spinel assemblage of the Ampahiry formation (a similar bulk composition to the Bakika formation, but with a low ferric iron content) predicts maximum temperatures of 830° C. Because the Ampahiry formation is interlayered with the Bakika formation near Tôlanaro, they presumably experienced a similar PT history; GAF-BGR (2008) concluded that the Ampahiry rocks reached >830° C where biotite was absent, and that either (a) the biotite formed on the retrograde path or (b) the biotite solution model used is wrong. Fortunately, the Ihosy Formation exists throughout much of the Anosyen Domain, providing thermal constraints across a large area (Figure 14).

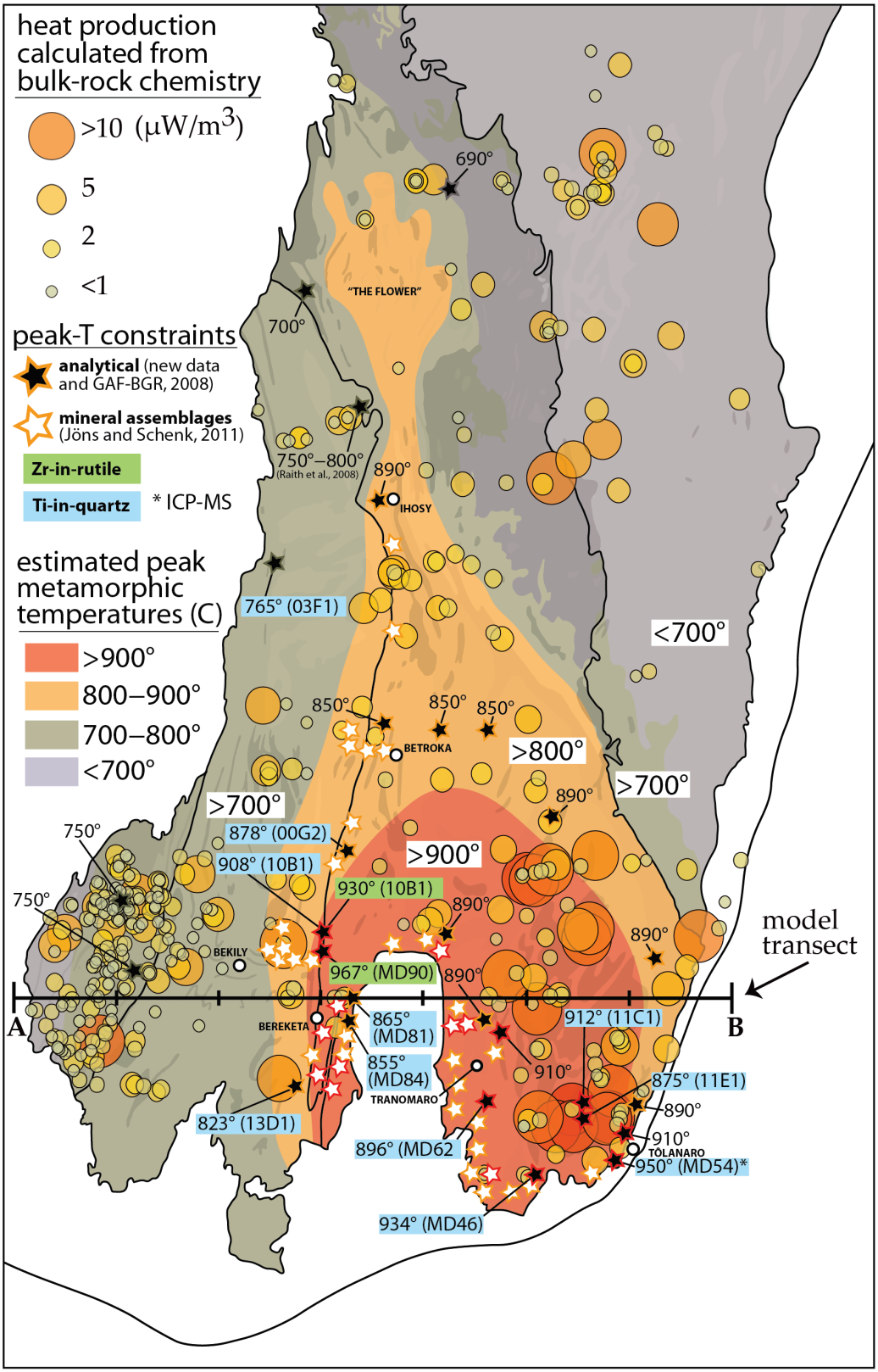

Figure 14. Map of southern Madagascar showing estimated peak isotherms based on mineral assemblages (Jöns and Schenk, 2008), pseudosections (GAF-BGR, 2008), and 4^{+} cation thermometry. Heat-production rates (at 550 Ma) based on bulk rock chemistry (GAF-BGR, 2008) are plotted as shaded circles.

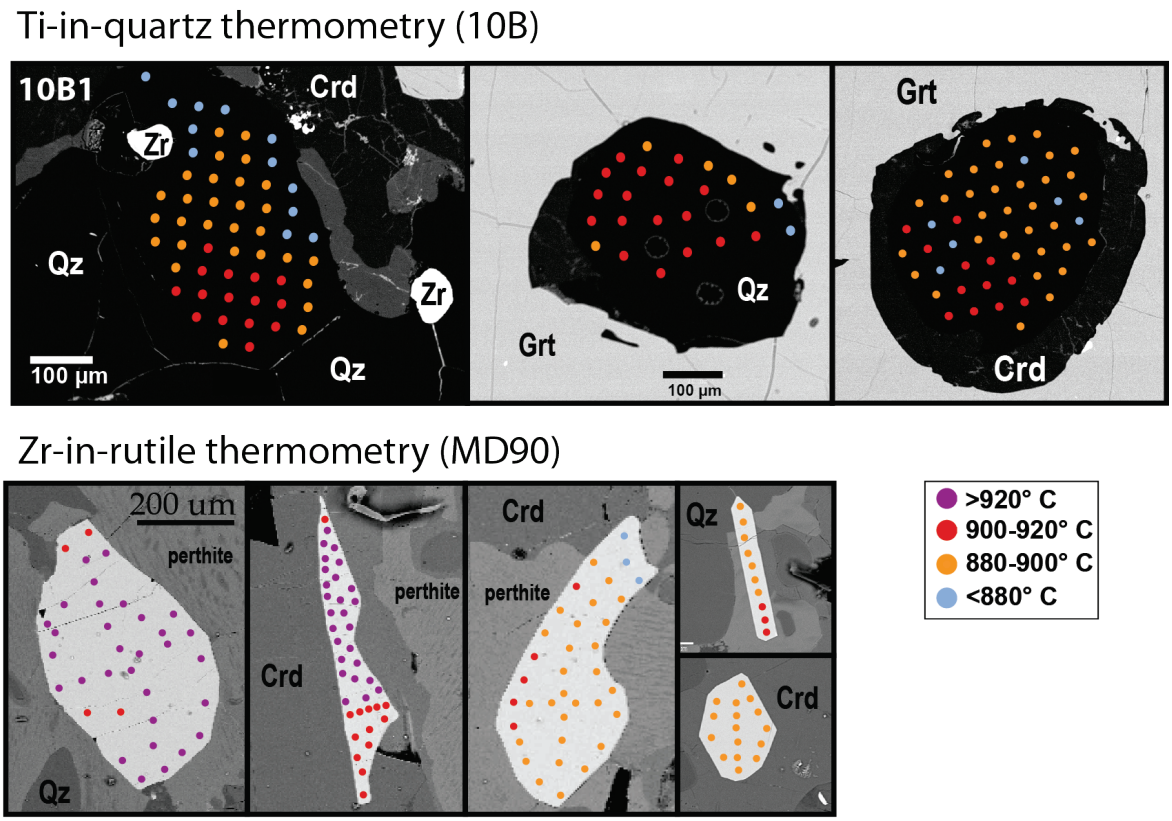

Figure 15. Representative electron backscatter grain maps showing 4+ cation thermometry results. Ti-in-quartz (after Thomas et al., 2010) temperatures and Zr-in-rutile (after Ferry and Watson, 2007) temperatures were calculated assuming a pressure of 10 kbar.

4.2. 4+ cation thermometry

I conducted Ti-in-quartz (using the calibration of Thomas et al., 2010) and Zr-in-rutile (Ferry and Watson, 2007) thermometry for 13 samples (Table 3; Figures 14 and 15). Electron probe microanalysis (EPMA) and laser ablation ICP-MS were used to measure Ti and Zr in quartz and rutile, respectively, and calibrated using NIST glass standards. EPMA 2σ uncertainty is <1% and ICP-MS 2σ uncertainty is ~5–8%, so EPMA-based temperatures are considered most reliable. Ti and Si activity was assumed to be unity based on the presence of ilmenite and/or rutile plus quartz in every sample. However, each sample exhibits a wide range of inter- and intragrain Ti concentrations (Figure 15). I am unable to say whether this resulted from (i) heterogeneity in Ti activity at the thin section scale, (ii) incomplete equilibration,

(iii) diffusion during cooling, and/or (iv) grain growth during cooling. Because calculated temperatures are minimum estimates, I assume that the highest Ti concentration measured in each sample is representative of minimum peak conditions. Also, I assume a pressure of 10 kbar (GAF-BGR, 2008; Jöns and Schenk, 2011). If the pressure was lower, the Ti-in-quartz temperatures are reduced by ~25° C per kbar, and the Zr-in-rutile temperatures by <10° C per kbar.

Two rutile-bearing samples (10B1 and MD90) were collected from the southern Beraketa shear zone and both yield UHTM Zr-in-rutile temperatures (maxima of 930±° C and 967±° C, respectively). These two samples are considered the most robust evidence for UHTM in southern Madagascar because the rutile thermometer is not strongly pressure dependent. Ti-in-quartz temperatures for 10B1 (EPMA) and MD90 (ICP-MS) are consistent with the Zr-in-rutile results, reaching 908 ±° C (~925° C via ICP-MS) and 913° C, respectively; the discrepancy between maximum temperatures calculated for MD90 could be due to (a) differences in pressure or temperature of Ti and Zr entrapment, (b) diffusive loss of Ti from quartz (faster than Zr diffusion in rutile; Cherniak et al., 2007), or (c) too few analyses. In general, however, the consistency among thermometers for these two samples seems to justify using 10 kbar for the Ti-in-quartz thermometer.

Ti-in-quartz temperatures calculated for other samples also indicate UHTM: MD54 collected near Tôlanaro reached ~950° C, MD46 to the west reached 934°C, and 11C1 to the north reached 912° C. Samples 11E1 (875° C), MD62 (896° C), MD81 (865° C), and MD84 (855° C) yielded temperatures below 900° C; given their close proximity to higher-temperature rocks, however, these results may be underestimates of peak temperatures. Two other samples along the Beraketa shear zone—00G2 (878° C) and 13D1 (823° C)—are from locations outside the zone of demonstrable UHTM; their temperature estimates are assumed

to be representative of peak conditions. A sample from the northern Androyen Domain (03F1) has a lower maximum Ti-in-quartz temperature of 765° C, consistent with decreasing metamorphic grade to the north and west.

5. Thermal Modeling

To evaluate the role of heat production in southern Madagascar, I use a 2-D transient heat flow model (Supplementary File 1) based on the alternating-direction, implicit, finite-difference method described by Hinojosa and Mickus (2002). The model is a 350 × 150 km rectangular grid with 2-km node spacing. The initial temperatures are steady-state conditions for 40-km-thick crust in which the upper crust has RHP of 1.6 $\mu W/m^3$ (to 14 km depth) and the middle and lower crust has 0.7 $\mu W/m^3$; initial temperatures were reset when testing variable conductivities and mantle heat flows. Thermal conductivity and crustal thickness (60 km) are constant throughout model runs. Basal (mantle) heat flow is assumed to be constant and the upper boundary (surface) temperature is held at 0° C. Time steps of 1 Myr are used; smaller steps yield nearly-identical results. There is no material flow, except for simulations in which the node temperatures and RHP values are shifted upward to simulate erosion. Default parameters are listed in Table 4.

Table 3. Summary of 4+ cation thermometry results.

Sample ID	Latitude (° WGS84)	Longitude (° WGS84)	# of grains	# of analyses	Mean Ti (ppm)	Max. Ti (ppm)	Mean Temperature (° C)	Max. Temperature (° C)
Ti-in-Quartz (EPMA) after Thomas & Watson (2010)								
00G2	-23.812599	45.814301	4	32	184	265	827	878
03F1	-22.508819	45.556252	6	33	61	109	696	765
10B1	-24.073637	45.690013	10	69	214	327	845	908
11C1	-25.022338	46.647301	5	32	242	336	864	912
11E1	-24.793386	46.864845	3	53	208	259	844	875
13D1	-24.656649	45.556724	9	36	118	176	772	823
MD46	-25.02237778	46.64708056	6	189	288	388	888	934
MD62	-24.72223611	46.43896667	4	76	207	301	838	896
MD81	-24.33060556	45.83311667	4	82	170	241	816	865
MD84	-24.45060556	45.80064167	4	52	198	225	838	855
Ti-in-Quartz (ICP-MS) after Thomas & Watson (2010)								
10B1	-24.073637	45.690013	1	24	300	372	894	927
MD46	-25.02237778	46.64708056	1	11	338	389	912	934
MD54	-25.00815833	46.97716667	1	11	372	441	926	954
MD90	-24.107025	45.694725	4	28	232	339	856	913
Zr-in-Rutile (EPMA) after Ferry & Watson (2007)								
10B1	-24.073637	45.690013	8	139	2496	4499	836	930
MD90	-24.107025	45.694725	6	170	3559	5848	896	967

5.1. Heat production

To simulate burial of radiogenic crust during continental collision, the RHP in the middle to lower crust is approximated based on GAF-BGR (2008) bulk-rock analyses: A heat-production rate is calculated for each sample based on elemental abundances (corrected for 550 Myr of decay) and heat-production rates of U (97.1 μW/kg), Th (26.9 μW/kg), and K (3.58 nW/kg). The individual heat-production values south of the 23° S longitude are then projected onto an E–W transect (Figure 16) orthogonal to the dominant N-S structural trend south of 23°. Then average RHP rates were calculated for 8 segments along the transect. The RHP for each segment was assigned to all middle and lower crust nodes (Figure 16). Above, RHP in the upper crust (0–20 km) is assumed to be 1.6 $\mu W/m^3$. Beneath, the lowermost crust (to 60 km depth) and mantle (to 150 km depth) produce 0.7 $\mu W/m^3$ and 0.02 $\mu W/m^3$, respectively. The vertical gradient in RHP values was held constant throughout the simulations (i.e., HPEs are not moved from node to node due to melting or fluid migration), except when erosion removes the uppermost crust and the RHP values are shifted upward.

Table 4. Default parameters for thermal modelling.

Width	350	km
Height	150	km
Node spacing	2	km
Depth of crust	60	km
Lithosphere-asthenosphere boundary	150	km
Time step size	1	Myr
Duration of calculation	80	Myr
Thermal Conductivity	3	W/m K
Basal heat flow	17	mW/m2
Surface Temperature	0	° C
Asthenosphere Temperature	1350	° C
Erosion	0	km
Amount of thinning	0	km
RHP in uppermost crust	1.6	μW/m3
Extrapolated depth of measured RHP	20 to 50	km
RHP in lowermost crust	0.7	μW/m3
RHP in mantle	0.02	μW/m3

5.2. Mantle heat flux

The model is also sensitive to the mantle heat flux. Continental mantle heat flux is typically estimated by subtracting presumed heat production within the crust from the surface heat flow. Estimates vary greatly from 7–25 mW/m^2 for various continental regions; most are 12–18 mW/m^2 (Mareschal and Jaupart, 2013; and references therein). I explore the influence of mantle heat flow from 11 to 23 mW/m^2. In the model, higher mantle heat flow raises the initial geotherm, producing higher temperatures sooner (Figure 17). Moderate heat flow of 17 mW/m^2 predicted by Rudnick and Gao (2003, 2014) and Huang et al. (2013) is used as the preferred value.

5.3. Thermal conductivity

The rate of heating is also sensitive to thermal conductivity, which depends on mineralogy (e.g., McLaren et al., 1999; Hofmeister et al., 2006) and temperature (e.g., Whittington et al., 2009). The bulk thermal conductivity measured for felsic, intermediate, and mafic granulites across southern India ranges from 2.4 to 3.5 W/m/K (Ray et al., 2015); rocks in southern Madagascar are likely similar. The conductivity of rocks in the now-eroded upper crust—most important for insulation—is unknown and accounting for temporal changes in conductivity is beyond the scope of this model; I assume a constant conductivity of 2.5, 3.0 or 3.5 W/m/K. Lowering conductivity accelerates heating by insulating the heat-producing layer (Figure 17); I consider a conservative conductivity of 3.0 W/m/K to be typical, but acknowledge that the middle and lower crust must have had lower conductivities after heating above ~600° C, especially if partial melt persisted for extended periods (e.g., Whittington et al., 2009).

5.4. Erosion

Erosion influences heating by changing the distribution of HPEs and advecting heat upward. Denudation rates <0.1 mm/yr do not significantly affect the thermal evolution of the middle crust (Figure 17). In contrast, erosion rates of 0.2 mm/yr accelerate heating >2° C/Myr for the first 20 Myr. An even faster erosion rate of 0.3 mm/yr (18 km in 60 Myr) transfers the high-HPE layer into the less-insulated upper crust, resulting in peak temperatures colder than observed. The Tibetan plateau—the best modern analogue for the Pan-African collision zone—has experienced slow regional denudation rates of ~0.01 mm/yr (Hetzel et al., 2011) to 0.03 mm/yr (Lal et al., 2003). If denudation of the Pan African orogen was analogous to Tibet, erosion probably had a negligible effect on the overall thermal evolution of the central

part of the orogen. I use an erosion rate of zero to approximate slow denudation of the orogenic plateau.

5.5. Crustal thinning

Crustal thinning that outpaces conduction compresses the geotherm. For example, exhumation of lower crustal rocks at >900° C to mid-crustal depths could explain the type of UHTM seen in southern Madagascar. Although most of the Tibetan plateau is thickening (Liang et al., 2013), some portions, such as the southeastern portion between the eastern syntaxis and the Sichuan Basin (Enkelmann, 2006) may by thinning in response to outward-directed flow (e.g., Clark and Royden, 2000).

5.6. Thickness of heat-producing layer

Thermobarometric constraints for the Anosyen Domain (9–10 kbar: GAF-BGR, 2008; Jöns and Schenk, 2011; Boger et al., 2012) suggest that exposed rocks were buried to a depths of 30 km. The highest heat producing segment across the model transect is 10-km-wide, but most segments with distinct RHP rates (Figure 16) are >30-km-wide. Androyen and Anosyen lithologies are oriented subvertically, which is taken as an indication that focused zones of RHP were probably at least as thick as they were wide (10–40 km). The vertical distribution of RHP in the now-eroded upper crust is poorly constrained, so I assume that the heat-producing layer begins at 20 km depth. Because sample-based RHP values are higher—in eastern segments by more than a factor of five—than the upper and lower crust, the thickness of the high-RHP layer strongly affects the model. Highly radiogenic crustal layers thicker than ~25 km produce UHT at 30 km depth in <60 Myr (Figure 17).

5.7. Timescale of heating

Burial of radiogenic rocks to depths of 30 km presumably occurred due to tectonic thickening of the crust. It remains unclear whether and to what extent the accretion of the Vohibory Arc caused thickening of the crust prior to 600 Ma. Magmatism and metamorphism occurred across hundreds of km from ~580–515, which is consistent with the existence of a thickened orogenic plateau for ~65 Myr. Without conclusive evidence of prior tectonic burial of the UHTM terrane, I assume that heating occurred for approximately 60 Myr.

5.8. Successful models

A successful model must replicate the UHT conditions across a 150-km-wide zone in the middle crust within ~65 Myr. By extending the thickness of the heat-producing layer from 20 km to 50 km depth and assuming reasonable mantle heat flow and thermal conductivity values of 25 mW/m^2 and 3.0 W/m/K, respectively, the highest heat-producing segments of the model (southern Anosyen Domain) reach 900° C at a depth of 30 km in <60 Myr and the geotherm becomes inverted in the lowermost crust. Heating across the model transect is strongly asymmetric (Figure 18): in the west (Vohibory Domain), temperatures remain below 700° C in the middle crust, even after 60 Myr. Surface heat flow in this scenario increases from 59 to 85 mW/m^2 in the west and from 59 to 123 mW/m^2 in the east; these values are well within the range observed across the Tibetan plateau (30–140 mW/m^2: Hu et al., 2000). A lower thermal conductivity (~2.5 W/m/K) or a thicker highly radiogenic layer (~40 km thick) cause UHTM in the east in <40 Myr. Conversely, if the highly radiogenic layer is <25 km thick or if it resided in the upper 30 km of the crust, UHTM is not reached in <80 Myr. Lower mantle heat flow and/or rapid erosion would have also moderated heating.

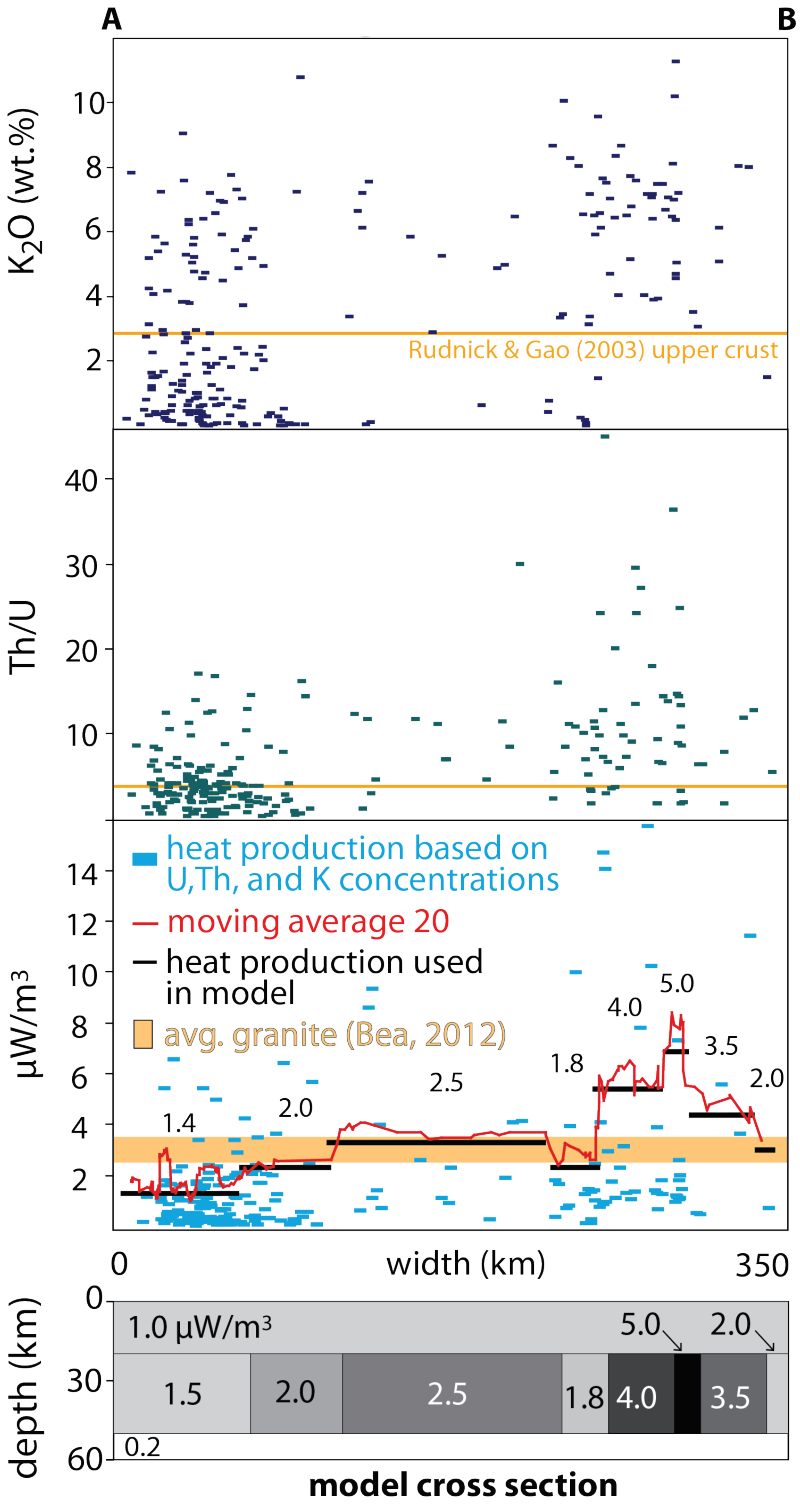

Figure 16. Heat-producing element distribution across southern Madagascar. Because lithologies are generally N–W trending, bulk rock samples south of 23° S were projected onto the A–B transect (see Figure 14). Segments of the transect were delineated using a 20-point moving average and mean heat production for each segment was compiled and input into thermal models as a radiogenic layer in the middle crust.

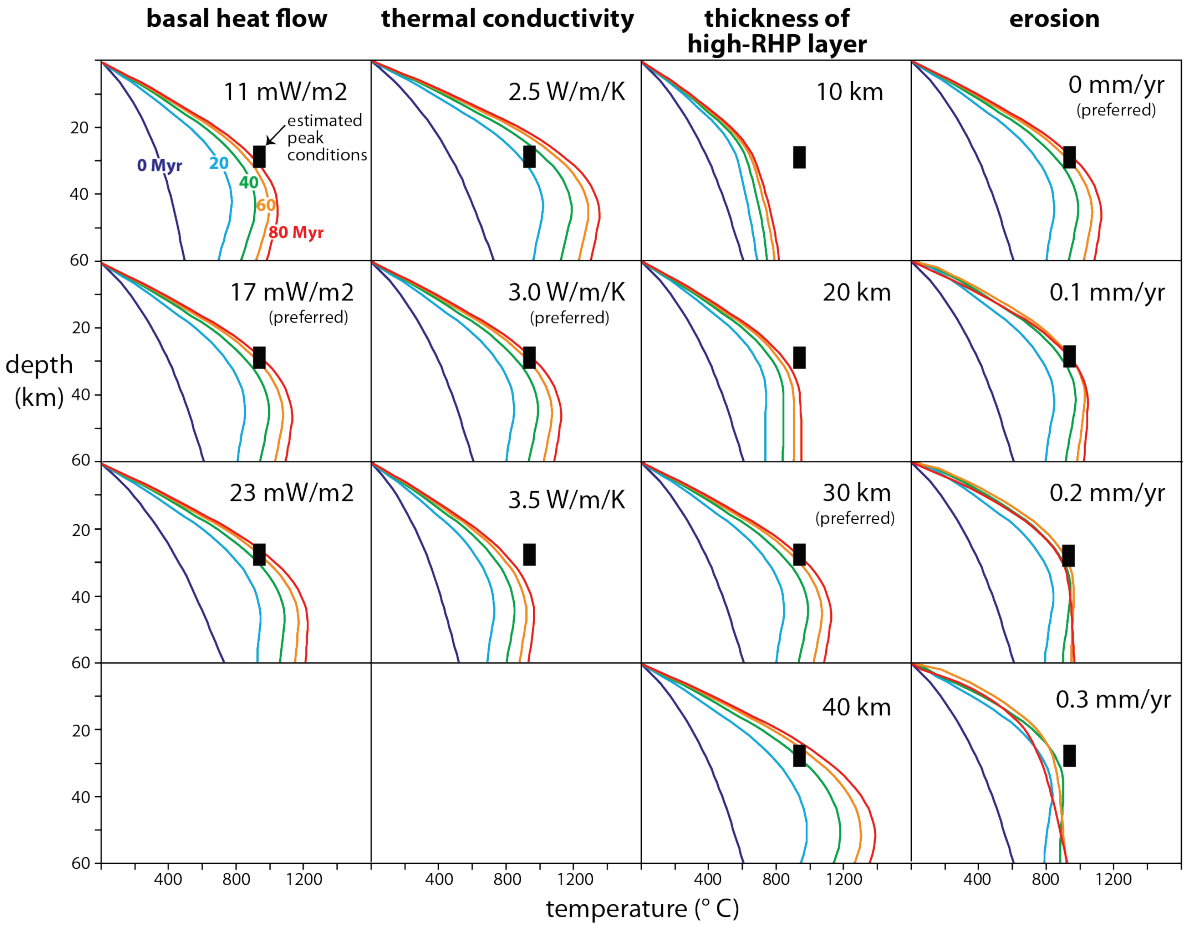

Figure 17. Sensitivity tests for various thermal model parameters. The geotherm plotted is 275 km east of (A) on the model transect (Figures 14 and 16) and the black rectangle represents estimated peak conditions for the UHTM zone in southern Madagascar. Note that heating is asymmetric and that the geotherm plotted represents the hottest segment of the thermal model. See text for details.

6. Discussion

6.1. Tectonometamorphic evolution of southern Madagascar terranes

The lack of consensus about the timing of orogenesis in southern Madagascar has been due in part to analytical techniques that dated only single metamorphic grains or bulk separates, and in part to the long, complex orogenic cycle. My data shed new light on several critical aspects of the continental collision.

The presence of inherited Paleoproterozoic monazite and zircon that are not detrital indicates that much, perhaps all, of the Anosyen Domain metasedimentary rock was

deposited prior to ~2 Ga (e.g., Tucker et al., 2014) rather than during the Neoproterozoic (e.g., GAF-BGR, 2008). However, volcanogenic beds derived from Neoproterozoic arc magmatism may have become deposited on those rocks are been structurally interleaved with the Paleoproterozoic metasediments during collision.

A pre-600 Ma metamorphic event affected both the Androyen Domain and western Anosyen Domain. Monazite that grew during this older event ranges from 622 ± 13 Ma (13D1) to 593 ± 13 Ma (00G2) and exhibits textures and trace-element signatures indicative of garnet-absent growth (high Lu/Dy and Y) in the presence of melt (oscillatory zoning and Eu anomalies) (Figure 13); the distinctive monazite trace-element signature and limited spatial extent of an early ~600 Ma event are compatible with an accretion of the Vohibory Arc to the Androyen and Anosyen domains well before the onset of the East–West Gondwana collision prior to 620 Ma (e.g., de Wit et al., 2001). I cannot rule out, however, that the Vohibory and Androyen/Anosyen domains were already attached to their respective East and West Gondwana margins prior to this event. Whether the Androyen and Anosyen domains were thickened—and remained so—by this event is difficult to quantify due to subsequent reworking. I speculate that the juxtaposition of hot arc rocks next to the Androyen Domain heated the continental margin to the solidus along counter-clockwise PT path before crust became especially thick. This is compatible with oceanic arc magmatism in the Vohibory Domain until ~630 Ma (GAF-BGR, 2008) and monazite growth in the presence of melt less than 10 Myr later within the Androyen and Anosyen domains.

The existence of pre-600 Ma metamorphic dates in the Anosyen domain contradicts the tectonic model proposed by GAF-BGR (2008) in which the final suturing of East and West Gondwana occurred along the contact between the Androyen and Anosyen domains after 600 Ma. Furthermore, it is difficult to reconcile the existence of a west-facing ~850–700 Ma

continental arc that produced the Imorona–Itsindro Suite (Müller et al., 2000; GAF-BGR, 2008; Moine et al., 2014; Ichiki et al., 2015; but see counterview in Tucker et al., 2014) with a model in which outboard terranes (i.e., Androyen and Anosyen domains) were contiguous with older cratonic portions of East Gondwana since the Paleoproterozoic (e.g., Tucker et al., 2014). Rather, the inferences that the Vohibory Arc was oceanic until ~630 Ma and that the Imorona–Itsindro magmatism (until ~700 Ma) represents an east-directed subduction of oceanic crust necessitate that there were oceans on both sides of an Androyen–Anosyen microcontinent prior to final Gondwana assembly. Regardless of whether the Antananarivo Domain was part of the hypothesized Azania microcontinent (Collins and Piseravsky, 2005; Collins, 2006) or East Gondwana (Tucker et al., 2014), a separate Androyen–Anosyen microcontinent must have existed to the west.

The timing of final suturing of the Androyen–Anosyen domains to East and West Gondwana remains uncertain. On the western edge of the Androyen Domain, garnet-present monazite growth may have started as early as ~590 Ma (14G1), but most analyses with low heavy rare-earth elements abundances (indicative of garnet in the rock) occur after 570 Ma (Figure 13). Whether there was a 10–20 Myr tectonic/metamorphic hiatus after arc accretion cannot be resolved with the chronologic precision achieved in this study. However, the ubiquitous metamorphic dates and Ambalavao granite intrusions across southern Madagascar beginning at 580–570 Ma (e.g., Tucker et al., 2014) suggest that the main stage of continental collision began prior to this time. The central and northern parts of the Antananarivo Domain did not experience metamorphism and magmatism until ~560 Ma, compatible with ~100–200 km northeastward propagation of the orogen during a span of 10–20 Myr. I envisage that continent–continent collision metamorphism occurred first within a moderately pre-thickened and recently active western margin of an Androyen–

Anosyen microcontinent, after which regional metamorphism extended eastward at a rate commensurate with eastward crustal thickening.

Previously published petrology and my new 4+ thermometry allow us to map peak isotherms in detail (Figure 14); by assuming that mineral assemblage constraints and quantitative thermometry are lower bounds for peak metamorphic temperatures, spatially coherent thermal zones emerge from the data. UHTM affected a 150-km-wide zone in the southern Anosyen Domain (and probably the southeasternmost Androyen Domain) between Beraketa and Tôlanaro; the north–south extent of UHTM may have been >150 km as well and probably extends into southern India, Sri Lanka, and Antarctica. In Madagascar alone, UHTM influenced >20,000 km^2. Nearly all of the Androyen Domain and the eastern Androyen Domain experienced temperatures in excess of 800° C. The decreasing thermal gradient to the north (<1° C/km) in the northern Anosyen Domain was probably accompanied by a slight decrease in peak pressures (GAF-BGR, 2008; Jöns and Schenk, 2011). The peak metamorphic gradients are steeper (>2° C/km) to the east and west, but it is unclear to what extent these have contracted during shearing along the Ranotsara and Beraketa shear zones. Nevertheless, the Anosyen domain reached peak temperatures that were considerably hotter at comparable depths than in the adjacent domains to the east and west. This phenomenon cannot be explained entirely by post-peak-metamorphic rejuxtaposition because there is no evidence of large vertical displacements in southern Madagascar. Notably, peak temperatures do not correlate spatially with the Vohibory Arc, which suggests that arc accretion was not the principal heat source.

Across southern Madagascar, metamorphic growth of monazite and zircon ended between 525 Ma and 515 Ma during post-deformation Ambalavao granite emplacement. Regional isothermal decompression (e.g., Jöns and Schenk, 2011), as well as the coeval

cessation of metamorphism, magmatism, and deformation, is consistent with N–S extensional collapse of the orogen (e.g., Dewey, 1988) perpendicular to the E–W Gondwanan convergence. The southern Anosyen domain was extruded southward as a somewhat-cohesive crustal wedge (e.g., Martelat et al., 2000; Schreurs et al., 2010), whereas the northern Anosyen domain was extruded northward, flowing into a "flower" shape (e.g., Tucker et al., 2014) while the overlying Ikalamavony Domain was deformed into a fold–thrust belt (GAF-BGR, 2008). Cooling of the UHTM domain was probably accommodated by exhumation to shallower crustal depths and the extraction of granite melts.

6.2. The role of radiogenic heat production

Based on bulk-rock HPE concentrations, the Anosyen Domain has RHP rates that are much higher than average Proterozoic crust (0.73–0.90 $\mu W/m^3$: Jaupart and Mareschal, 2003). Moreover, some metasedimentary rocks in southern Madagascar are more radiogenic than HPE-rich granites, the conventional culprit for heterogeneous heat production (e.g., McLaren et al., 1999; McLaren and Powell, 2014; Bea, 2012). Assuming bulk rock-based rates represent heat production in the middle crust during orogenesis, static models produce ultrahigh temperatures at 30 km depth and at lengthscales and over timescales similar to that of the UHTM zone in southern Madagascar (Figures 14, 17, and 18). Considering that the models reproduce an E–W geothermal gradient comparable to that observed in Madagascar in a time frame compatible with geochronologic constraints, radioactive decay was probably the primary control on the thermal evolution of the middle crust. For this to be the case, however, several conditions must have been met. First, the thickness of the sample-based highly radiogenic layer must have been at least ~25 km thick and resided at >20 km depth for the duration of heating. If U were removed during melting and granite magmatism,

however, RHP could have been even higher and a thinner radiogenic layer would have provided sufficient heat. Either way, heat production would have been severely limited if denudation removed >20 km of the upper crust. Second, the upper crust above the highly radiogenic layer must have provided sufficient insulation, probably requiring an average thermal conductivity of 3.0 W/m/K or less. Third, heat flow from the mantle as low as 11 mW/m^2 may have been sufficient for UHTM to occur within 65 Myr. Lastly, surface heat flow during UHTM in the middle crust must have been very high, probably exceeding 100 mW/m^2.

Although focused RHP appears to have been the primary driver of UHTM in southern Madagascar, other heat sources may have contributed. For example, the accretion of the Vohibory Arc to the Androyen Domain likely caused regional heating and the geothermal gradient may not have relaxed entirely prior to the main stage of orogenesis. However, the peak UHT temperatures were not reached adjacent to the Vohibory Domain, indicating that heat from the arc was not the primary cause for UHTM. At temperatures less than 600° C, mechanical heat production could have been significant: doubling the thickness of crust with a density of 2700 kg/m^3 and specific heat of 1000 J/kg/K theoretically produces 37° C (Stüwe, 2007). In most modeled scenarios, however, temperatures in the Anosyen Domain reach 600° C in <20 Myr, after which mechanical heating would have become inconsequential due to thermal weakening. Changes in the mantle heat flux are also potentially important; as noted by Bea (2012), a modest increase in heat flux from the mantle due to lithospheric delamination, mantle wedge convection, or ponding of deep magma would have exaggerated heating of crust with elevated heat production. Seismic transects across the Tibetan Plateau suggest that asthenosphere is upwelling in response to the delamination of mantle lithosphere beneath Tibet and the rollback of the subducting Indian

slab (Shi et al., 2015). There is no evidence in southern Madagascar that the UHTM was caused by heat advection by mantle magmas. Charnockites in the Anosyen Domain have been interpreted as igneous rocks (e.g., Jöns and Schenk, 2011), but convincing evidence found in identical rocks in southern India (Taylor et al., 2014; Whitehouse et al., 2014) indicates that the charnockites were instead formed due to infiltration of CO_2-rich fluids during the waning stages of orogenesis. Furthermore, the charnockites are felsic (GAF-BGR, 2008), so even if they were igneous, their low heat capacities would have limited the extent to which they could transfer heat from the mantle.

Concentrated RHP in southern Madagascar caused an extreme thermal anomaly in the middle crust: My results demonstrate that the heterogeneous distribution of HPEs in southern Madagascar led to asymmetric heating, with a difference between the cool and hot segments of the model of up to 300° C at 30 km depth. Because rock strength is temperature dependent, focused RHP would have caused focused weakening of the crust. Without taking into account melt weakening, an increase in temperature at the base of a crustal column by 100° C can lead to a reduction in bulk strength by a factor of 2–3 (Sandiford and McLaren, 2002). The southern Anosyen Domain undoubtedly underwent even greater thermal weakening, but precise estimates of strength are difficult to make due to the complex lithologic heterogeneity of the region and the potential role of melt weakening. It is possible that the thermal weakening exceeded the threshold of gravitational stability of the thickened crust (e.g., Lexa et al., 2011), causing extensional collapse of the orogen (e.g., Dewey, 1988) that was accommodated by the N–S extrusion of the Anosyen Domain from 525–515 Ma.

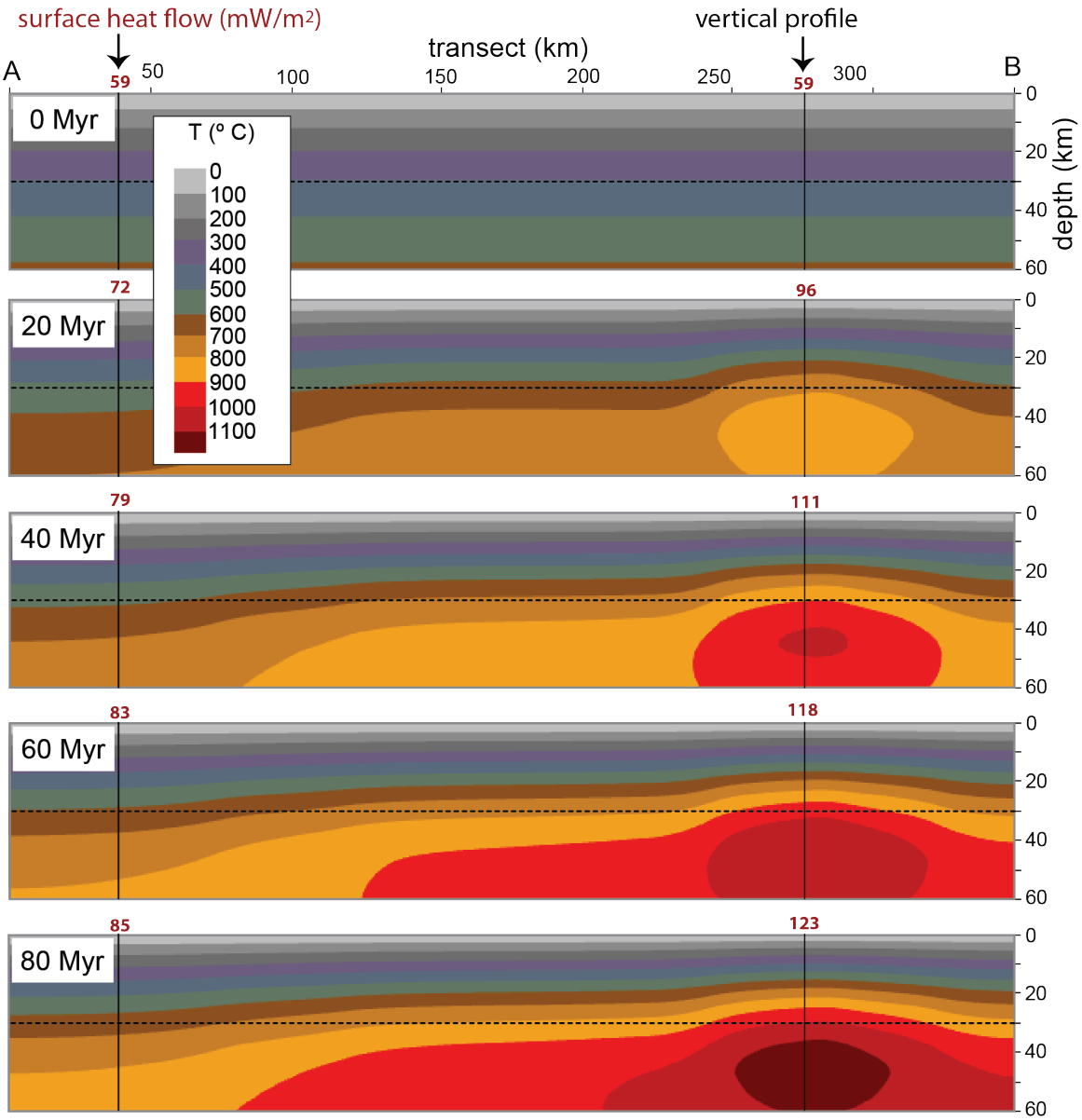

Figure 18. Time slices for the preferred parameterization of the model (see text for justification). Approximately 65 Myr is necessary to reproduce temperatures at 30 km depth that are representative of peak conditions across southern Madagascar.

6.3. (Re)distribution of heat-producing elements

Compared to the model upper continental crust of Rudnick and Gao (2003; 2014), the southern Anosyen samples have, on average, roughly the same amount of U (2.7 ppm), one and a half times as much K (4.2 wt.%), and 4–5 times as much Th (51 ppm). For typical crustal Th/U ratios of 4 to 1, Th and U produce similar amounts of heat: At 550 Ma, the

Rudnick and Gao (2003) upper crustal abundances of U, Th, and K would have produced roughly 41%, 39%, and 19% of the total heat production, respectively. Samples from southern Madagascar have much higher average Th abundances, such that Th produced nearly 75% of the heat, with U and K producing 15% and 10%, respectively.

The protoliths of the highly radiogenic metasedimentary rocks in southern Madagascar may also have had elevated concentrations of HPEs. Globally, sedimentary rocks show an increase in U by a factor >2 and an increase in Th by a factor >3 associated with the Archean–Proterozoic boundary (McLennan et al., 1980) just prior to the deposition of the Anosyen Domain. This sedimentary enrichment may have been caused by unprecedented late Archean intracrustal melting and potassic granitic magmatism that transported large volumes of U and Th to the upper crust (McLennan et al., 1980). Paleoproterozoic subaerial exposure and oxidative weathering of Anosyen protoliths could have caused pre-metamorphic fractionation of Th and U; high U concentrations in shales indicate that, from 2.4 Ga to 2.0 Ga, oxidative weathering on the continents preferentially transported U to the oceans (Partin et al., 2013).

The mobility of U and Th during metamorphism is largely controlled by the stability of accessory phases (Rudnick and Presper, 1990). Of the Th- and U-bearing phases in high-grade metamorphic rocks, monazite is especially important because apatite is more soluble in felsic melts (Wolf and London, 1995) and xenotime is consumed during prograde garnet growth (Bea and Montero, 1999). Zircon can be stable under granulite-facies conditions, but typically has much lower U and Th concentrations than monazite (most zircon has greater than 2 orders of magnitude less Th). During partial melting, monazite solubility in peraluminous granitic melt depends on the light rare earth element (LREE) concentration of the source (Rapp and Watson, 1986), but in most cases LREE saturation probably prevents

the complete dissolution of monazite at temperatures below ~800° C (Rapp et al., 1987) and favors monazite retention in the residue. Anhydrous melting (Watt and Harley, 1993) or metamorphism (Bingen and van Breeman, 1998) of metapelite at higher temperatures can also result in residual monazite. Thus, monazite tends to be retained in the residue when (i) the source contains high initial concentrations of LREEs or P that can saturate the melt; (ii) monazite growth precedes partial melting, retarding dissolution; (iii) hydrous melting occurs at less than ~800° C; and/or (iv) melts and fluids that react with the rock above ~800° C are anhydrous.

U is generally more mobile than Th during metamorphism and melting because lattice-bound U^{4+} can be oxidizing into soluble U^{6+} and mobilized by fluids and melts. Granulite terranes typically are depleted in U (Rudnick and Presper, 1990), especially when monazite is present (Bea and Montero, 1999). Monazite grown during high-temperature metamorphism tends to have high Th/U (e.g., Bingen and van Breeman, 1998) because U is preferentially retained in melt or metamorphic fluid while Th is incorporated into monazite. In Madagascar, Paleoproterozoic metamorphism led to monazite growth in the Androyen and Anosyen domains (e.g., sample 06C1), effectively preconditioning the crust by armoring the Th in relatively large grains. During Gondwana amalgamation, partial melting probably occurred at <800° C or under anhydrous conditions that that were unfavorable for monazite dissolution. High-temperature metamorphism dissolved some preexisting monazite, but the prevalence of metamorphic monazite rims suggests that a significant fraction of dissolved monazite was reprecipitated on older grains rather than being extracted from the middle crust. If U was extracted during melting and metamorphism, the bulk-rock analyses used to calculate the RHP may be underestimates for the early stages of orogenesis. Depending on

initial abundances, however, complementary depletion of U and enrichment of Th may have left the total heat production relatively unchanged (e.g., Bea and Montero, 1999).

7. Conclusions

My geochronologic results elucidate the protracted tectonic history of the UHTM domain exposed in southern Madagascar: rocks that were metamorphosed in the Paleoproterozoic collided with the Vohibory Arc at ~630 Ma, after which the collision between East and West Gondwana thrust them into thickened crust by ~580 Ma. New quantitative thermometry helps delineate a broad zone of UHTM, almost entirely in the southern Anosyen Domain. RHP rates calculated from bulk-rock compositions suggest that heat production was sufficiently high to explain UHTM within 65 Myr if the radiogenic layer was at least 25 km thick, leading me to surmise that RHP was the principal source of heat responsible for the UHTM. Moreover, focused heating caused by very high Th concentrations can explain why peak temperatures were much higher in the east. I conclude that the initial enrichment in HPEs, prior metamorphism, and the resiliency of monazite during orogenesis allowed enough Th to be retained to eventually cause UHTM.

Although neglected in most numerical models, accessory phase stability and heterogeneous HPE distributions in the crust may exert major influence on the thermomechanical evolution of orogens. Over long timescales, thickened crust can only be maintained if average crustal heat production is low and if HPEs are concentrated in the uppermost crust (e.g., Sandiford and McLaren, 2002; Mareschal and Jaupart, 2013); in lieu of magmatic/metasomatic redistribution of HPEs or rapid surface denudation, long term stability of the crustal column may be attained if HPE-rich domains are transferred magmatically or structurally to shallower depths. Extreme temperatures, thermal weakening,

and gravitational collapse—such as the exhumation of the Anosyen Domain—may be the inevitable result of HPEs trapped in the lower portions of tectonically thickened crust. Until we better understand why and how HPEs are mobilized during high-temperature processes, the extent to which RHP governs orogenic dynamics will remain uncertain. Microanalysis of metamorphic monazite—a major host of Th as well as a datable accessory mineral—shows promise as a way of tracking HPEs. Monazite stability under various high temperature conditions deserves renewed attention, both experimentally and in regional metamorphic studies.

III. Did phosphorus derived from the weathering of large igneous provinces fertilize the Neoproterozoic ocean?

1. Introduction

The Neoproterozoic era was punctuated by profound tectonic, evolutionary, and environmental change; the feedbacks among the breakup of the Rodinia supercontinent, 'Snowball Earth' glaciations, atmospheric oxygenation, and rapid biologic diversification remain controversial. Biologic and climatic conditions may have been especially sensitive to fluctuations in seawater phosphorus (P), believed to have been the biolimiting nutrient at the time (e.g., Van Cappellen and Ingall, 1996; Papineau, 2010; Laakso and Schrag, 2014; Lenton et al., 2014). During the Archean and early Proterozoic, the limited bioavailability of P (Bjerrum and Canfield, 2002; Jones et al., 2015) and trace metals (Anbar and Knoll, 2002; Konhauser et al., 2009) may have severely restricted the rate of photosynthesis and therefore the rise of atmospheric oxygen. High seawater phosphate levels during the Neoproterozoic would have increased the burial of organic carbon, triggering a marine redox shift—O_2 in the ocean and atmosphere increased from <0.1% (Lyons et al., 2014; Planavsky et al., 2014) to >10% (Canfield, 2005) of present atmospheric levels—correlated with the rise of metazoans (Van Cappellen and Ingall, 1996; Planavsky et al., 2010). The increase of O_2 in the oceans may have removed an environmental barrier preventing the evolution of larger, more complex life (e.g., Nursall, 1959; Canfield and Teske, 1996), although the ways in which photosynthetic oxygen production influenced biologic diversification remain uncertain (Knoll and Sperling, 2014; Mills and Canfield, 2014).

Complex feedbacks govern the ocean–atmosphere P cycle. For example, weathering rates for P-bearing minerals are temperature dependent (e.g., Guidry and Mackenzie, 2000) and recycling of P from the seafloor is redox dependent (e.g., Van Cappellen and Ingall, 1996). Further complicating matters, our chronologic resolution for the Neoproterozoic cannot resolve climate fluctuations on 1000 to 10,000 year timescales, making it difficult to distinguish the causes of oxygenation from the effects. There is, however, general consensus among modelers that P (and possibly nitrogen: Anbar and Knoll, 2002; Fennel et al., 2005) was the limiting control on primary production and thus oxygenation over million year timescales (e.g., Van Cappellen and Ingall, 1996; Schrag et al., 2002), and that the Neoproterozoic oxygenation event involved an increased rate of bioavailable P delivery to the ocean (e.g., Lenton and Watson, 2004; Laakso and Schrag, 2014; Mills et al., 2014). Such changes in the P cycle are recorded in Neoproterozoic sediments: significantly elevated marine phosphate concentrations have been postulated for the Sturtian deglaciation (Planavsky et al., 2010) at ~660 Ma (Rooney et al., 2015), and carbonates with high distributed P contents were formed during the Ediacaran and early Cambrian periods (Shimura et al., 2014). Furthermore, microfossils with phosphate scales have been identified in pre-Sturtian sediments (Cohen et al., 2011); surplus dissolved phosphate in the ocean could explain why protists utilized P at that time (Cohen and Knoll, 2012).

Because P in the ocean derives from weathering of continental crust, proposed mechanisms for elevated P fluxes to the Neoproterozoic ocean have included enhanced weathering of P during biologic colonization of the continents (Lenton and Watson, 2004), accelerated glacial weathering (Planavsky et al., 2010), and high surface topography (Campbell and Squire, 2010). I propose an alternative hypothesis: that the weathering of voluminous large igneous provinces (LIPs) associated with the breakup of the Rodinia

supercontinent increased the bioavailable P flux to the ocean. If indeed LIP magmatism periodically fertilized the Precambrian ocean, tectonic processes may have played a central role in fostering complex life in the oceans. To evaluate this hypothesis, I review the major controls on the global marine P flux, examine evidence for LIP magmatism in the Neoproterozoic, and present simple models to assess the effects of LIP weathering. Based on these results, I discuss the tectonic factors that favor efficient transfer of igneous P to the oceans, and postulate that complementary tectonic conditions aligned in the Neoproterozoic to facilitate an unprecedented and sustained P flux to the ocean. If so, LIP magmatism may help explain why the Neoproterozoic era was conducive to the evolution of complex life.

2. The Phosphorus Cycle

Phosphorus is a biolimiting nutrient that influences the production of organic matter in marine environments. Most P was incorporated into Earth's core during early differentiation, so the bulk silicate Earth contains only trace concentrations (90 ppm: McDonough and Sun, 1995). Because P behaves as an incompatible element during mantle melting and during early stages of mafic magma crystallization (Watson, 1980), continental crust contains higher P concentrations (~570 ppm: Rudnick and Gao, 2003) than the primitive mantle, although mantle xenoliths reveal that metasomatized mantle locally reaches >4000 ppm P (O'Reilly and Griffin, 2000). The concentration in the ocean depends on the relative rates of P input (i.e. continental weathering and subaqueous sedimentary P remobilization) and the sequestration of P (i.e. bioaccumulation, burial of sediments, and hydrothermal activity). Although P in the ocean today derives from terrestrial weathering of both igneous fluorapatite and marine sedimentary carbonate fluorapatite, nearly all the P that cycles

through sedimentary and biologic systems must have initially derived from continental weathering of igneous rocks.

The reactive P flux to the ocean may be modulated by changes in continental silicate weathering rates (e.g., Föllmi, 1996; Schrag et al., 2002), but can also be influenced by the rate of P liberation during weathering (e.g., Lenton and Watson, 2004). Only a fraction of riverine P enters the oceans in a biologically reactive form, so changes in the fraction of nonreactive P bound in Fe-oxides will influence primary productivity (e.g., Laakso and Schrag, 2014). An increased flux of bioavailable P to the ocean, as proposed for the Neoproterozoic, requires some combination of (i) an increase in overall silicate weathering rate, (ii) an increase in P weathering relative to the total silicate weathering rate, and/or (iii) a greater fraction of weathering-derived P that became bioavailable. Factors that potentially influence the reactive P flux include high continental surface topography, land colonization, and the composition of continental surfaces.

2.1. Topographic relief

Continental weathering rates are highly sensitive to topographic relief. The extensive Gondwanan continent-continent collisions that occurred in the late Neoproterozoic were expressed on Earth's surface as thousands of km of high mountains and likely resulted in large fluxes of nutrients to the ocean (Squire et al., 2006). A secular shift to cooler metamorphic gradients in the Neoproterozoic (e.g., Maruyama and Liou, 1998; Brown, 2006) suggests that surface topography reached unprecedented heights at that time. Rapid erosion of the mountain belts would have increased global sediment flux; this may have accelerated carbon burial and increased the flux of P and Fe to the ocean, and induced atmospheric oxygenation (Campbell and Squire, 2010). The steady increase in $^{87}Sr/^{86}Sr$

(Figure 19) in carbonates from 850 to 500 Ma probably reflects an increase in silicate weathering rate on continents during that period (e.g., Shields, 2007). However, this hypothesis fails to explain the pronounced increase in primary productivity in the Cryogenian and the Sturtian glaciation, both of which occurred during a rift-dominated period of the Wilson Cycle. High topographic relief associated with the Neoproterozoic continental assembly—widespread orogenesis began at ~650 Ma (e.g., Meert and Lieberman, 2008)—cannot explain the elevated primary productivity inferred from $\delta^{13}C_{carbonate}$ > 5‰ (Halverson et al., 2005; Och and Shields-Zhou, 2012) that preceded Gondwana assembly by >100 Myr. Instead, high weathering rates during the breakup of Rodinia were likely due to the dispersion of continents and a low latitude continental configuration (e.g., Donnadieu et al., 2004).

2.2. Land colonization

An increase in overall silicate weathering rate and/or P weathering efficiency caused by the colonizing biota could have fertilized the oceans, increasing organic carbon burial and O_2 production (Lenton and Watson, 2004). Although highly controversial, $\delta^{13}C$ fractionation trends in carbonates may suggest that simple land biota propagated sometime after 850 Ma (Knauth and Kennedy, 2009), and molecular clock estimations correspondingly indicate that land plants may have existed by 700 Ma (Heckman et al., 2001). An increase in clays relative to quartz in shaly sediments has also been attributed to an expansion in land biota; in response, organic carbon burial rates—proportional to clay content in ocean margins—may have increased by 600–700 % sometime between 800 and 500 Ma (Kennedy et al., 2006). However, the modal increase in clay is apparently due to micaceous rather than weathering-derived clays inputs, suggesting that accelerated physical erosion rather than land

colonization is responsible for the trend (Tosca et al., 2010). Unfortunately, the timing and overall impacts of land colonization remain poorly understood.

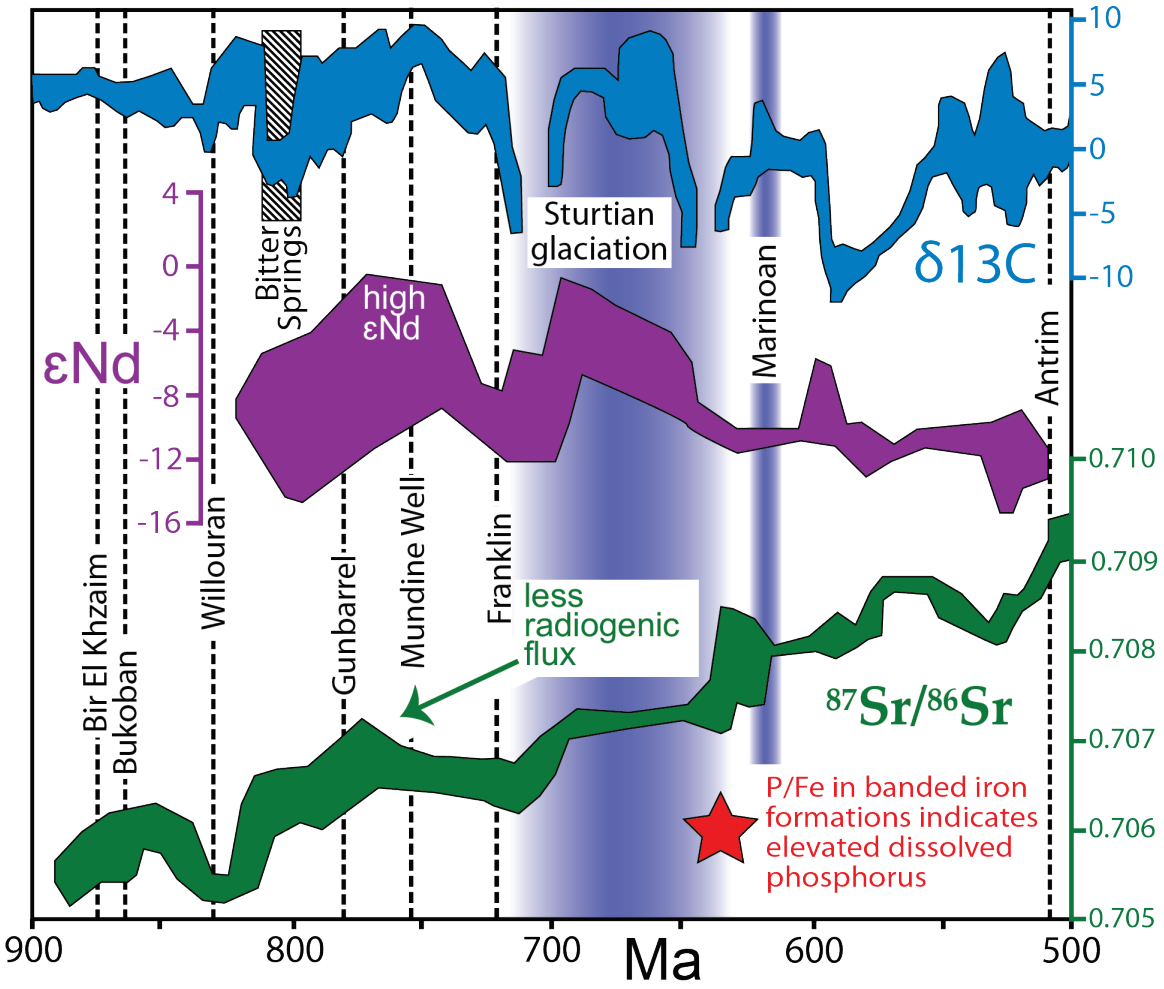

Figure 19. $\delta^{13}C$ (MacDonald et al., 2010), εNd (Halverson et al., 2010), and $^{87}Sr/^{86}Sr$ (Asmerom et al., 1991; Halverson et al., 2010) records for Neoproterozoic marine sedimentary rock. Elevated marine dissolved P concentrations have been inferred from P/Fe ratios of banded iron formations associated with the Sturtian deglaciation (Planavsky et al., 2010). Large igneous provinces (LIPs) with mafic dike swarms that cover an area greater than 2×10^5 km^2 (dotted lines) are based on Ernst and Buchan (2001), and coincide with high εNd and a less radiogenic $^{87}Sr/^{86}Sr$ flux—indicators of young mantle-derived rock entering the ocean. 'Snowball Earth' glaciations (Rooney et al., 2015) are shown as dark blue bands.

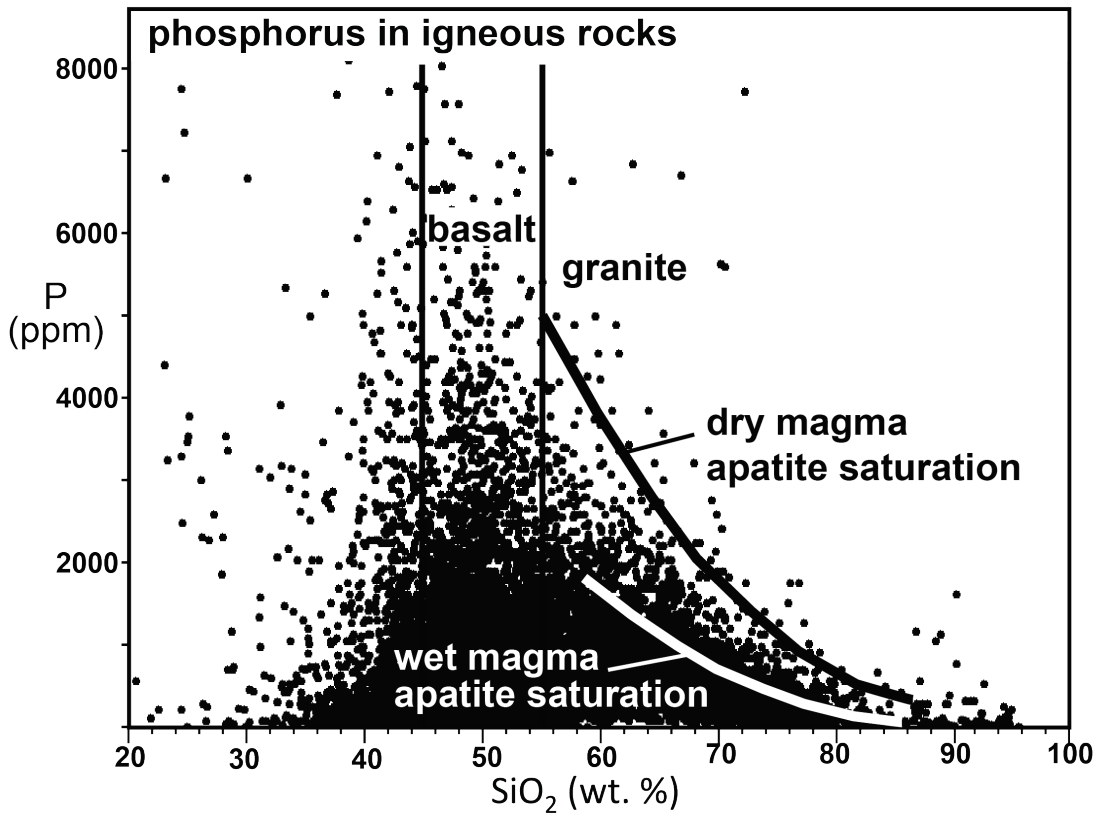

Figure 20. P vs. silica content for all igneous rocks >500 Ma (Phanerozoic data are similar) in the EarthChem database (http://www.earthchem.org/). Apatite saturation in felsic magmas limits the P concentration in granitic rocks. P concentrations can be much higher in basalts.

2.3. Surface lithology

Phosphorus behaves as an incompatible element in most igneous environments: low degrees of partial melting (or fractional crystallization and segregation of a P-poor phase) in the crust or mantle generally produces magmas with elevated P concentrations. In arcs, granitic and intermediate rocks typically have low P concentrations due to apatite saturation and crystal-liquid segregation (Figure 20) (Lee and Bachmann, 2014). Likewise, S-type granites can become P saturated at low concentrations, so P minerals are commonly retained in the restite. Apatite saturation occurs at higher P concentrations when magmas have lower silica and water contents, and when temperatures are higher (Lee and Bachmann, 2014), which explains why mafic rocks typically contain more P. Mid-ocean ridge basalt (MORB) derived

from depleted mantle has ~800 ppm P (Gale et al., 2013), but alkali basalts and nephelinites can contain 2000–9000 ppm P when apatite exists in the source region (Beswick and Carmichael, 1978). Despite having higher P concentrations than upper continental crust and covering >70% of solid Earth's surface, submarine basalt acts as a P sink because hydrothermal processes at spreading ridges sequester P in Fe-oxides (Wheat et al., 1996). On the other hand, the weathering of subaerial basalt can release P into the oceans.

Silicate minerals in mafic igneous rocks can contain up to 25% of bulk rock P because P^{5+} readily substitutes for Si^{4+} (Koritnig, 1965). Olivine, for instance, can contain >0.4 wt.% P, but such high-P contents only occurs when crystal growth outpaces P^{5+} diffusion in the magma because P preferentially partitions into residual melt (Milman-Barris et al., 2008). Instead, P is incorporated into fluorapatite or, if quenched before apatite precipitates, preserved in basaltic glass (e.g., Brunet and Chazot, 2001). Experiments indicate that fluorapatite dissolution in aqueous solutions is pH dependent, increasing from 10^{-11} to 10^{-10} mol/m^2/s at pH 6–8 to 10^{-7} mol/m^2/s at pH 2 (Guidry and Mackenzie, 2003; Chaïrat et al., 2007); dissolution rates for quartz and feldspars (major constituents of felsic rocks) are more than an order of magnitude slower across the same pH range (Bandstra and Brantley, 2008). At pH lower than 6, basalt also dissolves slower than fluorapatite, but at pH 6–8 the dissolution rates of basalt and fluorapatite are comparable (Guidry and Mackenzie, 2003; Bandstra and Brantley, 2008). Depending on composition, sedimentary carbonate fluorapatite dissolution is probably slower than for fluorapatite at moderate pH (Guidry and Mackenzie, 2003). The crystallinity of the basalt strongly influences dissolution rate: basaltic glass can weather an order of magnitude faster than crystalline basalt (Gilason and Hans, 1987). Similarly, the dissolution rate for apatite is influenced by surface area, so larger grains will release dissolved P slower. These observations suggest that weathering of

fluorapatite and basaltic glass will typically release P at higher rates than weathering of mafic and felsic rocks at moderate to low pH. In general, basaltic volcanic rocks probably release P efficiently during weathering because they are, on average, richer in P than felsic rocks, prone to rapid chemical weathering (e.g., Dessert et al., 2001), and more likely to host P in basaltic glass or fine-grained fluorapatite that can dissolve quickly.

3. Large Igneous Provinces

LIPs are typically defined as volumetrically large (>0.1 Mkm^2) magmatic provinces erupted or emplaced rapidly, commonly in less than 5 Myr (e.g., Ernst, 2007). LIPs are dominantly composed of tholeiitic basalt and occur in both oceanic and continental settings. No pre-Mesozoic intraoceanic LIPs (i.e., ocean plateaus) still exist and only the 'plumbing system' of feeder dikes are well preserved for Precambrian LIPs (Ernst, 2007). Pulses of geographically isolated LIPs are associated with every supercontinent breakup of the Wilson Cycle (Ernst and Bleeker, 2010). The breakup of Rodinia was no exception: rifting may have initiated with a superplume at ~825 Ma (Li et al., 2013) and was punctuated by major LIPs until ~720 Ma (Ernst et al., 2008). As discussed below, a significant fraction of Earth's land surface may have been covered by flood basalts—enriched in P relative to average continental crust—during the breakup of the Rodinia supercontinent.

3.1. Timing of LIP events

LIP magmatism has occurred since ~3.5 Ga with an average frequency of 20 Myr (Ernst, 2007), with above-average rates of LIP magmatism during periods of supercontinent breakup. In particular, there are were frequent LIP events associated with the breakup of Nuna (1600–1200 Ma) and Rodinia (825–750), but less-frequent (yet still large) LIP events

during the intervening period of Rodinia assembly (Ernst et al., 2008). This could have been due to intracontinental rifting that occurred even during periods of prevailingly collisional tectonics. The updated LIP database (http://www.largeigneousprovinces.org/) based on Ernst and Buchan (2001) lists 26 large mafic magmatic events between 900 and 500 Ma (unless noted, the age and volume of LIPs are from their database). Of these, this study excludes 12 LIPs without size constraints and five LIPs that have imprecise age constraints (uncertainty >100 Myr).

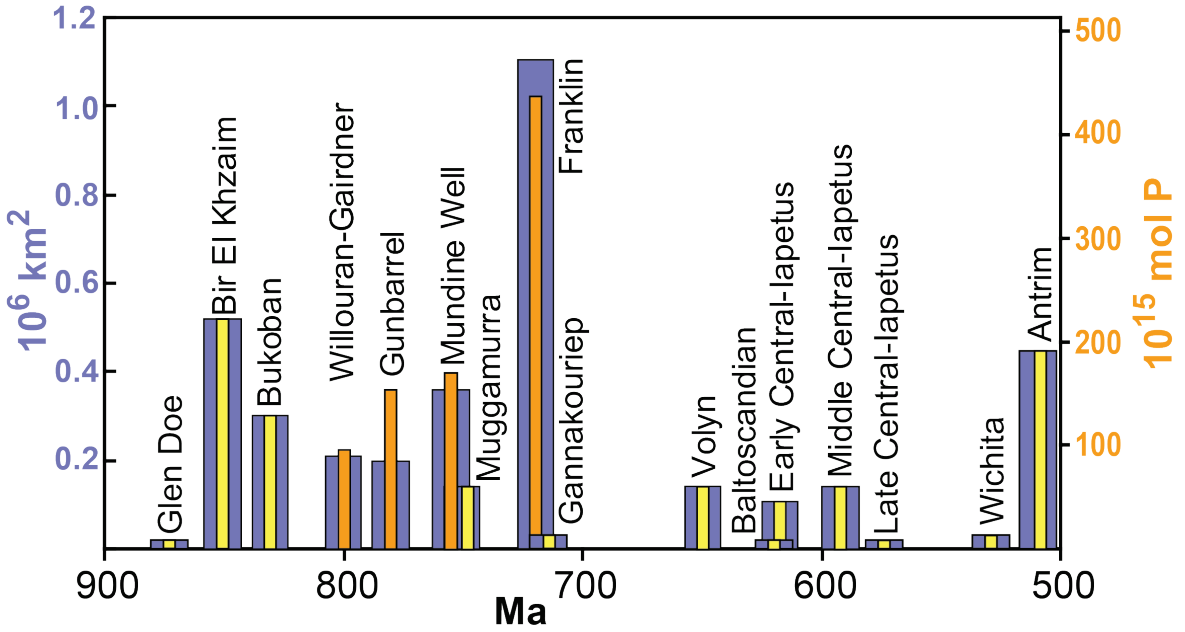

Figure 21. Area of mafic dike swarms (purple) and estimated P content (yellow/orange) for Neoproterozoic and Early Cambrian LIPs. Orange bars are based on median P concentrations for LIPs (Appendix 13). Yellow bars are based on P concentration of average MORB (802 ppm: Gale et al., 2013).

3.2. Volume of LIP events

Due to the susceptibility of mafic volcanic rock to subaerial weathering, Precambrian LIPs have largely been eroded, and their eruptive volumes must be estimated from dike swarms. Mafic dike swarms that occurred between 900 and 500 Ma cover 3.7×10^6 km^2 (Figure 21), or ~4% of the total Neoproterozoic land surface (assumed to be 90×10^6 km^2: Goddéris et al., 2003). However, length-based and width-based estimates of dike swarm area are

generally conservative (Ernst and Buchan, 2001) because portions of LIPs may be missing or not exposed. And because flood basalts can flow great distances, the areas of LIP flood basalts were presumably greater than the area of mafic feeder dike swarms; Abbott and Isley (2002) found that the feeder dikes of the Colombia River basalt province represent 52% of the total flood basalt province. Thus, assuming that flood basalts cover areas twice as large as LIP feeder dikes, flood basalts in the Neoproterozoic may have collectively covered 7.4×10^6 km^2, or ~8% of the land surface. This estimate is consistent with models of Neoproterozoic climate (Goddéris et al., 2003; Donnadieu et al., 2004) that use basalt flow areas of $4–8 \times 10^6$ km^2. For comparison, a single Mesozoic LIP, the Central Atlantic Magmatic Province, spanned a similar area (Marzoli et al., 1999), so Neoproterozoic continental flood basalts could have, conceivably, covered an even greater area. (Note that although submarine LIPs can be much larger than continental LIPs, only extrusive continental volcanic rocks would have been immediately exposed to subaerial chemical weathering that transported reactive P into the ocean.)

The original thicknesses of LIP flood basalts are unknown. Better-preserved Phanerozoic LIPs provide some insight: The Cretaceous-Tertiary Deccan traps originally covered an area of 1.8×10^6 km^2 and had a volume of 8.6×10^6 km^3 (Eldholm and Coffin, 2000), implying a thickness of >4 km. On the other hand, the Jurassic Karroo province averages 2.5 km thick (2.5×10^6 km^3 over 10^6 km^2) and the preserved extrusive portion of the Permian-Triassic Siberian traps is ~1 km thick over an area of 0.34×10^6 km^2 (Sharma, 1997). Based on such analogues, it seems reasonable to assume that Neoproterozoic LIPs were 1–4 km thick.

Evidence of extensive Neoproterozoic continental flood basalt weathering is preserved in the marine sedimentary record. Although $^{87}Sr/^{86}Sr$ systematically increases from ~830 Ma to 550 Ma, with sharp inflections during glaciation events, there is an apparent decline between

~775 and 720 Ma (Figure 19) that is consistent with intense weathering of flood basalts with an unradiogenic mantle signature (Halverson et al., 2007). Sediments from ~750–720 Ma also have distinctly unradiogenic $^{187}Os/^{188}Os$ that can be explained by weathering of voluminous juvenile basalt (Rooney et al., 2015). A coincident increase in $^{143}Nd/^{144}Nd$ at ~740 Ma has also been attributed to the weathering of flood basalts (Figure 19) (Barovich and Foden, 2000), but the two records are from disjunct sedimentary successions that are difficult to correlate (Halverson et al., 2010). Most notably, the εNd value of –12 at 800 Ma increased to an εNd of ~0 at 750 Ma (Figure 19), and these high values were presumably sustained until ~600 Ma (Barovich and Foden, 2000). The biggest LIPs were emplaced during this time interval: of the 17 considered in this study, LIPs emplaced from 850 to 700 Ma constitute ~75% of the overall LIP area, and the 720 Ma Franklin Province alone makes up 29% of the total area.

3.3. Phosphorus content of LIPs

Median P concentrations for mafic rocks related to the rifting of Rodinia range from 741 ppm (Franklin Province) to >1000 ppm (Glen Doe and Gunbarrel events). Most LIPs exhibit considerable compositional variability, so median values may not be representative. Notably, the largest LIP (Franklin Province) has the lowest P—lower even than average MORB. Neoproterozoic median P concentrations are comparable to other major LIPs, but the Gunbarrel (~2200 ppm) event may have had elevated P concentrations. All LIP flood basalts, however, likely had higher P concentrations than average Neoproterozoic upper continental crust. For comparison, the Archean Baltic Shield and Superior Province both have median P less than 500 ppm, which is less than typical granite concentrations of ~650 ppm P. Thus, assuming that P-rich sedimentary rocks constituted a negligible fraction of the

land surface in the Neoproterozoic, LIP basalts that covered a significant fraction of continents had higher P concentrations than other land surfaces by a factor of 1.5 to >2.

4. Weathering Models

Numerous factors—many of which are poorly understood for the Neoproterozoic—influence the rate of bioavailable P production by the chemical weathering of LIPs, but simple models can provide basic constraints. The models presented here are based on: (i) the geologic record of LIP magmatism, including the P concentrations and areal extents of mafic dike swarms; (ii) Phanerozoic LIPs that are well preserved; and (iii) modern weathering and erosion rates. In the model (Supplementary File 2), flood basalts are emplaced instantaneously and are proportional in size to the preserved mafic dike swarms. P is released from the flood basalts at a constant rate until the basalt has been fully denuded by chemical weathering and physical erosion; the total P released to the ocean is the sum of the P fluxes from the exposed LIP basalts. The model spans the Neoproterozoic to early Cambrian period of interest from 900 to 500 Ma. The approach is to use reasonable values from the rock record and previous studies as inputs and then conduct sensitivity tests for each variable. Given the interdependence and natural variability of many input parameters, these models are extreme simplifications; the results are approximations.

Table 5. Default parameters used for models.

Parameter	Default value	Units
P concentration	802	ppm
Flood basalt thickness	3	km
Flood basalt area	2	multiple of mafic dike swarm area
Basalt density	2.75	g/cm^3
Chemical weathering rate	4×10^7	$g/km^2/yr$
Physical erosion rate	4×10^7	$g/km^2/yr$
Bioavailable fraction	0.4	
Background Proterozoic P flux	1.5×10^9	mol/yr

4.1. Input parameters

For each LIP with basalt geochemical data, the median P concentration (Appendix 9) is assumed to be representative of the entire LIP. All other LIPs are assigned a MORB-like P concentration of 802 ppm (Gale et al., 2013). The total flood basalt area is assumed to be twice (see rational in Abbott and Isley, 2002) that of mafic dike swarm areas (from Ernst and Buchan, 2001). An average chemical weathering rate of 40 t/km^2/yr is assumed based on modern weathering rates for basaltic watersheds in temperate regions with moderate runoff (Millot et al., 2002; Dessert et al., 2003). This is considerably lower than rates observed in high runoff areas; Reunion Island, for example, has chemical weathering rates of 63–170 t/km^2/yr (Louvat and Allègre, 1997). Physical denudation rates in modern settings can be many times greater than chemical weathering rates (e.g., Millot et al., 2002), but a default physical erosion rate equal to the chemical weathering rate has been adopted here to evaluate the maximum potential P extraction from LIP flood basalts.

Weathering fluxes from Neoproterozoic flood basalts are compared to weathering fluxes from granitic crust: assuming a continental area of 9×10^7 km^2 (Goddéris et al., 2003), an average chemical weathering rate of 2 t/km^2/yr (reasonable for granitic catchments: Millot et al., 2002), that 40% weathered P became bioavailable, and an average granitic P concentration of 650 ppm (although Archean shield samples are on average much lower), the total reactive P flux would have been ~1.5×10^9 mol P/yr, or less than a percent of the modern flux (~25–30 $\times 10^{10}$ mol P/yr: Ruttenberg, 2004). Considering that a low reactive P flux of <10% of the modern preagricultural flux may have been necessary to stabilize low Proterozoic pO_2 (Laakso and Schrag, 2014), such a low pre-LIP flux seems reasonable. Although the weathering of sediments could have also contributed to the pre-LIP flux, 1.5 ×

10^9 mol P/yr is used as a background flux for the models to highlight the role of flood basalt weathering relative to average crust.

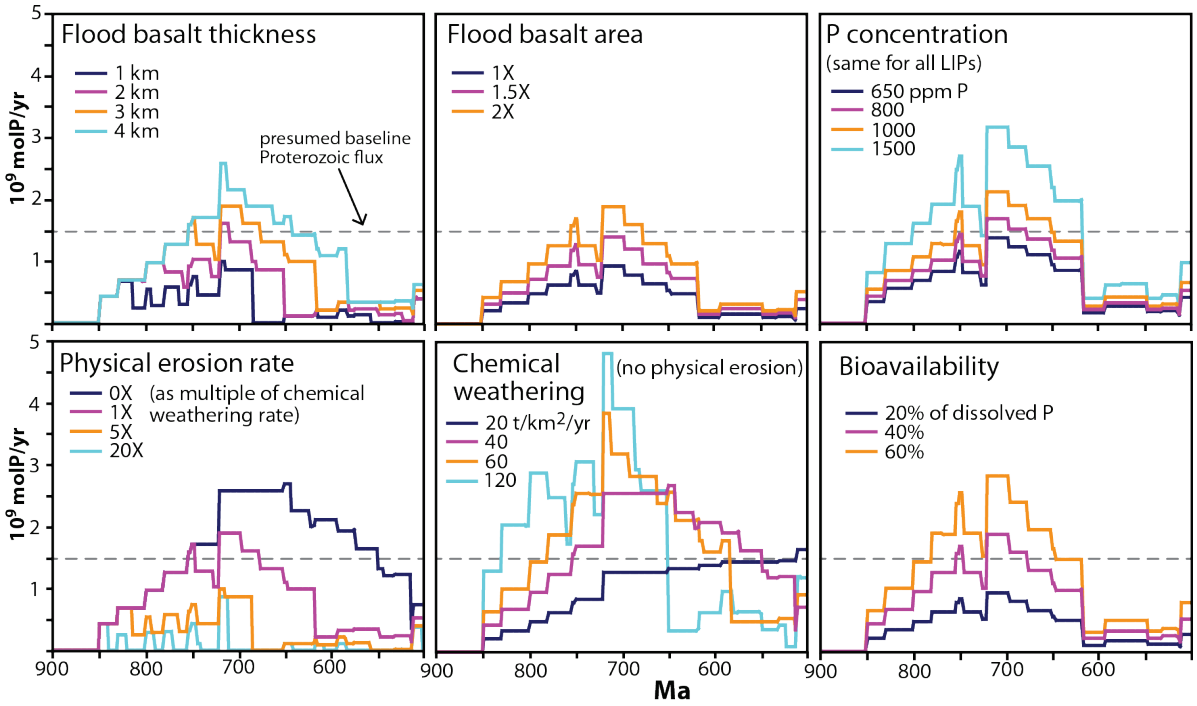

Figure 22. Sensitivity tests for P flux models. Unless noted, default parameters in Table 5 are used. See text for details.

4.2. Sensitivity tests

Several parameters affect the calculated P flux independent of flux duration (Figure 22). Doubling the flood basalt area, for example, will double the P flux. Likewise, higher P concentrations in the basalt and greater fractions of reactive P will proportionally increase the P flux. Input ranges for each variable with otherwise default parameters (Table 5) produce maximum P fluxes at ~720 Ma of 1–3 × 10^9 mol P/yr, or roughly twice the background Proterozoic P flux. Compounded increases in areal extent, P concentrations, and higher bioavailable fractions of weathered P cause much higher fluxes.

P fluxes are especially sensitive to parameters that affect the duration and magnitude of P transfer from individual LIPs. Thicker flood basalts provide a longer and more-consistent P

flux to the ocean, and increase the total P transferred to the ocean. Tripling the LIP thickness from 1 to 3 km creates a sustained rather than punctuated P flux for ~200 Myr and doubles the peak flux, which is reached for all the models at ~720 Ma when the Franklin Province is emplaced. The relative rates of chemical weathering and physical erosion have similar effects: high rates of physical erosion increase the fraction of P retained in detrital particulate matter and therefore decrease the overall reactive P flux while hastening the denudation of the basalt. Conversely, increasing chemical weathering relative to physical erosion not only increases the total dissolved P flux, but also hastens denudation. A physical erosion rate 20 times that of the chemical weathering rate releases P in short 10 Myr bursts that never exceed the background Proterozoic P flux. Model runs with 100% chemical weathering, however, reach peak P fluxes four times as high as the background flux.

Table 6: LIP age and size (after Ernst and Buchan, 2001), as well as calculated P contents.

Large igneous province	Approx. Age	Dike swarm area	Median P concentration	Estimated P content	Estimated P flux (including iron-bound P)
	(Ma)	(10^3 km^2)	(ppm)	(10^{15} mol)	(10^6 mol/yr)
Glen Doe	873	2	1264	1	7
Bir El Khzaim	850	520	-	222	1077
Bukoban	830	300	-	128	622
Willouran-Gairdner	800	210	828	93	449
Gunbarrel	780	200	2254	153	743
Mundine Well	755	360	872	167	811
Muggamurra	750	140	-	60	290
Franklin	720	1100	741	434	2106
Gannakouriep	720	30	-	13	62
Volyn	650	140	-	60	290
Baltoscandian	619	10	-	4	21
Early Central-Iapetus	617	105	-	45	218
Middle Central-Iapetus	592	140	-	60	290
Late Central-Iapetus	575	7	-	3	15
Wichita	530	30	-	13	62
Antrim	510	450	-	192	932
Total		3744		1648	7995

5. Discussion

Neoproterozoic P fluxes are difficult to assess due to poor constraints for LIP volumes, physical erosion rates, and the fraction of Fe-bound P that remains nonreactive. Nevertheless, the models presented here provide a basis for evaluating the effects of Neoproterozoic LIP weathering. Below, I discuss complex feedbacks that complicate the interpretation of these results, hypothesize that geochemical enrichment of LIP magmas prior to eruption contributed to the reactive P flux, and evaluate the potential effects of LIP weathering.

5.1. The timing of LIP-related P fluxes

Although LIP events occurred regularly throughout the Neoproterozoic, LIP sizes vary from 2000 km^2 (Glen Doe) to 1,100,000 km^2 (Franklin). Sizeable LIPs that were emplaced from 850 to 720 Ma include the Bir El Khazaim (520,000 km^2), Bukoban (300,000 km^2), Willouran–Gairdner (210,000 km^2), Gunbarrel (200,000 km^2), Mundine Well (360,000 km^2), Muggamurra (140,000 km^2), and Gannakourie (180,000 km^2) events and culminated with the enormous Franklin Province. During this 130 Myr period, continental surfaces were repeatedly covered with abnormally large volumes of mantle-derived magma. Considering that Phanerozoic traps such as the Siberian, Karroo–Ferrar, and Deccan still exist after tens to hundreds of Myr, multiple LIP flood basalts most likely coexisted for much of the late Neoproterozoic. The εNd anomaly in the Neoproterozoic indicates that juvenile (i.e., mantle-derived) material entered the ocean over a prolonged period from ~750 to ~600 (Figure 19) (Barovich and Foden, 2000). This is inconsistent with physical erosion rates fast enough to have denuded LIPs in less than 10 Myr. Rather, the εNd sedimentary record points to protracted chemical weathering of LIPs. If so, and unless denudation rates were exceedingly

slow, the surface area covered by flood basalts likely peaked at ~720 Ma with the emplacement of the Franklin Province, before steadily declining. Increasingly radiogenic $^{187}Os/^{188}Os$ in sediments from 660 to 630 Ma (Rooney et al., 2015) may reflect this decline. Magmatism associated with the opening of the Iapetus contributed relatively minor volumes of basalt from 620 to 575 Ma, and the next sizable LIP event occurred at ~510 Ma, on the tail end of Gondwana assembly.

5.2. P fluxes prior to Neoproterozoic LIP volcanism

The degree to which LIP-derived P perturbed oxygen and carbon cycles in the Neoproterozoic depends on the background Proterozoic P flux. In modern rivers, greater than 90% of the P is bound to suspended particulate matter; dissolved P in river water (3.2–5.8 × 10^{10} mol P/yr) and aerosol P (2–5 × 10^{10} mol P/yr) make up the rest of the flux to the ocean (Froelich, 1988; Ruttenberg, 2003). Of the suspended particulate-bound P, roughly 20–40% is organic and the rest is mostly oxyhydroxides and detrital apatite (Ruttenberg, 2003). An estimated 25–45% (15–29 × 10^{10} mol/yr, Ruttenberg, 2003) of the total particulate flux is mobilized upon reaching the ocean, such that the combined dissolved riverine, particulate-bound, and aerosol P fluxes contribute 12–40 × 10^{10} mol P/yr—and most likely 25–30 × 10^{10} mol P/yr (Ruttenberg, 2003)—of bioavailable P to the ocean. The global marine burial flux of reactive P—roughly half of which occurs in marine shelf environments with high productivity (Filippelli, 1997)—is nearly as large (18–24 × 10^{10} mol P/yr: Ruttenberg, 2003). The majority of reactive P is buried as authigenic carbonate fluorapatite (2–9 × 10^{10} mol/yr: Ruttenberg, 1993); most of the remainder is removed from seawater by hydrothermal activity at mid-ocean ridges (1.4 × 10^{10} mol/yr: Wheat et al., 1996) and the burial organic matter (1–4 × 10^{10} mol/yr), non-hydrothermal Fe-oxides (0.4–4

$\times 10^{10}$ mol/yr), and minerals with loosely-bound P on their surfaces (1.3×10^{10} mol/yr) (Ruttenberg, 1993, 2003).

Prior to Neoproterozoic LIP volcanism, the flux of reactive P from the continents was probably much less than the preagricultural modern flux. Laakso and Schrag (2014) produced models to evaluate steady state low atmospheric pO_2, concluding that 10% modern pre-agricultural reactive P flux could have stabilized pO_2 at ~1% of modern atmospheric levels. But atmospheric pO_2 in the middle Proterozoic may have been $\leq$0.1% of present levels (Planavsky et al., 2014), which could imply an even smaller middle Proterozoic P flux to the ocean. Assuming weathering of granitic continental surfaces was the dominant source of P, an unrealistically high chemical weathering rate of ~20 t/km^2/yr of rock with 650 ppm P over modern continental land surface areas would have been necessary (assuming 40% of weathered P became bioavailable) to sustain $>10^{10}$ mol P/yr flux. Thus, the background reactive P flux to the ocean may have been low enough that the weathering of LIPs (possibly reaching $1–5 \times 10^9$ mol P/yr) would have constituted a major nutrient source.

5.3. Iron-bound P

Most of the bioavailable P entering the ocean is released from Fe-oxides (e.g., Froelich, 1988; Benitez-Nelson, 2000). Experiments show that Fe-oxides derived from Fe^{2+} in the presence of modest amounts of dissolved Si can incorporate up to 0.2 mol P/mol Fe in freshwater (Mayer and Jarrell, 2000), but that dissolved Si limits P incorporation into oxides when present in higher concentrations in seawater (Jones et al., 2015). Lattice-bound P in Fe-oxides generally remains biologically unavailable for as long as the oxide remains insoluble, whereas P bound to Fe-oxide surfaces is susceptible to desorption (Froelich, 1988; Ruttenberg and Sulak, 2011). When Fe-oxides are buried, terrestrial weathering-derived P

that co-precipitated with the oxides or sorbed to oxide surfaces can bypass the biologic cycle. However, Fe-oxides that enter the ocean can rapidly release surface-sorbed P (over the course of minutes) because seawater phosphate concentrations are lower than in rivers and because seawater contains anions that compete for surface sites (Froelich, 1988). After the removal of loosely-bound surface P, additional P is slowly released (on the order of days) from the interior of Fe-oxide particles (Ruttenberg and Sulak, 2011). If Fe-oxides reach a reducing environment—such as settling into anoxic waters—oxides can dissolve, releasing any remaining P into the water column.

Laakso and Schrag (2014) propose that the low pO_2 Proterozoic environment slowed the oxidation of iron enough that Fe^{2+} could be transported from the subsurface to rivers and estuaries, where Fe-oxides precipitated in the presence of higher dissolved P concentrations. If so, and assuming that the Fe-bound P was permanently buried, the fraction of weathered P that became incorporated into Fe-oxides—and, thus the fraction that bypassed the biologic cycle—would have been greater. If, on the other hand, Proterozoic atmospheric oxygen levels were low enough that not all weathering-derived Fe was oxidized before reaching the ocean, a higher fraction of the weathered P would be expected to enter the ocean in solution. Also, if anoxic conditions were common below the storm wave base in the Neoproterozoic ocean (Canfield et al., 2008), a greater fraction of settling Fe-oxides may have dissolved and released bioavailable P. These uncertainties regarding the oxidation state of various Neoproterozoic environments make it difficult to estimate the fraction of LIP-derived P that became bioavailable.

In addition to having higher average P concentrations than granitic rocks, basalts also contain more Fe. Therefore, compared to granite weathering, basalt weathering releases more Fe into groundwater and rivers that can be precipitated as oxides. However, average

P/Fe in mafic and felsic rocks are comparable: molar P/Fe of Karoo-Ferrar (0.014) and Deccan Traps (0.021) rocks compare closely with that of upper continental crust (0.017: Rudnick and Gao, 2003) and andesite (~0.018: GeoRoc Database, http://georoc.mpch-mainz.gwdg.de/georoc/). And, because Fe oxyhydroxides have high sorption capacities (P/Fe of ~0.5; Gunnars et al., 2002), the Fe contents of most crustal rocks do not limit the capacity of Fe-oxides to fix dissolved P during weathering. Thus, the weathering of LIPs would not have necessarily yielded a greater or lesser fraction Fe-bound P compared to average crust.

5.4. P enrichment beneath thick lithosphere

Subaerial tholeiitic basalt provides more P to the ocean than average crust. Basalts with higher P concentrations—which some Neoproterozoic LIP rocks contained—yield even more reactive P. Geochemical enrichment can explain the elevated P concentrations observed in LIP basalts and the correspondingly-high reactive P fluxes that may have resulted from their weathering.

Lithosphere thickness can influence the composition of asthenosphere-derived magmas. Upwelling asthenosphere undergoes higher degrees of decompression melting at shallower depths, so thick lithosphere that inhibits the ascent of asthenosphere will limit the degree of melting (Kerr, 1994). In addition, asthenosphere plumes that pond beneath or within thick lithosphere incubate for longer periods of time (e.g., Kent et al., 1992), which can lead to higher degrees of liquid-crystal segregation. P concentration in high degree/shallow (low P) and low-degree/deep (higher P) melts probably do not differ by more than a factor of 2–3, but these differences can become exaggerated by fractional crystallization and liquid-crystal segregation, which occurs for longer periods beneath or within thick lithosphere. Such trends

are apparent in Karoo samples: high-Ti and high-P concentrations are restricted to areas above thick lithosphere and can be explained by low degrees of partial melting beneath thick lithosphere and fractional crystallization (Jourdan et al., 2007). P-enriching fractional crystallization trends are observed for the Karoo-Ferrar, Deccan Traps, and North Atlantic Igneous Province (Figure 23), and are characteristic of LIPs generated beneath thick lithosphere. In contrast, the Central Atlantic Magmatic Province magmas probably formed with lower initial P concentrations due to high degrees of partial melting and underwent less P enrichment during fractional crystallization. Interestingly, the Karoo-Farrar samples have both a high-P and a low-P enrichment trend, reflecting generation beneath thick and thin lithosphere, respectively (Jourdan et al., 2007).

Thick (>180 km) lithosphere is believed to have existed since the Archean because the removal of heavy elements during high degrees of melting in the hot Archean mantle produced buoyant residue (Djomani et al., 2001). It is unclear why pre-Neoproterozoic LIPs were apparently less enriched in P by fractional crystallization than the strongly fractionated Phanerozoic LIPs. Perhaps higher mantle temperatures in the pre-Neoproterozoic mantle caused higher degrees of melting and thus lower P concentrations in primary magmas. Limited fractional crystallization for pre-Neoproterozoic LIPs may simply reflect the fact that the LIPs for which we have data were emplaced through thinner lithosphere. Data (albeit relatively sparse) from Neoproterozoic LIPs exhibit a liquid-crystal segregation enrichment trend analogous to that of Phanerozoic LIPs (Figure 23). Higher degrees of liquid–crystal segregation decrease melt volume, so fractional crystallization may not ultimately yield more total P; this may explain why the largest Neoproterozoic LIP (Franklin Province) has the lowest median P concentration. P concentrations in some Neoproterozoic LIP basalts may have increased by a factor of 2–3 during liquid-crystal segregation, but most samples were

not enriched to that extent. Fe also becomes enriched during liquid-crystal segregation, so P/Fe of LIP magmas does not systematically increase.

5.5. P enrichment via incorporation of subcontinental mantle

LIP magmas are not exclusively derived from the asthenosphere. Phanerozoic plume-related continental flood basalts are mixtures of asthenosphere and metasomatically enriched subcontinental lithosphere melts (Zhang and O'Reilly, 1997; Jourdan et al., 2007; Song et al., 2008), suggesting that rising asthenosphere incorporates lithosphere. At least six major flood basalt eruptions since the Mesoproterozoic are temporally and spatially associated with metasomatism-related carbonatite, lamproite, and kimberlite magmas (Rao and Lehmann, 2011; and references therein) that were partially engulfed by the voluminous tholeiitic magmas. Metasomatism by K-rich brines and CO_2 readily partitions and redistributes P from common mantle minerals: although P in the primitive mantle range from 60 to 100 ppm, mantle xenoliths from metasomatized mantle can have >4000 ppm (O'Reilly and Griffin, 2000). LIP magmas can be enriched in P when rising asthenosphere melts preexisting metasomatized mantle, or by releasing and then reincorporating metasomatic fluids.

Volatile-rich, highly potassic magmatism is only associated with LIPs younger than ~1 Ga (e.g., Rao and Lehmann, 2011) and, in general, few alkaline silica-undersaturated rocks exist in the Precambrian rock record (e.g., Gupta, 2015). Neither of these observations is adequately explained by poor preservation. Rather, the widespread appearance of these rocks may reflect a secular change in the thermal structure of continents (e.g., Brown, 2007) and subduction zones in particular (e.g., Dasgupta, 2013). Little evidence exists of crust having subducted to depths greater than 150 km—e.g., blueschists and eclogites—and returning to continental depths prior to ~750 Ma (Jahn et al., 2001; Maruyama and Liou, 2005). This

suggests that there was a Neoproterozoic transition to a cooler subduction regime. In hot subduction zones, metasediment and metabasalt release most CO_2 at crustal depths (Kerrick and Connolly, 2001) and any slab disintegration would have further limited transport of CO_2 to the mantle. In contrast, metasediments in cooler subduction zones retain CO_2 beyond subarc depths (~140 km) unless external H_2O infiltrates the slab (Kerrick and Connolly, 2001; Gorman et al., 2006). Pre-Neoproterozoic warmer subduction presumably caused carbonate to decompose at shallow depths, but in cooler Neoproterozoic–Phanerozoic subduction zones, the release of CO_2 from metasedimentary rock caused widespread carbonate metasomatism in mantle wedges behind the arc (Dasgupta and Hirschmann, 2010; Dasgupta, 2013). Thus, metasomatized P-rich subcontinental mantle—which provides a fertile P source for rising asthenosphere during LIP magmatism—may have only existed since ~1 Ga.

Quantifying the fraction of metasomatic P in modern LIPs is difficult due to sampling bias (for example, kimberlites are disproportionately analyzed compared to tholeiitic basalts), and even more difficult for Neoproterozoic LIPs that have been largely eroded. Many high-P LIP rocks that are not associated fractional crystallization trends (scatter in the upper right corners of MgO versus P_2O_5 plots; Figure 23) may contain a metasomatic component. Rocks that were enriched beyond P/Fe >0.2 would have been especially fertile sources of P because Fe-oxides derived from them during weathering could have become saturated with P. Even though volatile-rich magmas can contain multiple weight percent P_2O_5, metasomatic melt components probably contribute less than half of the total P of any given LIP. Nevertheless, metasomatic P enrichment of LIPs—a process that became widespread in the Neoproterozoic—provides another link between tectonic processes and the flux of bioavailable P to the ocean.

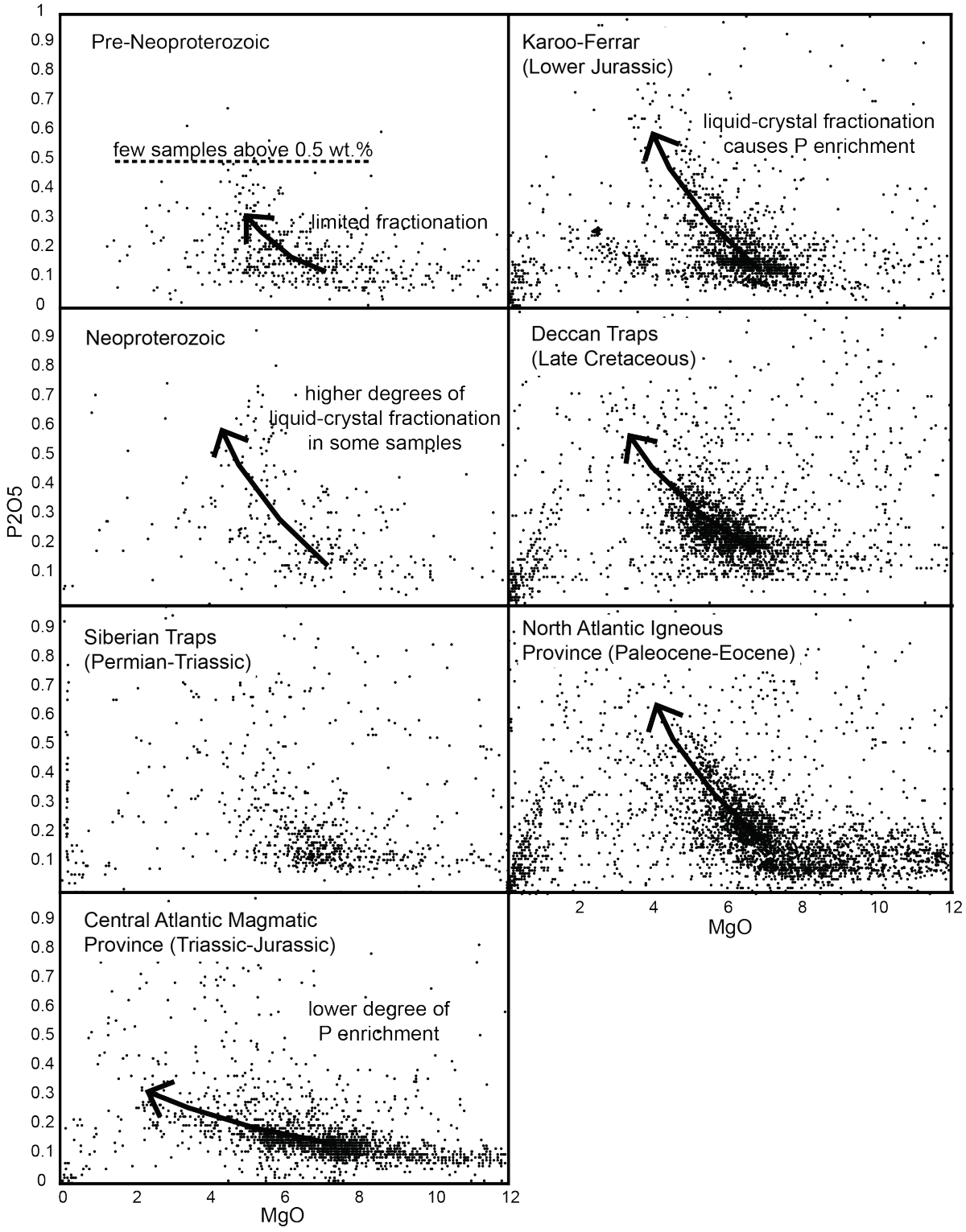

Figure 23. MgO vs. P_2O_5 for LIPs (Pre-Neoproterozoic and Neoproterozoic data in Appendix 9). Siberian Traps, Central Atlantic Magmatic Province, Karoo-Ferrar, Deccan Traps, and North Atlantic Igneous Province data are from the GeoRoc database (http://georoc.mpch-mainz.gwdg.de/georoc/). Pre-Neoproterozoic LIPs exhibit limited liquid–crystal fraction that increases P concentrations. Some Neoproterozoic and Phanerozoic LIPs, however, show strong enrichment trends.

5.6. Consequences of an elevated Neoproterozoic P flux

If Neoproterozoic flood basalts covered twice the areas of preserved mafic dike swarms (7.4×10^6 km^2) and were 3 km thick, the basalt provinces are estimated to have contained 1.7×10^{18} mol P. Despite high dissolution rates at moderate to high pH, some fluorapatite resisted weathering and bypassed the biologic cycle as detritus; this fraction is assumed to be 50% of the total P. Of the P released during over the course of LIP weathering and transported to the ocean, probably <10% was dissolved and >90% was Fe bound. If modern preagricultural conditions are representative, 25–45% (e.g., Ruttenberg, 2003) of the particulate-bound P may have become bioavailable upon reaching the ocean. Thus, assuming 40% of the combined Fe-bound and dissolved fractions became reactive in the ocean, only ~20% of the total P in the LIPs could have reached the ocean in a bioavailable form. Even so, the calculations summarized in Table 6 and Figure 22 suggest that $1–4 \times 10^{17}$ mol P from LIPs could have fertilized the ocean between 900 and 500 Ma, approximately the same amount of P that would have been derived from the total silicate weathering of the continents (of presumed average granitic composition) for the same period. Up to 5 times as much could have been released if none of the LIP-derived P was buried in Fe-oxides or detrital apatite.

Modeling by Laakso and Schrag (2014) suggests that organic carbon burial rates were very sensitive to the P supply in the low oxygen Proterozoic environment. If so, modest increases in reactive P may have caused pronounced increases in atmospheric oxygen. Weathering of Neoproterozoic LIPs could have more than doubled the reactive P flux and sustained an elevated flux for tens of millions of years, but fails to explain the 10-fold increase reactive P deemed necessary by Laakso and Schrag (2014) to stabilize an atmosphere with present-day pO_2. They propose that the reactive P supply was oxygen dependent and that slower oxidation of Fe in ground waters caused more uptake of P into Fe-

oxides; if this mechanism produces two biogeochemical steady states (i.e., low pO_2 Proterozoic and high pO_2 Phanerozoic), then LIP weathering may have raised pO_2 enough to prompt a switch to the higher pO_2 state. Alternatively, modest oxygenation caused by the weathering of LIP basalts may have permitted the colonization of continental surfaces by microorganisms that expedite P release from rocks and soils (e.g., Lenton and Watson, 2004), irreversibly increasing the reactive P supply to the ocean.

The consumption of CO_2 during basalt weathering and the resulting burial of calcium carbonate can cool the global climate (e.g., Dessert et al., 2001), and it has been postulated that the weathering of LIP basalts triggered the Sturtian glaciation (Goddéris et al., 2003). The model presented in this study reaches a maximum flood basalt area of 3.66×10^6 km^2—roughly half of the area of current exposed subaerial basalt (Dessert et al., 2003)—when the Franklin Province was erupted at ~720 Ma; if Neoproterozoic CO_2 consumption rates were similar to modern rates, we might expect that the weathering of LIPs to consume CO_2 at half the rate of modern basalts, or $\sim 1.5 \times 10^{12}$ mol CO_2/yr (Dessert et al., 2003). The burial of organic carbon would have also consumed atmospheric CO_2: assuming that the reactive P flux from LIPs reached $1–5 \times 10^9$ mol/yr, and that all that reactive P was buried with a C:P ratio between 106 and 170 (Shaffer, 1996), then LIP-induced organic carbon burial could account for an additional $0.1–0.9 \times 10^{12}$ mol CO_2/yr. This first order approximation may explain high pre-Sturtian $\delta^{13}C_{carbonate}$ values that suggest organic carbon made up >32% of total carbon burial (Hayes et al., 1999). Although organic carbon burial would have declined precipitously at the outset of glaciation, the reactive P flux from LIPs likely contributed to the destabilization of the climate prior to glaciation.

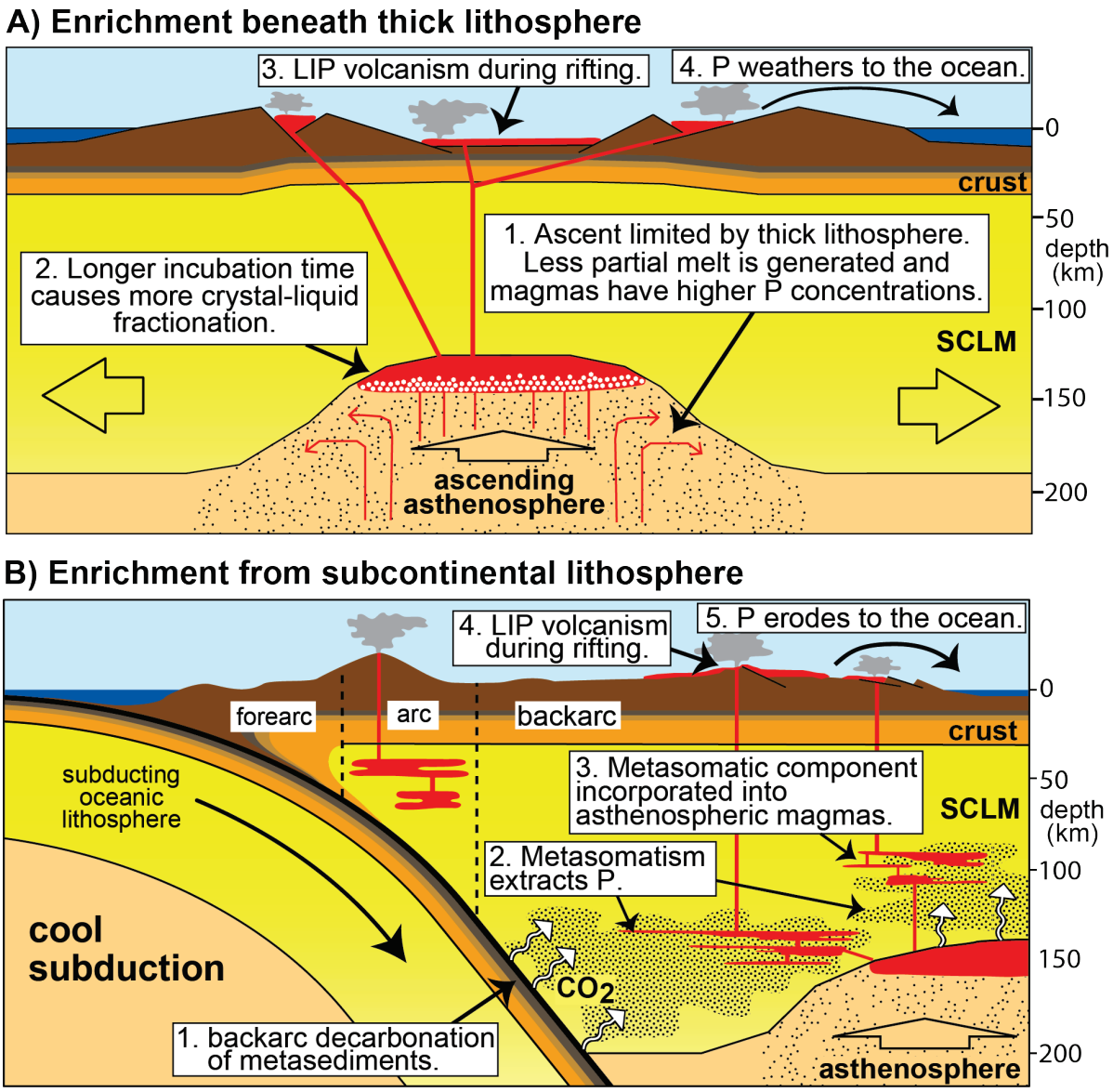

Figure 24. Magmatic and metasomatic processes that cause P enrichment in LIP basalts. A) When thick lithosphere inhibits the ascent of asthenosphere, less decompression melting occurs and longer incubation allows for more crystal–liquid fractionation. B) Metasomatic fluids from subducting ocean crust and/or rising asthenosphere extract P from subcontinental lithosphere (SCLM) and metasomatic components become incorporated into tholeiitic magmas from the asthenosphere.

6. Conclusions

Tectonic conditions converged in the Neoproterozoic such that mantle-derived P could fertilize the ocean at an unprecedented rate. Voluminous flood basalts associated with the breakup of the Rodinia supercontinent covered a significant fraction of continental surfaces, and the low latitude continental configuration facilitated chemical weathering. Some Neoproterozoic LIPs had elevated P concentrations due to fractional crystallization beneath thick cratonic lithosphere and by the incorporation of metasomatic P from lithospheric mantle (Figure 24). The large uncertainties regarding the P content of flood basalts, weathering rates, and the fraction of Fe-bound P in continental runoff make it difficult to assess the overall effects of LIP-derived P fluxes. Preliminary results presented here suggest that LIP-derived P fluxes were high enough to boost primary productivity and organic carbon burial rates. If so, the weathering of LIPs may have initiated the Neoproterozoic oxygenation of the ocean–atmosphere system, destabilized the climate, and set the stage for accelerated evolutionary developments.

References

Abbott, D. H., and A. E. Isley (2002), The intensity, occurrence, and duration of superplume events and eras over geological time, *Journal of Geodynamics*, **34**(2), 265–307.

Anbar, A. D., and A. H. Knoll (2002), Proterozoic ocean chemistry and evolution: a bioinorganic bridge? *Science*, **297**(5584), 1137–1142.

Annen, C., J. D. Blundy, and R. S. J. Sparks (2006), The genesis of intermediate and silicic magmas in deep crustal hot zones, *Journal of Petrology*, **47**(3), 505–539.

Aoya, M., S. R. Wallis, K. Terada, J. Lee, T. Kawakami, Y. Wang, and M. Heizler (2005), North-south extension in the Tibetan crust triggered by granite emplacement, *Geology*, **33**(11), 853–856.

Asmerom, Y., S. B. Jacobsen, A. H. Knoll, N. J. Butterfield, and K. Swett (1991), Strontium isotopic variations of Neoproterozoic seawater: implications for crustal evolution, *Geochimica et Cosmochimica Acta*, **55**(10), 2883–2894.

Bandstra, J. Z., and S. L. Brantley (2008), Data Fitting Techniques with Applications to Mineral Dissolution Kinetics, in *Kinetics of Water-Rock Interaction*, edited by S. L. Brantley, J. D. Kubicki, and A. F. White, pp. 211–257, Springer New York.

Barovich, K. M., and J. Foden (2000), A Neoproterozoic flood basalt province in southern-central Australia: geochemical and Nd isotope evidence from basin fill, *Precambrian Research*, **100**(1–3), 213–234.

Baxter, E.F., D.J. DePaolo, and P.R. Renne (2002), Spatially correlated anomalous $^{40}Ar/^{39}Ar$ "age" variations in biotites about a lithologic contact near Simplon Pass, Switzerland: a mechanistic explanation for excess Ar, *Geochimica et Cosmochimica Acta*, **66**, 1067–1083.

Bea, F. (2012), The sources of energy for crustal melting and the geochemistry of heat-producing elements, *Lithos*, **153**, 278–291.

Bea, F., and P. Montero (1999), Behavior of accessory phases and redistribution of Zr, REE, Y, Th, and U during metamorphism and partial melting of metapelites in the lower crust: an example from the Kinzigite Formation of Ivrea-Verbano, NW Italy, *Geochimica et Cosmochimica Acta*, **63**(7), 1133–1153.

Beaumont, C., Jamieson, R.A., Nguyen, M.H., and Lee, B. (2001), Himalayan tectonics explained by extrusion of a low-viscosity crustal channel coupled to focused surface denudation, *Nature*, **414**, 738–742.

Beaumont, C., R.A. Jamieson, M.H. Nguyen, and S. Medvedev (2004), Crustal channel flows: Numerical models with applications to the tectonics of the Himalayan-Tibetan orogen, *Journal of Geophysical Research*, **109**, B0406.

Beaumont, C., R. Jamieson, and M. Nguyen (2010), Models of large, hot orogens containing a collage of reworked and accreted terranes, *Canadian Journal of Earth Sciences*, **47**(4), 485–515.

Behn, M. D., P. B. Kelemen, G. Hirth, B. R. Hacker, and H.-J. Massonne (2011), Diapirs as the source of the sediment signature in arc lavas, *Nature Geoscience*, **4**, 641–646.

Benitez-Nelson, C. R. (2000), The biogeochemical cycling of phosphorus in marine systems, *Earth-Science Reviews*, **51**(1), 109–135.

Berger, A., E. Gnos, G. Schreurs, A. Fernandez, and M. Rakotondrazafy (2006), Late Neoproterozoic, Ordovician and Carboniferous events recorded in monazites from southern-central Madagascar, *Precambrian Research*, **144**(3), 278–296.

Beswick, A. E., and I. S. E. Carmichael (1978), Constraints on mantle source compositions imposed by phosphorus and the rare-earth elements, *Contributions to Mineralogy and Petrology*, **67**, 317–330.

Bjerrum, C. J., and D. E. Canfield (2002), Ocean productivity before about 1.9 Gyr ago limited by phosphorus adsorption onto iron oxides, *Nature*, **417**(6885), 159–162.

Bingen, B., and O. van Breemen (1998), U-Pb monazite ages in amphibolite-to granulite-facies orthogneiss reflect hydrous mineral breakdown reactions: Sveconorwegian Province of SW Norway, *Contributions to Mineralogy and Petrology*, **132**(4), 336–353.

Boger S.D., R.W. White, and B. Schulte (2012), The importance of iron speciation (Fe^{2+}/Fe^{3+}) in determining mineral assemblages: an example from high-grade aluminous metapelites of southern Madagscar, *Journal of Metamorphic Geology*, **30**, 997–1018.

Boger, S. D., W. Hirdes, C. A. M. Ferreira, B. Schulte, T. Jenett, and C.M. Fanning (2014), From passive margin to volcano-sedimentary forearc: The Tonian to Cryogenian evolution of the Anosyen Domain of southeastern Madagascar, *Precambrian Research*, **247**, 159–186.

Brown, M. (2006), Duality of thermal regimes is the distinctive characteristic of plate tectonics since the Neoarchean, *Geology*, **34**(11), 961.

Brown, M. (2007), Metamorphic conditions in orogenic belts: a record of secular change, *International Geology Review*, **49**(3), 193–234.

Brown, M. (2008), Characteristic thermal regimes of plate tectonics and their metamorphic imprint throughout Earth history: when did Earth first adopt a plate tectonics mode of behavior, *Geological Society of America Special Papers*, **440**, 97–128.

Brun, J.-P., and J. Pons (1981), Strain patterns of pluton emplacement in a crust undergoing non-coaxial deformation, Sierra Morena, southern Spain, *Journal of Structural Geology*, **3**, 219–230.

Brunet, F., and G. Chazot (2001), Partitioning of phosphorus between olivine, clinopyroxene and silicate glass in a spinel lherzolite xenolith from Yemen, *Chemical Geology*, **176**(1), 51–72.

Burg, J.-P., and T. V. Gerya (2005), The role of viscous heating in Barrovian metamorphism of collisional orogens: thermomechanical models and application to the Lepontine Dome in the Central Alps, *Journal of Metamorphic Geology*, **23**(2), 75–95.

Burg, J.P., M. Guiraud, G.M. Chen, and G.C. Li (1984), Himalayan metamorphism and deformations in the North Himalayan Belt (southern Tibet, China), *Earth and Planetary Science Letters*, **69**(2), 391–400.

Campbell, I. H., and R. J. Squire (2010), The mountains that triggered the Late Neoproterozoic increase in oxygen: the Second Great Oxidation Event, *Geochimica et Cosmochimica Acta*, **74**(15), 4187–4206.

Canfield, D. E. (2005), The early history of atmospheric oxygen: homage to Robert M. Garrels, *Annu. Rev. Earth Planet. Sci.*, **33**, 1–36.

Canfield, D. E., and A. Teske (1996), Late Proterozoic rise in atmospheric oxygen concentration inferred from phylogenetic and sulphur-isotope studies, *Nature*, **382**(6587), 127–132.

Canfield, D. E., S. W. Poulton, A. H. Knoll, G. M. Narbonne, G. Ross, T. Goldberg, and H. Strauss (2008), Ferruginous conditions dominated later Neoproterozoic deep-water chemistry, *Science*, **321**(5891), 949–952.

Chaïrat, C., J. Schott, E. H. Oelkers, J.-E. Lartigue, and N. Harouiya (2007), Kinetics and mechanism of natural fluorapatite dissolution at 25 C and pH from 3 to 12, *Geochimica et Cosmochimica Acta*, **71**(24), 5901–5912.

Chen, Z., Y. Liu, K. V. Hodges, B. C. Burchfiel, L. H. Royden, and C. Deng (1990), The Kangmar dome: A metamorphic core complex in southern Xizang (Tibet), *Science*, **250**(4987), 1552–1556.

Cherniak, D. J., E. B. Watson, and D. A. Wark (2007), Ti diffusion in quartz, *Chemical Geology*, **236**(1), 65–74.

Clark, C., D. Healy, T. Johnson, A. S. Collins, R. J. Taylor, M. Santosh, and N. E. Timms (2014), Hot orogens and supercontinent amalgamation: A Gondwanan example from southern India, *Gondwana Research*, doi:10.1016/j.gr.2014.11.005.

Clark, C., I. C. W. Fitzsimons, D. Healy, and S. L. Harley (2011), How Does the Continental Crust Get Really Hot? *Elements*, **7**(4), 235.

Clark, M. K., and L. H. Royden (2000), Topographic ooze: Building the eastern margin of Tibet by lower crustal flow, *Geology*, ***28***(8), 703–706.

Cohen, P. A., and A. H. Knoll (2012), Scale Microfossils from the Mid-Neoproterozoic Fifteenmile Group, Yukon Territory, *Journal of Paleontology*, **86**(5), 775–800.

Cohen, P. A., J. W. Schopf, N. J. Butterfield, A. B. Kudryavtsev, and F. A. Macdonald (2011), Phosphate biomineralization in mid-Neoproterozoic protists, *Geology*, **39**(6), 539–542.

Collins, A. S. (2006), Madagascar and the amalgamation of Central Gondwana, *Gondwana Research*, *9*(1), 3–16.

Collins, A. S., and B. F. Windley (2002), The tectonic evolution of central and northern Madagascar and its place in the final assembly of Gondwana, *The Journal of geology*, **110**(3), 325–339.

Collins, A. S., and S. A. Pisarevsky (2005), Amalgamating eastern Gondwana: The evolution of the Circum-Indian Orogens, *Earth-Science Reviews*, **71**(3–4), 229–270.

Collins, A. S., C. Clark, and D. Plavsa (2014), Peninsular India in Gondwana: the tectonothermal evolution of the Southern Granulite Terrain and its Gondwanan counterparts, *Gondwana Research*, **25**(1), 190–203.

Collins, A. S., P. D. Kinny, and T. Razakamanana (2012), Depositional age, provenance and metamorphic age of metasedimentary rocks from southern Madagascar, *Gondwana Research*, **21**(2), 353–361.

Currie, C. A., and R. D. Hyndman (2006), The thermal structure of subduction zone back arcs, *Journal of Geophysical Research: Solid Earth (1978–2012)*, **111**, B08404.

Dasgupta, R. (2013), Ingassing, storage, and outgassing of terrestrial carbon through geologic time, *Rev Mineral Geochem*, **75**(1), 183–229.

Dasgupta, R., and M. M. Hirschmann (2010), The deep carbon cycle and melting in Earth's interior, *Earth and Planetary Science Letters*, **298**, 1–13.

de Wit, M. J. (2003), Madagascar: heads it's a continent, tails it's an island, *Annual Review of Earth and Planetary Sciences*, **31**(1), 213–248.

de Wit, M. J., S. A. Bowring, L. D. Ashwal, L. G. Randrianasolo, V. P. Morel, and R. A. Rambeloson (2001), Age and tectonic evolution of Neoproterozoic ductile shear zones in southwestern Madagascar, with implications for Gondwana studies, *Tectonics*, **20**(1), 1–45.

Deeken, A., R. C. Thiede, E. R. Sobel, J. K. Hourigan, and M. R. Strecker (2011), Exhumational variability within the Himalaya of northwest India, *Earth and Planetary Science Letters*, **305**(1), 103–114.

Dessert, C., B. Dupré, J. Gaillardet, L. M. François, and C. J. Allegre (2003), Basalt weathering laws and the impact of basalt weathering on the global carbon cycle, *Chemical Geology*, **202**(3), 257–273.

Dessert, C., B. Dupré, L. M. François, J. Schott, J. Gaillardet, G. Chakrapani, and S. Bajpai (2001), Erosion of Deccan Traps determined by river geochemistry: impact on the global climate and the $^{87}Sr/^{86}Sr$ ratio of seawater, *Earth and Planetary Science Letters*, **188**(3), 459–474.

Dewey, J. F. (1988), Extensional collapse of orogens, *Tectonics*, **7**(6), 1123–1139.

Dewey, J. F., L. Robb, and L. Van Schalkwyk (2006), Did Bushmanland extensionally unroof Namaqualand? *Precambrian Research*, **150**(3), 173–182.

Dèzes, P.J, J.-C. Vannay, A. Steck, and F. Bussy, (1999), Synorogenic extension: Quantitative constraints on the age and displacement of the Zanskar shear zone (northwest Himalaya), *Geologic Society of America Bulletin*, **111**, 364–374.

Dèzes, P.J. (1999), Tectonic and metamorphic evolution of the central Himalayan domain in southeast Zanskar (Kashmir, India), PhD thesis, University of Lausanne, Lausanne, Switzerland, 160 pp.

Dixon, J.M., and J.M. Summers (1983), Patterns for total and incremental strain in subsiding troughs: experimental centrifuged models of inter-diapir synclines, *Canadian Journal of Earth Sciences,* **20**, 1843–1861.

Djomani, Y. H. P., S. Y. O'Reilly, W. L. Griffin, and P. Morgan (2001), The density structure of subcontinental lithosphere through time, *Earth and Planetary Science Letters*, **184**(3–4), 605–621.

Donnadieu, Y., Y. Goddéris, G. Ramstein, A. Nédélec, and J. Meert (2004), A "snowball Earth"climate triggered by continental break-up through changes in runoff, *Nature*, **428**(6980), 303–306.

Dufek, J., and G. W. Bergantz (2005), Lower crustal magma genesis and preservation: a stochastic framework for the evaluation of basalt–crust interaction, *Journal of Petrology*, **46**(11), 2167–2195.

Eldhom, O., and M. F. Coffin (2000), Large igneous provinces and plate tectonics, in *The history and dynamics of global plate motions* (Geologic Society of America, Boulder, CO)*,* 309–326.

Emmel, B., N. Jöns, A. Kröner, J. Jacobs, J.-A. Wartho, V. Schenk, T. Razakamanana, and A. Austegard (2008), From closure of the mozambique ocean to gondwana breakup: new evidence from geochronological data of the vohibory terrane, Southwest Madagascar, *The Journal of Geology*, **116**(1), 21–38.

England, P. C., and A. B. Thompson (1984), Pressure-temperature-time paths of regional metamorphism I. Heat transfer during the evolution of regions of thickened continental crust, *Journal of Petrology*, **25**(4), 894–928.

Enkelmann, E., L. Ratschbacher, R. Jonckheere, R. Nestler, M. Fleischer, R. Gloaguen, B. R. Hacker, Y. Q. Zhang, and Y.-S. Ma (2006), Cenozoic exhumation and deformation of northeastern Tibet and the Qinling: Is Tibetan lower crustal flow diverging around the Sichuan Basin? *Geological Society of America Bulletin*, **118**(5–6), 651–671.

Epard, J.-L., and A. Steck (2004), The eastern prolongation of the Zanskar shear zone (western Himalaya), *Eclogae Geologicae Helvetiae*, **97**(2), 193–212.

Ernst, R. E. (2007), Mafic-ultramafic large igneous provinces (LIPs): Importance of the pre-Mesozoic record, *Episodes*, **30**(2), 108.

Ernst, R. E., and K. L. Buchan (2001), Mantle plumes: their identification through time, Geological Society of America, Denver, Colorado, 593 pp.

Ernst, R. E., M. T. D. Wingate, K. L. Buchan, and Z.-X. Li (2008), Global record of 1600–700Ma Large Igneous Provinces (LIPs): implications for the reconstruction of the proposed Nuna (Columbia) and Rodinia supercontinents, *Precambrian Research*, **160**(1), 159–178.

Ernst, R., and W. Bleeker (2010), Large igneous provinces (LIPs), giant dyke swarms, and mantle plumes: significance for breakup events within Canada and adjacent regions from 2.5 Ga to the Present, *Canadian Journal of Earth Sciences*, **47**(5), 695–739.

Fennel, K., M. Follows, and P. G. Falkowski (2005), The co-evolution of the nitrogen, carbon and oxygen cycles in the Proterozoic ocean, *American Journal of Science*, **305**(6–8), 526–545.

Ferrara, G., B. Lombardo, S. Tonarini, and B. Turi (1991), Sr, Nd and O isotopic characterization of the Gophu La and Gumburanjun leucogranites (High Himalaya), *Schweiz. Mineral. Petrogr. Mitt*, **71**, 35–51.

Ferry, J. M., and E. B. Watson (2007), New thermodynamic models and revised calibrations for the Ti-in-zircon and Zr-in-rutile thermometers, *Contributions to Mineralogy and Petrology*, **154**(4), 429–437.

Filippelli, G. M. (1997), Controls on phosphorus concentration and accumulation in oceanic sediments, *Marine Geology*, **139**(1), 231–240.

Finch, M., P. Hasalova, R.F. Weinberg, and C.M. Fanning (2014), Switch from thrusting to normal shearing in the Zanskar shear zone, NW Himalaya: Implications for channel flow, *Geological Society of America Bulletin*, **126**(7–8), 892–924.

Föllmi, K. B. (1996), The phosphorus cycle, phosphogenesis and marine phosphate-rich deposits, *Earth-Science Reviews*, **40**(1), 55–124.

Frank, W., M. Thöni, and F. Purtscheller (1977), Geology and petrography of Kulu-South Lahul area, *Colloq. Int. Cent. Natl. Rech. Sci*, 147–172.

Froelich, P. N. (1988), Kinetic control of dissolved phosphate in natural rivers and estuaries: A primer on the phosphate buffer mechanism1, *Limnology and oceanography*, **33**(4), 649–668.

Furlong, K. P., and D. S. Chapman (2013), Heat flow, heat generation, and the thermal state of the lithosphere, *Annual Review of Earth and Planetary Sciences*, **41**, 385–410.

GAF-BGR, 2008, Final Report: Réalisation des travaux de cartographie géologique de Madagascar, révision approfondie de la cartographie géologique et minière aux échelles 1/100 000 et 1/500 000 zone Sud. République de Madagascar, Ministère de l'Energie et des Mines EM/SG/DG/UCP/PGRM.

Gale, A., C. A. Dalton, C. H. Langmuir, Y. Su, and J.-G. Schilling (2013), The mean composition of ocean ridge basalts, *Geochemistry, Geophysics, Geosystems,* **14**(3), 489–518.

Gehrels, G.E., DeCelles, P.G., Martin, A., Ojha, T.P., Pinhassi, G., and Upreti, B.N. (2003), Initiation of the Himalayan orogen as an early Paleozoic thin-skinned thrust belt, *GSA Today*, **13**(9), 4–9.

Giese, J., A. Berger, G. Schreurs, and E. Gnos (2011), The timing of the tectono-metamorphic evolution at the Neoproterozoic-Phanerozoic boundary in central southern Madagascar, *Precambrian Research*, **185**(3), 131–148.

Gilason, S. R., and P. E. Hans (1987), Meteoric water-basalt interactions I: A laboratory study, *Geochimica et Cosmochimica Acta*, **51**(10), 2827–2840.
Goddéris, Y., Y. Donnadieu, A. Nédélec, B. Dupré, C. Dessert, A. Grard, G. Ramstein, and L. M. Francois (2003), The Sturtian "snowball"glaciation: fire and ice, *Earth and Planetary Science Letters*, **211**(1), 1–12.
Gorman, P., D. Kerrick, and J. Connolly (2006), Modeling open system metamorphic decarbonation of subducting slabs, *Geochem. Geophys. Geosyst*, **7**, Q04007.
Grove, M., and Harrison, T. (1996), ^{40}Ar* Diffusion in Fe-rich biotite, *The American Mineralogist*, **81**(7–8), 940–951.
Grujic, D., L.S. Hollister, and R.R. Parrish (2002), Himalayan metamorphic sequence as an orogenic channel: insight from Bhutan, *Earth and Planetary Science Letters*, **198**(1), 177–191.
Guidry, M. W., and F.T. Mackenzie (2000), Apatite weathering and the Phanerozoic phosphorus cycle, *Geology*, **28**(7), 631–634.
Guidry, M. W., and F.T. Mackenzie (2003), Experimental study of igneous and sedimentary apatite dissolution: control of pH, distance from equilibrium, and temperature on dissolution rates, *Geochimica et Cosmochimica Acta*, **67**(16), 2949–2963.
Gunnars, A., S. Blomqvist, P. Johansson, and C. Andersson (2002), Formation of Fe (III) oxyhydroxide colloids in freshwater and brackish seawater, with incorporation of phosphate and calcium, *Geochimica et Cosmochimica Acta*, **66**(5), 745–758.
Guo, L., J. Zhang, and B. Zhang (2008), Structures, kinematics, thermochronology and tectonic evolution of the Ramba gneiss dome in the northern Himalaya, *Progress in Natural Science*, **18**(7), 851–860.
Gupta, A. K. (2015), Origin of Potassium-rich Silica-deficient Igneous Rocks, Springer, New Delhi, India, 536 pp.
Hacker, B. R., E. Gnos, L. Ratschbacher, M. Grove, M. McWilliams, S. V. Sobolev, J. Wan, and W. Zhenhan (2000), Hot and dry deep crustal xenoliths from Tibet, *Science*, **287**(5462), 2463.
Hacker, B. R., P. B. Kelemen, and M. D. Behn (2011), Differentiation of the continental crust by relamination, *Earth and Planetary Science Letters*, **307**(3), 501–516.
Hacker, B. R., P. B. Kelemen, and M. D. Behn (2015), Continental Lower Crust, *Annual Review of Earth and Planetary Sciences*, **43**(1), 167–205.
Halverson, G. P., F. Ö. Dudás, A. C. Maloof, and S. A. Bowring (2007), Evolution of the 87Sr/86Sr composition of Neoproterozoic seawater, *Palaeogeography, Palaeoclimatology, Palaeoecology*, **256**(3), 103–129.
Halverson, G. P., B. P. Wade, M. T. Hurtgen, and K. M. Barovich (2010), Neoproterozoic chemostratigraphy, *Precambrian Research*, **182**(4), 337–350.
Halverson, G. P., P. F. Hoffman, D. P. Schrag, A. C. Maloof, and A. H. N. Rice (2005), Toward a Neoproterozoic composite carbon-isotope record, *Geological Society of America Bulletin*, **117**(9–10), 1181–1207.
Handke, M. J. (2001), Neoproterozoic magmatism in the Itremo region, central Madagascar: geochronology, geochemistry, and petrogenesis, PhD thesis, Department of Earth and Planetary Sciences, Washington University.
Handke, M. J., R. D. Tucker, and L. D. Ashwal (1999), Neoproterozoic continental arc magmatism in west-central Madagascar, *Geology*, **27**(4), 351–354.
Harley, S. L. (2008), Refining the P–T records of UHT crustal metamorphism, *Journal of Metamorphic Geology*, **26**(2), 125–154.

Harris, N., D. Vance, and M. Ayres (2000), From sediment to granite: timescales of anatexis in the upper crust, *Chemical Geology*, **162**(2), 155–167.

Harrison, T. M., J. Célérier, A. B. Aikman, J. Hermann, and M. T. Heizler (2009), Diffusion of< sup> 40</sup> Ar in muscovite, *Geochimica et Cosmochimica Acta*, **73**(4), 1039–1051.

Harrison, T. M., O. M. Lovera, and M. Grove (1997), New insights into the origin of two contrasting Himalayan granite belts, *Geology*, **25**(10), 899–902.

Hasalova, P. and R.F. Weinberg (2011), Pure and Simple Shear Partitioning at Microscale Revealed by Quartz Fabric in the South Tibetan Detachment, Zanskar, NW India, *American Geophysical Union,* Fall Meeting 2011, Abstract #T43C-2330.

Hauck, M. L., K. D. Nelson, L. D. Brown, W. Zhao, and A. R. Ross (1998), Crustal structure of the Himalayan orogen at 90° east longitude from Project INDEPTH deep reflection profiles, *Tectonics*, **17**(4), 481–500.

Hayes, J. M., H. Strauss, and A. J. Kaufman (1999), The abundance of ^{13}C in marine organic matter and isotopic fractionation in the global biogeochemical cycle of carbon during the past 800 Ma, *Chemical Geology*, **161**(1), 103–125.

Heckman, D. S., D. M. Geiser, B. R. Eidell, R. L. Stauffer, N. L. Kardos, and S. B. Hedges (2001), Molecular evidence for the early colonization of land by fungi and plants, *Science*, **293**(5532), 1129–1133.

Herren, E., 1987, The Zanskar shear zone: Northeast-southwest extension within the Higher Himalayas (Ladakh, India): *Geology*, v. 15, p. 409–413.

Hetzel, R., I. Dunkl, V. Haider, M. Strobl, H. von Eynatten, L. Ding, and D. Frei (2011), Peneplain formation in southern Tibet predates the India-Asia collision and plateau uplift, *Geology*, **39**(10), 983–986.

Hinojosa, J. H., and K. L. Mickus (2002), Thermoelastic modeling of lithospheric uplift: a finite-difference numerical solution, *Computers & geosciences*, **28**(2), 155–167.

Hintersberger, E., Thiede, R.C., Strecker, M.R., and Hacker, B.R. (2010), East-west extension in the NW Indian Himalaya, *Geological Society of America Bulletin*, 122(9–10), 1499–1515.

Hofmeister, A. M., M. Pertermann, J. M. Branlund, and A. G. Whittington (2006), Geophysical implications of reduction in thermal conductivity due to hydration, *Geophysical research letters*, **33**(11), L11310.

Honegger, K., V. Dietrich, W. Frank, A. Gansser, M. Thöni, and V. Trommsdorff (1982), Magmatism and metamorphism in the Ladakh Himalayas (the Indus-Tsangpo suture zone), *Earth and Planetary Science Letters*, **60**, 53–292.

Horton, F., and M.L. Leech (2013), Age and origin of granites in the Karakoram shear zone and Greater Himalaya Sequence, NW India, *Lithosphere*, **5**(3), 300–320.

Hudleston, P.J., S.H. Treagus, and L. Lan (1996), Flexural flow folding: Does it occur in nature? *Geology*, **24**(3), 203–206.

Ichiki, T., M. Ishikawa, J.-I. Kimura, R. Senda, and R. Rakotondrazafy (2015), Crustal assembly of the Antananarivo and Masora domains, central–eastern Madagascar: constraints from U–Pb zircon geochronology and whole–rock geochemistry of meta–granitoids, *Journal of Mineralogical and Petrological Sciences*, *J-STAGE Advance Publication*, doi:10.2465/jmps.141225.

Inger, S. (1998), Timing of an extensional detachment during convergent orogeny: New Rb-Sr geochronological data from the Zanskar shear zone, northwestern Himalaya, *Geology*, **26**, 223–226.

Jahn, B., R. Caby, and P. Monie (2001), The oldest UHP eclogites of the world: age of UHP metamorphism, nature of protoliths and tectonic implications, *Chemical Geology*, **178**(1–4), 143–158.

Jamieson, R.A., C. Beaumont, M.H. Nguyen, and D. Grujic (2006), Provenance of the Greater Himalayan Sequence and associated rocks: predictions of channel flow models, *Geological Society, London, Special Publications*, **268**(1), 165–182.

Jaupart, C., and J. C. Mareschal (2003), Constraints on crustal heat production from heat flow data, in *Treatise on Geochemistry, The Crust* (edited by R. L.Rudnick, Permagon, New York, New York).

Jelsma, H.A., P.A. Van Der Beek, and M.L. Vinyu (1993), Tectonic evolution of the Bindura–Shamva greenstone belt (northern Zimbabwe): progressive deformation around diapiric batholiths, *Journal of Structural Geology,* **15**, 163–176.

Jones, C., S. Nomosatryo, S. A. Crowe, C. J. Bjerrum, and D. E. Canfield (2015), Iron oxides, divalent cations, silica, and the early earth phosphorus crisis, *Geology*, **43**(2), 135–138.

Jöns, N., and V. Schenk (2008), Relics of the Mozambique Ocean in the central East African Orogen: evidence from the Vohibory Block of southern Madagascar, *Journal of Metamorphic Geology*, **26**(1), 17–28.

Jöns, N., and V. Schenk (2011), The ultrahigh temperature granulites of southern Madagascar in a polymetamorphic context: implications for the amalgamation of the Gondwana supercontinent, *European Journal of Mineralogy*, **23**(2), 127.

Jourdan, F., H. Bertrand, U. Schärer, J. Blichert-Toft, G. Féraud, and A. B. Kampunzu (2007), Major and trace element and Sr, Nd, Hf, and Pb isotope compositions of the Karoo large igneous province, Botswana–Zimbabwe: lithosphere vs mantle plume contribution, *Journal of Petrology*, **48**(6), 1043–1077.

Kelsey, D. E. (2008), On ultrahigh-temperature crustal metamorphism, *Gondwana Research*, **13**(1), 1–29.

Kelsey, D. E., and M. Hand (2014), On ultrahigh temperature crustal metamorphism: Phase equilibria, trace element thermometry, bulk composition, heat sources, timescales and tectonic settings, *Geoscience Frontiers*, **6**(3), 311–356.

Kennedy, M., M. Droser, L. M. Mayer, D. Pevear, and D. Mrofka (2006), Late Precambrian oxygenation; inception of the clay mineral factory, *Science*, **311**(5766), 1446–1449.

Kent, R. W., M. Storey, and A. D. Saunders (1992), Large igneous provinces: Sites of plume impact or plume incubation? *Geology*, **20**(10), 891–894.

Kerr, A. C. (1994), Lithospheric thinning during the evolution of continental large igneous provinces: A case study from the North Atlantic Tertiary province, *Geology*, **22**(11), 1027–1030.

Kerrick, D. M., and J. A. D. Connolly (2001), Metamorphic devolatilization of subducted marine sediments and the transport of volatiles into the Earth's mantle, *Nature*, **411**(6835), 293–296.

Kincaid, C., and P. Silver (1996), The role of viscous dissipation in the orogenic process, *Earth and Planetary Science Letters*, **142**(3), 271–288.

Kirschner, D.L., M.A. Cosca, H. Masson, and J.C. Hunziker (1996), Staircase $^{40}Ar/^{39}Ar$ spectra of fine-grained white mica: Timing and duration of deformation and empirical constraints on argon diffusion, *Geology*, **24**(8), 747–750.

Knauth, L. P., and M. J. Kennedy (2009), The late Precambrian greening of the Earth, *Nature*, **460**(7256), 728–732.

Knoll, A. H., and E. A. Sperling (2014), Oxygen and animals in Earth history, *Proceedings of the National Academy of Sciences*, **111**(11), 3907–3908.

Konhauser, K. O., E. Pecoits, S. V. Lalonde, D. Papineau, E. G. Nisbet, M. E. Barley, N. T. Arndt, K. Zahnle, and B. S. Kamber (2009), Oceanic nickel depletion and a methanogen famine before the Great Oxidation Event, *Nature*, **458**(7239), 750–753.

Koritnig, S. (1965), Geochemistry of phosphorus–I. The replacement of Si 4+ by P 5+ in rock-forming silicate minerals, *Geochimica et Cosmochimica Acta*, **29**(5), 361–371.

Kröner, A., B. F. Windley, P. Jaeckelt, T. S. Brewer, and T. Razakamanana (1999), New zircon ages and regional significance for the evolution of the Pan-African orogen in Madagascar, *Journal of the Geological Society*, **156**(6), 1125–1135.

Kuiper, K. F., A. Deino, F. J. Hilgen, W. Krijgsman, P. R. Renne, and J. R. Wijbrans (2008), Synchronizing rock clocks of Earth history, *Science*, **320**(5875), 500–504.

Kündig, R. (1989), Domal structures an high-grade metamorphism in the Higher Himalayan Crystalline, Zanskar Region, northwest Himalaya, India, *Journal of Metamorphic Geology*, **7**, 43–55.

Kylander-Clark, A.R., B.R. Hacker, and J.M. Cottle (2013), Laser-ablation split-stream ICP petrochronology, *Chemical Geology*, **345**, 99–112.

Laakso, T. A., and D. P. Schrag (2014), Regulation of atmospheric oxygen during the Proterozoic, *Earth and Planetary Science Letters*, **388**, 81–91.

Lal, D., N. B. Harris, K. K. Sharma, Z. Gu, L. Ding, T. Liu, W. Dong, M. W. Caffee, and A. J. T. Jull (2004), Erosion history of the Tibetan Plateau since the last interglacial: constraints from the first studies of cosmogenic ^{10}Be from Tibetan bedrock, *Earth and Planetary Science Letters*, **217**(1), 33–42.

Langille, J., J. Lee, B. Hacker, and G. Seward (2010), Middle crustal ductile deformation patterns in southern Tibet: Insights from vorticity studies in Mabja Dome, *Journal of Structural Geology*, **32**(1), 70–85.

Law, R. D., M. J. Jessup, M. P. Searle, M. K. Francsis, D. J. Waters, and J. M. Cottle (2011), Telescoping of isotherms beneath the South Tibetan Detachment System, Mount Everest Massif, *Journal of Structural Geology*, **33**(11), 1569–1594.

Le Fort, P. (1986), Metamorphism and magmatism during the Himalayan collision, *Geological Society, London, Special Publications*, **19**(1), 159–172.

Le Fort, P., M. Cuney, C. Deniel, C. France-Lanord, S. M. F. Sheppard, B. N. Upreti, and P. H. Vidal (1987), Crustal generation of the Himalayan leucogranites, *Tectonophysics*, **134**(1), 39–57.

Le Pichon, X., P. Henry, and B. Goffé (1997), Uplift of Tibet: from eclogites to granulites—implications for the Andean Plateau and the Variscan belt, *Tectonophysics*, **273**(1), 57–76.

Lederer, G. W., J. M. Cottle, M. J. Jessup, J. M. Langille, and T. Ahmad (n.d.), Timescales of partial melting in the Himalayan middle crust: insight from the Leo Pargil dome, northwest India, *Contributions to Mineralogy and Petrology*, 1–27.

Lee, C.-T. A., and O. Bachmann (2014), How important is the role of crystal fractionation in making intermediate magmas? Insights from Zr and P systematics, *Earth and Planetary Science Letters*, **393**, 266–274.

Lee, J., B. Hacker, and Y. Wang (2004), Evolution of North Himalayan gneiss domes: structural and metamorphic studies in Mabja Dome, southern Tibet, *Journal of Structural Geology*, **26**(12), 2297–2316.

Lee, J., B. R. Hacker, W. S. Dinklage, Y. Wang, P. Gans, A. Calvert, J. Wan, W. Chen, A. E. Blythe, and W. McClelland (2000), Evolution of the Kangmar Dome, southern Tibet: Structural, petrologic, and thermochronologic constraints, *Tectonics*, **19**(5), 872–895.

Lee, J., W. McClelland, Y. Wang, A. Blythe, and M. McWilliams (2006), Oligocene-Miocene middle crustal flow in southern Tibet: geochronology of Mabja Dome, *Geological Society, London, Special Publications*, **268**(1), 445–469.

Lenton, T. M., and A. J. Watson (2004), Biotic enhancement of weathering, atmospheric oxygen and carbon dioxide in the Neoproterozoic, *Geophysical Research Letters*, **31**(5), L05202.

Lenton, T. M., R. A. Boyle, S. W. Poulton, G. A. Shields-Zhou, and N. J. Butterfield (2014), Co-evolution of eukaryotes and ocean oxygenation in the Neoproterozoic era, *Nature Geoscience*, **7**(4), 257–265.

Lexa, O., K. Schulmann, V. Janoušek, P. Štípská, A. Guy, and M. Racek (2011), Heat sources and trigger mechanisms of exhumation of HP granulites in Variscan orogenic root, *Journal of Metamorphic Geology*, **29**(1), 79–102.

Li, Z.-X., D. A. Evans, and G. P. Halverson (2013), Neoproterozoic glaciations in a revised global palaeogeography from the breakup of Rodinia to the assembly of Gondwanaland, *Sedimentary Geology*, **294**, 219–232.

Liang, S., W. Gan, C. Shen, G. Xiao, J. Liu, W. Chen, X. Ding, and D. Zhou (2013), Three-dimensional velocity field of present-day crustal motion of the Tibetan Plateau derived from GPS measurements, *Journal of Geophysical Research: Solid Earth*, **118**(10), 5722–5732.

Louvat, P., and C. J. Allègre (1997), Present denudation rates on the island of Reunion determined by river geochemistry: basalt weathering and mass budget between chemical and mechanical erosions, *Geochimica et Cosmochimica Acta*, **61**(17), 3645–3669.

Lyons, T. W., C. T. Reinhard, and N. J. Planavsky (2014), The rise of oxygen in Earth/'s early ocean and atmosphere, *Nature*, **506**(7488), 307–315.

Lyubetskaya, T., and J. J. Ague (2009), Effect of metamorphic reactions on thermal evolution in collisional orogens, *Journal of Metamorphic Geology*, **27**(8), 579–600.

Macdonald, F. A., M. D. Schmitz, J. L. Crowley, C. F. Roots, D. S. Jones, A. C. Maloof, J. V. Strauss, P. A. Cohen, D. T. Johnston, and D. P. Schrag (2010), Calibrating the Cryogenian, *Science*, **327**(5970), 1241–1243.

Makovsky, Y., S. L. Klemperer, L. Ratschbacher, and D. Alsdorf (1999), Midcrustal reflector on INDEPTH wide-angle profiles: An ophiolitic slab beneath the India-Asia suture in southern Tibet? *Tectonics*, **18**(5), 793–808.

Mareschal, J.-C., and C. Jaupart (2013), Radiogenic heat production, thermal regime and evolution of continental crust, *Tectonophysics*, **609**, 524–534.

Markl, G., J. Bäuerle, and D. Grujic (2000), Metamorphic evolution of Pan-African granulite facies metapelites from Southern Madagascar, *Precambrian Research*, **102**(1), 47–68.

Martelat, J., C. Nicollet, J. Lardeaux, G. Vidal, and R. Rakotondrazafy (1997), Lithospheric tectonic structures developed under high-grade metamorphism in the southern part of Madagascar, *Geodinamica Acta*, **10**(3), 94–114.

Martelat, J.-E., J.-M. Lardeaux, C. Nicollet, and R. Rakotondrazafy (2000), Strain pattern and late Precambrian deformation history in southern Madagascar, *Precambrian research*, **102**(1), 1–20.

Martelat, J.-E., B. Randrianasolo, K. Schulmann, J.-M. Lardeaux, and J.-L. Devidal (2014), Airborne magnetic data compared to petrology of crustal scale shear zones from southern

Madagascar: A tool for deciphering magma and fluid transfer in orogenic crust, *Journal of African Earth Sciences*, **94**, 74–85.
Maruyama, S. M., and J. G. L. Iou (1998), Initiation of ultrahigh-pressure metamorphism and its significance on the Proterozoic–Phanerozoic boundary, *Island Arc*, **7**(1–2), 6–35.
Maruyama, S., and J. G. Liou (2005), From Snowball to Phaneorozic Earth, *International Geology Review*, **47**(8), 775–791.
Marzoli, A., P. R. Renne, E. M. Piccirillo, M. Ernesto, G. Bellieni, and A. De Min (1999), Extensive 200-million-year-old continental flood basalts of the Central Atlantic Magmatic Province, *Science*, **284**(5414), 616–618.
Mayer, T. D., and W. M. Jarrell (2000), Phosphorus sorption during iron (II) oxidation in the presence of dissolved silica, *Water Research*, **34**(16), 3949–3956.
McDonough, W. F., and S. S. Sun (1995), The composition of the Earth, *Chemical Geology*, **120**(3–4), 223–253.
McKenzie, D., and K. Priestley (2008), The influence of lithospheric thickness variations on continental evolution, *Lithos*, ***102***(1), 1–11.
McLaren, S., and R. Powell (2014), Magmatism, orogeny and the origin of high-heat-producing granites in Australian Proterozoic terranes, *Journal of the Geological Society*, **171**(2), 149–152.
McLaren, S., M. Sandiford, and M. Hand (1999), High radiogenic heat–producing granites and metamorphism—An example from the western Mount Isa inlier, Australia, *Geology*, **27**(8), 679–682.
McLennan, S. M., W. B. Nance, and S. R. Taylor (1980), Rare earth element-thorium correlations in sedimentary rocks, and the composition of the continental crust, *Geochimica et Cosmochimica Acta*, **44**(11), 1833–1839.
Meert, J. G., and B. S. Lieberman (2008), The Neoproterozoic assembly of Gondwana and its relationship to the Ediacaran–Cambrian radiation, Gondwana Research, **14**(1), 5–21.
Mehta, P.K. (1977), Rb-Sr geochronology of the Kulu-Mandi belt: its implications for the Himalayan tectogenesis, *Geologische Rundschau*, **66**, 156–175.
Millot, R., J. Gaillardet, B. Dupré, and C. J. Allègre (2002), The global control of silicate weathering rates and the coupling with physical erosion: new insights from rivers of the Canadian Shield, *Earth and Planetary Science Letters*, 196(1), 83–98.
Mills, B., T. M. Lenton, and A. J. Watson (2014), Proterozoic oxygen rise linked to shifting balance between seafloor and terrestrial weathering, *Proceedings of the National Academy of Sciences*, **111**(25), 9073–9078.
Mills, D. B., and D. E. Canfield (2014), Oxygen and animal evolution: Did a rise of atmospheric oxygen "trigger" the origin of animals? *BioEssays*, **36**(12), 1145–1155.
Milman-Barris, M. S., J. R. Beckett, M. B. Baker, A. E. Hofmann, Z. Morgan, M. R. Crowley, D. Vielzeuf, and E. Stolper (2008), Zoning of phosphorus in igneous olivine, *Contributions to Mineralogy and Petrology*, **155**(6), 739–765.
Moine, B., V. Bosse, J.-L. Paquette, and E. Ortega (2014), The occurrence of a Tonian–Cryogenian (850Ma) regional metamorphic event in Central Madagascar and the geodynamic setting of the Imorona–Itsindro (800Ma) magmatic suite, *Journal of African Earth Sciences*, **94**, 58–73.
Montgomery, D.R., and Stolar, D.B. (2006), Reconsidering Himalayan river anticlines, *Geomorphology*, **82**(1), 4–15.
Müller, B. G. (2011), The evolution and significance of the Bongolava-Ranotsara shear zone, Madagascar, *PhD Thesis*, University of Johannesburg, South Africa, 125 pp.

Nabelek, P. I., A. G. Whittington, and A. M. Hofmeister (2010), Strain heating as a mechanism for partial melting and ultrahigh temperature metamorphism in convergent orogens: Implications of temperature-dependent thermal diffusivity and rheology, *Journal of Geophysical Research*, **115**(B12), B12417.

Nédélec, A., E.W. Stephens, and A.E. Fallick (1995), The Panafrican stratoid granites of Madagascar: alkaline magmatism in a post-collisional extensional setting, *Journal of Petrology*, **36**(5), 1367–1391.

Nelson, K. D., W. Zhao, L. D. Brown, J. Kuo, J. Che, X. Liu, S. L. Klemperer, Y. Makovsky, R. Meissner, and J. Mechie (1996), Partially molten middle crust beneath southern Tibet: Synthesis of project INDEPTH results, *Science*, **274**(5293), 1684–1688.

Nicollet, C. (1990), Crustal evolution of the granulites of Madagascar, *Granulites and Crustal evolution*, **31**, 291–310.

Nicollet, C. (1989), L'eclogite de Faratsiho (Madagascar): un cas exceptionnel de métamorphisme de haute-P-basse-T au Protérozoïque supérieur, *Precambrian research*, **45**(4), 343–352.

Noble, S.R., and M.P. Searle (1995), Age of crustal melting and leucogranite formation from U-Pb zircon and monazite dating in the western Himalaya, Zanskar, India, *Geology*, **23**, 1135–1138.

Noble, S.R., M.P. Searle, and C.B. Walker (2001), Age and tectonic significance of Permian granites in Western Zanskar, High Himalaya, *The Journal of Geology*, **109**, 127–135.

Nursall, J. R. (1959), Oxygen as a prerequisite to the origin of the Metazoa, *Nature*, **183**(4669), 1170–1172.

O'Reilly, S. Y., and W. Griffin (2000), Apatite in the mantle: implications for metasomatic processes and high heat production in Phanerozoic mantle, *Lithos*, **53**(3–4), 217–232.

Och, L. M., and G. A. Shields-Zhou (2012), The Neoproterozoic oxygenation event: environmental perturbations and biogeochemical cycling, *Earth-Science Reviews*, **110**(1), 26–57.

Papineau, D. (2010), Global biogeochemical changes at both ends of the Proterozoic: insights from phosphorites, *Astrobiology*, **10**(2), 165–181.

Paquette, J. L., A. Nédélec, B. Moine, and M. Rakotondrazafy (1994), U-Pb, single zircon Pb-evaporation, and Sm-Nd isotopic study of a granulite domain in SE Madagascar, *The Journal of Geology*, **102**, 523–538.

Paquette, J. L., and A. Nédélec (1998), A new insight into Pan-African tectonics in the East-West Gondwana collision zone by U-Pb zircon dating of granites from central Madagascar, *Earth and planetary science letters*, **155**(1–2), 45–56.

Parrish, R.R. (1990), U-Pb dating of monazite and its application to geological problems, *Canadian Journal of Earth Sciences*, **27**, 1431–1450.

Partin, C. A. et al. (2013), Large-scale fluctuations in Precambrian atmospheric and oceanic oxygen levels from the record of U in shales, *Earth and Planetary Science Letters*, **369**, 284–293.

Paton, C., J. D. Woodhead, J. C. Hellstrom, J. M. Hergt, A. Greig, and R. Maas (2010), Improved laser ablation U-Pb zircon geochronology through robust downhole fractionation correction, *Geochemistry, Geophysics, Geosystems*, **11**(3), Q0AA06.

Planavsky, N. J., C. T. Reinhard, X. Wang, D. Thomson, P. McGoldrick, R. H. Rainbird, T. Johnson, W. W. Fischer, and T. W. Lyons (2014), Low Mid-Proterozoic atmospheric oxygen levels and the delayed rise of animals, *Science*, **346**(6209), 635–638.

Planavsky, N. J., O. J. Rouxel, A. Bekker, S. V. Lalonde, K. O. Konhauser, C. T. Reinhard, and T. W. Lyons (2010), The evolution of the marine phosphate reservoir, *Nature*, **467**(7319), 1088–1090.

Pognante, U. (1992), Migmatites and leucogranites of Tertiary age from the High Himalayan Crystallines of Zanskar (NW India): A case history of anatexis of Palaeozoic orthogneisses, *Mineralogy and Petrology*, **46**, 291–313.

Pognante, U., and B. Lombardo (1989), Metamorphic evolution of the High Himalayan crystallines in SE Zanskar, India, *Journal of Metamorphic Geology*, **7**(1), 9–17.

Pognante, U., D. Castelli, P. Benna, G. Genovese, F. Oberli, M. Meier, and S. Tonarini (1990), The crystalline units of the High Himalayas in the Lahul–Zanskar region (northwest India): metamorphic–tectonic history and geochronology of the collided and imbricated Indian plate, *Geological Magazine*, **127**, 101–116.

Quigley, M., Y. Liangjun, L. Xiaohan, C. J. Wilson, M. Sandiford, and D. Phillips (2006), $^{40}Ar/^{39}Ar$ thermochronology of the Kampa Dome, southern Tibet: Implications for tectonic evolution of the North Himalayan gneiss domes: *Tectonophysics*, **421**(3), 269–297.

Rao, N. C., and B. Lehmann (2011), Kimberlites, flood basalts and mantle plumes: new insights from the Deccan Large Igneous Province, *Earth-Science Reviews*, **107**(3), 315–324.

Rapp, R. P., and E. B. Watson (1986), Monazite solubility and dissolution kinetics: implications for the thorium and light rare earth chemistry of felsic magmas, *Contributions to Mineralogy and Petrology*, **94**(3), 304–316.

Rapp, R. P., F. J. Ryerson, and C. F. Miller (1987), Experimental evidence bearing on the stability of monazite during crustal anatexis, *Geophysical Research Letters*, **14**(3), 307–310.

Ray, L., H.-J. Förster, A. Förster, S. Fuchs, R. Naumann, and O. Appelt (2015), Tracking the thermal properties of the lower continental crust: Measured versus calculated thermal conductivity of high-grade metamorphic rocks (Southern Granulite Province, India), *Geothermics*, **55**, 138–149.

Rey, P.F., C. Teyssier, S.C. Kruckenberg, and D.L. Whitney (2011), Viscous collision in channel explains double domes in metamorphic core complexes, *Geology*, **39**(4), 387–390.

Robyr, M., J.-L. Epard, and A. El Korh (2014), Structural, metamorphic and geochronological relations between the Zanskar Shear Zone and the Miyar Shear Zone (NW Indian Himalaya): Evidence for two distinct tectonic structures and implications for the evolution of the High Himalayan Crystalline of Zanskar, *Journal of Asian Earth Sciences*, **79**(Part A), 1–15.

Robyr, M., B.R. Hacker, and J.M. Mattinson (2006), Doming in compressional orogenic settings: New geochronological constraints from the NW Himalaya, *Tectonics*, **25**, TC2007.

Robyr, M., J.C. Vannay, J.L. Epard, and A. Steck (2002), Thrusting, extension, and doming during the polyphase tectonometamorphic evolution of the High Himalayan Crystalline Zone in NW India, *Journal of Asian Earth Sciences*, **21**, 221–239.

Rooney, A. D., J. V. Strauss, A. D. Brandon, and F. A. Macdonald (2015), A Cryogenian chronology: Two long-lasting synchronous Neoproterozoic glaciations, *Geology*, **43**(5), 459–462.

Rosenberg, C.L., and M.R. Handy (2005), Experimental deformation of partially melted granite revisited: implications for the continental crust, *Journal of Metamorphic Geology*, **23**, 19–28.

Rudnick, R. L., and I. Jackson (1995), Measured and calculated elastic wave speeds in partially equilibrated mafic granulite xenoliths: Implications for the properties of an underplated lower continental crust, *Journal of Geophysical Research: Solid Earth (1978–2012)*, **100**(B6), 10211–10218.

Rudnick, R. L., and S. Gao (2003), Composition of the continental crust, *Treatise on geochemistry*, **3**, 1–64.

Rudnick, R. L., and S. Gao (2014), Composition of the continental crust, *Treatise on geochemistry*, ***3***, 1–51.

Rudnick, R. L., and T. Presper (1990), Geochemistry of intermediate/-to high-pressure granulites, in *Granulites and crustal evolution* (Springer, New York, New York), 523–550.

Ruttenberg, K. C. (1993), Reassessment of the oceanic residence time of phosphorus, *Chemical Geology*, **107**(3), 405–409.

Ruttenberg, K. C. (2003), The global phosphorus cycle, *Treatise on Geochemistry*, **8**, 585–643.

Ruttenberg, K. C., and D. J. Sulak (2011), Sorption and desorption of dissolved organic phosphorus onto iron (oxyhydr)oxides in seawater, *Geochimica et Cosmochimica Acta*, **75**(15), 4095–4112.

Sandiford, M., and S. McLaren (2002), Tectonic feedback and the ordering of heat producing elements within the continental lithosphere, *Earth and Planetary Science Letters*, **204**(1–2), 133–150.

Schärer, U. (1984), The effect of initial ^{230}Th disequilibrium on young U-Pb ages: the Makalu case, Himalaya, *Earth and Planetary Science Letters*, **67**(2), 191–204.

Schrag, D. P., R. A. Berner, P. F. Hoffman, and G. P. Halverson (2002), On the initiation of a snowball Earth, *Geochemistry, Geophysics, Geosystems*, **3**(6), 1–21.

Schreurs, G., J. Giese, A. Berger, and E. Gnos (2010), A new perspective on the significance of the Ranotsara shear zone in Madagascar, *International Journal of Earth Sciences*, **99**(8), 1827–1847.

Schwerdtner, W.M., R.H. Sutcliff, B. Troeng (1978), Patterns of total strain in the crustal region of immature diapirs, *Canadian Journal of Earth Sciences,* **15**, 1437–1447.

Searle, M.P., and B.J. Fryer (1986), Garnet, tourmaline and muscovite-bearing leucogranites, gneisses and migmatites of the Higher Himalayas from Zanskar, Kulu, Lahoul and Kashmir, *Geological Society of London Special Publications*, **19**, 185–201.

Searle, M.P., and A.J. Rex (1989), Thermal model for the Zanskar Himalaya, *Journal of Metamorphic Geology*, **7**, 127–134.

Searle, M. P., R. L. Simpson, R. D. Law, R. R. Parrish, and D. J. Waters (2003), The structural geometry, metamorphic and magmatic evolution of the Everest massif, High Himalaya of Nepal–South Tibet, *Journal of the Geological Society*, **160**(3), 345–366.

Searle, M.P., B. Stephenson, J. Walker, and C. Walker (2007), Restoration of the Western Himalaya: Implications for metamorphic protoliths, thrust and normal faulting, and channel flow models, *Episodes*, **30**, 242–257.

Searle, M.P., D.J. Waters, M.W. Dransfield, B.J. Stephenson, C.B. Walker, J.D. Walker, and D.C. Rex (1999), Thermal and mechanical models for the structural and metamorphic

evolution of the Zanskar High Himalaya, *Geological Society of London Special Publications*, **164**, 139–156.

Shaffer, G. (1996), Biogeochemical cycling in the global ocean: 2. New production, Redfield ratios, and remineralization in the organic pump, *Journal of Geophysical Research: Oceans (1978–2012)*, **101**(C2), 3723–3745.

Sharma, M. (1997), Siberian traps, Large igneous provinces: Continental, oceanic, and planetary flood volcanism (American Geophysical Union, Washington, D.C.), 273–295.

Shi, D., Z. Wu, S. L. Klemperer, W. Zhao, G. Xue, and H. Su (2015), Receiver function imaging of crustal suture, steep subduction, and mantle wedge in the eastern India–Tibet continental collision zone, *Earth and Planetary Science Letters*, **414**, 6–15.

Shields, G. A. (2007), A normalised seawater strontium isotope curve: possible implications for Neoproterozoic-Cambrian weathering rates and the further oxygenation of the Earth, *eEarth*, **2**(2), 35–42.

Shimura, T., Y. Kon, Y. Sawaki, T. Hirata, J. Han, D. Shu, and T. Komiya (2014), In-situ analyses of phosphorus contents of carbonate minerals: Reconstruction of phosphorus contents of seawater from the Ediacaran to early Cambrian, *Gondwana Research*, **25**(3), 1090–1107.

Shurtleff, B., J. Lee, C. Hager, D. Stockli, D. Van Vleck, and A. Blythe (2013), Rapid middle to late Miocene slip along the Zanskar normal fault, Greater Himalayan Range, NW, India: Constraints from low-temperature thermochronometry, *Geological Society of America Abstracts with Programs*, **45**(7), 23.

Song, X.-Y., H.-W. Qi, P. T. Robinson, M.-F. Zhou, Z.-M. Cao, and L.-M. Chen (2008), Melting of the subcontinental lithospheric mantle by the Emeishan mantle plume; evidence from the basal alkaline basalts in Dongchuan, Yunnan, Southwestern China, *Lithos*, **100**(1), 93–111.

Spring, L., F. Bussy, J.C. Vannay, S. Huon, and M.A. Cosca (1993), Early Permian granitic dykes of alkaline affinity in the Indian High Himalaya of Upper Lahul and SE Zanskar: geochemical characterization and geotectonic implications, *Geological Society of London Special Publications*, **74**, 251–264.

Squire, R. J., I. H. Campbell, C. M. Allen, and C. J. Wilson (2006), Did the Transgondwanan Supermountain trigger the explosive radiation of animals on Earth? *Earth and Planetary Science Letters*, **250**(1), 116–133.

Stahr, D.W. (2013), Kinematic evolution, metamorphism, and exhumation of the Greater Himalayan Series, Sutlej River and Zanskar regions of NW India, *PhD Thesis*, Virginia Polytechnic Institute and State University, Blacksburg, Virginia, 115 pp.

Stäubli, A. (1989), Polyphase metamorphism and the development of the Main Central Thrust, *Journal of Metamorphic Geology*, **7**(1), 73–93.

Steck, A. (2003), Geology of the NW Indian Himalaya, *Eclogae Geologicae Helvetiae*, **96**, 147–196.

Steck, A., L. Spring, J. C. Vannay, H. Masson, E. Stutz, H. Bucher, R. Marchant, and J. C. Tieche (1993), Geological transect across the northwestern Himalaya in eastern Ladakh and Lahul (a model for the continental collision of India and Asia), *Eclogae Geologicae Helvetiae*, **86**(1), 219–263.

Stephenson, B.J., M.P. Searle, D.J. Waters, and D.C. Rex (2001), Structure of the Main Central Thrust zone and extrusion of the High Himalayan deep crustal wedge, Kishtwar-Zanskar Himalaya, *Journal of the Geological Society*, **158**, 637–652.

Stern, R. J. (1994), Arc-Assembly and Continental Collision in the Neoproterozoic African Orogen: Implications for the Consolidation of Gondwanaland, *Annual Review of Earth and Planetary Sciences*, **22**, 319–351.

Stutz, E., and M. Thöni (1987), The lower Paleozoic Nyimaling Granite in the Indian Himalaya (Ladakh): New Rb/Sr data versus zircon typology, *Geologische Rundschau*, **76**, 307–315.

Stüwe, K. (1998), Heat sources of Cretaceous metamorphism in the Eastern Alps—a discussion, *Tectonophysics*, **287**(1), 251–269.

Stüwe, K. (2007), Geodynamics of the lithosphere: An introduction (Springer Science & Business Media, New York, New York), 493 pp.

Taylor, R. J., C. Clark, I. C. Fitzsimons, M. Santosh, M. Hand, N. Evans, and B. McDonald (2014), Post-peak, fluid-mediated modification of granulite facies zircon and monazite in the Trivandrum Block, southern India, *Contributions to Mineralogy and Petrology*, **168**(2), 1–17.

Teyssier, C., and D.L. Whitney (2002), Gneiss domes and orogeny, *Geology*, **30**(12), 1139–1142.

Thakur, V.C. (1998), Structure of the Chamba nappe and position of the Main Central Thrust in Kashmir Himalaya, *Journal of Asian Earth Sciences*, **16**, 269–282.

Thomas, J. B., E. B. Watson, F. S. Spear, P. T. Shemella, S. K. Nayak, and A. Lanzirotti (2010), TitaniQ under pressure: the effect of pressure and temperature on the solubility of Ti in quartz, *Contributions to Mineralogy and Petrology*, **160**(5), 743–759.

Thompson, A. B., and J. A. Connolly (1995), Melting of the continental crust: some thermal and petrological constraints on anatexis in continental collision zones and other tectonic settings, *Journal of Geophysical Research: Solid Earth (1978–2012)*, **100**(B8), 15565–15579.

Tosca, N. J., D. T. Johnston, A. Mushegian, D. H. Rothman, R. E. Summons, and A. H. Knoll (2010), Clay mineralogy, organic carbon burial, and redox evolution in Proterozoic oceans, *Geochimica et Cosmochimica Acta*, **74**(5), 1579–1592.

Tucker, R. D., J. Y. Roig, B. Moine, C. Delor, and S. G. Peters (2014), A geological synthesis of the Precambrian shield in Madagascar, *Journal of African Earth Sciences*, ***94***, 9–30.

Tucker, R. D., T. M. Kusky, R. Buchwaldt, and M. J. Handke (2007), Neoproterozoic nappes and superposed folding of the Itremo Group, west-central Madagascar, *Gondwana Research*, **12**(4), 356–379.

Tucker, R., J. Roig, P. Macey, C. Delor, Y. Amelin, R. Armstrong, M. Rabarimanana, and A. Ralison (2011), A new geological framework for south-central Madagascar; and its relevance to the, *Precambrian Research*, **185**(3), 109–130.

Unsworth, M. J. et al. (2005), Crustal rheology of the Himalaya and Southern Tibet inferred from magnetotelluric data, *Nature*, **438**(7064), 78–81.

Valli, F., P. H. Leloup, J. L. Paquette, N. Arnaud, H. Li, P. Tapponnier, R. Lacassin, S. Guillot, D. Liu, and E. Deloule (2008), New U-Th/Pb constraints on timing of shearing and long-term slip-rate on the Karakorum fault, *Tectonics*, **27**(5), TC5007.

Van Cappellen, P., and E. D. Ingall (1996), Redox stabilization of the atmosphere and oceans by phosphorus-limited marine productivity, *Science*, **271**(5248), 493.

Van Den Eeckhout, B., B. Grocott, and R. Vissers (1986), On the role of diapirism in the segregation, ascent and final emplacement of granitoid magmas—discussion, *Tectonophysics,* **127**, 161–169.

Vance, D., and N. Harris (1999), Timing of prograde metamorphism in the Zanskar Himalaya, *Geology*, **27**, 395–398.

Vannay, J.-C., B. Grasemann, M. Rahn, W. Frank, A. Carter, V. Baudraz, and M. Cosca (2004), Miocene to Holocene exhumation of metamorphic crustal wedges in the NW Himalaya: Evidence for tectonic extrusion coupled to fluvial erosion, *Tectonics*, **23**(1), TC1014.

Vannay, J-C. and A. Steck (1995), Tectonic evolution of the High Himalaya in Upper Lahu (NW Himalaya, India), *Tectonics*, **14**, 253–263.

Walker, C.B., M.P. Searle, and D.J. Waters (2001), An integrated tectonothermal model for the evolution of the High Himalaya in western Zanskar with constraints from thermobarometry and metamorphic modeling, *Tectonics*, **20**, 810–833.

Walker, J.D., M.W. Martin, S.A. Bowring, M.P. Searle, D.J. Waters, and K.V. Hodges (1999), Metamorphism, melting, and extension: age constraints from the High Himalayan slab of southeast Zanskar and northwest Lahaul, *The Journal of geology*, **107**, 473–495.

Watson, E. B. (1980), Apatite and phosphorus in mantle source regions: an experimental study of apatite/melt equilibria at pressures to 25 kbar, *Earth and Planetary Science Letters*, **51**(2), 322–335.

Watt, G. R., and S. L. Harley (1993), Accessory phase controls on the geochemistry of crustal melts and restites produced during water-undersaturated partial melting, *Contributions to Mineralogy and Petrology*, **114**(4), 550–566.

Watts, D.R., and N.B. Harris (2005), Mapping granite and gneiss in domes along the North Himalayan antiform with ASTER SWIR band ratios, *Geological Society of America Bulletin*, **117**(7–8), 879–886.

Webb, A.A.G., A. Yin, and C.S. Dubey (2013), U-Pb zircon geochronology of major lithologic units in the eastern Himalaya: Implications for the origin and assembly of Himalayan rocks, *Geological Society of America Bulletin*, **125**(3–4), 499–522.

Webb, A.A.G., A. Yin, T.M. Harrison, J. Célérier, and W.P. Burgess (2007), The leading edge of the Greater Himalayan Crystalline complex revealed in the NW Indian Himalaya: Implications for the evolution of the Himalayan orogen, *Geology*, **35**(10), 955–958.

Wheat, G. C., R. A. Feely, and M. J. Mottl (1996), Phosphate removal by oceanic hydrothermal processes: An update of the phosphorus budget in the oceans, *Geochimica et cosmochimica acta*, **60**(19), 3593–3608.

Whitney, D.L., C. Teyssier, and O. Vanderhaeghe (2004), Gneiss domes and crustal flow, *Geological Society of America Special Papers*, **380**, 15–33.

Whittington, A. G., A. M. Hofmeister, and P. I. Nabelek (2009), Temperature-dependent thermal diffusivity of the Earth's crust and implications for magmatism, *Nature*, **458**(7236), 319–321.

Windley, B. F., A. Razafiniparany, T. Razakamanana, and D. Ackermand (1994), Tectonic framework of the Precambrian of Madagascar and its Gondwana connections: a review and reappraisal, *Geologische Rundschau*, **83**(3), 642–659.

Wolf, M. B., and D. London (1995), Incongruent dissolution of REE-and Sr-rich apatite in peraluminous granitic liquids: Differential apatite, monazite, and xenotime solubilities during anatexis, *American Mineralogist*, **80**(7), 765–775.

Yin, A. (2006), Cenozoic tectonic evolution of the Himalayan orogen as constrained by along-strike variation of structural geometry, exhumation history, and foreland sedimentation, *Earth Science Reviews*, **76**(1), 1–131.

Zhang, M., and S. Y. O'Reilly (1997), Multiple sources for basaltic rocks from Dubbo, eastern Australia: geochemical evidence for plume—lithospheric mantle interaction, *Chemical Geology*, **136**(1), 33–54.

Appendix 1. U/Th-Pb Analytical Data

Analysis number	Approx. U/Th	$^{208}Pb/^{232}Th$	±2σ	$^{206}Pb/^{238}U$	±2σ	$^{207}Pb/^{206}Pb$	±2σ
GBD-5c							
1	0.080	0.00110	0.00002	0.00382	0.00008	0.07980	0.00241
2	0.095	0.00109	0.00002	0.00374	0.00007	0.07200	0.00201
3	0.161	0.00109	0.00002	0.00378	0.00008	0.07060	0.00206
4	0.082	0.00109	0.00002	0.00382	0.00009	0.08630	0.00272
5	0.143	0.00109	0.00002	0.00374	0.00010	0.07100	0.00199
6	0.205	0.00111	0.00003	0.00374	0.00010	0.08150	0.00368
GBD-29b							
1	2.434	0.00179	0.00005	0.00558	0.00011	0.04627	0.00096
2	6.265	0.00185	0.00004	0.00548	0.00007	0.04549	0.00092
3	5.300	0.00181	0.00006	0.00525	0.00011	0.04526	0.00093
4	4.976	0.00182	0.00005	0.00552	0.00008	0.04432	0.00090
5	5.230	0.00180	0.00005	0.00545	0.00008	0.04395	0.00089
6	6.100	0.00180	0.00005	0.00536	0.00008	0.04376	0.00089
7	0.588	0.00164	0.00003	0.00595	0.00004	0.04057	0.00083
8	0.653	0.00165	0.00004	0.00596	0.00008	0.04028	0.00082
9	0.582	0.00167	0.00004	0.00606	0.00009	0.04051	0.00083
10	5.010	0.00183	0.00004	0.00555	0.00008	0.04281	0.00087
11	2.156	0.00178	0.00005	0.00566	0.00009	0.04656	0.00095
12	0.496	0.00165	0.00004	0.00613	0.00008	0.04124	0.00087
13	0.553	0.00165	0.00004	0.00592	0.00010	0.04414	0.00090
14	0.542	0.00166	0.00004	0.00593	0.00010	0.04415	0.00091
15	0.588	0.00169	0.00004	0.00596	0.00010	0.04428	0.00091
16	0.578	0.00171	0.00005	0.00617	0.00012	0.04414	0.00090
17	0.511	0.00165	0.00004	0.00591	0.00009	0.04426	0.00091
18	0.574	0.00167	0.00004	0.00587	0.00009	0.04441	0.00091
19	0.526	0.00167	0.00005	0.00592	0.00011	0.04432	0.00091
20	0.625	0.00170	0.00004	0.00605	0.00005	0.04427	0.00091
21	0.527	0.00167	0.00003	0.00616	0.00004	0.04412	0.00091
22	0.572	0.00167	0.00003	0.00609	0.00004	0.04437	0.00091
23	5.410	0.00183	0.00005	0.00540	0.00009	0.04604	0.00094
24	5.650	0.00184	0.00005	0.00547	0.00007	0.04567	0.00093
GBD-33							
1	0.054	0.00101	0.00002	0.00335	0.00006	0.07930	0.00390
2	0.076	0.00102	0.00002	0.00329	0.00006	0.06340	0.00240
3	0.066	0.00103	0.00002	0.00332	0.00005	0.05370	0.00200
4	0.058	0.00105	0.00002	0.00344	0.00006	0.06120	0.00380
5	0.078	0.00104	0.00002	0.00329	0.00006	0.06210	0.00640
6	0.061	0.00103	0.00002	0.00335	0.00006	0.05980	0.00300
7	0.074	0.00104	0.00002	0.00345	0.00010	0.07700	0.01100
8	0.072	0.00105	0.00002	0.00347	0.00006	0.10050	0.00290
9	0.062	0.00101	0.00002	0.00334	0.00006	0.06180	0.00220
10	0.078	0.00100	0.00002	0.00333	0.00007	0.08290	0.00250
11	0.072	0.00101	0.00002	0.00332	0.00008	0.07110	0.00490
12	0.081	0.00101	0.00002	0.00336	0.00007	0.08640	0.00460
GBD-45b							
1	0.038	0.00110	0.00003	0.00388	0.00007	0.09950	0.00360
2	0.036	0.00111	0.00003	0.00392	0.00010	0.10760	0.00877
3	0.044	0.00112	0.00003	0.00365	0.00009	0.08630	0.00320
4	0.029	0.00107	0.00003	0.00381	0.00008	0.07670	0.00364
5	0.063	0.00107	0.00004	0.00374	0.00012	0.07810	0.00514
6	0.091	0.00112	0.00003	0.00394	0.00007	0.10710	0.00307
7	0.063	0.00112	0.00003	0.00404	0.00008	0.13760	0.00407
8	0.047	0.00112	0.00003	0.00371	0.00007	0.07530	0.00327

GBD-51b

1	0.165	0.00180	0.00008	0.00565	0.00025	0.05599	0.00082
2	0.132	0.00181	0.00008	0.00573	0.00025	0.05800	0.00100
3	0.140	0.00165	0.00007	0.00540	0.00023	0.05401	0.00075
4	0.137	0.00180	0.00008	0.00572	0.00026	0.05673	0.00078
5	0.162	0.00182	0.00008	0.00577	0.00026	0.05535	0.00074
6	0.183	0.00165	0.00007	0.00529	0.00023	0.05285	0.00084
7	0.179	0.00180	0.00008	0.00563	0.00027	0.05613	0.00071
8	0.178	0.00174	0.00008	0.00553	0.00025	0.05528	0.00084
9	0.153	0.00178	0.00008	0.00555	0.00025	0.05567	0.00087
10	0.189	0.00177	0.00008	0.00560	0.00025	0.05340	0.00078
11	0.160	0.00172	0.00008	0.00550	0.00024	0.05590	0.00120
12	0.158	0.00178	0.00008	0.00562	0.00025	0.05583	0.00087
13	0.210	0.00180	0.00008	0.00561	0.00024	0.05342	0.00071
14	0.172	0.00163	0.00007	0.00528	0.00023	0.05402	0.00072
15	0.177	0.00163	0.00007	0.00521	0.00023	0.05355	0.00088
16	0.222	0.00179	0.00008	0.00558	0.00025	0.05767	0.00091
17	0.192	0.00166	0.00008	0.00531	0.00024	0.05461	0.00077
18	0.096	0.00172	0.00008	0.00565	0.00027	0.05745	0.00089
19	0.177	0.00161	0.00007	0.00520	0.00024	0.05447	0.00083
20	0.183	0.00162	0.00007	0.00520	0.00024	0.05445	0.00080
21	0.183	0.00178	0.00008	0.00563	0.00025	0.05507	0.00080
22	0.196	0.00180	0.00008	0.00562	0.00026	0.05498	0.00069
23	0.097	0.00167	0.00008	0.00549	0.00026	0.05900	0.00110
24	0.198	0.00176	0.00008	0.00542	0.00025	0.05314	0.00080
25	0.134	0.00166	0.00007	0.00542	0.00024	0.05470	0.00120
26	0.279	0.00166	0.00007	0.00516	0.00023	0.05229	0.00060
27	0.176	0.00162	0.00007	0.00518	0.00023	0.05507	0.00082
28	0.158	0.00169	0.00008	0.00542	0.00024	0.05415	0.00083
29	0.179	0.00167	0.00008	0.00536	0.00025	0.05352	0.00056
30	0.089	0.00175	0.00008	0.00550	0.00026	0.05930	0.00095

GBD-52b

1	0.001	0.02318	0.00038	0.07480	0.00120	0.05726	0.00118
2	0.001	0.02243	0.00042	0.07350	0.00150	0.05649	0.00116
3	0.001	0.02243	0.00033	0.07330	0.00100	0.05676	0.00115
4	0.000	0.02308	0.00030	0.07650	0.00100	0.05685	0.00118
5	0.001	0.02271	0.00036	0.07580	0.00120	0.05728	0.00116
6	0.002	0.01997	0.00035	0.07040	0.00110	0.05706	0.00117
7	0.001	0.02236	0.00038	0.07320	0.00120	0.05690	0.00116
8	0.002	0.02236	0.00032	0.07314	0.00099	0.05666	0.00115
9	0.001	0.02241	0.00039	0.07360	0.00130	0.05649	0.00115
10	0.001	0.02194	0.00039	0.07320	0.00120	0.05691	0.00116
11	0.001	0.02318	0.00031	0.07600	0.00100	0.05677	0.00119
12	0.001	0.02123	0.00037	0.07270	0.00130	0.05642	0.00118
13	0.001	0.02189	0.00039	0.07460	0.00130	0.05688	0.00120
14	0.001	0.02316	0.00037	0.07690	0.00130	0.05678	0.00119
15	0.001	0.02360	0.00038	0.07510	0.00100	0.05682	0.00119

GBD-63b

1	0.442	0.00106	0.00003	0.00335	0.00005	0.06440	0.00163
2	0.514	0.00107	0.00003	0.00322	0.00005	0.07000	0.00154
3	0.680	0.00106	0.00003	0.00333	0.00006	0.05765	0.00126
4	0.449	0.00108	0.00003	0.00328	0.00005	0.06121	0.00148
5	0.231	0.00103	0.00003	0.00325	0.00006	0.06929	0.00168
6	0.423	0.00106	0.00003	0.00321	0.00008	0.07470	0.00226
7	0.431	0.00106	0.00003	0.00330	0.00006	0.06305	0.00150
8	0.276	0.00105	0.00003	0.00333	0.00006	0.06970	0.00178
9	0.417	0.00106	0.00003	0.00332	0.00007	0.06401	0.00154
10	0.419	0.00100	0.00003	0.00319	0.00007	0.06320	0.00168
11	0.729	0.00104	0.00003	0.00321	0.00006	0.05573	0.00123

GBD-64d

8	0.078	0.00184	0.00003	0.00594	0.00009	0.05340	0.00110
4	0.101	0.00185	0.00003	0.00582	0.00009	0.05160	0.00120
7	0.080	0.00185	0.00003	0.00587	0.00008	0.05400	0.00110
17	0.080	0.00185	0.00003	0.00585	0.00010	0.05180	0.00110
20	0.111	0.00185	0.00003	0.00587	0.00009	0.05100	0.00100
31	0.082	0.00186	0.00004	0.00596	0.00012	0.05270	0.00120
13	0.078	0.00186	0.00003	0.00592	0.00010	0.05420	0.00100
11	0.104	0.00186	0.00003	0.00589	0.00009	0.05360	0.00120
3	0.097	0.00186	0.00003	0.00587	0.00009	0.05272	0.00089
14	0.086	0.00186	0.00006	0.00597	0.00023	0.05210	0.00210
23	0.096	0.00186	0.00004	0.00590	0.00012	0.05240	0.00110
15	0.084	0.00188	0.00003	0.00597	0.00010	0.05190	0.00110

GBD-90b

1	0.128	0.02069	0.00052	0.07260	0.00150	0.05762	0.00118
2	0.174	0.02229	0.00053	0.07320	0.00110	0.05698	0.00115
3	0.115	0.02191	0.00055	0.07180	0.00130	0.05635	0.00114
4	0.069	0.02236	0.00053	0.07470	0.00110	0.05634	0.00117
5	0.266	0.02224	0.00051	0.07052	0.00086	0.05703	0.00116
6	0.123	0.02217	0.00059	0.07290	0.00140	0.05659	0.00116
7	0.072	0.02226	0.00051	0.07490	0.00110	0.05675	0.00117
8	0.262	0.02233	0.00051	0.07135	0.00087	0.05692	0.00115
9	0.294	0.02259	0.00056	0.07200	0.00120	0.05701	0.00116
10	0.131	0.02203	0.00052	0.07210	0.00110	0.05661	0.00116
11	0.061	0.02244	0.00055	0.07510	0.00130	0.05648	0.00117
12	0.073	0.02245	0.00055	0.07640	0.00140	0.05678	0.00116
13	0.092	0.02186	0.00058	0.07310	0.00140	0.05638	0.00116
14	0.113	0.02223	0.00052	0.07580	0.00140	0.05672	0.00116
15	0.117	0.02250	0.00056	0.07430	0.00140	0.05657	0.00117
16	0.063	0.02229	0.00057	0.07530	0.00120	0.05693	0.00119
17	0.282	0.02256	0.00056	0.07260	0.00100	0.05717	0.00116
18	0.151	0.02176	0.00057	0.07260	0.00130	0.05693	0.00116
19	0.116	0.02144	0.00052	0.07400	0.00120	0.05788	0.00119
20	0.016	0.02220	0.00056	0.07590	0.00140	0.05770	0.00138
21	0.021	0.02201	0.00056	0.07480	0.00130	0.05803	0.00132
22	0.057	0.02104	0.00057	0.07320	0.00190	0.05717	0.00118
23	0.037	0.02197	0.00079	0.07540	0.00230	0.05748	0.00128
24	0.055	0.02129	0.00049	0.07300	0.00110	0.05697	0.00118
25	0.065	0.02124	0.00053	0.07260	0.00120	0.05732	0.00118
26	0.029	0.02170	0.00060	0.07330	0.00140	0.05703	0.00125

GBD-101b

1	0.002	0.00115	0.00003	0.00366	0.00008	0.05290	0.00160
2	0.001	0.00113	0.00003	0.00365	0.00005	0.05273	0.00137
3	0.003	0.00114	0.00003	0.00362	0.00005	0.05195	0.00139
4	0.001	0.00112	0.00003	0.00363	0.00004	0.05116	0.00140
5	0.006	0.00117	0.00003	0.00364	0.00005	0.05239	0.00132
6	0.002	0.00115	0.00003	0.00366	0.00005	0.05080	0.00131
7	0.006	0.00112	0.00003	0.00369	0.00005	0.05272	0.00135
8	0.002	0.00111	0.00003	0.00367	0.00006	0.05130	0.00143
9	0.001	0.00113	0.00003	0.00369	0.00005	0.05488	0.00139
10	0.001	0.00113	0.00003	0.00367	0.00005	0.05367	0.00132
11	0.001	0.00114	0.00003	0.00369	0.00005	0.05091	0.00133
12	0.001	0.00113	0.00003	0.00368	0.00004	0.05149	0.00129
13	0.003	0.00111	0.00003	0.00367	0.00006	0.05083	0.00142
14	0.003	0.00110	0.00003	0.00364	0.00005	0.05250	0.00159
15	0.004	0.00112	0.00003	0.00370	0.00005	0.05230	0.00152
16	0.003	0.00113	0.00003	0.00370	0.00005	0.05271	0.00142

Appendix 2. LASS geochronology methods for Chapter I.

For each thin section, 5–10 monazite grains were ablated with 10 μm spots for a total of 20–30 spots per sample. Methods are described in Kylander-Clark et al. (2013). Monazite data were normalized to standard 44069 (Aleinikoff et al., 2006), corrected for downhole fractionation, and processed using Iolite software (Paton et al., 2010). Young monazite ^{238}U–^{206}Pb dates are affected by the presence of ^{206}Pb generated by ^{230}Th incorporated during monazite growth (Schärer, 1984; Parrish, 1990) and $^{207}Pb/^{235}U$ dates are less precise, so we present ^{232}Th–^{208}Pb dates for Cenozoic monazites. Paleozoic isotopic data are shown in Tera–Wasserburg diagrams, whereas younger dates are shown on $^{206}Pb/^{238}U$–$^{208}Pb/^{232}Th$ concordia. 2-sigma uncertainties are reported for all dates. Prior to analysis, individual grain x-ray maps of Y, La, Nd, Th, and U were made on a Cameca SX-100 electron microprobe using a 1 μm step size; LASS spot locations were chosen using these maps.

Appendix 3. Petrologic descriptions of monazite geochronology samples.

GBD-5c pegmatite dike. Equigranular, weakly deformed rock with feldspars that have moderate undulatory extinction and mechanical twins. Quartz has moderate to strong undulatory extinction, and moderate to strong subgrain development.

GBD-29b orthogneiss dike. Strongly deformed plagioclase has undulatory extinction, mechanical twins, and annealed microfractures. Quartz grains are elongate with weak to moderate undulatory extinction and moderate subgrain development; foliation is defined by white mica and elongate feldspar.

GBD-33 biotite migmatite. Plagioclase has moderate undulatory extinction and mechanical twins in a strong amphibolite-facies fabric with foliation defined by biotite. Quartz has equant, well-developed subgrains.

GBD-45b Kade orthogneiss. An orthogneiss with a strong amphibolite-facies fabric and plagioclase porphyroclasts with weak to moderate undulatory extinction, mechanical twins, and moderate subgrain development. Anastomozing foliation is composed of mica, and quartz has moderate undulatory extinction and strong subgrain development.

GBD-51b Kade orthogneiss. Cm-size K-feldspar porphyroclasts with undulatory extinction and microcracks are set in a matrix of 1–2 mm grains of K-feldspar, plagioclase, biotite, muscovite, and quartz. Plagioclase has moderate undulatory extinction and mechanical twins. Quartz has moderate undulatory extinction and extensive subgrain development. Foliation is defined by elongate feldspar and mica. Lower amphibolite-facies fabric is cut by discrete S2 shear bands composed of 10–100 um grains that likely developed at greenschist-facies conditions.

GBD-52b Kade orthogneiss. Mylonitic rock with K-feldspar porphyroclasts set in a matrix of strongly deformed feldspar quartz and mica. Porphyroclasts have moderate undulatory extinction, microcracks, and recrystallized tails made of 10 μm grains. Quartz is recrystallized to chiefly 200–500 μm subgrains. Feldspar and biotite have undergone the most grain-size reduction to very fine aggregates of 10–100 μm and 20–200 μm grains, respectively. These textures are consistent with upper greenschist-facies deformation.

GBD-63b nondeformed two-mica granite. Equigranular rock with weak amphibolite-facies fabric. Feldspars have moderate undulatory extinction and mechanical twins. Quartz has moderate to strong undulatory extinction and moderate to strong subgrain development.

GBD-64d orthogneiss. A strong amphibolite-facies fabric composed of relatively equant grains of xenoblastic feldspar, quartz, and mica. Foliation is defined by biotite seams and elongate quartz and feldspar. Feldspar shows weak undulatory extinction, minor mechanical twins, and weak subgrain development. Quartz has moderate undulatory extinction and strong subgrain development.

GBD-90b orthogneiss. Orthogneiss with a strong amphibolite-facies fabric and plagioclase porphyroclasts with weak to moderate undulatory extinction, mechanical twins, and moderate subgrain development. Anastomozing foliation is composed of mica, and quartz has moderate undulatory extinction and strong subgrain development.

GBD-101b migmatite. Equigranular rock with K-feldspars showing strong undulatory extinction and microcracks. Plagioclase has weak undulatory extinction and minor mechanical twins. Quartz has moderate undulatory extinction, and weak subgrain development. Feldspar and quartz grain boundaries are lobate and have local thin films of

feldspar or quartz. These textures are compatible with grain-boundary sliding and solution–precipitation at hypersolidus conditions.

Appendix 4. Thermochronology analytical data table.

Watts	Relative Isotopic Abundances (amps x10^{-11})											Derived Results							
	^{40}Ar	± 1S	^{39}Ar	± 1S	^{38}Ar	± 1S	^{37}Ar	± 1S	^{36}Ar	± 1S		^{39}Ar Mol ¥ 10^{-17}	^{39}Ar % of total	% $(^{36}Ar)_{Ca}$	Ca/K	± 1S	% $^{40}Ar^{*}$	Age (Ma)	± 2S
GBD-5c - biotite																			
J(±1 S) = 0.000423 ± 0.000001																			
0.01	10.6369	0.0134	0.1570	0.0010	0.0054	0.0004	0.0011	0.0023	0.0170	0.0004		3.47	2.0	0.0	0.014	0.029	52.2	26.8	1.1
0.05	14.3727	0.0190	0.4134	0.0017	0.0077	0.0005	0.0086	0.0038	0.0083	0.0003		9.13	5.2	0.0	0.041	0.018	82.7	21.8	0.4
0.10	16.5478	0.0180	0.5564	0.0016	0.0067	0.0005	0.0014	0.0022	0.0027	0.0003		12.29	7.0	0.0	0.005	0.008	95.2	21.5	0.3
0.20	11.0388	0.0143	0.3773	0.0021	0.0048	0.0005	0.0000	0.0021	0.0004	0.0003		8.34	4.7	0.0	0.000	0.011	99.0	22.0	0.4
0.30	15.7841	0.0143	0.5494	0.0016	0.0063	0.0005	0.0000	0.0022	0.0001	0.0003		12.13	6.9	0.0	0.000	0.008	99.9	21.8	0.3
0.40	15.2611	0.0267	0.5432	0.0020	0.0070	0.0006	0.0000	0.0023	0.0006	0.0003		12.00	6.8	0.0	0.000	0.008	98.9	21.1	0.3
0.50	16.8844	0.0190	0.6006	0.0019	0.0061	0.0006	0.0006	0.0025	0.0000	0.0003		13.26	7.5	0.5	0.002	0.008	100.0	21.3	0.3
0.60	9.2355	0.0152	0.3245	0.0014	0.0036	0.0005	0.0000	0.0023	0.0008	0.0003		7.17	4.1	0.0	0.000	0.014	97.5	21.1	0.4
0.70	11.4276	0.0162	0.3982	0.0014	0.0051	0.0005	0.0003	0.0024	0.0000	0.0003		8.80	5.0	0.4	0.001	0.012	100.0	21.8	0.4
0.80	13.8383	0.0316	0.4867	0.0015	0.0064	0.0005	0.0000	0.0023	0.0002	0.0003		10.75	6.1	0.0	0.000	0.009	99.6	21.5	0.3
0.90	93.1538	0.0802	3.2982	0.0069	0.0460	0.0007	0.0126	0.0020	0.0056	0.0004		72.82	41.3	0.1	0.008	0.001	98.2	21.1	0.1
1.00	5.6062	0.0125	0.1942	0.0011	0.0031	0.0004	0.0033	0.0022	0.0010	0.0003		4.29	2.4	0.1	0.033	0.022	94.8	20.8	0.7
1.50	2.2927	0.0089	0.0810	0.0007	0.0011	0.0004	0.0093	0.0023	0.0013	0.0003		1.79	1.0	0.2	0.224	0.056	83.0	17.8	1.5
GBD-26c - biotite																			
J(±1 S) = 0.000423 ± 0.000001																			
0.05	3.4950	0.0091	0.0867	0.0017	0.0024	0.0005	0.0056	0.0024	0.0053	0.0003		1.91	1.9	0.0	0.127	0.053	55.2	16.9	1.6
0.10	6.4462	0.0109	0.1885	0.0015	0.0020	0.0004	0.0003	0.0023	0.0040	0.0003		4.16	4.2	0.0	0.003	0.023	81.5	21.1	0.8
0.20	5.3306	0.0101	0.1662	0.0015	0.0019	0.0005	0.0045	0.0022	0.0014	0.0003		3.67	3.7	0.1	0.053	0.025	92.5	22.5	0.9
0.30	8.0696	0.0125	0.2612	0.0017	0.0044	0.0004	0.0030	0.0020	0.0024	0.0003		5.77	5.8	0.0	0.022	0.015	91.2	21.4	0.6
0.40	6.7035	0.0171	0.2271	0.0019	0.0036	0.0004	0.0076	0.0021	0.0009	0.0003		5.01	5.0	0.2	0.066	0.018	95.9	21.5	0.7
0.50	7.7159	0.0115	0.2671	0.0011	0.0034	0.0005	0.0025	0.0024	0.0006	0.0003		5.90	5.9	0.1	0.018	0.018	97.8	21.4	0.5
0.60	5.2578	0.0104	0.1832	0.0011	0.0035	0.0004	0.0040	0.0023	0.0000	0.0004		4.05	4.1	2.2	0.042	0.025	99.8	21.7	0.9
0.70	6.9988	0.0105	0.2432	0.0010	0.0034	0.0004	0.0077	0.0021	0.0012	0.0003		5.37	5.4	0.2	0.062	0.017	94.9	20.7	0.5

0.80	7.3414	0.0190	0.2513	0.0011	0.0033	0.0004	0.0000	0.0023	0.0007	0.0003	5.55	5.6	0.0	0.000	0.018	97.0	21.5	0.6
0.90	7.7928	0.0228	0.2764	0.0010	0.0040	0.0004	0.0024	0.0023	0.0000	0.0003	6.10	6.1	1.2	0.017	0.016	99.8	21.4	0.5
1.00	9.5381	0.0286	0.3243	0.0011	0.0047	0.0005	0.0000	0.0024	0.0005	0.0003	7.16	7.2	0.0	0.000	0.014	98.4	22.0	0.5
1.50	56.8021	0.0613	1.9843	0.0032	0.0264	0.0006	0.0035	0.0022	0.0028	0.0003	43.82	44.1	0.0	0.003	0.002	98.5	21.4	0.1
2.00	1.1700	0.0088	0.0444	0.0007	0.0000	0.0004	0.0024	0.0021	0.0003	0.0003	0.98	1.0	0.2	0.108	0.094	91.8	18.4	2.7

GBD-101b - biotite

J(±1 s) = 0.000423 ± 0.000001

0.05	2.0738	0.0084	0.0341	0.0006	0.0000	0.0004	0.0000	0.0023	0.0023	0.0003	0.75	0.5	0.0	0.000	0.131	66.8	30.7	3.9
0.10	39.3921	0.0444	1.2253	0.0027	0.0178	0.0006	0.0000	0.0026	0.0097	0.0003	27.06	17.9	0.0	0.000	0.004	92.7	22.6	0.2
0.20	13.4468	0.0316	0.4524	0.0016	0.0067	0.0004	0.0000	0.0021	0.0003	0.0003	9.99	6.6	0.0	0.000	0.009	99.4	22.4	0.3
0.30	17.3018	0.0238	0.5879	0.0016	0.0083	0.0005	0.0008	0.0021	0.0000	0.0003	12.98	8.6	0.5	0.003	0.007	99.9	22.3	0.3
0.40	13.9005	0.0162	0.4672	0.0012	0.0059	0.0005	0.0000	0.0024	0.0000	0.0005	10.32	6.8	0.0	0.000	0.010	99.9	22.6	0.5
0.50	13.6552	0.0125	0.4585	0.0015	0.0062	0.0005	0.0000	0.0020	0.0001	0.0005	10.13	6.7	0.0	0.000	0.008	99.8	22.5	0.5
0.60	8.1597	0.0180	0.2747	0.0017	0.0038	0.0004	0.0003	0.0023	0.0007	0.0003	6.07	4.0	0.0	0.002	0.016	97.5	22.0	0.6
0.70	9.0157	0.0110	0.3017	0.0011	0.0042	0.0005	0.0000	0.0021	0.0004	0.0003	6.66	4.4	0.0	0.000	0.014	98.7	22.4	0.4
0.80	7.7474	0.0134	0.2552	0.0013	0.0037	0.0004	0.0008	0.0021	0.0004	0.0003	5.64	3.7	0.1	0.006	0.016	98.6	22.7	0.6
0.90	10.7531	0.0152	0.3602	0.0013	0.0032	0.0004	0.0008	0.0026	0.0000	0.0003	7.95	5.3	2.9	0.005	0.014	100.0	22.7	0.4
1.00	20.5639	0.0306	0.6902	0.0018	0.0079	0.0004	0.0007	0.0025	0.0000	0.0003	15.24	10.1	0.4	0.002	0.007	99.9	22.6	0.2
1.50	49.2398	0.0563	1.6879	0.0044	0.0232	0.0006	0.0000	0.0024	0.0000	0.0003	37.27	24.7	0.6	0.000	0.003	100.1	22.2	0.2

GBS-36b - biotite

J(±1 s) = 0.000423 ± 0.000001

0.01	69.7507	0.0573	1.7851	0.0033	0.0358	0.0006	0.0012	0.0020	0.0567	0.0005	39.42	19.9	0.0	0.001	0.002	75.7	22.5	0.2
0.05	50.9045	0.0494	1.6294	0.0030	0.0241	0.0006	0.0000	0.0019	0.0077	0.0003	35.98	18.2	0.0	0.000	0.002	95.5	22.6	0.2
0.10	30.7168	0.0703	1.0059	0.0026	0.0127	0.0005	0.0000	0.0022	0.0014	0.0003	22.21	11.2	0.0	0.000	0.004	98.6	22.8	0.2
0.20	17.9437	0.0180	0.5984	0.0020	0.0087	0.0006	0.0009	0.0022	0.0000	0.0003	13.21	6.7	0.6	0.003	0.007	99.9	22.7	0.3
0.30	20.0872	0.0190	0.6723	0.0017	0.0102	0.0005	0.0028	0.0025	0.0016	0.0003	14.84	7.5	0.0	0.008	0.007	97.7	22.1	0.3
0.40	10.3447	0.0125	0.3457	0.0012	0.0043	0.0004	0.0001	0.0023	0.0007	0.0003	7.63	3.9	0.0	0.000	0.013	98.1	22.3	0.4
0.50	10.1293	0.0209	0.3353	0.0013	0.0065	0.0004	0.0090	0.0024	0.0016	0.0003	7.40	3.7	0.1	0.053	0.014	95.3	21.9	0.4

0.60	6.4027	0.0180	0.2112	0.0010	0.0042	0.0004	0.0037	0.0024	0.0014	0.0003	4.66	2.4	0.1	0.034	0.022	93.5	21.5	0.7
0.70	9.8316	0.0209	0.3239	0.0014	0.0040	0.0004	0.0003	0.0024	0.0000	0.0003	7.15	3.6	0.6	0.002	0.014	100.0	23.0	0.5
0.80	11.8505	0.0533	0.3983	0.0020	0.0058	0.0005	0.0072	0.0021	0.0018	0.0003	8.79	4.4	0.1	0.035	0.010	95.5	21.6	0.4
0.90	23.1357	0.0375	0.7657	0.0023	0.0099	0.0004	0.0002	0.0022	0.0005	0.0003	16.90	8.5	0.0	0.001	0.006	99.4	22.8	0.2
1.00	12.7563	0.0209	0.4248	0.0017	0.0054	0.0005	0.0002	0.0027	0.0000	0.0003	9.38	4.7	0.1	0.001	0.012	99.9	22.8	0.4
1.50	14.4424	0.0228	0.4800	0.0019	0.0074	0.0005	0.0016	0.0022	0.0008	0.0003	10.60	5.3	0.0	0.006	0.009	98.3	22.5	0.3

GBD-45b - biotite

J(±1 S) = 0.000423 ± 0.000001

0.01	6.1437	0.0171	0.0815	0.0007	0.0039	0.0004	0.0000	0.0025	0.0132	0.0003	1.80	1.2	0.0	0.000	0.060	35.9	20.6	1.9
0.05	15.1119	0.0152	0.3487	0.0012	0.0071	0.0004	0.0042	0.0023	0.0154	0.0004	7.70	5.0	0.0	0.024	0.013	69.5	22.9	0.5
0.10	17.3068	0.0345	0.5865	0.0016	0.0087	0.0004	0.0010	0.0025	0.0017	0.0003	12.95	8.4	0.0	0.003	0.008	97.2	21.8	0.3
0.20	12.0704	0.0218	0.4164	0.0013	0.0061	0.0005	0.0029	0.0023	0.0008	0.0003	9.19	5.9	0.1	0.014	0.011	98.0	21.6	0.4
0.30	14.2656	0.0228	0.4951	0.0015	0.0050	0.0005	0.0001	0.0024	0.0000	0.0003	10.93	7.0	0.1	0.000	0.010	100.0	21.9	0.3
0.40	12.6532	0.0180	0.4400	0.0015	0.0045	0.0005	0.0000	0.0023	0.0001	0.0003	9.71	6.3	0.0	0.000	0.010	99.8	21.8	0.3
0.50	12.6666	0.0355	0.4364	0.0015	0.0066	0.0005	0.0040	0.0025	0.0010	0.0003	9.63	6.2	0.1	0.018	0.011	97.7	21.5	0.4
0.60	9.2503	0.0306	0.3190	0.0013	0.0038	0.0004	0.0010	0.0023	0.0000	0.0003	7.04	4.5		0.006	0.014	100.0	22.0	0.5
0.70	8.4943	0.0180	0.2929	0.0013	0.0046	0.0004	0.0000	0.0023	0.0000	0.0003	6.47	4.2	0.0	0.000	0.015	99.9	22.0	0.5
0.80	10.1774	0.0643	0.3491	0.0015	0.0040	0.0004	0.0002	0.0024	0.0000	0.0003	7.71	5.0	0.2	0.001	0.014	99.9	22.1	0.5
0.90	15.6324	0.0190	0.5386	0.0026	0.0058	0.0005	0.0000	0.0024	0.0001	0.0003	11.89	7.7	0.0	0.000	0.009	99.8	22.0	0.3
1.00	22.3022	0.0316	0.7716	0.0017	0.0107	0.0005	0.0000	0.0020	0.0007	0.0003	17.04	11.0	0.0	0.000	0.005	99.1	21.7	0.2
1.50	56.9666	0.0474	1.9487	0.0036	0.0274	0.0005	0.0096	0.0026	0.0038	0.0003	43.03	27.7	0.1	0.010	0.003	98.0	21.7	0.1

GBD-52b - biotite

J(±1 S) = 0.000420 ± 0.000001

0.01	50.6018	0.0464	0.8631	0.0017	0.0249	0.0006	0.0000	0.0021	0.0637	0.0005	19.06	5.7	0.0	0.000	0.005	62.4	27.5	0.3
0.05	59.2159	0.0663	1.5148	0.0022	0.0281	0.0005	0.0064	0.0023	0.0182	0.0004	33.45	9.9	0.0	0.008	0.003	90.8	26.7	0.2
0.10	65.0328	0.0613	1.8287	0.0038	0.0273	0.0005	0.0000	0.0022	0.0094	0.0004	40.39	12.0	0.0	0.000	0.002	95.7	25.6	0.2
0.20	42.8913	0.0504	1.1969	0.0025	0.0207	0.0005	0.0029	0.0024	0.0099	0.0003	26.43	7.8	0.0	0.005	0.004	93.1	25.1	0.2
0.30	39.6808	0.0395	1.1514	0.0025	0.0183	0.0005	0.0059	0.0022	0.0049	0.0003	25.43	7.5	0.0	0.010	0.004	96.3	25.0	0.2

0.40	27.2289	0.0405	0.8099	0.0022	0.0117	0.0004	0.0036	0.0024	0.0014	0.0003	17.89	5.3	0.1	0.009	0.006	98.5	24.9	0.2
0.50	22.2233	0.0326	0.6658	0.0019	0.0092	0.0005	0.0000	0.0023	0.0003	0.0003	14.70	4.4	0.0	0.000	0.007	99.5	25.0	0.3
0.60	16.7887	0.0171	0.5017	0.0014	0.0058	0.0005	0.0000	0.0023	0.0000	0.0003	11.08	3.3	0.0	0.000	0.009	100.0	25.1	0.3
0.70	16.4177	0.0190	0.4957	0.0024	0.0068	0.0005	0.0000	0.0022	0.0006	0.0003	10.95	3.2	0.0	0.000	0.009	98.9	24.6	0.4
0.80	16.3276	0.0180	0.4941	0.0029	0.0070	0.0005	0.0000	0.0022	0.0000	0.0003	10.92	3.2	0.0	0.000	0.009	100.0	25.1	0.4
0.90	28.5646	0.0405	0.8600	0.0031	0.0127	0.0004	0.0008	0.0025	0.0016	0.0003	19.00	5.6	0.0	0.002	0.006	98.3	24.6	0.3
1.00	51.0018	0.0494	1.4921	0.0025	0.0228	0.0006	0.0022	0.0024	0.0032	0.0003	32.96	9.8	0.0	0.003	0.003	98.1	25.2	0.2
1.20	89.6294	0.0713	2.5949	0.0033	0.0407	0.0005	0.0120	0.0024	0.0067	0.0003	57.31	17.0	0.0	0.009	0.002	97.8	25.4	0.1
1.50	17.1450	0.0190	0.5002	0.0016	0.0089	0.0005	0.0116	0.0024	0.0017	0.0003	11.05	3.3	0.2	0.046	0.009	97.1	25.0	0.3
1.80	9.8801	0.0643	0.2838	0.0013	0.0048	0.0004	0.0053	0.0024	0.0004	0.0003	6.27	1.9	0.3	0.037	0.017	98.7	25.8	0.6

GBD-57a - biotite

J(±1 S) = 0.000420 ± 0.000001

0.01	11.8410	0.0238	0.3350	0.0013	0.0074	0.0004	0.0000	0.0023	0.0115	0.0003	7.40	2.7	0.0	0.000	0.013	71.0	18.9	0.5
0.05	15.8362	0.0162	0.4926	0.0013	0.0073	0.0006	0.0103	0.0021	0.0089	0.0003	10.88	4.0	0.0	0.041	0.008	83.3	20.2	0.3
0.10	16.7403	0.0134	0.5438	0.0017	0.0084	0.0005	0.0000	0.0026	0.0067	0.0003	12.01	4.4	0.0	0.000	0.009	88.1	20.4	0.3
0.20	17.3048	0.0180	0.5774	0.0016	0.0075	0.0005	0.0002	0.0026	0.0040	0.0003	12.75	4.7	0.0	0.001	0.009	93.1	21.0	0.3
0.30	19.0032	0.0180	0.6387	0.0018	0.0087	0.0005	0.0000	0.0026	0.0057	0.0003	14.10	5.2	0.0	0.000	0.008	91.0	20.4	0.3
0.40	21.5840	0.0494	0.7357	0.0018	0.0092	0.0005	0.0000	0.0021	0.0060	0.0003	16.25	6.0	0.0	0.000	0.006	91.7	20.3	0.2
0.50	22.0734	0.0414	0.7530	0.0020	0.0097	0.0005	0.0022	0.0022	0.0065	0.0003	16.63	6.1	0.0	0.006	0.006	91.2	20.1	0.2
0.60	12.0564	0.0134	0.4103	0.0012	0.0044	0.0005	0.0011	0.0030	0.0021	0.0003	9.06	3.3	0.0	0.005	0.014	94.7	20.9	0.3
0.70	18.3099	0.0162	0.6214	0.0018	0.0098	0.0004	0.0018	0.0024	0.0053	0.0003	13.72	5.0	0.0	0.006	0.008	91.3	20.3	0.3
0.80	19.8132	0.0143	0.6639	0.0018	0.0085	0.0005	0.0000	0.0022	0.0060	0.0003	14.66	5.4	0.0	0.000	0.006	91.0	20.4	0.3
0.90	37.0489	0.0405	1.2282	0.0028	0.0181	0.0006	0.0000	0.0024	0.0116	0.0004	27.12	9.9	0.0	0.000	0.004	90.6	20.6	0.2
1.00	86.5214	0.0673	2.9453	0.0035	0.0452	0.0008	0.0000	0.0026	0.0236	0.0004	65.05	23.8	0.0	0.000	0.002	91.9	20.3	0.1
1.20	71.1600	0.0643	2.4149	0.0053	0.0343	0.0008	0.0244	0.0025	0.0184	0.0004	53.34	19.5	0.0	0.020	0.002	92.3	20.5	0.1

GBD-60b - biotite

J(±1 S) = 0.000420 ± 0.000001

0.01	52.1004	0.0543	1.3790	0.0030	0.0250	0.0006	0.0145	0.0023	0.0421	0.0004	30.46	10.7	0.0	0.021	0.003	75.9	21.6	0.2

0.05	44.3179	0.0543	1.3536	0.0026	0.0216	0.0006	0.0218	0.0022	0.0197	0.0003	29.89	10.5	0.0	0.032	0.003	86.7	21.4	0.2
0.10	40.9088	0.0494	1.2986	0.0036	0.0195	0.0005	0.0186	0.0025	0.0139	0.0003	28.68	10.1	0.0	0.028	0.004	89.9	21.3	0.2
0.20	17.7061	0.0180	0.5539	0.0013	0.0106	0.0004	0.0150	0.0023	0.0067	0.0003	12.24	4.3	0.1	0.053	0.008	88.7	21.4	0.3
0.30	26.1295	0.0424	0.8208	0.0032	0.0120	0.0005	0.0150	0.0027	0.0103	0.0003	18.13	6.4	0.0	0.036	0.006	88.3	21.2	0.3
0.40	14.2458	0.0162	0.4406	0.0022	0.0058	0.0006	0.0144	0.0023	0.0060	0.0003	9.73	3.4	0.1	0.064	0.010	87.4	21.3	0.4
0.50	27.0575	0.0365	0.8313	0.0021	0.0120	0.0005	0.0203	0.0025	0.0117	0.0004	18.36	6.5	0.0	0.048	0.006	87.1	21.3	0.2
0.60	14.5896	0.0257	0.4426	0.0023	0.0075	0.0005	0.0242	0.0028	0.0074	0.0003	9.78	3.4	0.1	0.107	0.012	84.8	21.1	0.4
0.70	29.9891	0.0444	0.8685	0.0018	0.0136	0.0005	0.0143	0.0023	0.0181	0.0004	19.18	6.8	0.0	0.032	0.005	82.0	21.3	0.2
0.80	47.0605	0.0524	1.3946	0.0047	0.0236	0.0006	0.0171	0.0024	0.0280	0.0004	30.80	10.9	0.0	0.024	0.003	82.2	20.9	0.2
0.90	43.0734	0.0553	1.3037	0.0026	0.0212	0.0006	0.0196	0.0026	0.0203	0.0004	28.79	10.2	0.0	0.029	0.004	85.9	21.4	0.2
1.00	48.1242	0.0474	1.4652	0.0023	0.0218	0.0006	0.0194	0.0023	0.0208	0.0004	32.36	11.4	0.0	0.026	0.003	87.1	21.5	0.2
1.20	26.4120	0.0663	0.6854	0.0028	0.0119	0.0005	0.0812	0.0042	0.0117	0.0004	15.14	5.3	0.2	0.232	0.012	86.8	25.2	0.4

GBD-63b - biotite

J(±1 S) = 0.000420 ± 0.000001

0.01	17.2641	0.0190	0.3957	0.0016	0.0103	0.0005	0.0082	0.0028	0.0261	0.0004	8.74	2.9	0.0	0.041	0.014	54.9	18.1	0.5
0.05	28.3521	0.0405	1.0446	0.0020	0.0131	0.0005	0.0000	0.0020	0.0037	0.0003	23.07	7.8	0.0	0.000	0.004	96.2	19.7	0.2
0.10	37.4424	0.0474	1.4188	0.0026	0.0194	0.0006	0.0068	0.0024	0.0039	0.0003	31.33	10.6	0.0	0.009	0.003	96.9	19.3	0.2
0.20	31.2547	0.0335	1.1759	0.0026	0.0151	0.0006	0.0017	0.0023	0.0009	0.0003	25.97	8.8	0.0	0.003	0.004	99.1	19.8	0.2
0.30	42.4126	0.0444	1.6030	0.0037	0.0213	0.0006	0.0032	0.0024	0.0011	0.0003	35.40	11.9	0.1	0.004	0.003	99.2	19.8	0.2
0.40	20.5543	0.0209	0.7815	0.0020	0.0085	0.0005	0.0000	0.0025	0.0003	0.0003	17.26	5.8	0.0	0.000	0.006	99.6	19.7	0.2
0.50	19.8621	0.0162	0.7527	0.0018	0.0085	0.0005	0.0000	0.0021	0.0000	0.0003	16.62	5.6	0.0	0.000	0.006	100.0	19.9	0.2
0.60	12.7748	0.0238	0.4769	0.0025	0.0051	0.0005	0.0004	0.0024	0.0007	0.0004	10.53	3.6	0.0	0.001	0.010	98.4	19.8	0.4
0.70	17.4267	0.0152	0.6582	0.0018	0.0089	0.0004	0.0112	0.0027	0.0007	0.0003	14.54	4.9	0.4	0.033	0.008	98.8	19.7	0.3
0.80	25.3024	0.0395	0.9664	0.0034	0.0128	0.0005	0.0029	0.0024	0.0009	0.0003	21.34	7.2	0.1	0.006	0.005	99.0	19.5	0.2
0.90	90.5296	0.0752	3.4342	0.0042	0.0443	0.0007	0.0063	0.0024	0.0017	0.0003	75.86	25.6	0.1	0.004	0.001	99.4	19.7	0.1
1.00	13.5338	0.1002	0.5032	0.0017	0.0065	0.0005	0.0300	0.0026	0.0001	0.0003	11.12	3.7	13.3	0.117	0.010	99.9	20.2	0.4
1.20	5.7817	0.0117	0.2113	0.0011	0.0025	0.0004	0.1918	0.0031	0.0004	0.0003	4.67	1.6	13.1	1.780	0.030	98.4	20.3	0.6

GBD-64c - biotite

J(±1 s) = 0.000416 ± 0.000002

0.01	56.6385	0.0524	1.2760	0.0021	0.0300	0.0006	0.0016	0.0022	0.0763	0.0005	28.18	10.4	0.0	0.002	0.003	59.8	19.8	0.3
0.05	96.4992	0.0683	3.4339	0.0056	0.0496	0.0008	0.0007	0.0026	0.0237	0.0004	75.83	28.1	0.0	0.000	0.001	92.7	19.4	0.2
0.10	45.4624	0.0543	1.6916	0.0050	0.0224	0.0006	0.0006	0.0024	0.0042	0.0003	37.35	13.8	0.0	0.001	0.003	97.3	19.5	0.2
0.20	15.2127	0.0180	0.5716	0.0042	0.0064	0.0004	0.0000	0.0024	0.0001	0.0003	12.62	4.7	0.0	0.000	0.008	99.9	19.8	0.4
0.30	27.8159	0.0414	1.0262	0.0032	0.0118	0.0005	0.0000	0.0024	0.0011	0.0003	22.66	8.4	0.0	0.000	0.005	98.8	20.0	0.3
0.40	16.1877	0.0143	0.5936	0.0016	0.0063	0.0006	0.0000	0.0021	0.0019	0.0003	13.11	4.9	0.0	0.000	0.007	96.5	19.7	0.3
0.50	24.7771	0.0414	0.9073	0.0023	0.0114	0.0004	0.0000	0.0023	0.0012	0.0003	20.04	7.4	0.0	0.000	0.005	98.5	20.1	0.3
0.60	14.7220	0.0143	0.5399	0.0017	0.0076	0.0004	0.0040	0.0023	0.0027	0.0003	11.92	4.4	0.0	0.014	0.008	94.6	19.3	0.3
0.70	17.0333	0.0199	0.6315	0.0018	0.0088	0.0005	0.0000	0.0023	0.0021	0.0003	13.95	5.2	0.0	0.000	0.007	96.3	19.4	0.3
0.80	18.5651	0.0152	0.6837	0.0017	0.0083	0.0004	0.0000	0.0021	0.0013	0.0003	15.10	5.6	0.0	0.000	0.006	98.0	19.9	0.3
0.90	15.1655	0.0171	0.5614	0.0021	0.0073	0.0004	0.0000	0.0025	0.0014	0.0003	12.40	4.6	0.0	0.000	0.009	97.3	19.6	0.3
1.00	5.1632	0.0114	0.1858	0.0009	0.0031	0.0004	0.0000	0.0025	0.0006	0.0003	4.10	1.5	0.0	0.000	0.027	96.8	20.1	0.7
1.20	3.1564	0.0101	0.1129	0.0007	0.0024	0.0004	0.0008	0.0027	0.0002	0.0003	2.49	0.9	0.1	0.013	0.047	98.6	20.6	1.2

GBD-64d - biotite

J(±1 s) = 0.000416 ± 0.000002

0.01	7.9216	0.0134	0.1989	0.0009	0.0054	0.0004	0.0059	0.0021	0.0099	0.0003	4.39	1.2	0.0	0.058	0.021	62.9	18.7	0.8
0.05	20.0413	0.0152	0.7105	0.0018	0.0105	0.0005	0.0052	0.0024	0.0052	0.0003	15.69	4.4	0.0	0.014	0.007	92.3	19.4	0.3
0.10	34.0306	0.0504	1.2609	0.0024	0.0166	0.0005	0.0000	0.0021	0.0006	0.0003	27.85	7.8	0.0	0.000	0.003	99.5	20.0	0.2
0.20	29.2952	0.0533	1.0998	0.0021	0.0145	0.0006	0.0000	0.0026	0.0004	0.0003	24.29	6.8	0.0	0.000	0.005	99.6	19.8	0.3
0.30	36.2438	0.0434	1.3564	0.0027	0.0180	0.0004	0.0010	0.0024	0.0001	0.0003	29.96	8.4	0.2	0.001	0.003	99.9	19.9	0.2
0.40	32.2352	0.0444	1.2153	0.0020	0.0172	0.0005	0.0023	0.0023	0.0006	0.0003	26.84	7.6	0.1	0.004	0.004	99.4	19.7	0.2
0.50	26.2665	0.0385	0.9833	0.0026	0.0126	0.0005	0.0000	0.0025	0.0002	0.0003	21.72	6.1	0.0	0.000	0.005	99.7	19.9	0.3
0.60	21.5229	0.0277	0.7991	0.0018	0.0097	0.0005	0.0045	0.0024	0.0004	0.0003	17.65	5.0	0.3	0.011	0.006	99.4	20.0	0.3
0.70	18.9912	0.0143	0.7090	0.0018	0.0086	0.0005	0.0056	0.0025	0.0000	0.0003	15.65	4.4	0.0	0.016	0.007	100.0	20.0	0.3
0.80	24.9025	0.0385	0.9295	0.0021	0.0100	0.0005	0.0000	0.0024	0.0003	0.0004	20.52	5.8	0.0	0.000	0.005	99.7	19.9	0.3
0.90	43.0479	0.0385	1.6133	0.0030	0.0215	0.0006	0.0033	0.0025	0.0005	0.0003	35.62	10.0	0.2	0.004	0.003	99.7	19.9	0.2
1.00	62.2537	0.0474	2.3385	0.0041	0.0303	0.0006	0.0043	0.0025	0.0004	0.0003	51.64	14.5	0.3	0.004	0.002	99.8	19.8	0.2
1.20	57.9173	0.0543	2.1708	0.0031	0.0277	0.0006	0.0357	0.0028	0.0002	0.0003	47.93	13.5	3.7	0.032	0.003	99.9	19.9	0.2
1.50	18.9328	0.0180	0.6997	0.0018	0.0101	0.0005	0.0852	0.0031	0.0005	0.0003	15.45	4.4	4.4	0.239	0.009	99.3	20.1	0.3

GBD-79c - biotite

J(±1 S) = 0.000416 ± 0.000002

0.05	69.4175	0.1002	1.0578	0.0022	0.0425	0.0006	0.0017	0.0022	0.1564	0.0007	23.36	6.4	0.0	0.003	0.004	32.7	16.0	0.4
0.10	24.8897	0.0395	0.6196	0.0019	0.0124	0.0005	0.0000	0.0024	0.0259	0.0004	13.68	3.8	0.0	0.000	0.008	69.0	20.7	0.4
0.20	68.9885	0.0663	2.0210	0.0034	0.0298	0.0006	0.0103	0.0027	0.0260	0.0004	44.63	12.3	0.0	0.010	0.003	88.7	22.6	0.3
0.30	71.7180	0.0633	2.2053	0.0042	0.0309	0.0007	0.0000	0.0024	0.0126	0.0004	48.71	13.4	0.0	0.000	0.002	94.8	23.0	0.3
0.40	48.4378	0.0524	1.5024	0.0052	0.0207	0.0006	0.0055	0.0023	0.0111	0.0004	33.19	9.1	0.0	0.007	0.003	93.1	22.4	0.3
0.50	49.2493	0.0504	1.4870	0.0030	0.0218	0.0006	0.0087	0.0030	0.0134	0.0003	32.84	9.0	0.0	0.012	0.004	91.9	22.7	0.3
0.60	34.0128	0.0444	1.0249	0.0019	0.0152	0.0006	0.0051	0.0023	0.0099	0.0003	22.64	6.2	0.0	0.010	0.004	91.4	22.6	0.3
0.70	58.0864	0.0524	1.7449	0.0034	0.0268	0.0005	0.0109	0.0023	0.0160	0.0003	38.53	10.6	0.0	0.012	0.003	91.8	22.8	0.3
0.80	48.4876	0.0444	1.4709	0.0033	0.0214	0.0007	0.0016	0.0024	0.0117	0.0003	32.49	9.0	0.0	0.002	0.003	92.8	22.8	0.3
0.90	28.0451	0.0375	0.8631	0.0019	0.0115	0.0005	0.0000	0.0026	0.0062	0.0003	19.06	5.3	0.0	0.000	0.006	93.5	22.7	0.3
1.00	35.9615	0.0424	1.1217	0.0023	0.0155	0.0006	0.0020	0.0024	0.0064	0.0003	24.77	6.8	0.0	0.004	0.004	94.7	22.6	0.3
1.20	42.1268	0.0424	1.3148	0.0037	0.0170	0.0005	0.0050	0.0026	0.0062	0.0003	29.04	8.0	0.0	0.008	0.004	95.6	22.8	0.3

GBD-90b - biotite

J(±1 S) = 0.000416 ± 0.000002

0.05	34.8751	0.0454	0.3137	0.0011	0.0197	0.0005	0.0000	0.0028	0.0862	0.0005	6.93	1.9	0.0	0.000	0.018	26.2	21.7	0.8
0.10	21.4704	0.0228	0.6421	0.0020	0.0091	0.0005	0.0000	0.0025	0.0083	0.0003	14.19	3.9	0.0	0.000	0.008	88.4	22.1	0.3
0.20	65.8137	0.0533	2.2069	0.0040	0.0314	0.0005	0.0000	0.0023	0.0054	0.0003	48.77	13.5	0.0	0.000	0.002	97.6	21.7	0.2
0.30	81.8705	0.0673	2.8135	0.0038	0.0384	0.0007	0.0000	0.0024	0.0025	0.0003	62.17	17.2	0.0	0.000	0.002	99.1	21.5	0.2
0.40	40.2895	0.0395	1.3879	0.0033	0.0159	0.0005	0.0001	0.0027	0.0000	0.0003	30.66	8.5	0.1	0.000	0.004	100.0	21.7	0.3
0.50	35.9440	0.0484	1.2374	0.0034	0.0169	0.0005	0.0000	0.0023	0.0010	0.0003	27.34	7.6	0.0	0.000	0.004	99.2	21.5	0.3
0.60	27.8333	0.0375	0.9653	0.0024	0.0117	0.0005	0.0000	0.0027	0.0000	0.0003	21.32	5.9	9.7	0.000	0.006	100.0	21.5	0.3
0.70	41.5563	0.0474	1.4368	0.0028	0.0188	0.0006	0.0000	0.0029	0.0006	0.0003	31.74	8.8	0.0	0.000	0.004	99.5	21.5	0.2
0.80	62.2053	0.0992	2.1449	0.0030	0.0281	0.0005	0.0101	0.0038	0.0012	0.0003	47.39	13.1	0.2	0.009	0.003	99.4	21.5	0.2
0.90	34.9027	0.0792	1.2057	0.0026	0.0167	0.0005	0.0019	0.0029	0.0015	0.0003	26.63	7.4	0.0	0.003	0.005	98.7	21.3	0.3
1.00	34.0022	0.0474	1.1702	0.0030	0.0159	0.0004	0.0000	0.0027	0.0010	0.0003	25.85	7.1	0.0	0.000	0.005	99.1	21.5	0.3
1.20	19.8118	0.0335	0.6857	0.0030	0.0100	0.0004	0.0000	0.0029	0.0014	0.0003	15.15	4.2	0.0	0.000	0.008	97.9	21.1	0.3
1.50	4.5607	0.0125	0.1619	0.0015	0.0009	0.0004	0.0019	0.0029	0.0001	0.0003	3.58	1.0	0.3	0.023	0.035	99.1	20.8	0.9

GBD-100b - biotite

J(±1 S) = 0.000414 ± 0.000002

0.05	48.4221	0.0514	1.1536	0.0022	0.0258	0.0005	0.0000	0.0029	0.0541	0.0004	25.49	7.3	0.0	0.000	0.005	66.6	20.8	0.3
0.10	48.7143	0.0633	1.0687	0.0020	0.0248	0.0004	0.0001	0.0027	0.0597	0.0005	23.61	6.8	0.0	0.000	0.005	63.4	21.4	0.3
0.20	81.6384	0.1202	2.7533	0.0032	0.0403	0.0006	0.0015	0.0032	0.0163	0.0003	60.84	17.4	0.0	0.001	0.002	94.0	20.7	0.2
0.30	62.6430	0.0563	2.2081	0.0052	0.0268	0.0005	0.0000	0.0034	0.0024	0.0003	48.79	14.0	0.0	0.000	0.003	98.9	20.8	0.2
0.40	42.1173	0.0653	1.4765	0.0036	0.0214	0.0005	0.0003	0.0024	0.0032	0.0003	32.62	9.4	0.0	0.000	0.003	97.7	20.7	0.2
0.50	52.8278	0.0494	1.8152	0.0043	0.0254	0.0005	0.0002	0.0030	0.0046	0.0003	40.11	11.5	0.0	0.000	0.003	97.4	21.0	0.2
0.60	36.8261	0.0464	1.2763	0.0027	0.0181	0.0006	0.0018	0.0028	0.0034	0.0003	28.20	8.1	0.0	0.003	0.004	97.2	20.8	0.2
0.70	40.4503	0.0494	1.3877	0.0026	0.0197	0.0005	0.0002	0.0030	0.0027	0.0003	30.66	8.8	0.0	0.000	0.004	98.0	21.2	0.2
0.80	33.8104	0.0414	1.1172	0.0038	0.0152	0.0005	0.0005	0.0028	0.0026	0.0004	24.68	7.1	0.0	0.001	0.005	97.8	21.9	0.3
0.90	29.3042	0.0414	1.0011	0.0020	0.0133	0.0005	0.0004	0.0027	0.0012	0.0003	22.12	6.3	0.0	0.001	0.005	98.8	21.5	0.2
1.00	15.3889	0.0385	0.5323	0.0014	0.0073	0.0004	0.0007	0.0028	0.0019	0.0003	11.76	3.4	0.0	0.003	0.010	96.4	20.7	0.3

GBD-51b - biotite

J(±1 S) = 0.000414 ± 0.000002

0.05	80.2594	0.0653	1.3428	0.0026	0.0366	0.0006	0.0005	0.0027	0.0835	0.0005	29.66	7.9	0.0	0.001	0.004	69.0	30.5	0.3
0.10	50.4107	0.0922	1.2437	0.0023	0.0220	0.0006	0.0000	0.0029	0.0144	0.0003	27.47	7.3	0.0	0.000	0.005	91.5	27.5	0.3
0.20	88.8247	0.0573	2.3338	0.0040	0.0388	0.0007	0.0000	0.0027	0.0110	0.0004	51.55	13.7	0.0	0.000	0.002	96.3	27.2	0.2
0.30	95.4465	0.0713	2.6698	0.0035	0.0420	0.0007	0.0000	0.0027	0.0051	0.0003	58.97	15.6	0.0	0.000	0.002	98.4	26.1	0.2
0.40	56.2825	0.0494	1.5931	0.0026	0.0248	0.0006	0.0000	0.0031	0.0029	0.0003	35.19	9.3	0.0	0.000	0.004	98.4	25.8	0.2
0.50	45.0619	0.0434	1.2758	0.0038	0.0198	0.0004	0.0015	0.0028	0.0025	0.0003	28.18	7.5	0.0	0.002	0.004	98.4	25.7	0.3
0.60	45.6740	0.0484	1.2975	0.0023	0.0212	0.0005	0.0000	0.0025	0.0021	0.0003	28.66	7.6	0.0	0.000	0.004	98.6	25.7	0.2
0.70	45.3506	0.0434	1.2773	0.0023	0.0198	0.0005	0.0051	0.0030	0.0022	0.0003	28.21	7.5	0.1	0.008	0.005	98.5	25.9	0.2
0.80	43.1823	0.0424	1.1955	0.0018	0.0181	0.0005	0.0000	0.0027	0.0035	0.0003	26.41	7.0	0.0	0.000	0.005	97.6	26.1	0.2
0.90	26.4413	0.0385	0.7309	0.0032	0.0108	0.0005	0.0000	0.0026	0.0025	0.0003	16.15	4.3	0.0	0.000	0.007	97.2	26.0	0.4
1.00	22.2489	0.0405	0.6187	0.0027	0.0083	0.0005	0.0000	0.0027	0.0018	0.0003	13.67	3.6	0.0	0.000	0.009	97.6	26.0	0.4
1.20	11.4990	0.0553	0.3112	0.0020	0.0044	0.0004	0.0006	0.0028	0.0008	0.0003	6.87	1.8	0.0	0.004	0.018	97.9	26.8	0.6
1.50	24.0922	0.0375	0.6790	0.0017	0.0099	0.0005	0.0000	0.0031	0.0017	0.0003	15.00	4.0	0.0	0.000	0.009	97.9	25.7	0.3

1.80	5.0494	0.0117	0.1439	0.0008	0.0015	0.0004	0.0003	0.0028	0.0000	0.0002	3.18	0.8	0.3	0.004	0.038	99.8	26.0	0.8
2.00	12.5876	0.0316	0.3512	0.0014	0.0054	0.0004	0.0000	0.0030	0.0005	0.0003	7.76	2.1	0.0	0.000	0.017	98.9	26.3	0.5

GBD-34 - biotite

J(±1 S) = 0.000414 ± 0.000002

0.20	25.6234	0.0375	0.7263	0.0026	0.0111	0.0006	0.0000	0.0028	0.0112	0.0004	16.05	2.0	0.0	0.000	0.008	87.0	22.8	0.3
0.30	70.7752	0.0653	2.2475	0.0052	0.0315	0.0006	0.0032	0.0029	0.0059	0.0003	49.65	6.2	0.0	0.003	0.003	97.5	22.8	0.2
0.40	100.5449	0.0752	3.2609	0.0067	0.0450	0.0006	0.0040	0.0027	0.0023	0.0003	72.04	9.0	0.0	0.002	0.002	99.3	22.7	0.2
0.50	131.1617	0.0922	4.2090	0.0084	0.0575	0.0007	0.0034	0.0031	0.0040	0.0003	92.98	11.7	0.0	0.002	0.001	99.1	22.9	0.2
0.60	81.4183	0.0982	2.6284	0.0063	0.0332	0.0007	0.0007	0.0029	0.0008	0.0003	58.06	7.3	0.0	0.001	0.002	99.7	22.9	0.2
0.70	83.5427	0.0573	2.6871	0.0052	0.0344	0.0005	0.0000	0.0032	0.0011	0.0004	59.36	7.5	0.0	0.000	0.002	99.6	23.0	0.2
0.80	66.9374	0.0733	2.1651	0.0048	0.0292	0.0005	0.0007	0.0030	0.0001	0.0003	47.83	6.0	0.1	0.001	0.003	99.9	22.9	0.2
0.90	60.9209	0.0583	1.9510	0.0045	0.0280	0.0005	0.0123	0.0026	0.0023	0.0003	43.10	5.4	0.1	0.012	0.003	98.9	22.9	0.2
1.00	73.9734	0.0653	2.3713	0.0055	0.0315	0.0007	0.0073	0.0030	0.0018	0.0003	52.39	6.6	0.1	0.006	0.003	99.3	23.0	0.2
1.20	98.7240	0.0683	3.1679	0.0054	0.0427	0.0005	0.0163	0.0031	0.0027	0.0004	69.95	8.8	0.1	0.010	0.002	99.2	22.9	0.2
1.50	196.5530	0.1002	6.2870	0.0084	0.0833	0.0008	0.0298	0.0031	0.0026	0.0004	138.82	17.4	0.3	0.009	0.001	99.6	23.1	0.2
1.80	105.3612	0.0802	3.3762	0.0066	0.0459	0.0007	0.0697	0.0026	0.0021	0.0003	74.56	9.4	0.8	0.040	0.002	99.4	23.0	0.2
2.00	30.6259	0.0504	0.9756	0.0025	0.0135	0.0004	0.1153	0.0033	0.0001	0.0003	21.54	2.7	36.6	0.232	0.007	100.0	23.3	0.3

GBD-33 - biotite

J(±1 S) = 0.000414 ± 0.000002

0.10	27.7087	0.0433	0.3032	0.0013	0.0152	0.0006	0.0108	0.0035	0.0627	0.0005	6.70	1.1	0.0	0.070	0.023	32.5	22.0	0.9
0.20	18.7311	0.0187	0.2849	0.0015	0.0121	0.0007	0.0029	0.0037	0.0351	0.0005	6.29	1.0	0.0	0.020	0.026	44.1	21.5	0.8
0.30	63.3712	0.0503	1.5831	0.0033	0.0323	0.0007	0.0000	0.0038	0.0538	0.0005	34.96	5.7	0.0	0.000	0.005	74.7	22.2	0.2
0.40	105.5884	0.0732	3.3450	0.0042	0.0548	0.0008	0.0013	0.0037	0.0217	0.0004	73.88	12.1	0.0	0.001	0.002	93.9	22.0	0.2
0.50	121.6514	0.0871	4.0337	0.0079	0.0593	0.0008	0.0023	0.0038	0.0078	0.0004	89.09	14.6	0.0	0.001	0.002	98.1	21.9	0.2
0.60	95.8084	0.0672	3.1788	0.0039	0.0467	0.0007	0.0000	0.0036	0.0046	0.0004	70.21	11.5	0.0	0.000	0.002	98.6	22.0	0.2
0.70	76.9192	0.0743	2.5993	0.0063	0.0368	0.0007	0.0190	0.0038	0.0036	0.0004	57.23	9.4	0.1	0.014	0.003	98.6	21.7	0.2
0.80	77.3556	0.0644	2.5482	0.0036	0.0383	0.0007	0.0155	0.0038	0.0052	0.0004	56.10	9.2	0.1	0.012	0.003	98.0	22.1	0.2
0.90	68.5287	0.0683	2.2636	0.0033	0.0329	0.0006	0.0136	0.0039	0.0045	0.0004	49.84	8.2	0.1	0.012	0.003	98.1	22.0	0.2

1.00	77.4572	0.0495	2.5570	0.0031	0.0371	0.0008	0.0111	0.0036	0.0059	0.0004	56.30	9.3	0.0	0.008	0.003	97.7	22.0	0.2
1.20	60.6738	0.0564	2.0165	0.0052	0.0270	0.0007	0.0057	0.0038	0.0037	0.0004	44.39	7.3	0.0	0.006	0.004	98.2	21.9	0.2
1.50	64.2495	0.0962	2.1089	0.0038	0.0299	0.0006	0.0194	0.0035	0.0067	0.0004	46.42	7.6	0.1	0.018	0.003	96.9	21.9	0.2
1.80	17.8303	0.0202	0.5964	0.0020	0.0072	0.0005	0.0042	0.0036	0.0023	0.0004	13.13	2.2	0.0	0.014	0.012	96.1	21.3	0.4
2.00	5.7266	0.0183	0.2047	0.0011	0.0016	0.0005	0.0163	0.0035	0.0001	0.0004	4.51	0.7	4.4	0.156	0.033	99.5	20.7	0.8

GBD-5c - muscovite

J(±1 S) = 0.000423 ± 0.000001

0.10	33.7943	0.0522	0.9535	0.0033	0.0151	0.0007	0.0000	0.0027	0.0219	0.0004	21.05	9.7	0.0	0.000	0.006	80.6	21.7	0.3
0.20	76.6561	0.0692	2.7185	0.0060	0.0380	0.0008	0.0000	0.0029	0.0036	0.0004	60.03	27.7	0.0	0.000	0.002	98.6	21.1	0.1
0.30	79.6893	0.0761	2.8816	0.0062	0.0395	0.0007	0.0152	0.0029	0.0048	0.0004	63.64	29.3	0.1	0.010	0.002	98.2	20.6	0.1
0.40	34.8004	0.0522	1.2665	0.0036	0.0154	0.0006	0.0005	0.0031	0.0004	0.0004	27.97	12.9	0.0	0.001	0.005	99.6	20.8	0.2
0.50	22.9870	0.1101	0.8380	0.0041	0.0096	0.0006	0.0000	0.0030	0.0000	0.0004	18.51	8.5	0.0	0.000	0.007	100.0	20.8	0.4
0.60	10.7875	0.0931	0.3759	0.0026	0.0062	0.0006	0.0058	0.0030	0.0024	0.0004	8.30	3.8	0.1	0.030	0.016	93.4	20.3	0.6
0.70	7.2313	0.0323	0.2528	0.0016	0.0053	0.0006	0.0080	0.0027	0.0008	0.0004	5.58	2.6	0.2	0.062	0.021	96.7	21.0	0.7
0.80	3.3754	0.0102	0.1199	0.0014	0.0021	0.0006	0.0001	0.0027	0.0006	0.0004	2.65	1.2	0.0	0.001	0.044	94.9	20.3	1.5
0.90	6.2539	0.0254	0.2223	0.0017	0.0034	0.0006	0.0055	0.0032	0.0005	0.0004	4.91	2.3	0.3	0.048	0.028	97.7	20.9	0.8

GBD-26c - muscovite

J(±1 S) = 0.000423 ± 0.000001

0.10	35.3202	0.0535	1.2359	0.0035	0.0176	0.0006	0.0153	0.0037	0.0075	0.0004	27.21	12.7	0.0	0.024	0.006	93.6	20.3	0.2
0.20	115.0248	0.0933	3.8735	0.0065	0.0584	0.0009	0.0199	0.0034	0.0308	0.0006	85.26	39.9	0.0	0.010	0.002	92.0	20.7	0.1
0.30	84.1143	0.0624	2.9982	0.0060	0.0400	0.0008	0.0572	0.0037	0.0078	0.0004	66.00	30.9	0.2	0.037	0.002	97.3	20.7	0.1
0.40	9.2888	0.0309	0.3195	0.0021	0.0048	0.0005	0.0213	0.0035	0.0024	0.0004	7.03	3.3	0.2	0.131	0.022	92.3	20.4	0.6
0.50	5.3919	0.0123	0.1772	0.0017	0.0020	0.0005	0.0296	0.0039	0.0022	0.0004	3.90	1.8	0.3	0.328	0.043	87.9	20.3	1.0
0.60	16.1915	0.0241	0.5883	0.0028	0.0069	0.0006	0.0864	0.0036	0.0014	0.0004	12.95	6.1	1.5	0.288	0.012	97.4	20.4	0.4
0.70	7.8871	0.0149	0.2820	0.0023	0.0041	0.0005	0.0228	0.0033	0.0006	0.0003	6.21	2.9	0.9	0.159	0.023	97.8	20.8	0.7
0.80	6.4968	0.0132	0.2349	0.0020	0.0031	0.0005	0.0153	0.0052	0.0006	0.0004	5.17	2.4	0.6	0.128	0.044	97.2	20.4	0.8

GBD-36b - muscovite

J(±1 S) = 0.000423 ± 0.000001

0.05	55.9583	0.0553	1.2293	0.0042	0.0314	0.0006	0.0327	0.0108	0.0705	0.0005	27.09	6.6	0.0	0.052	0.017	62.4	21.6	0.3
0.10	86.9421	0.0592	3.1558	0.0066	0.0434	0.0007	0.0000	0.0108	0.0022	0.0004	69.55	16.8	0.0	0.000	0.007	99.2	20.8	0.1
0.20	78.5547	0.0573	2.8314	0.0049	0.0394	0.0006	0.0374	0.0126	0.0031	0.0003	62.40	15.1	0.3	0.026	0.009	98.8	20.8	0.1
0.30	149.0137	0.0882	5.4106	0.0078	0.0743	0.0008	0.0346	0.0108	0.0047	0.0004	119.23	28.8	0.2	0.013	0.004	99.1	20.7	0.1
0.40	50.8951	0.0533	1.8630	0.0045	0.0254	0.0005	0.0146	0.0112	0.0013	0.0004	41.05	9.9	0.3	0.015	0.012	99.3	20.6	0.2
0.50	9.2424	0.0140	0.3308	0.0021	0.0048	0.0004	0.0300	0.0109	0.0008	0.0003	7.29	1.8	0.9	0.178	0.065	97.4	20.7	0.5
0.60	4.3270	0.0131	0.1583	0.0010	0.0017	0.0005	0.0236	0.0105	0.0000	0.0003	3.49	0.8	13.7	0.292	0.130	99.7	20.7	1.0
0.70	4.6508	0.0140	0.1664	0.0011	0.0028	0.0004	0.0233	0.0106	0.0000	0.0003	3.67	0.9	38.0	0.275	0.125	99.9	21.2	0.9
0.80	6.5854	0.0207	0.2357	0.0016	0.0043	0.0005	0.0258	0.0110	0.0000	0.0003	5.20	1.3	16.6	0.214	0.092	99.9	21.2	0.7
0.90	6.7142	0.0111	0.2440	0.0017	0.0025	0.0004	0.0211	0.0110	0.0003	0.0004	5.38	1.3	2.0	0.169	0.089	98.9	20.7	0.8
1.00	21.3973	0.0523	0.7709	0.0018	0.0106	0.0005	0.0117	0.0109	0.0003	0.0004	17.00	4.1	0.9	0.030	0.028	99.5	21.0	0.3
1.00	26.5007	0.0433	0.9660	0.0033	0.0131	0.0005	0.0402	0.0112	0.0003	0.0003	21.29	5.1	3.7	0.082	0.023	99.7	20.8	0.2
1.50	38.7367	0.0423	1.4032	0.0031	0.0194	0.0005	0.0167	0.0106	0.0000	0.0003	30.93	7.5	13.2	0.023	0.015	100.0	21.0	0.2

GBD-52b - muscovite

J(±1 S) = 0.000420 ± 0.000001

0.10	26.7943	0.0355	0.6873	0.0025	0.0128	0.0005	0.0000	0.0029	0.0201	0.0003	15.11	5.4	0.0	0.000	0.008	77.6	22.8	0.3
0.20	84.0230	0.0603	2.6069	0.0056	0.0381	0.0005	0.0000	0.0029	0.0219	0.0004	57.34	20.4	0.0	0.000	0.002	92.2	22.4	0.2
0.30	99.9334	0.0713	3.4761	0.0061	0.0461	0.0008	0.0098	0.0050	0.0044	0.0003	76.46	27.2	0.1	0.006	0.003	98.7	21.4	0.1
0.40	48.2436	0.0514	1.6710	0.0044	0.0234	0.0005	0.0000	0.0029	0.0026	0.0003	36.76	13.1	0.0	0.000	0.003	98.4	21.4	0.2
0.50	15.7934	0.0257	0.5514	0.0022	0.0066	0.0004	0.0000	0.0024	0.0007	0.0003	12.13	4.3	0.0	0.000	0.009	98.7	21.3	0.3
0.60	8.5449	0.0209	0.2975	0.0024	0.0041	0.0004	0.0000	0.0026	0.0005	0.0003	6.55	2.3	0.0	0.000	0.017	98.3	21.3	0.5
0.70	7.9383	0.0143	0.2707	0.0020	0.0034	0.0004	0.0000	0.0031	0.0002	0.0003	5.96	2.1	0.0	0.000	0.022	99.4	21.9	0.5
0.80	19.3950	0.0267	0.6727	0.0027	0.0096	0.0005	0.0014	0.0033	0.0003	0.0003	14.80	5.3	0.1	0.004	0.010	99.5	21.6	0.3
0.90	46.9360	0.0375	1.6346	0.0041	0.0216	0.0006	0.0000	0.0029	0.0018	0.0003	35.98	12.8	0.0	0.000	0.004	98.9	21.4	0.2
1.00	26.5778	0.0414	0.9059	0.0030	0.0108	0.0004	0.0000	0.0028	0.0000	0.0003	19.94	7.1	0.0	0.000	0.006	99.9	22.1	0.2

GBD-57a - muscovite

J(±1 S) = 0.000420 ± 0.000001

0.01	4.2646	0.0112	0.1052	0.0008	0.0018	0.0003	0.0000	0.0028	0.0042	0.0003	2.32	1.7	0.0	0.000	0.053	71.0	21.7	1.2
0.01	1.9540	0.0095	0.0611	0.0006	0.0000	0.0003	0.0031	0.0032	0.0001	0.0003	1.34	1.0	1.3	0.101	0.103	99.1	23.8	2.0
0.05	2.1716	0.0125	0.0701	0.0008	0.0000	0.0004	0.0046	0.0030	0.0009	0.0003	1.54	1.2	0.1	0.128	0.085	87.2	20.3	1.8
0.10	0.2093	0.0078	0.0065	0.0004	0.0004	0.0004	0.0028	0.0030	0.0007	0.0002	0.14	0.1	0.1	0.839	0.904	5.8	1.4	17.4
0.20	3.9765	0.0113	0.1284	0.0009	0.0019	0.0004	0.0028	0.0029	0.0019	0.0003	2.83	2.1	0.0	0.042	0.044	85.8	20.0	1.0
0.30	5.3796	0.0107	0.1774	0.0009	0.0024	0.0004	0.0089	0.0028	0.0026	0.0003	3.90	2.9	0.1	0.098	0.031	85.6	19.6	0.7
0.40	18.5191	0.0180	0.6446	0.0020	0.0086	0.0004	0.0000	0.0031	0.0016	0.0003	14.18	10.7	0.0	0.000	0.010	97.4	21.1	0.2
0.50	11.4747	0.0238	0.3924	0.0013	0.0053	0.0004	0.0000	0.0031	0.0017	0.0003	8.63	6.5	0.0	0.000	0.015	95.5	21.0	0.4
0.60	10.5139	0.0218	0.3700	0.0021	0.0051	0.0003	0.0000	0.0027	0.0016	0.0002	8.14	6.1	0.0	0.000	0.014	95.4	20.4	0.4
0.70	23.2043	0.0375	0.8369	0.0029	0.0112	0.0004	0.0000	0.0031	0.0020	0.0003	18.42	13.8	0.0	0.000	0.007	97.5	20.4	0.2
0.80	12.5138	0.0238	0.4553	0.0012	0.0066	0.0004	0.0093	0.0028	0.0014	0.0003	10.02	7.5	0.2	0.040	0.012	96.7	20.0	0.3
0.90	12.3736	0.0209	0.4495	0.0020	0.0055	0.0004	0.0000	0.0032	0.0010	0.0002	9.89	7.4	0.0	0.000	0.014	97.7	20.2	0.3
1.00	13.4395	0.0218	0.4849	0.0027	0.0065	0.0005	0.0014	0.0028	0.0021	0.0003	10.67	8.0	0.0	0.006	0.012	95.5	19.9	0.4
1.25	11.1033	0.0134	0.4045	0.0021	0.0045	0.0004	0.0000	0.0031	0.0011	0.0002	8.90	6.7	0.0	0.000	0.015	96.9	20.0	0.4
1.50	13.1043	0.0134	0.4679	0.0017	0.0068	0.0004	0.0005	0.0029	0.0012	0.0003	10.30	7.7	0.0	0.002	0.012	97.3	20.5	0.3
1.75	15.1592	0.0375	0.5443	0.0017	0.0066	0.0004	0.0021	0.0031	0.0000	0.0003	11.98	9.0	0.0	0.008	0.011	100.0	21.0	0.3
2.00	14.1502	0.0162	0.4441	0.0013	0.0059	0.0004	0.0103	0.0030	0.0011	0.0002	9.77	7.3	0.2	0.045	0.013	97.7	23.4	0.3

GBD-60b - muscovite

J(±1 S) = 0.000420 ± 0.000001

0.05	2.4361	0.0112	0.0762	0.0009	0.0005	0.0004	0.0305	0.0078	0.0004	0.0003	1.68	1.3	1.7	0.785	0.200	94.8	22.8	2.0
0.10	2.7574	0.0106	0.0869	0.0009	0.0018	0.0004	0.0448	0.0075	0.0020	0.0003	1.92	1.5	0.6	1.011	0.170	78.6	18.8	1.7
0.20	5.8341	0.0152	0.1782	0.0010	0.0021	0.0004	0.0261	0.0076	0.0025	0.0003	3.93	3.0	0.3	0.287	0.084	87.0	21.5	0.9
0.30	4.8401	0.0114	0.1553	0.0010	0.0018	0.0004	0.0309	0.0076	0.0010	0.0003	3.42	2.6	0.8	0.390	0.097	93.9	22.0	1.0
0.40	12.0930	0.0247	0.4064	0.0017	0.0055	0.0004	0.0157	0.0078	0.0015	0.0003	8.96	6.9	0.3	0.076	0.038	96.3	21.6	0.4
0.50	12.8823	0.0237	0.4346	0.0015	0.0054	0.0005	0.0001	0.0082	0.0011	0.0003	9.58	7.4	0.0	0.001	0.037	97.4	21.7	0.4
0.60	11.7429	0.0189	0.3920	0.0014	0.0039	0.0004	0.0246	0.0075	0.0019	0.0003	8.64	6.6	0.3	0.123	0.038	95.3	21.5	0.4
0.70	14.7076	0.0228	0.5078	0.0013	0.0068	0.0005	0.0209	0.0077	0.0017	0.0003	11.19	8.6	0.3	0.081	0.030	96.6	21.1	0.3
0.80	19.0160	0.0152	0.6491	0.0017	0.0099	0.0005	0.0225	0.0082	0.0031	0.0003	14.31	11.0	0.2	0.068	0.025	95.1	21.0	0.3
0.90	36.4431	0.0573	1.2175	0.0027	0.0183	0.0005	0.0967	0.0082	0.0058	0.0003	26.83	20.6	0.4	0.156	0.013	95.2	21.5	0.2

1.00	19.6207	0.0228	0.5979	0.0016	0.0077	0.0005	0.0317	0.0073	0.0024	0.0003	13.17	10.1	0.3	0.104	0.024	96.3	23.8	0.3
1.50	50.5387	0.0563	1.1974	0.0025	0.0170	0.0005	0.2120	0.0091	0.0082	0.0004	26.38	20.3	0.6	0.347	0.015	95.2	30.2	0.2

GBD-63b - muscovite

J(±1 S) = 0.000420 ± 0.000001

0.10	11.3759	0.0171	0.1038	0.0008	0.0066	0.0004	0.0000	0.0034	0.0287	0.0003	2.28	0.8	0.0	0.000	0.065	24.6	20.3	1.5
0.20	43.3651	0.0385	1.5015	0.0027	0.0219	0.0005	0.0000	0.0028	0.0123	0.0003	33.04	12.2	0.0	0.000	0.004	91.5	19.9	0.2
0.30	39.9993	0.0494	1.3781	0.0027	0.0205	0.0006	0.0000	0.0027	0.0125	0.0003	30.33	11.2	0.0	0.000	0.004	90.7	19.8	0.2
0.40	51.8044	0.0583	1.9280	0.0049	0.0254	0.0006	0.0000	0.0032	0.0045	0.0003	42.43	15.6	0.0	0.000	0.003	97.4	19.7	0.2
0.50	76.9018	0.0533	2.9005	0.0034	0.0374	0.0007	0.0000	0.0031	0.0032	0.0003	63.83	23.5	0.0	0.000	0.002	98.7	19.7	0.1
0.60	73.8561	0.0593	2.7909	0.0038	0.0383	0.0006	0.0038	0.0031	0.0032	0.0003	61.41	22.6	0.0	0.003	0.002	98.7	19.7	0.1
0.70	34.6575	0.0385	1.3030	0.0026	0.0177	0.0004	0.0000	0.0031	0.0009	0.0003	28.67	10.6	0.0	0.000	0.005	99.2	19.9	0.2
0.80	11.4529	0.0673	0.4376	0.0014	0.0051	0.0004	0.0000	0.0032	0.0002	0.0003	9.63	3.5	0.0	0.000	0.014	99.4	19.6	0.4

GBD-64c - muscovite

J(±1 S) = 0.000416 ± 0.000002

0.01	26.0060	0.0503	0.2180	0.0012	0.0149	0.0005	0.0180	0.0081	0.0684	0.0005	4.80	1.4	0.0	0.162	0.073	21.4	19.1	1.1
0.05	27.0818	0.0384	0.8175	0.0022	0.0141	0.0006	0.1291	0.0084	0.0187	0.0004	18.01	5.1	0.2	0.310	0.020	79.4	19.6	0.3
0.10	68.0901	0.0652	2.4777	0.0034	0.0342	0.0006	0.0002	0.0081	0.0079	0.0004	54.59	15.5	0.0	0.000	0.006	96.5	19.8	0.2
0.20	53.2475	0.0473	1.9131	0.0033	0.0273	0.0006	0.0013	0.0079	0.0086	0.0004	42.15	12.0	0.0	0.001	0.008	95.2	19.8	0.2
0.30	56.5658	0.0573	2.0985	0.0034	0.0283	0.0006	0.0007	0.0084	0.0037	0.0003	46.24	13.2	0.0	0.001	0.008	98.1	19.7	0.2
0.40	82.8559	0.0732	3.0927	0.0044	0.0421	0.0006	0.0010	0.0081	0.0024	0.0004	68.14	19.4	0.0	0.001	0.005	99.1	19.8	0.2
0.50	31.2962	0.0652	1.1680	0.0034	0.0150	0.0006	0.0002	0.0080	0.0017	0.0003	25.73	7.3	0.0	0.000	0.013	98.4	19.7	0.3
0.60	11.5026	0.0256	0.4244	0.0023	0.0059	0.0005	0.0122	0.0080	0.0016	0.0003	9.35	2.7	0.2	0.056	0.037	95.9	19.4	0.4
0.70	15.2876	0.0256	0.5645	0.0016	0.0082	0.0005	0.0240	0.0085	0.0012	0.0003	12.44	3.5	0.5	0.083	0.030	97.6	19.7	0.3
0.80	19.8519	0.0169	0.7482	0.0021	0.0100	0.0005	0.0038	0.0079	0.0010	0.0003	16.49	4.7	0.1	0.010	0.021	98.6	19.5	0.3
0.90	25.3385	0.0672	0.9559	0.0021	0.0107	0.0006	0.0012	0.0097	0.0000	0.0003	21.06	6.0	0.6	0.002	0.020	99.9	19.8	0.3
1.00	22.1551	0.0752	0.8241	0.0021	0.0101	0.0005	0.0004	0.0083	0.0010	0.0003	18.16	5.2	0.0	0.001	0.020	98.7	19.8	0.3
1.50	17.1444	0.0179	0.6470	0.0019	0.0083	0.0005	0.0005	0.0086	0.0000	0.0003	14.26	4.1	0.4	0.001	0.026	100.0	19.8	0.3

GBD-64d - muscovite

J(±1 s) = 0.000416 ± 0.000002

0.20	21.1461	0.0218	0.3058	0.0015	0.0112	0.0004	0.0059	0.0031	0.0424	0.0004	6.73	1.3	0.0	0.038	0.020	40.2	20.8	0.7
0.30	79.1181	0.0553	1.5159	0.0030	0.0429	0.0006	0.0015	0.0027	0.1254	0.0006	33.34	6.6	0.0	0.002	0.003	52.7	20.5	0.3
0.40	123.5169	0.1202	4.3392	0.0065	0.0607	0.0008	0.0000	0.0038	0.0224	0.0004	95.44	18.9	0.0	0.000	0.002	94.6	20.1	0.2
0.50	166.8237	0.1002	6.0929	0.0064	0.0815	0.0008	0.0000	0.0031	0.0101	0.0004	134.04	26.6	0.0	0.000	0.001	98.2	20.1	0.2
0.60	153.9665	0.0852	5.6617	0.0082	0.0761	0.0008	0.0000	0.0032	0.0041	0.0004	124.60	24.7	0.0	0.000	0.001	99.2	20.1	0.2
0.70	37.9843	0.0543	1.3744	0.0024	0.0169	0.0005	0.0000	0.0033	0.0039	0.0003	30.27	6.0	0.0	0.000	0.005	97.0	20.0	0.2
0.80	12.9255	0.0171	0.4690	0.0014	0.0061	0.0004	0.0000	0.0035	0.0012	0.0003	10.33	2.0	0.0	0.000	0.015	97.2	20.0	0.4
0.90	7.6379	0.0143	0.2775	0.0012	0.0031	0.0004	0.0000	0.0038	0.0009	0.0003	6.11	1.2	0.0	0.000	0.027	96.6	19.9	0.5
1.00	12.0025	0.0306	0.4456	0.0015	0.0056	0.0004	0.0000	0.0035	0.0008	0.0003	9.81	1.9	0.0	0.000	0.015	98.1	19.7	0.4
1.20	13.7478	0.0209	0.4989	0.0015	0.0062	0.0004	0.0000	0.0032	0.0000	0.0002	10.99	2.2	0.0	0.000	0.013	99.9	20.6	0.3
1.40	37.2687	0.0474	1.3868	0.0028	0.0157	0.0004	0.0000	0.0030	0.0000	0.0003	30.56	6.0	0.0	0.000	0.004	100.0	20.1	0.2
1.60	15.0539	0.0180	0.5602	0.0019	0.0058	0.0003	0.0000	0.0034	0.0000	0.0003	12.34	2.4	6.5	0.000	0.012	100.0	20.1	0.3

GBD-79c - muscovite

J(±1 s) = 0.000416 ± 0.000002

0.10	39.4301	0.0414	1.0274	0.0030	0.0205	0.0005	0.0028	0.0036	0.0378	0.0004	22.63	5.8	0.0	0.005	0.007	71.4	20.4	0.3
0.20	73.2695	0.0583	1.8957	0.0030	0.0381	0.0007	0.0033	0.0032	0.0721	0.0005	41.75	10.7	0.0	0.003	0.003	70.6	20.4	0.3
0.30	101.6768	0.0733	3.5070	0.0044	0.0499	0.0008	0.0000	0.0031	0.0193	0.0003	77.23	19.8	0.0	0.000	0.002	94.3	20.4	0.2
0.40	72.1654	0.0872	2.4877	0.0043	0.0347	0.0007	0.0035	0.0033	0.0144	0.0004	54.78	14.1	0.0	0.003	0.003	94.0	20.4	0.2
0.50	91.6769	0.0723	3.3135	0.0039	0.0451	0.0006	0.0000	0.0032	0.0029	0.0003	72.96	18.7	0.0	0.000	0.002	99.1	20.5	0.2
0.60	44.3419	0.0424	1.5992	0.0035	0.0199	0.0005	0.0000	0.0034	0.0018	0.0003	35.21	9.0	0.0	0.000	0.004	98.8	20.4	0.2
0.70	28.3162	0.0424	1.0283	0.0021	0.0139	0.0004	0.0000	0.0032	0.0013	0.0003	22.63	5.8	0.0	0.000	0.006	98.6	20.3	0.3
0.80	16.8792	0.0228	0.6038	0.0015	0.0094	0.0004	0.0000	0.0034	0.0013	0.0003	13.29	3.4	0.0	0.000	0.011	97.7	20.4	0.3
0.90	15.9875	0.0134	0.5769	0.0016	0.0066	0.0004	0.0000	0.0035	0.0000	0.0003	12.69	3.3	0.0	0.000	0.012	99.9	20.7	0.3
1.00	8.9902	0.0326	0.3219	0.0012	0.0034	0.0004	0.0000	0.0031	0.0000	0.0002	7.09	1.8	0.0	0.000	0.019	99.9	20.8	0.5
1.20	18.1558	0.0171	0.6545	0.0017	0.0075	0.0004	0.0000	0.0034	0.0003	0.0003	14.40	3.7	0.0	0.000	0.010	99.5	20.6	0.3
1.40	5.1752	0.0143	0.1793	0.0013	0.0028	0.0004	0.0147	0.0031	0.0011	0.0003	3.95	1.0	0.3	0.160	0.034	93.4	20.1	0.9
1.60	13.4053	0.0171	0.4848	0.0014	0.0047	0.0004	0.0000	0.0030	0.0001	0.0003	10.67	2.7	0.0	0.000	0.012	99.9	20.6	0.3

GBD-67a - muscovite

J(±1 S) = 0.000416 ± 0.000002

0.10	80.5428	0.0713	2.6904	0.0062	0.0410	0.0007	0.0000	0.0032	0.0276	0.0004	59.22	27.5	0.0	0.000	0.002	89.8	20.1	0.2
0.20	36.3284	0.0533	0.8632	0.0035	0.0189	0.0004	0.0031	0.0035	0.0450	0.0004	19.00	8.8	0.0	0.007	0.008	63.0	19.8	0.4
0.30	56.0832	0.0553	1.9137	0.0050	0.0274	0.0006	0.0000	0.0033	0.0160	0.0003	42.13	19.5	0.0	0.000	0.003	91.5	20.0	0.2
0.40	36.2004	0.0405	1.0518	0.0025	0.0177	0.0005	0.0000	0.0029	0.0264	0.0003	23.15	10.7	0.0	0.000	0.005	78.3	20.1	0.3
0.50	50.7703	0.0543	1.8676	0.0050	0.0262	0.0005	0.0018	0.0034	0.0041	0.0003	41.11	19.1	0.0	0.002	0.004	97.6	19.8	0.2
0.60	7.0791	0.0209	0.2476	0.0012	0.0035	0.0004	0.0124	0.0032	0.0022	0.0003	5.45	2.5	0.1	0.098	0.025	90.9	19.4	0.6
0.70	14.9388	0.0762	0.5410	0.0016	0.0072	0.0005	0.0000	0.0033	0.0018	0.0002	11.91	5.5	0.0	0.000	0.012	96.4	19.9	0.4
0.80	3.6973	0.0143	0.1375	0.0011	0.0012	0.0003	0.0000	0.0031	0.0005	0.0003	3.03	1.4	0.0	0.000	0.044	95.7	19.2	0.9
0.90	7.2555	0.0199	0.2707	0.0011	0.0018	0.0004	0.0000	0.0038	0.0002	0.0002	5.96	2.8	0.0	0.000	0.027	99.4	19.9	0.5
1.00	5.5522	0.0171	0.2109	0.0015	0.0024	0.0003	0.0000	0.0035	0.0002	0.0003	4.64	2.2	0.0	0.000	0.033	99.0	19.5	0.7

GBD-90b - muscovite

J(±1 S) = 0.000416 ± 0.000002

0.10	26.9304	0.0463	0.6052	0.0022	0.0136	0.0006	0.0000	0.0060	0.0332	0.0004	13.32	3.7	0.0	0.000	0.019	63.2	21.0	0.4
0.20	118.3579	0.0912	4.2069	0.0046	0.0564	0.0008	0.0039	0.0060	0.0136	0.0004	92.59	25.6	0.0	0.002	0.003	96.6	20.3	0.2
0.30	100.0031	0.0772	3.4457	0.0036	0.0475	0.0008	0.0051	0.0061	0.0231	0.0004	75.82	20.9	0.0	0.003	0.004	93.1	20.2	0.2
0.40	89.6305	0.0682	3.2672	0.0048	0.0436	0.0008	0.0069	0.0060	0.0051	0.0004	71.89	19.8	0.0	0.004	0.004	98.3	20.1	0.2
0.50	24.6898	0.0364	0.8844	0.0025	0.0117	0.0006	0.0078	0.0061	0.0027	0.0004	19.46	5.4	0.1	0.017	0.014	96.8	20.2	0.3
0.60	22.3742	0.0354	0.8170	0.0022	0.0091	0.0005	0.0074	0.0064	0.0000	0.0003	17.98	5.0	6.4	0.018	0.015	100.0	20.4	0.3
0.70	13.8522	0.0265	0.5061	0.0017	0.0057	0.0005	0.0077	0.0067	0.0000	0.0003	11.14	3.1	4.3	0.030	0.026	99.9	20.4	0.4
0.80	23.9688	0.0423	0.8850	0.0023	0.0124	0.0006	0.0092	0.0062	0.0004	0.0003	19.48	5.4	0.5	0.020	0.014	99.4	20.1	0.3
0.90	15.6331	0.0236	0.5713	0.0017	0.0075	0.0005	0.0000	0.0062	0.0003	0.0003	12.58	3.5	0.0	0.000	0.021	99.5	20.3	0.4
1.00	14.9864	0.0344	0.5434	0.0018	0.0078	0.0005	0.0006	0.0060	0.0007	0.0003	11.96	3.3	0.0	0.002	0.022	98.6	20.3	0.4
1.20	12.3735	0.0354	0.4526	0.0015	0.0047	0.0005	0.0071	0.0063	0.0001	0.0003	9.96	2.7	2.2	0.031	0.027	99.8	20.4	0.4
1.40	4.2531	0.0108	0.1564	0.0008	0.0013	0.0005	0.0000	0.0061	0.0003	0.0003	3.44	0.9	0.0	0.000	0.076	98.1	19.9	1.0
1.60	3.3982	0.0098	0.1196	0.0009	0.0016	0.0005	0.0115	0.0061	0.0001	0.0003	2.63	0.7	5.1	0.189	0.100	99.5	21.1	1.3

GBD-100b - muscovite

J(±1 s) = 0.000414 ± 0.000002

0.20	30.1607	0.0355	0.5868	0.0014	0.0131	0.0005	0.0065	0.0035	0.0250	0.0004	12.92	7.4	0.0	0.022	0.012	75.3	28.6	0.4
0.30	13.7697	0.0723	0.4723	0.0016	0.0069	0.0004	0.0040	0.0038	0.0034	0.0003	10.40	6.0	0.0	0.017	0.016	92.6	20.0	0.4
0.40	88.7174	0.0713	2.7109	0.0037	0.0435	0.0006	0.0339	0.0032	0.0398	0.0004	59.69	34.2	0.0	0.024	0.002	86.6	21.0	0.2
0.50	53.1240	0.0474	1.6963	0.0029	0.0266	0.0006	0.0331	0.0031	0.0159	0.0003	37.35	21.4	0.1	0.038	0.004	91.1	21.2	0.2
0.60	43.2120	0.0444	1.5627	0.0029	0.0209	0.0005	0.0001	0.0032	0.0025	0.0003	34.41	19.7	0.0	0.000	0.004	98.3	20.2	0.2
0.70	10.6932	0.0228	0.3891	0.0012	0.0053	0.0004	0.0052	0.0032	0.0009	0.0003	8.57	4.9	0.1	0.026	0.016	97.4	19.9	0.4
0.80	7.8257	0.0134	0.2900	0.0011	0.0034	0.0004	0.0011	0.0033	0.0005	0.0002	6.38	3.7	0.1	0.007	0.023	98.2	19.7	0.4
0.90	5.6862	0.0134	0.2110	0.0011	0.0027	0.0004	0.0016	0.0035	0.0004	0.0003	4.64	2.7	0.1	0.015	0.033	98.2	19.6	0.6

GBD-15 - muscovite

J(±1 s) = 0.000414 ± 0.000002

0.20	29.8922	0.0524	0.7192	0.0023	0.0119	0.0004	0.0002	0.0038	0.0252	0.0004	15.83	2.2	0.0	0.001	0.010	74.9	23.1	0.3
0.30	67.8874	0.1002	2.2487	0.0056	0.0328	0.0006	0.0000	0.0033	0.0181	0.0004	49.50	6.8	0.0	0.000	0.003	92.0	20.6	0.2
0.40	106.5071	0.1002	3.5468	0.0072	0.0504	0.0007	0.0064	0.0057	0.0252	0.0004	78.06	10.8	0.0	0.004	0.003	92.9	20.7	0.2
0.50	120.4179	0.0962	4.2031	0.0100	0.0577	0.0007	0.0053	0.0052	0.0101	0.0004	92.53	12.8	0.0	0.002	0.002	97.5	20.7	0.2
0.60	119.1565	0.0842	4.1987	0.0070	0.0565	0.0007	0.0002	0.0039	0.0074	0.0004	92.44	12.7	0.0	0.000	0.002	98.1	20.7	0.2
0.70	192.2692	0.1002	6.7724	0.0097	0.0935	0.0009	0.0056	0.0034	0.0146	0.0004	149.09	20.6	0.0	0.002	0.001	97.7	20.6	0.2
0.80	179.9210	0.1002	6.1789	0.0120	0.0826	0.0009	0.0000	0.0063	0.0184	0.0004	136.05	18.8	0.0	0.000	0.002	96.9	20.9	0.2
0.90	26.5075	0.0832	0.8496	0.0033	0.0131	0.0004	0.0109	0.0034	0.0052	0.0003	18.71	2.6	0.1	0.025	0.008	94.2	21.8	0.3
1.00	24.6468	0.0673	0.8207	0.0028	0.0093	0.0005	0.0001	0.0035	0.0012	0.0003	18.07	2.5	0.0	0.000	0.008	98.6	22.0	0.3
1.20	38.1102	0.0533	1.3057	0.0023	0.0157	0.0005	0.0005	0.0035	0.0023	0.0003	28.75	4.0	0.0	0.001	0.005	98.2	21.3	0.2
1.40	46.8606	0.0533	1.5614	0.0052	0.0205	0.0005	0.0004	0.0036	0.0016	0.0003	34.38	4.7	0.0	0.000	0.005	99.0	22.0	0.2
1.60	17.0317	0.0474	0.5373	0.0017	0.0053	0.0004	0.0000	0.0036	0.0008	0.0003	11.83	1.6	0.0	0.000	0.013	98.7	23.2	0.3

GBD-29b - muscovite

J(±1 s) = 0.000414 ± 0.000002

0.01	29.1372	0.0464	0.2410	0.0018	0.0156	0.0006	0.0000	0.0075	0.0662	0.0005	5.31	1.0	0.0	0.000	0.062	32.2	28.8	1.1
0.05	18.4828	0.0181	0.2748	0.0019	0.0090	0.0005	0.0000	0.0071	0.0272	0.0004	6.06	1.2	0.0	0.000	0.051	56.1	27.9	0.8
0.10	21.3899	0.0454	0.4169	0.0021	0.0106	0.0005	0.0225	0.0073	0.0245	0.0004	9.19	1.8	0.0	0.106	0.034	65.8	25.0	0.5
0.20	69.3848	0.0683	1.7145	0.0050	0.0342	0.0006	0.0058	0.0077	0.0622	0.0005	37.78	7.2	0.0	0.007	0.009	73.2	22.0	0.3
0.30	73.9020	0.0643	2.2864	0.0048	0.0345	0.0006	0.0040	0.0074	0.0317	0.0004	50.37	9.6	0.0	0.003	0.006	87.2	20.9	0.2
0.40	101.4929	0.0783	3.2940	0.0052	0.0475	0.0006	0.0063	0.0080	0.0315	0.0005	72.58	13.9	0.0	0.004	0.005	90.7	20.7	0.2
0.50	92.8486	0.0753	2.9665	0.0055	0.0469	0.0006	0.0284	0.0076	0.0346	0.0006	65.35	12.5	0.0	0.019	0.005	88.9	20.6	0.2
0.60	90.8810	0.0713	2.9544	0.0053	0.0455	0.0006	0.0137	0.0073	0.0307	0.0004	65.08	12.5	0.0	0.009	0.005	89.9	20.5	0.2
0.70	102.7111	0.0852	3.2964	0.0061	0.0520	0.0008	0.0222	0.0076	0.0363	0.0004	72.61	13.9	0.0	0.013	0.005	89.4	20.7	0.2
0.80	48.0502	0.0524	1.6402	0.0040	0.0232	0.0005	0.0143	0.0076	0.0100	0.0004	36.12	6.9	0.0	0.017	0.009	93.8	20.4	0.2
0.90	24.7012	0.0346	0.8596	0.0030	0.0127	0.0005	0.0202	0.0075	0.0034	0.0003	18.94	3.6	0.1	0.046	0.017	95.9	20.5	0.3
1.00	27.7272	0.0355	0.9623	0.0040	0.0143	0.0006	0.0072	0.0118	0.0024	0.0003	21.20	4.1	0.1	0.015	0.024	97.4	20.8	0.3
1.50	79.1919	0.0713	2.7866	0.0054	0.0366	0.0006	0.0038	0.0078	0.0041	0.0003	61.39	11.8	0.0	0.003	0.005	98.5	20.8	0.2

GBD-38 - muscovite

J(±1 s) = 0.000414 ± 0.000002

0.20	118.8728	0.0912	3.0562	0.0032	0.0603	0.0006	0.0000	0.0032	0.1056	0.0005	67.28	25.7	0.0	0.000	0.002	73.5	21.2	0.2
0.30	61.0785	0.0583	1.9411	0.0026	0.0279	0.0006	0.0000	0.0034	0.0187	0.0004	42.73	16.3	0.0	0.000	0.003	90.8	21.2	0.2
0.40	160.2396	0.0832	4.6771	0.0063	0.0803	0.0008	0.0000	0.0039	0.0922	0.0005	102.96	39.3	0.0	0.000	0.002	82.8	21.1	0.2
0.50	20.5264	0.0405	0.7095	0.0023	0.0082	0.0004	0.0000	0.0034	0.0008	0.0003	15.62	6.0	0.0	0.000	0.010	98.9	21.2	0.3
0.60	12.5703	0.0643	0.4293	0.0012	0.0056	0.0004	0.0067	0.0032	0.0012	0.0003	9.45	3.6	0.1	0.030	0.015	97.3	21.1	0.4
0.70	17.9014	0.0267	0.6338	0.0016	0.0089	0.0005	0.0000	0.0035	0.0002	0.0002	13.95	5.3	0.0	0.000	0.011	99.7	20.9	0.3
0.80	13.4503	0.0296	0.4659	0.0020	0.0056	0.0004	0.0000	0.0030	0.0000	0.0003	10.26	3.9	0.0	0.000	0.013	100.0	21.4	0.4

Note: All isotopes corrected for blanks, radioactive decay and interfering nucleogenic isotope production. Reported ages calculated using an atmospheric ^{40}A

Data collected on a Mass Analyser Products 215-50 mass spectrometer using an electron multiplier in analog mode; sensitivity = 2.317 x 10^{-14} mol/nA.

Appendix 5. $^{40}Ar/^{39}Ar$ Methods.

The $^{40}Ar/^{39}Ar$ analyses were performed at the USGS in Denver, CO. High purity mineral separates together with standards were irradiated for 2 megawatt hours in the central thimble position of the USGS TRIGA reactor using cadmium lining to prevent nucleogenic production of ^{40}Ar. The neutron flux was monitored using Fish Canyon Tuff sanidine, using an age of 28.201 Ma ± 0.08 Ma (Kuiper et al. 2008), and isotopic production ratios were determined from irradiated CaF_2 and KCl salts. For this irradiation, the following argon production values from calcium and potassium were measured: ^{36}Ar derived from ^{37}Ca = $2.447 \times 10^{-4} \pm 0.47 \times 10^{-4}$; ^{39}Ar derived from $^{37}Ca = 6.5 \times 10^{-4} \pm 0.13 \times 10^{-4}$; and ^{38}Ar derived from $^{39}K = 1.29 \times 10^{-2} \pm 0.02 \times 10^{-2}$. The irradiated samples and standards were loaded into 3 mm wells within a stainless steel planchette attached to a fully automated ultra-high vacuum extraction line constructed of stainless steel. One to five grains from each sample were incrementally degassed and/or fused using a 20 W CO_2 laser equipped with a beam homogenizing lens. The gas was expanded and purified by exposure to a stainless steel cold finger maintained at -140^{o} C and two hot SAES GP50 getters. Following purification the gas was expanded into a Mass Analyzer Products 215–50 mass spectrometer and argon isotopes were measured by peak jumping using an electron multiplier operated in analog mode. Data were acquired during 10 cycles and time zero intercepts were determined by best-fit regressions to the data. Ages were calculated from data that were corrected for mass discrimination, blanks, radioactive decay subsequent to irradiation, and interfering nucleogenic reactions.

Appendix 6. Biotite 40Ar/39Ar age spectra for Miyar and Gianbul valleys. The shaded steps are those used to determine the weighted mean plateau age or preferred age (*); errors are reported to ±1 σ.

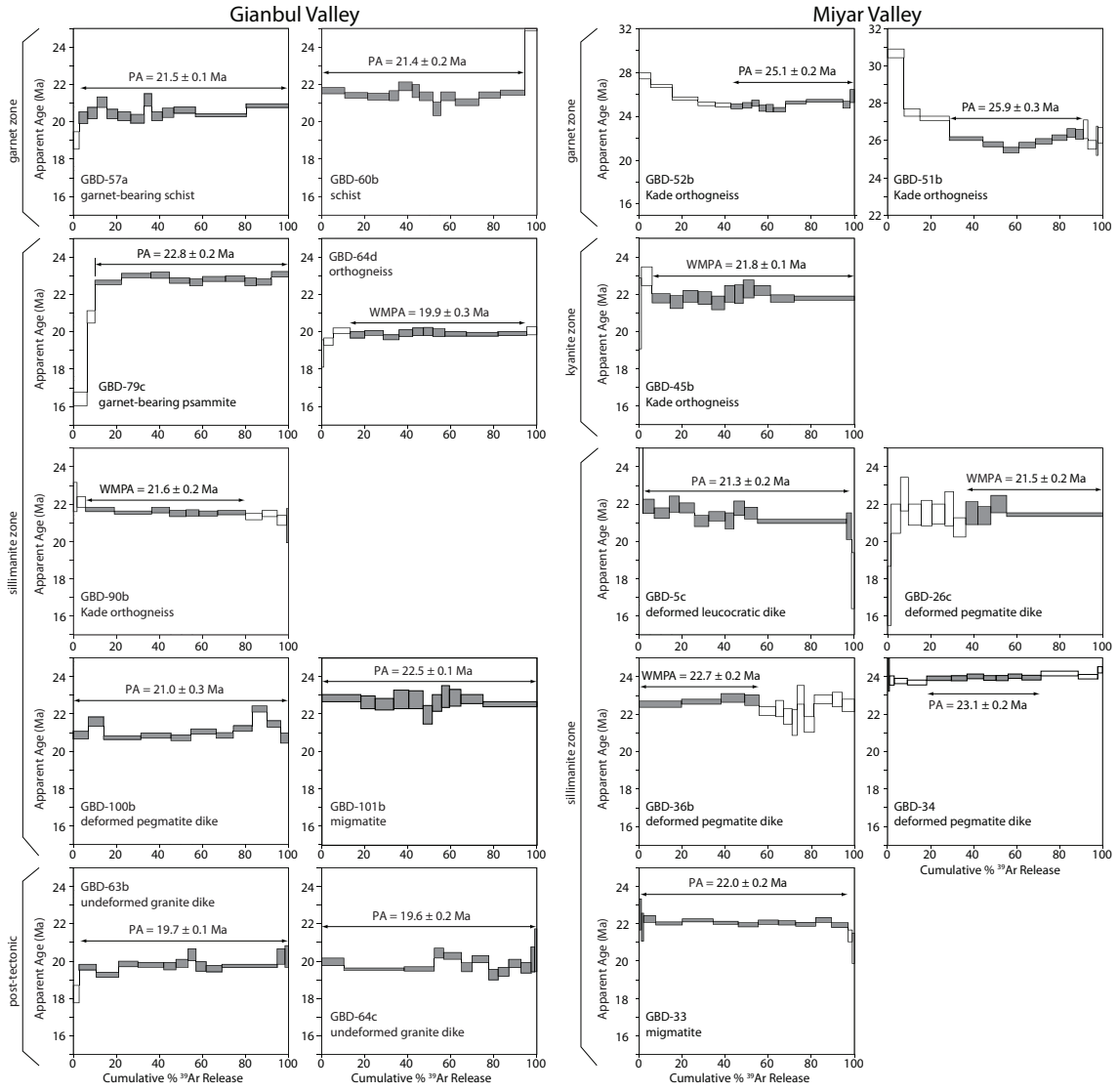

Appendix 7. LASS geochronology methods for Chapter II.

For each thin section, 5–10 monazite and zircon grains were ablated with 7 μm and 10 μm spots, respectively, for a total of 50–70 spots per sample. Methods are described in Kylander-Clark et al. (2013). Monazite data were normalized to standard 44069 (Aleinikoff et al., 2006), corrected for downhole fractionation, and processed using Iolite software (Paton et al., 2010). 2-sigma uncertainties are reported for all dates. Prior to analysis, individual monazite grain x-ray maps of Y, La, Nd, Th, and U were made on a Cameca SX-100 electron microprobe using a 1 μm step size; LASS spot locations were chosen using these maps. For zircon grains, cathodoluminescence images were uses to select spot locations. Some discordant analyses and those with inheritance ages have been excluded from concordia plots and data tables. The long term reproducibility for the ICP-MS facility is estimated to be within 2%, so 2% uncertainty has been added to reported ^{238}U-^{206}Pb dates.

Appendix 8. U-Pb and trace element data.

sample	analysis no.	mineral	^{238}U / ^{206}Pb	± 2σ	^{207}Pb / ^{206}Pb	± 2σ	error correlation	^{238}U-^{206}Pb Age* (Ma)	± 2σ	U ppm	Th ppm	Pb ppm	Hf ppm	La ppm	Ce ppm	Pr ppm	Nd ppm	Sm ppm	Eu ppm	Gd ppm	Tb ppm	Dy ppm	Ho ppm	Er ppm	Tm ppm	Yb ppm	Lu ppm
00G2	1	m	11.61	0.26	0.0573	0.0012	-0.0914	533	12	8760	34250	1414		53000	91200	10400	32200	110	127	9770	1243	5270	557	647	44	83	3
00G2	2	m	11.68	0.26	0.0573	0.0012	0.2887	530	12	7240	36080	1471		47200	95100	10600	38200	55	146	10980	1707	7690	820	1033	70	118	4
00G2	3	m	11.81	0.25	0.0574	0.0012	0.0456	524	11	7350	37860	1536		52900	98200	11000	41100	33	153	11280	1640	6	830	1034	73	119	4
00G2	4	m	11.76	0.28	0.0571	0.0012	0.1427	526	12	8740	37280	1497		62000	110400	11800	41000	5500	494	5460	642	3260	361	436	31	44	1
00G2	5	m	11.86	0.27	0.0567	0.0012	-0.0392	522	12	10110	38500	1538		67100	120100	12610	46700	5850	412	5260	592	2260	178	149	9	10	0
00G2	6	m	10.26	0.23	0.0588	0.0013	-0.0636	600	13	5940	31060	1421		60000	116500	10960	47500	4830	334	3850	502	3040	383	610	61	106	4
00G2	7	m	12.00	0.27	0.0570	0.0012	0.2629	516	11	7850	36940	1480		64600	119800	12130	47400	5820	423	5190	561	2150	184	219	16	27	1
00G2	8	m	10.57	0.24	0.0587	0.0012	0.4080	583	13	5520	34940	1554		66800	116200	11500	47000	5770	430	5340	557	2120	144	125	7	7	0
00G2	10	m	10.35	0.24	0.0590	0.0013	0.0260	594	14	5280	32810	1499		64700	120100	12020	40300	5870	520	4850	607	3260	410	607	52	87	3
00G2	11	m	11.86	0.28	0.0564	0.0012	0.0342	522	12	4840	34120	1377		64300	121000	12500	43700	8	372	4550	556	2930	320	441	39	61	2
00G2	12	m	10.48	0.24	0.0581	0.0012	0.0572	588	13	4290	29840	1341		65100	110500	12800	45200	17	139	7900	766	3100	305	368	28	46	2
00G2	13	m	10.31	0.22	0.0590	0.0012	0.1012	597	13	4250	25840	1181		68300	119200	12700	45700	10	427	4340	489	2377	264	379	31	59	2
00G2	14	m	10.31	0.25	0.0593	0.0013	0.0005	597	14	3500	28720	1296		59400	104200	11900	44700	24	160	9710	1444	6820	684	898	63	96	3
00G2	15	m	10.25	0.25	0.0591	0.0012	0.0097	600	14	3302	32110	1487		57100	107900	11760	49800	34	147	8860	1058	4430	434	496	38	64	2
00G2	16	m	10.18	0.23	0.0594	0.0012	-0.1173	604	13	3509	25000	1180		58500	111500	13600	47500	31	155	7660	813	3070	278	322	22	41	1
00G2	17	m	10.19	0.23	0.0597	0.0013	0.0434	603	14	3580	29810	1397		60400	106700	12900	46600	40	160	8040	807	3450	315	398	30	53	2
00G2	18	m	10.21	0.21	0.0596	0.0013	-0.0098	602	12	3154	30610	1436		54900	108100	11800	39300	40	167	9590	1123	4370	423	535	38	68	2
00G2	19	m	10.24	0.22	0.0597	0.0013	0.2558	601	13	3436	30590	1429		62600	114400	12300	44100	76	148	7560	740	2880	244	277	21	34	1
00G2	20	m	10.33	0.23	0.0597	0.0012	0.0942	595	13	4481	27270	1278		62900	120000	12400	42200	102	147	7580	715	2660	220	246	18	30	1
00G2	21	m	10.45	0.22	0.0593	0.0012	0.1598	589	12	2932	31290	1429		61500	108700	14400	45400	0	127	2790	170	308	13	5	0	1	0
00G2	22	m	11.88	0.27	0.0580	0.0012	0.0246	521	12	5790	38700	1603		61500	111100	14000	40600	0	132	2240	109	193	8	4	1	1	0
00G2	24	m	11.82	0.26	0.0583	0.0012	0.1157	524	11	3950	38100	1559		62600	110200	13700	46900	0	117	2760	147	269	12	7	1	0	0
00G2	30	m	10.26	0.29	0.0616	0.0017	0.0839	599	17	1773	40800	1882		60200	114500	13100	42100	155	197	2750	124	199	8	6	0	0	0
00G2	33	m	10.45	0.31	0.0602	0.0017	0.0978	589	17	1514	37500	1723		61300	108100	13100	43300	433	178	2690	110	147	5	1	0	0	0
00G2	34	m	10.30	0.24	0.0604	0.0015	0.1913	597	14	1651	39000	1786		62100	116700	14400	45000	350	189	2730	119	159	5	4	0	1	0
00G2	35	m	10.54	0.28	0.0596	0.0013	0.0848	584	15	3350	34300	1559		63100	112600	14440	46400	350	235	3840	323	1200	123	158	13	23	1
00G2	36	m	10.45	0.28	0.0592	0.0015	0.1303	589	15	1407	37120	1691		61200	118800	14700	48200	740	149	2520	109	160	6	5	0	1	0
00G2	37	m	10.35	0.27	0.0614	0.0017	-0.0417	594	15	1196	32060	1481		62400	109900	13400	38700	960	169	2480	99	128	4	2	0	0	0
00G2	38	m	10.25	0.26	0.0593	0.0014	0.0099	600	15	2190	36310	1651		62600	114700	14500	44100	1550	239	3390	233	682	52	54	3	5	0
00G2	39	m	10.55	0.26	0.0592	0.0013	0.1302	584	14	1998	33850	1530		58100	107800	13700	36700	0	313	4080	326	1002	90	88	6	5	0
00G2	40	m	10.40	0.26	0.0591	0.0015	-0.2560	592	15	960	34480	1581		60800	121700	14100	46100	0	170	2650	104	139	4	2	0	1	0
00G2	41	m	10.32	0.27	0.0595	0.0016	0.1057	596	15	1013	36120	1672		65500	116900	13600	43300	0	171	2690	109	137	4	1	0	0	0
00G2	43	m	10.38	0.27	0.0588	0.0016	-0.0203	593	15	886	38450	1758		57700	119800	10600	34400	0	138	2140	94	126	4	1	0	0	0
00G2	44	m	10.26	0.25	0.0610	0.0016	-0.0406	600	14	1157	36070	1661		60100	129500	13200	40900	0	198	2770	147	333	15	14	1	1	0
00G2	45	m	10.31	0.28	0.0602	0.0015	-0.0911	596	16	816	37680	1723		61700	121000	12600	41200	0	163	2640	107	151	4	1	0	0	0
00G2	46	m	10.22	0.25	0.0596	0.0014	-0.0987	602	14	1137	38000	1759		59500	118700	12400	47700	0	314	3830	210	404	20	19	1	2	0
00G2	47	m	10.54	0.28	0.0599	0.0014	0.2675	584	15	1491	37490	1725		61400	121700	12700	37300	0	356	4250	311	820	62	70	6	10	0
00G2	48	m	10.48	0.27	0.0594	0.0013	-0.0734	587	15	2060	32500	1485		62100	115000	12500	40700	0	393	4920	470	1720	151	195	15	31	1
00G2	52	m	10.57	0.20	0.0600	0.0014	-0.0376	583	11	1771	37030	1664		59400	107700	10870	47600	2140	358	4740	402	1300	83	67	4	3	0
00G2	53	m	10.29	0.20	0.0601	0.0015	0.1284	598	12	918	34600	1579		61600	114200	12300	44000	2770	216	2950	124	187	7	4	0	0	0
00G2	54	m	10.37	0.20	0.0607	0.0014	0.1411	594	11	1844	37200	1681		56100	112000	11600	45400	3900	409	5310	484	1726	134	126	7	6	0
00G2	55	m	10.29	0.20	0.0595	0.0015	0.1091	598	11	1539	38410	1728		56800	110700	12770	47800	4460	301	4250	262	681	44	38	2	1	0
00G2	56	m	10.22	0.21	0.0610	0.0015	0.0379	602	12	1192	37300	1715		59700	111400	12500	41500	3450	264	3230	163	309	19	17	1	2	0
00G2	57	m	10.31	0.20	0.0613	0.0015	-0.0797	597	11	1276	38070	1701		60400	116400	12200	47400	5600	262	3390	180	332	16	10	1	0	0
00G2	59	m	10.43	0.22	0.0598	0.0016	0.1459	590	12	1209	36310	1622		60400	105800	14530	40400	15500	211	3190	159	302	13	11	0	0	0
00G2	60	m	10.40	0.20	0.0603	0.0014	0.0896	592	11	2037	35900	1621		54800	104500	13800	36500	23000	369	4750	394	1043	60	50	3	3	0
00G2	61	m	10.27	0.20	0.0603	0.0014	-0.3106	599	11	1875	39370	1780		64700	108900	15800	41200	22500	314	4740	391	1210	93	115	9	17	0
00G2	63	m	10.46	0.20	0.0599	0.0014	0.1022	589	11	1978	37800	1728		58300	109000	13250	40200	9600	354	4650	348	781	36	24	1	2	0
00G2	64	m	10.59	0.21	0.0593	0.0014	0.0184	582	11	1530	37460	1683		56200	100300	12530	37200	23300	208	3690	238	549	27	16	1	0	0
00G2	65	m	10.36	0.20	0.0606	0.0015	0.0221	594	11	1733	35360	1600		63000	109400	13600	35700	13500	334	4330	292	640	27	15	0	1	0
00G2	66	m	10.50	0.20	0.0587	0.0014	0.1285	586	11	1632	36600	1647		64400	109100	14800	33400	22700	324	4130	256	459	20	12	0	0	0
00G2	67	m	10.49	0.21	0.0594	0.0014	0.2588	587	12	1305	33580	1512		65300	113500	14900	43400	16400	232	3330	137	215	10	7	1	2	0

00G2	68	m	10.50	0.20	0.0595	0.0014	0.0702	587	11	1742	35300	1599	62000	112400	14700	37200	10200	310	4320	289	615	28	18	1	1	0
06A1	1	m	11.47	0.14	0.0587	0.0014	0.0233	539	13	1550	29110	1214	37000	100300	13500	65900		37	4340	213	629	54	50	1	2	0
06A1	2	m	11.36	0.21	0.0583	0.0013	0.1192	543	15	1650	28210	1176	36400	105300	13940	61100		40	3790	199	601	55	54	2	2	0
06A1	3	m	11.55	0.25	0.0584	0.0013	0.0517	535	15	1887	25290	1060	35600	101100	15200	64300		38	4150	194	554	49	45	1	2	0
06A1	4	m	11.44	0.18	0.0576	0.0013	-0.1659	540	14	1655	24710	1032	36700	103600	15100	65000	6700	40	4280	197	605	50	47	2	2	0
06A1	5	m	11.35	0.22	0.0576	0.0014	-0.0834	544	15	1335	23820	1001	37100	115600	15100	62700	6430	38	4660	250	679	65	55	1	1	0
06A1	6	m	11.26	0.22	0.0581	0.0013	0.1200	548	15	1579	23460	989	41100	106800	14100	59800	5500	59	4610	253	825	83	81	3	3	0
06A1	7	m	11.27	0.20	0.0585	0.0013	0.0527	548	15	2036	23630	1009	47100	111400	13400	49900	5300	146	5350	399	1610	199	223	10	15	2
06A1	8	m	11.24	0.21	0.0591	0.0013	0.2632	549	15	1325	25690	1095	44200	114800	12200	47000	7000	134	5310	403	1590	208	228	10	18	3
06A1	9	m	11.52	0.23	0.0578	0.0013	0.0482	536	15	1754	26180	1090	49700	115900	14900	50700	6500	186	5230	390	1690	195	225	9	15	2
06A1	10	m	12.00	0.22	0.0576	0.0013	0.1266	516	14	2160	27080	1115	42000	112100	15700	58600	7100	131	4690	302	1119	137	152	6	9	1
06A1	11	m	11.92	0.20	0.0582	0.0013	0.0271	520	13	1924	30700	1218	46500	116000	14800	47900	11100	277	5730	482	2000	248	290	11	17	3
06A1	12	m	11.56	0.20	0.0592	0.0015	0.0592	535	14	878	43500	1725	45700	101500	13860	49300	10800	245	5900	478	1830	227	277	11	20	3
06A1	13	m	11.86	0.20	0.0583	0.0014	-0.0035	522	13	884	38870	1447	44400	110200	13130	49200	12500	183	5440	416	1600	201	246	10	17	2
06A1	14	m	11.57	0.17	0.0575	0.0014	0.0266	534	13	1041	38240	1546	44100	117800	14600	48800	12900	124	5270	361	1522	189	218	9	15	2
06A1	15	m	11.38	0.18	0.0574	0.0013	0.0692	543	14	904	52700	2133	42900	108400	13920	48500	10900	91	4940	320	1180	145	154	6	9	1
06A1	16	m	11.79	0.19	0.0570	0.0013	-0.0130	525	14	1922	43750	1724	32600	109000	15700	57000	12600	49	2980	135	358	35	30	1	1	0
06A1	17	m	11.50	0.12	0.0591	0.0015	-0.0829	538	12	969	53200	2130	47400	101100	12400	40000	8300	461	5700	548	3130	461	705	38	84	14
06A1	18	m	11.07	0.13	0.0594	0.0012	0.1745	557	13	4720	33020	1412	42600	101000	12100	47600	8900	294	5330	430	1986	262	338	15	26	3
06A1	20	m	12.00	0.12	0.0575	0.0013	-0.0690	516	12	3112	56700	2188	49900	107500	12700	49900	8800	412	5660	560	2690	385	529	27	51	8
06A1	21	m	11.21	0.14	0.0580	0.0013	0.1244	551	13	1241	62900	2471	44200	103000	13090	48400	8200	234	5590	481	2190	319	428	21	40	5
06A1	22	m	10.45	0.14	0.0606	0.0013	-0.1791	589	14	4147	43490	1909	40000	107000	13200	50300	9400	285	5030	438	2020	295	403	17	30	3
06A1	24	m	10.24	0.12	0.0611	0.0013	0.2004	601	14	3892	38900	1736	30000	96500	12900	55900	8600	45	2610	120	345	34	29	1	1	0
06A1	25	m	11.44	0.13	0.0589	0.0012	0.1017	540	12	4180	47500	1915	44200	102700	13700	54100	9900	101	4520	321	1224	164	190	8	14	2
06A1	27	m	10.19	0.11	0.0612	0.0013	0.0958	604	14	5820	58190	2609	45300	111500	14100	52700	9000	433	5390	424	1651	204	219	8	9	1
06A1	28	m	10.11	0.14	0.0609	0.0013	-0.0749	608	15	4470	47390	2132	46900	102600	13260	50900	9100	377	6200	483	2170	287	353	14	25	3
06A1	29	m	11.10	0.15	0.0578	0.0014	-0.1961	556	13	1161	62800	2463	50700	106700	14100	49800	9300	424	6150	516	2284	329	385	16	29	4
06A1	30	m	11.48	0.13	0.0594	0.0013	-0.0907	539	12	2724	37320	1534	42500	104300	13080	50100	10800	197	6200	539	2500	327	435	22	43	6
06A1	31	m	10.41	0.12	0.0608	0.0012	0.0005	593	14	8405	28300	1311	46500	100200	13000	46300	8000	499	5800	536	2650	382	494	24	50	7
06A1	32	m	10.15	0.11	0.0609	0.0013	-0.2220	606	14	5250	34990	1595	42800	106500	12300	46100	11400	501	6260	510	2102	269	303	12	21	3
06A1	33	m	11.12	0.14	0.0587	0.0014	-0.1185	555	13	1335	42600	1713	48100	111500	13700	50500	9400	318	6040	479	2060	248	280	10	15	2
06A1	34	m	11.42	0.16	0.0580	0.0013	0.0578	541	13	1355	45300	1800	40400	96400	12700	45300	8700	539	6480	532	2130	236	230	8	11	1
06A1	35	m	12.05	0.16	0.0571	0.0012	-0.0283	514	12	2995	43540	1672	40000	99400	11900	44100	11700	349	6870	574	2520	333	440	18	35	5
06A1	36	m	11.67	0.18	0.0581	0.0014	-0.1562	530	13	991	52000	2062	40800	98300	12790	49900	8800	233	6750	567	2510	344	405	18	36	5
06A1	37	m	11.55	0.13	0.0581	0.0014	-0.1544	535	12	1047	40630	1612	42300	104700	13200	50900	11400	197	6940	535	2320	297	401	18	32	5
06A1	38	m	11.57	0.17	0.0590	0.0014	0.0083	534	13	1089	55200	2181	39200	90800	11290	38800	7700	716	5910	458	1930	222	222	8	12	1
06A1	39	m	10.22	0.14	0.0601	0.0012	-0.1558	601	14	7350	31420	1433	43600	107200	12600	49100	8600	282	6600	459	2000	249	307	14	26	4
06A1	41	m	12.05	0.13	0.0576	0.0013	0.0021	514	12	2532	32100	1260	43200	98800	11500	50900	7100	273	6900	516	2250	271	377	15	28	5
06A1	43	m	11.43	0.17	0.0580	0.0014	0.2112	541	13	1290	28220	1162	44700	108300	14600	53400	8800	84	6950	443	1850	197	226	10	16	3
06A1	44	m	11.72	0.18	0.0573	0.0013	-0.1699	528	13	1936	31480	1250	42500	100800	12400	45100	7800	130	7800	564	2601	351	467	24	44	9
06A1	45	m	10.20	0.12	0.0599	0.0012	0.0725	602	14	7460	31670	1403	45200	106900	14000	53900	7900	105	4520	195	711	68	74	3	3	0
06A1	46	m	11.42	0.14	0.0586	0.0013	-0.0448	541	13	2932	31600	1286	48900	108100	12940	47700	7100	234	5830	366	1520	176	191	7	10	2
06A1	47	m	11.31	0.14	0.0581	0.0012	-0.1441	546	13	2810	30010	1222	50300	101300	11300	44300	8000	630	6950	533	2830	402	568	29	60	13
06A1	48	m	11.34	0.17	0.0580	0.0012	-0.0357	545	13	2518	30200	1219	43700	101800	12510	46800	9400	260	7550	415	1650	190	201	7	10	2
06A1	49	m	11.22	0.19	0.0586	0.0014	-0.4173	550	14	1440	29600	1196	46400	101400	13200	50700	8100	315	7130	433	1740	200	218	8	13	2
06C1	1	m	11.58	0.08	0.0575	0.0013	-0.0249	534	11	2126	107800	4326	44400	99600	12230	52600	10100	168	8390	527	2330	314	394	19	35	8
06C1	2	m	11.29	0.11	0.0581	0.0013	-0.2203	547	12	1852	110100	4560	50500	99780	12100	46900	8300	372	7540	416	1890	250	313	16	33	6
06C1	3	m	11.31	0.12	0.0570	0.0012	-0.0069	546	12	1808	115200	4770	43900	104900	12610	51000	10700	235	8350	448	1800	213	255	9	13	2
06C1	4	m	11.40	0.11	0.0565	0.0012	0.0661	542	12	1994	118400	4800	44100	100200	12870	53400	8600	96	9120	497	2150	270	314	14	22	4
06C1	5	m	11.65	0.12	0.0574	0.0012	0.0257	531	12	2297	109000	4352	47300	102200	12500	49100	7700	192	9020	448	1830	222	233	8	12	2
06C1	6	m	11.61	0.12	0.0575	0.0012	-0.0860	534	12	1999	104700	4187	46600	107000	14120	50400	10000	109	10120	550	2450	283	339	12	19	3
06C1	7	m	11.04	0.10	0.0587	0.0013	-0.0502	559	12	1656	79300	3385	41500	111800	13700	48800	9300	172	10740	557	2470	299	355	13	22	3
06C1	8	m	11.19	0.10	0.0582	0.0013	0.1276	552	12	1703	79200	3322	44200	104500	13200	48200	12500	117	10830	462	2086	237	263	10	14	2
06C1	9	m	11.10	0.11	0.0582	0.0013	-0.0366	556	12	1522	65600	2853	41700	103400	12700	43600	10500	81	9200	398	1550	172	193	6	9	2
06C1	10	m	11.10	0.10	0.0580	0.0013	0.2617	556	12	1600	101700	4290	39800	98000	12080	51600	11900	178	11790	518	2230	269	296	10	16	2
06C1	11	m	11.24	0.13	0.0586	0.0013	-0.0113	550	13	1721	67600	2845	41200	101100	13400	53000	9400	97	8470	290	1040	108	111	4	5	1

06C1	12	m	11.18	0.10	0.0585	0.0013	0.0876	552	12	1756	74700	3145	49800	104600	13000	40800	8700	251	14280	701	3760	586	839	42	93	14
06C1	13	m	11.16	0.10	0.0587	0.0013	0.0631	553	12	1633	73100	3071	49500	106400	12300	48300	8700	247	14820	692	3830	561	843	43	93	12
06C1	14	m	11.12	0.11	0.0588	0.0014	-0.0311	555	12	1651	76300	3191	54500	109100	12300	44300	9400	230	15300	637	3580	547	815	40	86	13
06C1	15	m	11.18	0.10	0.0584	0.0013	0.1014	552	12	1635	83800	3570	49800	107900	12400	51600	10300	224	16900	679	3840	544	808	37	76	10
06C1	16	m	11.10	0.12	0.0588	0.0013	-0.1767	556	12	1795	155000	6330	46900	110600	12800	44600	7400	221	17900	699	3660	550	758	34	68	10
06C1	17	m	11.10	0.11	0.0592	0.0014	0.3549	556	12	1754	53800	2362	49900	108300	14200	42100	5200	274	19200	680	3840	548	775	36	69	10
06C1	18	m	11.48	0.11	0.0590	0.0013	-0.1656	538	12	1758	82300	3396	50600	108300	11800	39700	6800	396	18400	613	3490	501	708	34	81	11
06C1	19	m	10.89	0.10	0.0592	0.0013	-0.0205	566	12	2042	77200	3297	50600	108300	12500	43200	8800	223	19300	635	3520	538	817	42	91	13
06C1	20	m	11.13	0.09	0.0587	0.0013	-0.0287	555	12	2063	56500	2398	48000	105300	12590	51000	11500	187	23200	678	3450	587	854	43	98	15
06C1	21	m	9.40	0.10	0.0707	0.0015	0.0652	652	15	1865	82700	4267	47600	108500	13000	46900	8000	140	24800	707	3720	610	927	55	128	20
06C1	22	m	11.40	0.13	0.0577	0.0013	0.1961	542	12	2173	89100	3639	45800	117000	13100	48600	7300	132	35900	620	3660	552	804	41	105	16
06C1	23	m	11.25	0.10	0.0589	0.0013	0.1663	549	12	2314	59300	2470	44200	106100	13600	49300	10400	124	44100	648	3310	477	652	29	61	9
06C1	24	m	10.99	0.10	0.0584	0.0013	0.1131	562	12	2398	172500	7110	48900	115700	13600	44800	9800	192	45300	553	2690	365	496	22	46	7
06C1	25	m	11.06	0.11	0.0607	0.0014	0.2485	558	12	2078	101100	4240	45200	110600	13060	47300	7600	121	56900	682	3730	584	810	40	84	14
06C1	26	m	11.15	0.12	0.0590	0.0013	0.0288	554	12	2077	85100	3557	47000	115400	14090	51100	7000	130	67700	650	3260	464	640	27	60	9
06C1	27	m	11.00	0.12	0.0598	0.0014	-0.1405	561	13	2134	90600	3769	44900	113100	14000	45000	9000	128	82800	685	3940	633	983	53	131	20
06C1	28	m	11.21	0.10	0.0594	0.0013	0.0114	551	12	2385	92900	3875	42100	105500	12600	45900	9100	117	96400	626	3370	529	722	31	66	10
06C1	29	m	11.26	0.12	0.0591	0.0013	0.0157	549	12	2681	88400	3684	51900	111800	13410	45900	7700	921	209	618	3090	413	529	25	57	8
06C1	30	m	11.11	0.10	0.0586	0.0013	0.0017	556	12	2874	105500	4362	51000	111500	12680	40700	7200	696	448	637	3230	449	561	25	54	8
06C1	31	m	10.71	0.16	0.0605	0.0014	0.0186	575	14	2455	110400	4744	42000	106300	13600	47500	10500	108	650	707	4110	658	1098	63	154	26
06C1	32	m	11.04	0.17	0.0594	0.0013	-0.0865	559	14	2389	130400	5370	42400	110200	14200	50100	9000	160	0	657	3470	510	742	31	69	10
06C1	33	m	11.24	0.20	0.0599	0.0013	0.0694	549	15	2178	109600	4610	48400	102200	11330	39000	7400	879	0	637	3550	516	694	35	80	12
06C1	34	m	8.98	0.19	0.0654	0.0016	0.0006	680	20	1450	147300	7640	52700	113400	11820	45400	9900	1002	0	677	3790	527	722	36	82	13
06C1	35	m	9.37	0.22	0.0699	0.0018	-0.6900	653	19	1834	121100	6340	52800	114500	13800	47100	8600	604	0	602	3220	451	655	31	73	11
06C1	36	m	8.76	0.19	0.0740	0.0018	-0.3200	696	20	1576	110500	6200	52200	118800	13200	47900	8900	895	0	620	3330	446	595	28	65	10
06C1	37	m	8.50	0.14	0.0767	0.0017	-0.1295	717	18	1515	122400	6873	49200	109600	12100	42900	8200	1009	0	638	2980	345	346	13	23	3
06C1	38	m	9.39	0.17	0.0646	0.0014	-0.0022	652	17	2930	165700	8040	54500	112700	12800	48500	7800	941	0	630	3330	460	577	27	58	9
06C1	39	m	8.97	0.15	0.0726	0.0017	0.1859	681	18	1517	126200	6750	45300	108400	12900	50700	11600	163	0	614	3260	460	615	29	59	10
06C1	40	m	11.19	0.25	0.0592	0.0014	0.4140	552	16	1488	131200	5470	52200	117600	15100	56700	12000	1109	0	833	4150	520	610	26	50	8
06C1	41	m	10.40	0.13	0.0625	0.0014	-0.0642	592	14	2060	126100	5650	53200	112100	13900	48700	7400	542	1670	604	3180	458	664	32	70	12
06C1	42	m	7.08	0.11	0.0829	0.0018	-0.2332	852	21	1320	114200	7200	52900	112200	14100	47400	8700	1178	1350	804	3840	476	580	26	60	10
06C1	43	m	8.60	0.13	0.0736	0.0019	-0.1215	709	17	993	105800	5790	52500	111400	11530	44600	9600	1057	1240	641	3110	394	464	19	41	6
06C1	44	m	6.10	0.17	0.0896	0.0021	-0.6391	978	32	1145	94400	7080	47000	110000	12720	49400	9300	239	1860	600	3260	488	669	33	76	12
06C1	45	m	11.09	0.12	0.0587	0.0013	-0.1253	557	13	1901	125200	5331	46400	120300	15000	55200	8600	123	1800	690	3940	626	944	47	103	15
06C1	46	m	11.01	0.15	0.0611	0.0014	0.1141	560	13	1806	81200	3542	40500	97000	11820	44700	7300	107	1550	655	3620	607	942	57	142	23
06C1	47	m	10.67	0.11	0.0598	0.0013	0.1829	578	13	2276	83200	3742	44900	113600	13400	51800	7400	129	2490	638	3320	487	678	30	67	9
06C1	48	m	10.75	0.15	0.0603	0.0014	0.1965	573	14	1794	112000	4840	42800	104800	13600	48100	8400	121	2220	675	3640	550	818	35	78	11
06C1	49	m	10.32	0.22	0.0627	0.0015	-0.1551	596	17	1874	113800	5090	46000	116600	12160	57200	9600	118	2300	651	3420	501	671	32	64	10
06C1	50	m	8.29	0.16	0.0770	0.0017	0.0539	735	20	1466	101600	5870	57500	116000	12900	45500	7300	1029	2820	587	2690	319	437	20	45	7
06C1	51	m	10.76	0.24	0.0594	0.0014	-0.0374	572	17	1621	83100	3684	48400	116600	14700	57800	8500	149	10800	615	3020	461	734	39	102	14
06C1	52	m	11.25	0.20	0.0584	0.0014	-0.0036	549	14	1674	84200	3501	47600	112500	13400	46000	6100	147	15100	649	3450	576	939	55	127	19
06C1	53	m	9.68	0.15	0.0682	0.0016	0.0166	633	16	1254	90100	4220	49200	109400	13700	49800	8100	161	27300	615	3140	471	657	30	68	10
06C1	54	m	11.30	0.19	0.0586	0.0014	0.0231	547	14	1436	84800	3499	40100	89900	11160	39900	6000	179	15300	541	2820	410	588	27	62	8
06C1	55	m	11.22	0.20	0.0584	0.0015	-0.0758	552	14	1510	86100	3594	52700	111600	13420	46700	8600	239	19400	647	3270	501	738	35	79	10
06C1	56	m	11.06	0.18	0.0597	0.0013	0.0343	558	14	1542	75800	3197	54400	114100	13200	49500	6300	1050	14800	582	2440	251	293	12	23	2
06C1	57	m	11.21	0.16	0.0582	0.0013	-0.1428	551	13	1347	75000	3136	54900	109600	14750	48300	8400	661	12900	630	3220	456	627	30	63	8
06C1	58	m	11.21	0.18	0.0581	0.0013	0.1965	551	14	1431	81600	3380	57000	109600	12400	46900	7900	642	7900	593	3060	432	603	29	66	8
06C1	59	m	10.98	0.16	0.0600	0.0014	-0.0385	562	14	1335	79500	3378	55100	113300	14100	48600	8100	593	9700	612	3120	455	629	32	71	8
06C1	60	m	11.43	0.20	0.0586	0.0013	-0.0438	541	14	1806	97800	3982	47300	99000	12500	38600	7500	240	6000	582	2920	457	642	32	68	8
08A3	1	m	12.12	0.21	0.0586	0.0014	0.0610	511	13	1414	62400	2525														
08A3	2	m	11.95	0.17	0.0599	0.0016	0.0214	518	13	1234	68200	2759														
08A3	3	m	11.99	0.19	0.0598	0.0015	0.2669	517	13	1330	70200	2842														
08A3	4	m	12.09	0.16	0.0590	0.0014	0.1157	512	12	1494	66100	2662														
08A3	6	m	12.03	0.19	0.0597	0.0015	0.0068	515	13	1421	74100	2988														
08A3	7	m	12.17	0.15	0.0580	0.0014	0.0000	509	12	1681	72000	2817														
08A3	10	m	11.60	0.17	0.0583	0.0013	0.0235	533	13	1904	80400	3302														
08A3	13	m	11.99	0.17	0.0572	0.0014	0.1162	516	12	1539	83000	3296														

08A3	14	m	11.95	0.16	0.0571	0.0014	0.0056	518	12	1553	81300	3218																		
08A3	15	m	11.95	0.16	0.0564	0.0015	0.0168	518	12	1545	82500	3259																		
08A3	17	m	12.02	0.16	0.0566	0.0014	0.0388	515	12	1652	77200	3000																		
08A3	18	m	11.95	0.19	0.0565	0.0015	0.0364	518	13	1510	80400	3178																		
08A3	19	m	11.90	0.20	0.0565	0.0014	0.0501	520	13	1556	81500	3225																		
08A3	20	m	12.15	0.19	0.0559	0.0014	0.0000	510	13	1595	76000	2976																		
08A3	21	m	11.96	0.19	0.0565	0.0014	0.1246	518	13	1445	75600	2963																		
08A3	22	m	11.86	0.18	0.0570	0.0014	0.0051	522	13	1441	78400	3121																		
08A3	23	m	11.61	0.18	0.0577	0.0014	0.0000	532	13	1832	77700	3178																		
08A3	24	m	12.14	0.21	0.0568	0.0014	0.0379	510	13	1582	75800	2964																		
08A3	25	m	11.67	0.16	0.0565	0.0013	0.0000	530	13	1950	80700	3235																		
08A3	26	m	11.96	0.19	0.0570	0.0015	0.3176	518	13	1340	76500	3023																		
08A3	29	m	11.93	0.20	0.0578	0.0015	0.0847	519	13	1261	74100	2902																		
08A3	30	m	11.59	0.19	0.0579	0.0015	0.0300	534	14	1460	78900	3218																		
08A3	34	m	12.03	0.20	0.0577	0.0015	0.0000	514	13	1405	72800	2852																		
08A3	36	m	12.03	0.17	0.0586	0.0014	0.1636	515	13	1386	70500	2790																		
08A3	37	m	11.76	0.19	0.0577	0.0013	0.0000	526	13	1659	77600	3112																		
08A3	38	m	12.03	0.19	0.0578	0.0015	0.0000	514	13	1459	81100	3193																		
08A3	40	m	12.02	0.19	0.0582	0.0015	0.0726	515	13	1334	76500	3000																		
08A3	43	m	12.02	0.20	0.0583	0.0015	0.0278	515	13	1483	76600	3026																		
08A3	45	m	12.12	0.21	0.0595	0.0015	0.0000	511	13	1557	78900	3092																		
08A3	46	m	12.05	0.19	0.0589	0.0015	0.0000	514	13	1473	77800	3096																		
08A3	47	m	12.02	0.17	0.0596	0.0014	0.0000	515	13	1427	78800	3105																		
08A3	48	m	12.08	0.23	0.0582	0.0014	0.0000	512	14	1560	74700	2916																		
08A3	52	m	12.08	0.23	0.0592	0.0015	0.0000	514	14	1394	80800	3216																		
08A3	53	m	12.17	0.21	0.0582	0.0014	0.0340	509	13	1423	81800	3274																		
08A3	55	m	11.96	0.24	0.0581	0.0015	0.1675	518	14	1415	81800	3278																		
08A3	56	m	11.95	0.23	0.0586	0.0015	0.0816	518	14	1424	82400	3289																		
08A3	57	m	12.00	0.23	0.0576	0.0014	0.0000	516	14	1457	85200	3377																		
08A3	58	m	12.06	0.19	0.0582	0.0014	0.2177	513	13	1343	84600	3336																		
08A3	59	m	12.08	0.20	0.0584	0.0015	0.0325	513	13	1320	82300	3248																		
08A3	61	m	12.05	0.20	0.0584	0.0014	0.0000	514	13	1379	80700	3195																		
08A3	62	m	12.09	0.22	0.0595	0.0014	0.0000	512	13	1372	80000	3154																		
08A3	63	m	12.03	0.25	0.0583	0.0014	0.0699	514	14	1340	79300	3174																		
08A3	64	m	12.27	0.23	0.0588	0.0014	0.0300	505	14	1355	78400	3067																		
08A3	66	m	12.15	0.22	0.0596	0.0015	0.0000	510	14	1210	75200	2957																		
08A3	67	m	12.11	0.22	0.0590	0.0015	0.0000	511	14	1294	76600	3033																		
08A3	68	m	12.03	0.19	0.0574	0.0014	0.0000	515	13	1263	73300	2913																		
08A3	69	m	12.05	0.20	0.0587	0.0015	0.0000	514	13	1276	75200	2956																		
08A3	70	m	11.83	0.18	0.0589	0.0014	0.1853	523	13	1294	75300	3001																		
10B1	2	z	11.76	0.15	0.0582	0.0014	0.1514	526	12	179	34	9	9960	0	1	0	2	5	1	18	5	47	12	38	6	49	6
10B1	3	z	11.72	0.12	0.0576	0.0013	0.1542	528	12	163	25	6	10790	0	2	0	1	7	0	19	6	57	16	51	8	61	7
10B1	4	z	11.58	0.12	0.0585	0.0013	0.0974	534	12	153	23	6	10400	0	1	0	1	6	0	15	5	53	15	52	8	59	8
10B1	5	z	11.79	0.12	0.0580	0.0012	0.0079	525	12	311	82	21	10860	0	2	0	1	10	0	21	6	66	20	65	12	87	12
10B1	6	z	11.75	0.11	0.0584	0.0012	0.1925	527	12	323	77	19	11640	0	2	0	2	9	0	21	7	82	23	73	13	96	13
10B1	7	z	11.84	0.11	0.0584	0.0012	0.0012	523	11	328	76	20	11640	0	2	0	3	10	1	24	7	87	24	84	15	121	17
10B1	8	z	11.92	0.12	0.0580	0.0012	0.1168	519	12	342	83	20	10440	0	2	0	2	11	1	21	6	76	23	73	13	98	13
10B1	9	z	11.64	0.11	0.0582	0.0012	0.0017	531	12	266	52	13	10200	0	1	0	2	9	0	21	6	70	19	61	9	73	10
10B1	10	z	11.78	0.11	0.0583	0.0012	0.0912	525	11	344	87	22	10580	0	1	0	3	10	0	21	6	70	19	61	10	73	9
10B1	11	z	11.83	0.11	0.0586	0.0013	-0.1594	523	12	223	29	7	10920	2	1	3	2	8	1	19	6	69	20	68	13	94	14
10B1	12	z	11.30	0.14	0.0582	0.0014	0.2060	546	13	112	7	2	10180	0	1	0	1	5	1	19	7	87	23	64	9	58	7
10B1	13	z	10.92	0.11	0.0580	0.0013	0.1472	566	13	124	9	2	10220	0	1	1	1	5	0	14	6	81	24	84	15	124	22
10B1	14	z	11.94	0.13	0.0576	0.0012	0.2808	519	12	253	5	1	11400	0	1	0	1	5	0	21	10	112	31	90	13	85	11
10B1	15	z	11.80	0.13	0.0577	0.0012	0.0118	525	12	249	11	3	10650	0	2	1	2	7	1	30	12	130	36	101	15	88	12
10B1	16	z	11.78	0.12	0.0578	0.0013	-0.2283	525	12	199	6	2	11460	0	1	0	1	5	0	21	8	93	26	74	11	76	10
10B1	17	z	11.72	0.11	0.0583	0.0013	-0.0469	528	12	230	24	6	10730	0	1	0	2	6	0	24	9	87	24	64	10	61	9
10B1	18	z	11.61	0.11	0.0581	0.0012	-0.0900	532	12	484	145	35	11140	1	2	1	2	7	0	26	11	107	32	104	18	119	17

10B1	19	z	11.58	0.12	0.0585	0.0012	0.1496	534	12	367	88	23	11360	4	2	2	2	4	1	24	8	91	28	83	15	108	15
10B1	20	z	11.66	0.13	0.0576	0.0012	0.1373	530	12	383	95	24	11020	0	2	3	2	6	1	21	7	80	24	82	14	99	16
10B1	21	z	11.51	0.12	0.0580	0.0012	0.1050	537	12	406	102	27	11850	0	2	3	2	6	1	22	8	85	28	90	17	105	15
10B1	22	z	11.50	0.11	0.0583	0.0012	0.1508	538	12	409	110	28	11660	0	2	6	2	5	1	25	9	88	29	86	15	115	17
10B1	23	z	11.79	0.15	0.0583	0.0012	0.0613	525	12	437	115	28	12000	0	2	0	3	5	1	22	9	89	27	96	17	113	16
10B1	25	z	11.61	0.15	0.0583	0.0012	0.0406	532	12	436	72	18	12400	0	12	0	89	57	6	210	46	690	220	410	99	500	71
10B1	26	z	11.42	0.11	0.0582	0.0013	0.1464	542	12	269	46	12	12010	0	1	0	2	3	1	20	9	99	30	92	16	108	15
10B1	27	z	11.71	0.11	0.0590	0.0013	0.1303	528	12	202	21	6	11300	0	3	0	7	9	2	47	16	170	50	176	36	270	44
10B1	28	z	11.64	0.14	0.0582	0.0013	-0.0695	532	12	259	4	2	11300	0	2	0	1	4	1	31	11	94	25	57	9	53	7
10B1	29	z	11.25	0.12	0.0586	0.0013	0.0226	549	12	210	16	4	9880	0	1	0	1	3	1	18	7	69	20	70	16	131	21
10B1	30	z	11.10	0.15	0.0587	0.0013	-0.0679	556	13	299	19	5	11120	0	1	0	1	3	1	14	7	75	23	75	16	138	22
10B1	32	z	11.66	0.14	0.0594	0.0012	-0.0336	530	12	487	4	2	11350	0	2	0	2	4	1	42	28	417	166	664	148	1211	174
10B1	33	z	11.61	0.12	0.0585	0.0013	-0.1556	533	12	263	5	2	11560	0	1	0	0	1	1	9	6	88	38	169	41	397	66
10B1	35	z	11.39	0.12	0.0582	0.0013	-0.1799	542	12	152	2	1	10450	0	1	0	1	1	1	10	6	96	46	209	53	509	77
10B1	36	z	11.72	0.11	0.0584	0.0012	0.0087	528	12	382	13	3	10880	0	1	0	1	2	1	10	5	92	40	194	52	504	89
10B1	38	z	10.87	0.10	0.0593	0.0012	0.0449	567	12	556	8	3	12200	0	1	0	1	1	0	2	2	33	20	145	53	676	129
10B1	39	z	11.19	0.12	0.0586	0.0012	0.0100	552	12	850	8	2	12070	0	1	0	0	1	0	6	4	60	25	107	27	257	42
10B1	40	z	11.10	0.12	0.0597	0.0012	-0.1178	556	13	824	33	11	12900	0	1	0	0	1	1	7	5	69	33	184	60	712	132
10B1	41	z	11.60	0.12	0.0583	0.0013	0.0560	533	12	351	6	1	11400	0	1	0	0	1	1	7	5	62	27	115	29	289	47
10B1	42	z	11.52	0.15	0.0572	0.0013	0.0420	536	12	127	21	5	10360	0	1	0	1	3	1	12	6	67	22	72	14	110	15
10B1	43	z	11.36	0.13	0.0582	0.0012	0.0457	544	13	319	6	2	10550	0	0	0	1	3	1	9	6	82	31	131	32	275	49
10B1	44	z	11.86	0.12	0.0576	0.0013	-0.1466	522	12	235	63	15	10770	0	2	0	2	6	1	20	9	85	25	75	12	87	11
10B1	45	z	11.56	0.16	0.0582	0.0013	0.0008	535	13	131	4	1	8940	0	1	0	1	3	1	11	7	77	24	100	25	241	39
10B1	46	z	11.49	0.15	0.0585	0.0013	0.1773	538	13	161	14	3	9470	0	1	0	1	3	1	12	8	90	31	124	27	208	32
10B1	48	z	11.00	0.12	0.0586	0.0013	0.0310	561	13	163	16	4	7450	0	1	0	1	4	1	11	5	81	30	129	33	318	55
10B1	49	z	11.55	0.13	0.0585	0.0013	-0.0688	536	12	185	14	4	7450	0	1	0	0	2	1	9	5	62	24	102	26	257	46
10B1	51	z	11.43	0.13	0.0576	0.0013	-0.0562	541	12	140	19	5	7340	0	1	0	0	2	1	8	5	61	23	89	20	170	28
10B1	52	z	11.35	0.14	0.0592	0.0013	0.0076	544	13	191	10	3	7870	0	0	0	0	3	1	10	7	111	46	215	59	617	104
10B1	53	z	10.85	0.16	0.0584	0.0015	0.0572	569	14	72	9	3	6230	0	1	0	1	4	1	9	4	33	8	22	4	25	3
10B1	54	z	11.36	0.13	0.0581	0.0013	0.0094	544	12	163	33	8	7520	0	1	0	1	4	0	11	5	48	15	50	9	73	12
10B1	55	z	11.69	0.13	0.0585	0.0013	0.0021	529	12	165	4	1	9150	0	1	0	1	1	1	6	7	95	41	211	58	566	99
10B1	56	z	11.48	0.14	0.0585	0.0015	0.1349	539	13	83	3	1	9150	0	0	0	1	5	2	12	7	80	23	79	14	95	13
10B1	57	z	11.67	0.14	0.0584	0.0013	-0.0661	530	12	227	5	1	8530	0	1	0	0	2	1	9	7	109	47	235	62	601	108
13D1	1	m	11.75	0.21	0.0577	0.0013	0.2147	526	14	5040	32820	1204		64300	132200	14070	45900	10200	12	3750	188	496	47	48	2	4	1
13D1	2	m	11.64	0.16	0.0582	0.0013	0.1717	532	13	7020	32760	1236		56400	113400	12010	41700	7000	70	4160	395	1867	252	393	20	52	8
13D1	3	m	10.19	0.17	0.0606	0.0014	0.1094	603	15	4596	43450	1831		65000	117900	13500	36000	8900	371	5010	479	2320	327	552	35	102	15
13D1	4	m	10.57	0.17	0.0605	0.0013	0.1605	583	15	5220	41680	1721		64500	123000	11330	41300	8000	282	4960	454	2300	326	527	31	85	14
13D1	5	m	10.45	0.16	0.0595	0.0013	0.1718	589	15	4990	39090	1628		64000	115100	13100	41500	6800	319	5100	476	2290	327	544	34	85	14
13D1	6	m	11.86	0.24	0.0578	0.0013	0.1806	522	14	4490	29400	1098		67400	129000	14200	44800	5900	12	3390	166	407	32	25	1	1	0
13D1	7	m	11.14	0.14	0.0588	0.0013	0.3529	554	13	5840	39910	1565		58100	120400	13400	41000	8700	206	4770	466	2320	343	525	28	70	11
13D1	8	m	9.87	0.18	0.0614	0.0014	0.1912	622	17	3059	35520	1568		64300	120300	12620	36800	7900	399	4990	457	2330	329	559	36	103	16
13D1	9	m	9.80	0.13	0.0615	0.0015	0.0603	626	15	2811	34600	1547		61200	115800	13200	35000	8400	362	4800	437	2220	307	539	34	98	15
13D1	10	m	9.97	0.16	0.0618	0.0014	0.1043	616	16	3101	37400	1640		63000	118900	12900	35300	7500	404	5130	496	2430	335	598	41	111	18
13D1	11	m	11.71	0.22	0.0579	0.0013	-0.0026	528	14	2908	34660	1259		62300	126600	15500	49200	11400	12	3470	161	433	31	23	1	1	0
13D1	12	m	10.33	0.23	0.0604	0.0014	-0.2589	595	18	2170	35100	1499		63300	121200	13000	43000	7900	390	5150	470	2390	347	558	35	96	14
13D1	13	m	11.72	0.19	0.0577	0.0012	-0.1630	528	13	2758	34560	1279		64100	134600	15100	48700	8100	13	3480	168	423	34	27	1	1	0
13D1	14	m	11.39	0.17	0.0588	0.0013	0.1388	543	13	2807	29930	1165		67000	123600	14300	38800	8400	189	5120	450	2470	339	595	35	92	14
13D1	15	m	11.66	0.18	0.0578	0.0013	0.0134	530	13	2485	33540	1229		62100	133400	13500	46700	9600	10	3540	161	403	28	25	0	1	0
13D1	16	m	9.87	0.15	0.0623	0.0014	0.1309	622	15	1806	39400	1728		59000	117300	11900	39000	6000	390	5010	456	2216	335	547	39	112	16
13D1	17	m	11.56	0.19	0.0585	0.0013	0.1600	535	14	4140	33250	1252		64400	120400	14000	41700	5900	90	4850	440	2300	323	499	26	63	10
13D1	18	m	9.88	0.17	0.0617	0.0015	0.2732	622	16	1636	37320	1687		58100	118200	12690	42900	4700	379	4910	456	2340	335	569	34	103	16
13D1	19	m	11.78	0.21	0.0578	0.0013	-0.0506	525	14	2595	30390	1148		67000	126000	13700	41400	5800	58	4790	386	1880	245	350	18	45	8
13D1	20	m	11.67	0.16	0.0585	0.0013	0.3199	530	13	2518	32610	1231		61800	129100	14100	44500	6300	30	4450	335	1590	225	366	20	53	8
13D1	21	m	11.04	0.18	0.0589	0.0013	0.2270	559	14	3530	18870	718		64500	124700	11600	43300	6500	244	4980	410	2250	315	472	27	68	9
13D1	22	m	9.96	0.13	0.0606	0.0013	-0.0115	617	15	3077	6620	289		65900	124700	14300	40700	6800	352	4860	426	2110	313	509	34	90	12
13D1	23	m	9.90	0.17	0.0609	0.0013	-0.0164	620	16	2452	6980	317		67100	123300	14500	44100	5100	388	5110	444	2220	309	513	33	98	13
13D1	24	m	9.86	0.15	0.0608	0.0014	0.0771	623	15	1464	5730	250		70400	123400	14800	48900	7700	378	4760	418	2090	274	439	30	99	14

13D1	25	m	9.91	0.20	0.0614	0.0016	0.0182	619	17	1471	5638	247	69500	135100	13300	45000	5400	428	4650	442	2174	281	491	34	115	17
13D1	26	m	10.79	0.20	0.0597	0.0013	0.1032	571	15	3039	13470	524	72100	127100	14140	45400	6800	233	4730	433	2090	305	485	30	77	11
13D1	27	m	11.34	0.18	0.0585	0.0013	0.0170	545	14	2850	25440	934	69400	128200	14840	49900	8600	59	4490	382	1710	245	392	23	59	9
13D1	28	m	10.46	0.18	0.0598	0.0013	-0.0561	588	15	6910	6520	278	68000	124500	14010	42100	7300	284	4950	445	2270	313	501	30	78	10
13D1	29	m	11.64	0.27	0.0576	0.0015	-0.1305	531	16	2057	34160	1223	62000	124200	13440	52500	6300	11	3430	172	580	62	67	3	7	1
13D1	30	m	11.48	0.21	0.0579	0.0013	0.1273	538	15	2990	26330	968	64500	127600	14400	43300	7400	33	4530	411	2060	324	532	30	81	13
13D1	31	m	11.86	0.20	0.0584	0.0013	0.0805	522	13	3310	25070	900	68100	123200	13900	46000	8400	27	5370	421	1540	172	196	11	28	4
13D1	32	m	12.14	0.18	0.0576	0.0013	0.0653	511	12	2892	27840	982	64900	126700	13100	47600	7800	48	4400	315	1081	102	96	3	6	1
13D1	33	m	12.02	0.19	0.0582	0.0013	0.1201	515	13	2803	24750	885	65100	124400	15380	47000	6700	24	4970	410	1880	256	430	26	65	10
13D1	34	m	11.34	0.21	0.0584	0.0013	-0.0831	545	14	3201	23550	892	65000	122500	14200	43100	6100	40	4670	433	2240	354	542	34	83	13
13D1	35	m	10.66	0.16	0.0591	0.0012	0.0365	578	14	4840	6930	279	64900	131200	13500	47700	7900	492	4780	416	2030	265	361	19	42	5
13D1	36	m	9.86	0.11	0.0608	0.0013	-0.1949	622	14	2625	5223	229	70700	135000	13900	46500	6500	373	4710	438	2170	302	471	32	87	12
13D1	37	m	11.10	0.17	0.0587	0.0013	-0.1474	556	14	4960	7600	288	69300	133900	14500	39800	7800	333	4700	420	1990	267	397	22	47	5
13D1	38	m	11.49	0.24	0.0588	0.0014	0.0720	538	15	2320	23220	865	65200	123400	14400	44900	4500	26	4680	430	2260	348	607	37	95	15
13D1	39	m	11.53	0.19	0.0583	0.0014	-0.1162	536	14	1999	30710	1107	61900	125700	14400	43100	4600	17	4180	351	1767	276	445	26	60	10
13D1	40	m	11.99	0.19	0.0579	0.0013	-0.0455	516	13	2892	21600	753	56300	113200	12600	35500	7400	23	4670	397	1635	204	315	18	44	7
13D1	41	m	11.25	0.18	0.0587	0.0012	0.0736	549	14	4940	7740	308	72000	134900	14130	39600	7300	295	4790	447	2140	284	419	24	53	7
13D1	42	m	10.36	0.15	0.0597	0.0013	0.2046	594	14	4610	8070	330	67800	127200	13860	40600	7700	329	4860	437	2060	303	482	26	61	8
13D1	43	m	9.81	0.16	0.0607	0.0013	-0.0674	626	16	1743	4516	195	72300	132400	14410	46600	9800	409	4640	444	2020	292	465	34	97	15
13D1	44	m	9.82	0.20	0.0612	0.0013	-0.0968	625	17	2683	6470	291	74700	129300	13900	50300	8000	363	4600	422	2015	288	478	31	85	13
13D1	45	m	9.87	0.20	0.0612	0.0014	0.0063	622	17	2167	5890	254	71800	135300	14500	46900	9000	401	4570	437	2090	290	480	35	100	15
13D1	46	m	10.18	0.16	0.0601	0.0013	0.0970	604	15	2719	5120	218	64700	128500	14400	46500	7000	438	4310	410	1960	248	351	18	40	5
13D1	47	m	9.80	0.16	0.0607	0.0014	0.1060	626	16	1655	5280	231	71700	136000	13600	45400	5700	394	4550	427	1960	268	442	29	90	13
13D1	48	m	9.79	0.15	0.0603	0.0013	0.0167	627	16	2535	6600	286	66900	123400	13310	41500	6500	391	4740	443	2140	291	474	32	87	12
13D1	49	m	10.19	0.15	0.0600	0.0013	0.1008	603	14	3252	5470	226	72300	132900	13000	41700	7800	447	4550	441	2260	316	496	31	65	10
13D1	50	m	9.97	0.16	0.0605	0.0013	-0.1222	616	16	3842	8170	349	64600	130400	14400	50600	6100	372	4370	417	2064	314	466	28	71	10
13D1	51	m	9.87	0.19	0.0602	0.0013	-0.1546	622	17	4470	8470	379	64700	126500	12300	48000	6200	342	4160	396	1920	299	441	28	65	9
13D1	52	m	11.19	0.21	0.0588	0.0013	-0.0124	552	15	4560	28520	1051	59800	114400	11900	39700	7800	95	4320	382	1940	275	460	26	68	10
13D1	53	m	10.35	0.25	0.0597	0.0015	0.1102	594	18	2586	11310	477	70800	126600	12730	49700	7100	296	4150	392	1894	280	437	30	77	13
13D1	54	m	11.05	0.17	0.0588	0.0013	0.0626	559	14	4712	29700	1134	59400	115200	11410	41500	6700	126	4010	385	1790	255	365	21	47	5
13D1	55	m	9.70	0.23	0.0608	0.0014	-0.2421	632	19	2505	5040	225	62600	125400	12900	45600	6100	369	4440	410	1840	259	414	30	78	12
13D1	56	m	9.92	0.16	0.0606	0.0014	0.0051	619	15	2901	5783	257	60200	119800	13300	45800	5900	385	4590	428	2080	284	470	37	104	15
13D1	57	m	9.81	0.16	0.0604	0.0014	0.1480	625	16	5070	6980	315	62900	118400	12800	47900	6800	347	4500	439	2000	295	465	30	78	11
13D1	58	m	11.22	0.18	0.0583	0.0012	0.1475	550	14	7030	30960	1160	64200	117700	12150	39700	8900	128	4370	378	1920	291	431	25	51	8
13D1	59	m	9.99	0.16	0.0608	0.0013	-0.1360	615	15	4640	6276	281	69900	131100	13200	43900	9600	343	4440	391	1930	275	452	30	78	11
13D1	60	m	9.86	0.21	0.0604	0.0015	0.3611	623	18	3718	5850	262	66200	120000	13900	42900	8800	367	4460	391	1820	250	383	25	64	10
14G1	1	m	9.93	0.17	0.0607	0.0014	0.1091	618	16	2261	4970	233	66100	127000	13880	47500	4400	279	4440	352	1717	238	367	27	68	10
14G1	2	m	9.98	0.21	0.0608	0.0016	0.2674	615	17	2449	5730	259	71500	130200	15000	46800	9960	317	4310	364	1661	222	356	23	68	10
14G1	3	m	11.78	0.21	0.0579	0.0013	0.0526	526	14	3264	25290	947	64300	119800	13500	46600	5900	84	4270	356	1610	255	385	25	66	10
14G1	4	m	9.73	0.28	0.0606	0.0019	-0.0341	630	21	1652	4219	198	65500	122100	11800	44200	8600	372	4500	376	1710	241	375	27	75	11
14G1	5	m	12.39	0.34	0.0587	0.0015	0.1431	500	16	3390	29760	1068	62300	116000	12500	46200	9000	21	4450	314	1091	104	108	4	7	1
14G1	7	m	12.05	0.30	0.0581	0.0014	-0.3475	514	16	2880	30000	1088	61000	120300	13300	45000	10300	37	4210	297	1210	186	260	15	43	7
14G1	8	m	10.15	0.21	0.0606	0.0015	0.1466	605	17	1713	4947	222	70400	129300	12990	49700	9100	395	4630	396	1890	268	446	32	91	14
14G1	9	m	10.44	0.26	0.0602	0.0014	0.3859	590	18	3347	9210	389	70100	115400	12800	44400	6000	301	4600	413	1906	279	396	23	58	7
14G1	10	m	10.50	0.25	0.0601	0.0013	0.3426	586	18	4106	11100	478	68600	127400	13900	44700	10600	315	4840	433	2020	295	432	25	59	7
14G1	21	m	11.57	0.16	0.0601	0.0014	0.2153	534	13	1458	113800	4247	52600	112800	13300	47600	9700	37	3210	125	274	19	10	0	1	0
14G1	22	m	11.68	0.23	0.0597	0.0015	-0.0006	531	15	1449	113300	4220	51300	115100	14200	51100	6100	35	3210	126	276	18	13	0	1	0
14G1	23	m	11.56	0.20	0.0592	0.0013	-0.2392	535	14	3750	83000	3241	48600	114100	12000	51000	7000	78	5620	304	811	58	34	0	0	0
14G1	24	m	11.49	0.26	0.0587	0.0014	-0.0626	537	16	2540	76600	2962	53400	113000	13200	42900	9400	64	4850	255	576	36	21	1	1	0
14G1	25	m	11.30	0.17	0.0597	0.0013	0.0314	547	13	3008	64900	2500	55000	112300	13200	53300	7600	134	5370	340	1222	114	98	3	5	1
14G1	26	m	11.25	0.22	0.0595	0.0013	0.0441	549	15	3214	82700	3102	50000	106400	14300	49800	8800	127	5290	399	1571	169	169	7	15	2
14G1	27	m	11.30	0.18	0.0594	0.0013	-0.1548	548	14	3355	67400	2566	54700	112900	13400	47900	10100	148	5180	384	1629	173	155	5	8	1
14G1	30	m	11.31	0.36	0.0592	0.0013	0.0184	546	19	3615	56800	2253	50900	106400	12900	44000	9200	158	5830	489	2172	232	216	7	10	1
14G1	31	m	11.34	0.10	0.0588	0.0012	0.1443	545	12	3010	63000	2434	56200	115200	13500	50200	10200	112	5270	394	1531	132	94	2	4	0
14G1	32	m	11.33	0.13	0.0593	0.0014	0.0088	546	13	2089	78600	3024	55000	108700	13600	44900	11300	71	4380	249	574	33	21	1	0	0
14G1	34	m	11.17	0.11	0.0602	0.0013	-0.2481	553	12	3469	68000	2650	56000	116200	14300	50200	11700	116	5680	467	1670	146	118	4	4	1
14G1	35	m	11.19	0.11	0.0597	0.0013	0.2860	552	12	2266	80800	3090	50800	111300	13000	45100	8900	75	4270	233	570	33	19	0	0	0

14G1	38	m	11.11	0.17	0.0596	0.0018	-0.1419	556	14	1049	90200	3490		49400	111800	13600	54200	7400	39	2800	119	272	17	10	0	0	0
14G1	41	m	11.31	0.11	0.0598	0.0013	0.1290	546	12	2770	63000	2375		56700	117900	13500	46500	6200	171	6670	472	1900	222	238	12	19	3
14G1	42	m	10.35	0.16	0.0611	0.0014	-0.0138	595	15	2030	80700	3194		54900	117900	14600	43700	4800	252	5420	267	960	84	76	3	3	0
14G1	43	m	10.25	0.13	0.0608	0.0013	0.4593	601	14	3314	75500	3038		54300	105200	13400	40300	6900	288	7710	426	2000	234	262	9	16	2
14G1	45	m	10.29	0.10	0.0599	0.0014	-0.0042	598	13	3150	48900	2054		57400	107400	13000	38300	9900	255	11310	629	3370	476	611	28	50	7
14G1	47	m	11.07	0.15	0.0591	0.0015	0.2834	557	13	3600	63000	2496		53400	108100	13500	42300	8100	207	17900	635	3220	363	373	14	20	2
14G1	50	m	10.31	0.14	0.0607	0.0016	0.1370	597	14	2072	80300	3224		51600	110100	14300	43400	5500	199	30400	315	1246	143	164	7	15	2
14G1	51	m	11.03	0.18	0.0590	0.0014	0.3124	560	14	2023	71400	2734		54400	117000	14300	45900	9400	82	0	338	1079	98	77	2	2	0
14G1	56	m	11.22	0.12	0.0596	0.0014	0.1745	551	12	1919	87600	3235		54400	111400	14400	52800	6400	66	0	237	744	63	49	1	2	0
MD46	32	z	11.87	0.09	0.0576	0.0012	0.0746	521	11	595	150	37	16190	0	2	0	3	6	0	16	3	23	6	16	2	16	3
MD46	30	z	11.94	0.08	0.0577	0.0012	-0.0699	519	11	695	67	16	17450	0	1	0	1	3	0	20	6	46	9	22	3	17	2
MD46	27	z	12.14	0.09	0.0577	0.0012	0.0065	510	11	898	102	25	16210	0	2	0	2	7	0	25	6	47	12	35	6	40	6
MD46	25	z	12.35	0.09	0.0579	0.0012	0.0822	502	11	1080	135	31	17050	0	2	0	2	5	0	18	4	31	7	22	4	25	4
MD46	38	z	11.45	0.11	0.0582	0.0012	-0.0412	540	12	826	70	18	16700	0	1	0	1	3	0	17	5	42	10	26	4	27	4
MD46	34	z	11.74	0.11	0.0583	0.0012	0.0551	527	12	497	128	33	15250	0	4	0	4	6	0	20	4	33	9	29	5	36	6
MD46	26	z	12.17	0.08	0.0583	0.0012	-0.0030	509	11	1078	100	25	16410	0	1	0	1	3	0	17	4	38	8	24	4	26	4
MD46	31	z	11.90	0.09	0.0583	0.0012	0.0117	520	11	766	37	10	14910	0	3	0	3	10	0	34	7	59	16	49	8	61	10
MD46	28	z	12.06	0.10	0.0584	0.0012	0.0814	514	11	709	141	38	14710	0	3	0	3	8	0	22	4	29	7	23	4	26	4
MD46	37	z	11.53	0.12	0.0585	0.0012	-0.3105	536	12	950	94	24	17360	0	2	0	1	3	0	26	7	69	18	54	8	61	9
MD46	36	z	11.65	0.12	0.0585	0.0012	-0.1689	531	12	609	69	19	15480	0	2	0	2	4	0	18	5	42	10	32	5	38	6
MD46	29	z	11.98	0.08	0.0588	0.0012	-0.0288	517	11	789	71	18	14290	0	3	0	4	9	0	34	7	59	16	48	8	57	9
MD46	35	z	11.70	0.09	0.0589	0.0012	-0.1956	529	11	1186	146	36	18420	0	4	0	3	6	0	38	10	99	25	73	11	74	10
MD46	39	z	11.35	0.21	0.0593	0.0012	-0.4402	544	14	1031	128	35	14080	0	4	0	4	8	0	33	7	65	17	53	8	65	10
MD46	40	z	11.29	0.10	0.0595	0.0012	-0.1110	547	12	993	95	26	16070	0	2	0	1	3	0	23	7	63	16	47	7	56	9
MD46	42	z	10.87	0.11	0.0596	0.0012	-0.0923	567	13	729	55	16	16900	0	2	0	1	2	0	13	4	34	9	27	4	33	5
MD46	47	z	10.54	0.08	0.0599	0.0012	-0.2311	584	12	1451	131	38	17460	0	2	0	1	2	0	19	5	53	14	41	6	44	7
MD46	50	z	10.31	0.09	0.0600	0.0012	-0.0144	597	13	1212	108	32	16080	0	2	0	1	4	0	25	8	74	20	62	10	66	10
MD46	33	z	11.76	0.13	0.0601	0.0013	-0.0880	526	12	578	137	36	15880	0	4	0	4	5	0	21	5	44	11	32	5	42	7
MD46	49	z	10.37	0.10	0.0601	0.0012	-0.2485	593	13	867	70	20	16680	0	4	0	3	5	0	23	7	67	17	56	9	69	11
MD46	43	z	10.85	0.11	0.0601	0.0012	-0.1586	568	13	1228	76	22	16210	11	9	1	11	9	2	32	8	65	15	43	6	40	6
MD46	46	z	10.54	0.11	0.0602	0.0012	-0.3488	584	13	1640	98	29	16700	3	2	0	3	6	0	32	8	73	17	47	7	49	7
MD46	48	z	10.49	0.10	0.0605	0.0013	-0.4203	587	13	730	123	36	15450	0	3	0	2	4	0	21	5	49	12	39	6	46	7
MD46	45	z	10.63	0.09	0.0607	0.0012	-0.1862	580	12	1335	164	46	17000	0	7	1	7	7	1	40	11	98	26	74	12	83	12
MD46	44	z	10.79	0.12	0.0607	0.0013	-0.4576	572	13	1101	108	32	16280	0	2	0	2	4	0	27	8	78	21	64	11	89	15
MD46	52	z	10.06	0.09	0.0608	0.0012	-0.4669	612	13	1790	99	30	16010	0	1	0	2	7	0	37	9	72	18	45	6	43	7
MD46	51	z	10.06	0.08	0.0612	0.0012	0.1278	611	13	1258	124	40	15770	0	4	0	3	5	0	25	8	76	21	59	10	67	11

Appendix 9. Geochemical data for Precambrian large igneous provinces.

Source	Sample #	Rock type	Age	±	MgO	P2O5	P
			(Ma)		(wt.%)	(wt.%)	(ppm)
~3500 Ma							
Jahn et al. (1982)	5038	tholeiitic basalt	3560	240	4.22	0.20	872
Jahn et al. (1982)	5042	tholeiitic basalt	3560	240	10.95	0.16	698
Jahn et al. (1982)	5046	tholeiitic basalt	3560	240	10.79	0.14	610
Jahn et al. (1982)	5048	tholeiitic basalt	3560	240	19.43	0.12	523
Jahn et al. (1982)	5049	tholeiitic basalt	3560	240	11.70	0.13	567
Jahn et al. (1982)	5050	tholeiitic basalt	3560	240	12.88	0.15	654
Jahn et al. (1982)	5052	tholeiitic basalt	3560	240	10.94	0.13	567
Jahn et al. (1982)	5053	tholeiitic basalt	3560	240	7.52	0.15	654
Jahn et al. (1982)	5001	tholeiitic basalt	3560	240	9.01	0.08	349
Jahn et al. (1982)	5003	tholeiitic basalt	3560	240	10.60	0.10	436
Jahn et al. (1982)	5010	tholeiitic basalt	3560	240	6.32	0.07	305
Jahn et al. (1982)	5012	tholeiitic basalt	3560	240	8.74	0.13	567
Jahn et al. (1982)	5016	tholeiitic basalt	3560	240	5.76	0.15	654
Jahn et al. (1982)	5019	tholeiitic basalt	3560	240	34.18	0.05	218
Jahn et al. (1982)	5025	tholeiitic basalt	3560	240	5.59	0.14	610
Jahn et al. (1982)	5026	tholeiitic basalt	3560	240	10.62	0.11	480
Jahn et al. (1982)	5031	tholeiitic basalt	3560	240	31.34	0.07	305
Jahn et al. (1982)	5067	tholeiitic basalt	3560	240	9.79	0.08	349
Jahn et al. (1982)	SA39	tholeiitic basalt	3560	240	32.86	0.05	218
Jahn et al. (1982)	5077	tholeiitic basalt	3560	240	11.34	0.08	349
Jahn et al. (1982)	5080	tholeiitic basalt	3560	240	9.39	0.11	480
Jahn et al. (1982)	5084	tholeiitic basalt	3560	240	13.12	0.08	349
Jahn et al. (1982)	5085	tholeiitic basalt	3560	240	13.65	0.06	262
Jahn et al. (1982)	5088	tholeiitic basalt	3560	240	6.48	0.11	480
Jahn et al. (1982)	5092	tholeiitic basalt	3560	240	11.19	0.04	174
Jahn et al. (1982)	AB9	tholeiitic basalt	3560	240	11.52	0.06	262
Jahn et al. (1982)	AB9	tholeiitic basalt	3560	240	11.42	0.07	305
		n =	**27**			**Average =**	**455**
						Median =	**480**
~2700 Ma							
Crow and Condie (1988)	J3A	tholeiitic basalt	2725	25	1.86	0.21	916
Crow and Condie (1988)	J7A	tholeiitic basalt	2725	25	3.39	0.19	828
Crow and Condie (1988)	J17R	tholeiitic basalt	2725	25	4.75	0.20	872
Crow and Condie (1988)	D6M	tholeiitic basalt	2725	25	1.26	0.21	916
Crow and Condie (1988)	J25G	tholeiitic basalt	2725	25	4.49	0.68	2965
Crow and Condie (1988)	34E	tholeiitic basalt	2725	25	13.36	0.05	218
Crow and Condie (1988)	S21E	tholeiitic basalt	2725	25	8.20	0.07	305
Crow and Condie (1988)	S20L	tholeiitic basalt	2725	25	13.56	0.05	218
Crow and Condie (1988)	J28L	tholeiitic basalt	2725	25	7.17	0.16	698
Crow and Condie (1988)	C4L	tholeiitic basalt	2725	25	6.32	0.10	436
Crow and Condie (1988)	S10J	tholeiitic basalt	2725	25	4.99	0.12	523
Crow and Condie (1988)	J34J	tholeiitic basalt	2725	25	4.52	0.12	523
Crow and Condie (1988)	J35O	tholeiitic basalt	2725	25	4.98	0.13	567
Crow and Condie (1988)	S1O	tholeiitic basalt	2725	25	5.18	0.12	523
Crow and Condie (1988)	3-O	tholeiitic basalt	2725	25	11.46	0.10	436
Crow and Condie (1988)	3-M	tholeiitic basalt	2725	25	16.80	0.13	567
Crow and Condie (1988)	Allanridge	tholeiitic basalt	2725	25	3.83	0.32	1395
Crow and Condie (1988)	Reitgat	tholeiitic basalt	2725	25	4.37	0.49	2136
Crow and Condie (1988)	Makwassie	tholeiitic basalt	2725	25	2.51	0.22	959
Crow and Condie (1988)	Goedgenoeg	tholeiitic basalt	2725	25	5.60	0.57	2485
Crow and Condie (1988)	Edenville	tholeiitic basalt	2725	25	10.52	0.06	262
Crow and Condie (1988)	Loraine	tholeiitic basalt	2725	25	7.47	0.21	916
Crow and Condie (1988)	Jeannette	tholeiitic basalt	2725	25	4.90	0.12	523

Crow and Condie (1988)	Orkney	tholeiitic basalt	2725	25	5.30	0.13	567
Crow and Condie (1988)	Westonaria	tholeiitic basalt	2725	25	13.97	0.16	698
Schweitzer and Kroner (1985)	654	tholeiitic basalt	2725	25	7.16	0.08	349
Schweitzer and Kroner (1985)	831	tholeiitic basalt	2725	25	4.25	0.13	567
Schweitzer and Kroner (1985)	927	tholeiitic basalt	2725	25	5.51	0.14	610
Schweitzer and Kroner (1985)	1095	tholeiitic basalt	2725	25	4.00	0.12	523
Schweitzer and Kroner (1985)	999	tholeiitic basalt	2725	25	7.32	0.14	610
Schweitzer and Kroner (1985)	1481	tholeiitic basalt	2725	25	4.95	0.13	567
Schweitzer and Kroner (1985)	2935	tholeiitic basalt	2725	25	5.28	0.14	610
Schweitzer and Kroner (1985)	3130	tholeiitic basalt	2725	25	4.36	0.24	1046
Schweitzer and Kroner (1985)	3263	tholeiitic basalt	2725	25	2.91	0.13	567
Schweitzer and Kroner (1985)	3342	tholeiitic basalt	2725	25	3.35	0.17	741
Schweitzer and Kroner (1985)	3501	tholeiitic basalt	2725	25	3.82	0.19	828
Schweitzer and Kroner (1985)	3509	tholeiitic basalt	2725	25	3.81	0.08	349
Schweitzer and Kroner (1985)	3562	tholeiitic basalt	2725	25	1.54	0.07	305
Schweitzer and Kroner (1985)	3657	tholeiitic basalt	2725	25	5.70	0.12	523
Schweitzer and Kroner (1985)	3718	tholeiitic basalt	2725	25	2.96	0.03	131
Schweitzer and Kroner (1985)	3730	tholeiitic basalt	2725	25	3.42	0.14	610
Schweitzer and Kroner (1985)	763	tholeiitic basalt	2725	25	5.37	0.06	262
Schweitzer and Kroner (1985)	1095	tholeiitic basalt	2725	25	4.57	0.12	523
Schweitzer and Kroner (1985)	1174	tholeiitic basalt	2725	25	5.43	0.07	305
Schweitzer and Kroner (1985)	1231	tholeiitic basalt	2725	25	5.09	0.17	741
Schweitzer and Kroner (1985)	1337	tholeiitic basalt	2725	25	5.08	0.21	916
Schweitzer and Kroner (1985)	1513	tholeiitic basalt	2725	25	4.36	0.18	785
Schweitzer and Kroner (1985)	1542	tholeiitic basalt	2725	25	18.94	0.04	174
Schweitzer and Kroner (1985)	1548	tholeiitic basalt	2725	25	19.58	0.04	174
Schweitzer and Kroner (1985)	445	tholeiitic basalt	2725	25	5.85	0.11	480
Schweitzer and Kroner (1985)	673	tholeiitic basalt	2725	25	4.75	0.13	567
Schweitzer and Kroner (1985)	874	tholeiitic basalt	2725	25	5.13	0.14	610
Schweitzer and Kroner (1985)	903	tholeiitic basalt	2725	25	4.86	0.09	392
Schweitzer and Kroner (1985)	1025	tholeiitic basalt	2725	25	5.30	0.16	698
Schweitzer and Kroner (1985)	1042	tholeiitic basalt	2725	25	13.53	0.04	174
Schweitzer and Kroner (1985)	1055	tholeiitic basalt	2725	25	12.19	0.02	87
Hartlaub et al. (2004)	4700-0020	basalt	2720		6.36	0.21	916
Hartlaub et al. (2004)	4700-0023	basalt	2720		4.95	0.22	959
Hartlaub et al. (2004)	4700-0024	basalt	2720		7.79	0.14	610
Hartlaub et al. (2004)	4700-0031	basalt	2720		4.68	0.20	872
Hartlaub et al. (2004)	4700-0187	basalt	2720		5.41	0.17	741
Hartlaub et al. (2004)	4700-0313B	basalt	2720		5.62	0.18	785
Hartlaub et al. (2004)	4700-1049	basalt	2720		9.27	0.10	436
Hartlaub et al. (2004)	4700-4307	basalt	2720		8.14	0.07	305
Hartlaub et al. (2004)	4700-4341A	basalt	2720		7.30	1.42	6191
Hartlaub et al. (2004)	4700-4341B	basalt	2720		7.35	0.13	567
Hartlaub et al. (2004)	4700-4344A	basalt	2720		7.03	0.12	523
Hartlaub et al. (2004)	47-4344B	basalt	2720		6.71	0.15	654
Hartlaub et al. (2004)	4700-4537	basalt	2720		6.68	0.16	698
Hartlaub et al. (2004)	4700-4568	basalt	2720		5.01	0.16	698
Hartlaub et al. (2004)	4700-0320	gabbro	2720		6.43	0.31	1352
Hartlaub et al. (2004)	4700-0324	gabbro	2720		5.17	0.42	1831
Hartlaub et al. (2004)	4700-0416B	gabbro	2720		4.54	0.43	1875
Hartlaub et al. (2004)	4700-2057	gabbro	2720		7.37	0.13	567
Hartlaub et al. (2004)	4700-2280	gabbro	2720		6.88	0.12	523
Hartlaub et al. (2004)	4700-4343	gabbro	2720		5.35	0.20	872
Hartlaub et al. (2004)	4700-6147	gabbro	2720		5.85	0.40	1744
Hartlaub et al. (2004)	4700-6147/R	gabbro	2720		5.87	0.39	1700
Hartlaub et al. (2004)	4700-6148	gabbro	2720		5.96	0.39	1700
Hartlaub et al. (2004)	4700-0416A	gabbro	2720		5.46	0.41	1788
Fryer and Jenner (1978)	1	ultramafic flow	2700	300	32.09	0.00	0
Fryer and Jenner (1978)	2	ultramafic flow	2700	300	25.66	0.00	0

Fryer and Jenner (1978)	3	ultramafic flow	2700	300	32.34	0.00	0
Fryer and Jenner (1978)	4	ultramafic flow	2700	300	26.68	0.00	0
Fryer and Jenner (1978)	5	ultramafic flow	2700	300	7.65	0.07	305
Fryer and Jenner (1978)	6	ultramafic flow	2700	300	9.18	0.07	305
Fryer and Jenner (1978)	7	ultramafic flow	2700	300	8.11	0.06	262
Fryer and Jenner (1978)	8	ultramafic flow	2700	300	7.28	0.12	523
Fryer and Jenner (1978)	9	basalt	2700	300	6.64	0.08	349
Fryer and Jenner (1978)	10	basalt	2700	300	4.27	0.08	349
Fryer and Jenner (1978)	11	basalt	2700	300	8.68	0.07	305
Fryer and Jenner (1978)	12	basalt	2700	300	8.16	0.07	305
Fryer and Jenner (1978)	13	basalt	2700	300	8.15	0.06	262
Fryer and Jenner (1978)	14	basalt	2700	300	3.25	0.02	83
		n =	**94**			**Average =**	**737**
						Median =	**567**
~2400 Ma							
Kullerud et al. (2006)	R97-2,	gabbronorite	2403	3	20.19	0.09	392
Kullerud et al. (2006)	R97-4,	gabbronorite	2403	3	16.12	0.12	523
Kullerud et al. (2006)	R97-5,	gabbronorite	2403	3	21.47	0.09	392
Kullerud et al. (2006)	R99-25,	gabbronorite	2403	3	15.66	0.11	480
Kullerud et al. (2006)	R99-24,	gabbronorite	2403	3	15.30	0.08	349
Kullerud et al. (2006)	R97-3,	phyric dike	2403	3	5.65	0.20	872
Kullerud et al. (2006)	R97-8,	phyric dike	2403	3	6.02	0.18	785
Kullerud et al. (2006)	R97-10,	phyric dike	2403	3	6.44	0.17	741
Kullerud et al. (2006)	R97-11,	phyric dike	2403	3	6.72	0.17	741
Kullerud et al. (2006)	R97-13,	phyric dike	2403	3	5.09	0.28	1221
Kullerud et al. (2006)	R97-17,	phyric dike	2403	3	5.17	0.33	1439
Kullerud et al. (2006)	R97-18,	phyric dike	2403	3	4.83	0.32	1395
Kullerud et al. (2006)	R99-5,	phyric dike	2403	3	5.00	0.17	741
Kullerud et al. (2006)	R99-12,	phyric dike	2403	3	5.72	0.21	916
Kullerud et al. (2006)	R99-17,	phyric dike	2403	3	4.47	0.32	1395
Kullerud et al. (2006)	R99-18,	phyric dike	2403	3	5.55	0.20	872
Kullerud et al. (2006)	R99-26,	phyric dike	2403	3	5.62	0.22	959
Kullerud et al. (2006)	R99-1,	phyric dike	2403	3	6.53	0.12	523
Kullerud et al. (2006)	R99-2,	phyric dike	2403	3	8.07	0.20	872
Kullerud et al. (2006)	R99-4,	phyric dike	2403	3	4.78	0.27	1177
Kullerud et al. (2006)	R99-11,	phyric dike	2403	3	4.45	0.29	1264
Kullerud et al. (2006)	R99-13,	phyric dike	2403	3	5.08	0.24	1046
Kullerud et al. (2006)	R99-14,	phyric dike	2403	3	4.78	0.29	1264
Kullerud et al. (2006)	R99-15,	phyric dike	2403	3	6.36	0.22	959
Kullerud et al. (2006)	R99-16,	phyric dike	2403	3	4.88	0.24	1046
Kullerud et al. (2006)	R99-19,	phyric dike	2403	3	6.16	0.16	698
Kullerud et al. (2006)	R99-20,	phyric dike	2403	3	6.08	0.17	741
Kullerud et al. (2006)	R99-21,	phyric dike	2403	3	4.41	0.27	1177
Kullerud et al. (2006)	R99-30,	phyric dike	2403	3	5.41	0.26	1134
Kullerud et al. (2006)	R99-31,	phyric dike	2403	3	5.60	0.15	654
Kullerud et al. (2006)	R99-34,	phyric dike	2403	3	4.79	0.28	1221
Kullerud et al. (2006)	R99-35,	phyric dike	2403	3	5.94	0.21	916
Kullerud et al. (2006)	R99-36,	phyric dike	2403	3	5.10	0.25	1090
Kullerud et al. (2006)	R99-37,	phyric dike	2403	3	5.26	0.29	1264
Kullerud et al. (2006)	R99-38,	phyric dike	2403	3	5.73	0.16	698
Kullerud et al. (2006)	R99-39,	phyric dike	2403	3	6.59	0.14	610
French and Heaman (2010)	JEF-99-7	basaltic andesite	2369	1	11.07	0.13	567
Kumar et al. (2012)	KA6	basalt	2367	20	7.39	0.07	305
Kumar et al. (2012)	KA6-2	basalt	2367	20	7.74	0.06	262
Kumar et al. (2012)	KA8	basalt	2367	20	7.63	0.07	305
Kumar et al. (2012)	KA11	basalt	2367	20	8.56	0.07	305
Kumar et al. (2012)	KA13	basalt	2367	20	8.10	0.07	305
Kumar et al. (2012)	KA16	basalt	2367	20	8.26	0.05	218
Kumar et al. (2012)	KA65	basalt	2367	20	7.68	0.07	305

Kumar et al. (2012)	KA70	basalt	2367	20	8.62	0.04	174
Kumar et al. (2012)	KA73	basalt	2367	20	8.18	0.07	305
Kumar et al. (2012)	KA76	basalt	2367	20	8.13	0.07	305
Kumar et al. (2012)	KA78	basalt	2367	20	7.91	0.07	305
Kumar et al. (2012)	HY12	basalt	2367	20	8.87	0.13	567
Kumar et al. (2012)	HY15	basalt	2367	20	8.64	0.03	131
Kumar et al. (2012)	KB3-8-2	basalt	2367	20	4.63	0.16	698
Kumar et al. (2012)	KB3-11-4	basalt	2367	20	4.81	0.15	654
Kumar et al. (2012)	KB4-1-4	basalt	2367	20	4.63	0.13	567
Kumar et al. (2012)	KB6-5-2	basalt	2367	20	5.04	0.19	828
Kumar et al. (2012)	KB8-1-3	basalt	2367	20	4.93	0.31	1352
Kumar et al. (2012)	KB10-6-3	basalt	2367	20	4.74	0.42	1831
Kumar et al. (2012)	KB14-3-1	basalt	2367	20	6.50	0.14	610
Kumar et al. (2012)	KB16-9-1	basalt	2367	20	5.08	0.13	567
Kumar et al. (2012)	KB18-4-2	basalt	2367	20	4.92	0.12	523
Kumar et al. (2012)	KB18-7-2	basalt	2367	20	5.32	0.11	480
Kumar et al. (2012)	KB19-4A-2	basalt	2367	20	5.98	0.09	392
Kumar et al. (2012)	KB23-1-2	basalt	2367	20	5.87	0.15	654
Kumar et al. (2012)	KB24-1-2	basalt	2367	20	5.51	0.12	523
French and Heaman (2010)	JEF-99-6	basaltic andesite	2366	1	10.72	0.08	349
French and Heaman (2010)	JEF-99-1	basaltic andesite	2365	1	9.13	0.14	610
		n =	**65**			**Average =**	**732**
						Median =	**654**
~2200 Ma							
Manyeruke et al. (2004)		magnetite peridotite	2262	2	19.03	0.04	174
Manyeruke et al. (2004)		peridotite dike	2262	2	12.19	0.09	392
Manyeruke et al. (2004)		melatroctolite	2262	2	17.54	0.07	305
Manyeruke et al. (2004)		troctolite	2262	2	8.94	0.12	523
Manyeruke et al. (2004)		chilled troctolite	2262	2	8.08	0.15	654
Cornell et al. (1996)	77392	Basaltic andesite	2222	13	5.75	0.08	349
Cornell et al. (1996)	77396	Basaltic andesite	2222	13	6.90	0.09	392
Cornell et al. (1996)	77397	Basaltic andesite	2222	13	5.79	0.08	349
Cornell et al. (1996)	77394	Basaltic andesite	2222	13	6.08	0.12	523
Cornell et al. (1996)	77393	Basaltic andesite	2222	13	6.64	0.12	523
Cornell et al. (1996)	88BA6	Basaltic andesite	2222	13	6.71	0.10	436
Cornell et al. (1996)	88BA8	Basaltic andesite	2222	13	5.96	0.11	480
Cornell et al. (1996)	90BA20	Basaltic andesite	2222	13	5.73	0.11	480
Cornell et al. (1996)	90BAI9	Basaltic andesite	2222	13	6.22	0.12	523
Cornell et al. (1996)	77395	Basaltic andesite	2222	13	7.48	0.07	305
Cornell et al. (1996)	88BA5	Basaltic andesite	2222	13	6.22	0.08	349
Cornell et al. (1996)	90BA28	Basaltic andesite	2222	13	8.65	0.09	392
French and Heaman (2010)	JEF-00-55	basalt	2221	5	5.33	0.23	1003
French and Heaman (2010)	JEF-99-11	basalt	2209	3	15.51	0.06	262
French and Heaman (2010)	JEF-00-1	basalt	2181	1	5.45	0.15	654
French and Heaman (2010)	JEF-00-43	basalt	2176	4	2.77	0.24	1046
		n =	**21**			**Average =**	**482**
						Median =	**436**
~1800 Ma							
Hanson et al. (2004)	DB01.43	dolerite	1880	100	6.95	0.07	305
Hanson et al. (2004)	DB01.64	dolerite	1880	100	5.26	0.08	349
Hanson et al. (2004)	DB01.72	dolerite	1880	100	7.47	0.06	262
Hanson et al. (2004)	DB01.115	dolerite	1880	100	5.65	0.04	174
Hanson et al. (2004)	JP8	dolerite	1880	100	5.55	0.14	610
Hanson et al. (2004)	JP9	dolerite	1880	100	5.33	0.19	828
Hanson et al. (2004)	DB01.4	sill	1880	100	5.44	0.11	480
Bossi et al. (1993)	UR33	andesitic basalt	1860	120	5.69	0.12	523
Bossi et al. (1993)	UR46	andesitic basalt	1860	120	5.22	0.13	567
Bossi et al. (1993)	UK42	andesitic basalt	1860	120	4.39	0.15	654
Bossi et al. (1993)	UR28	andesitic basalt	1860	120	4.40	0.14	610

Bossi et al. (1993)	URI0	andesitic basalt	1860	120	4.35	0.15	654
Bossi et al. (1993)	URI	andesitic basalt	1860	120	4.16	0.16	698
Bossi et al. (1993)	UR4	andesitic basalt	1860	120	3.49	0.14	610
Bossi et al. (1993)	UR24	andesitic basalt	1860	120	3.67	0.18	785
Bossi et al. (1993)	UR58	andesite	1860	120	2.70	0.23	1003
Bossi et al. (1993)	UR13	andesite	1860	120	3.13	0.36	1570
Bossi et al. (1993)	URi6	andesite	1860	120	2.46	0.26	1134
Bossi et al. (1993)	UR30	andesite	1860	120	2.32	0.28	1221
Bossi et al. (1993)	UR23	andesite	1860	120	2.67	0.35	1526
Bossi et al. (1993)	UR49	andesite	1860	120	2.30	0.34	1482
Reis et al. (2013)	N-136	Subalkaline basalt	1794	3	5.07	0.40	1744
Reis et al. (2013)	AB-188	Subalkaline basalt	1794	3	5.00	0.24	1046
Reis et al. (2013)	AB-103A	Subalkaline basalt	1794	3	4.35	0.22	959
Reis et al. (2013)	NR-146	Andesite/basalt	1794	3	5.10	0.27	1177
Reis et al. (2013)	NR-294	Andesite/basalt	1794	3	6.18	0.15	654
Reis et al. (2013)	NR-498	Andesite/basalt	1794	3	9.47	0.07	305
Reis et al. (2013)	HC-172	Andesite/basalt	1794	3	7.58	0.07	305
Reis et al. (2013)	HC-88	Andesite/basalt	1794	3	5.68	0.12	523
Reis et al. (2013)	HC-90	Andesite/basalt	1794	3	5.07	0.14	610
		n =	**30**			**Average =**	**779**
						Median =	**654**
~1400 Ma							
Hoy (1989)	28161	basaltic	1445	11	5.86	0.17	741
Hoy (1989)	20803	basaltic	1445	11	6.44	0.16	698
Hoy (1989)	20802	basaltic	1445	11	9.55	0.15	654
Hoy (1989)	28162	basaltic	1445	11	7.53	0.09	392
Hoy (1989)	29596	basaltic	1445	11	5.86	0.07	305
Hoy (1989)	29597	basaltic	1445	11	7.10	0.09	392
Hoy (1989)	29595	basaltic	1445	11	6.83	0.46	2006
Hoy (1989)	28157	basaltic	1445	11	7.33	0.09	392
Hoy (1989)	28156	basaltic	1445	11	8.43	0.09	392
Hoy (1989)	28159	basaltic	1445	11	7.22	0.03	131
Hoy (1989)	28160	basaltic	1445	11	7.94	0.10	436
Hoy (1989)	26397	basaltic	1445	11	9.21	0.27	1177
Hoy (1989)	26396	basaltic	1445	11	8.33	0.00	0
Hoy (1989)	29598	basaltic	1445	11	8.25	0.55	2398
Hoy (1989)	28158	basaltic	1445	11	6.66	0.09	392
Hoy (1989)	22073	basaltic	1445	11	8.33	0.45	1962
Hoy (1989)	28151	basaltic	1445	11	8.25	0.09	392
Hoy (1989)	28154	basaltic	1445	11	6.66	0.20	872
Hoy (1989)	20797	basaltic	1445	11	6.83	0.18	785
Hoy (1989)	28155	basaltic	1445	11	6.15	0.09	392
Hoy (1989)	28149	basaltic	1445	11	8.55	0.30	1308
Hoy (1989)	20800	basaltic	1445	11	8.03	0.19	828
Hoy (1989)	28153	basaltic	1445	11	5.99	0.15	654
Hoy (1989)	20795	basaltic	1445	11	6.73	0.16	698
Hoy (1989)	24523	basaltic	1445	11	5.02	0.14	610
Hoy (1989)	28152	basaltic	1445	11	5.35	0.12	523
Hoy (1989)	28150	basaltic	1445	11	8.30	0.14	610
Hoy (1989)	20796	basaltic	1445	11	8.25	0.01	44
Upton et al. (2005)	273405	basal tholeiite	1382	2	10.19	0.13	567
Upton et al. (2005)	273407	basal tholeiite	1382	2	9.44	0.13	567
Upton et al. (2005)	273410.00	basal tholeiite	1382	2	8.93	0.12	523
Upton et al. (2005)	273419.00	aphyric tholeiite	1382	2	8.19	0.14	610
Upton et al. (2005)	273420.00	aphyric tholeiite	1382	2	8.06	0.14	610
Upton et al. (2005)	273426.00	aphyric tholeiite	1382	2	4.69	0.19	828
Upton et al. (2005)	273427.00	aphyric tholeiite	1382	2	4.16	0.18	785
Upton et al. (2005)	273430	aphyric tholeiite	1382	2	8.78	0.09	392
Upton et al. (2005)	273434	aphyric tholeiite	1382	2	8.37	0.09	392

Upton et al. (2005)	273436	aphyric tholeiite	1382	2	6.84	0.13	567
Upton et al. (2005)	273439	aphyric tholeiite	1382	2	7.41	0.12	523
Upton et al. (2005)	273442	porphyritic tholeiite	1382	2	6.69	0.13	567
Upton et al. (2005)	273446	porphyritic tholeiite	1382	2	7.48	0.09	392
Upton et al. (2005)	273447	porphyritic tholeiite	1382	2	7.84	0.09	392
Upton et al. (2005)	273451	porphyritic tholeiite	1382	2	6.63	0.10	436
Upton et al. (2005)	273470	porphyritic tholeiite	1382	2	7.13	0.10	436
Upton et al. (2005)	273473	porphyritic tholeiite	1382	2	7.32	0.10	436
Upton et al. (2005)	273478	porphyritic tholeiite	1382	2	7.51	0.09	392
Upton et al. (2005)	273479	porphyritic tholeiite	1382	2	8.18	0.09	392
Upton et al. (2005)	197402	porphyritic tholeiite	1382	2	8.30	0.10	436
Upton et al. (2005)	335774	porphyritic tholeiite	1382	2	5.87	0.26	1134
Upton et al. (2005)	273251	porphyritic tholeiite	1382	2	3.67	0.23	1003
Upton et al. (2005)	273493	porphyritic tholeiite	1382	2	4.57	0.09	392
		n =	**51**			**Average =**	**646**
						Median =	**523**

MacKenzie (~1267)

GEOROC database	DDH-MX-N-157	clinopyroxenite	1267	25.30	0.00	0
GEOROC database	HDB-2000-MX-04A	chromite	1267	15.10	0.00	0
GEOROC database	HDB-2000-MX-26A	chromite	1267	18.40	0.00	0
GEOROC database	HDB-2000-MX-40A	chromite	1267	17.70	0.00	0
GEOROC database	DDH-MX-N-75	dunite	1267	41.80	0.01	44
GEOROC database	DDH-MX-N-100	clinopyroxenite	1267	21.20	0.01	44
GEOROC database	DDH-MX-N-101	clinopyroxenite	1267	21.40	0.01	44
GEOROC database	DDH-MX-N-129	dunite	1267	41.40	0.01	44
GEOROC database	DDH-MX-N-141	dunite	1267	43.10	0.01	44
GEOROC database	DDH-MX-N-151	dunite	1267	32.10	0.01	44
GEOROC database	DDH-MX-S-44	dunite	1267	44.80	0.01	44
GEOROC database	DDH-MX-S-60	dunite	1267	43.00	0.01	44
GEOROC database	DDH-MX-S-69	dunite	1267	44.60	0.01	44
GEOROC database	DDH-MX-S-76	dunite	1267	43.00	0.01	44
GEOROC database	DDH-MX-N-59	peridotite	1267	35.00	0.02	87
GEOROC database	DDH-MX-N-97	peridotite	1267	41.70	0.02	87
GEOROC database	DDH-MX-N-104	peridotite	1267	35.50	0.02	87
GEOROC database	DDH-MX-N-111	dunite	1267	38.90	0.02	87
GEOROC database	DDH-MX-N-115	dunite	1267	40.20	0.02	87
GEOROC database	DDH-MX-S-51	dunite	1267	42.10	0.02	87
GEOROC database	DDH-MX-S-85	dunite	1267	43.00	0.02	87
GEOROC database	DDH-MX-S-93	dunite	1267	40.80	0.02	87
GEOROC database	DDH-MX-S-102	dunite	1267	42.20	0.02	87
GEOROC database	DDH-MX-S-123	clinopyroxenite	1267	36.10	0.02	87
GEOROC database	DDH-MX-S-128	dunite	1267	40.10	0.02	87
GEOROC database	DDH-MX-S-133	dunite	1267	38.80	0.02	87
GEOROC database	DDH-MX-N-66	peridotite	1267	35.50	0.03	131
GEOROC database	DDH-MX-N-85	peridotite	1267	39.90	0.03	131
GEOROC database	DDH-MX-N-122	dunite	1267	39.10	0.03	131
GEOROC database	DDH-MX-S-110	dunite	1267	41.30	0.03	131
GEOROC database	DDH-MX-S-121	dunite	1267	39.20	0.03	131
GEOROC database	DDH-MX-S-124	clinopyroxenite	1267	31.50	0.03	131
GEOROC database	DDH-MX-S-137	dunite	1267	37.80	0.03	131
GEOROC database	DDH-MX-S-144	dunite	1267	38.80	0.03	131
GEOROC database	MU 033.241.21	gabbro norite	1267	22.66	0.04	168
GEOROC database	MU 033.241.21	gabbro norite	1267	23.57	0.04	174
GEOROC database	DDH-MX-N-46	websterite	1267	13.70	0.04	174
GEOROC database	DDH-MX-N-55	websterite	1267	17.90	0.04	174
GEOROC database	DDH-MX-N-56	websterite	1267	18.10	0.04	174
GEOROC database	DDH-MX-S-151	dunite	1267	37.50	0.04	174
GEOROC database	DDH-MX-S-154	dunite	1267	37.00	0.04	174
GEOROC database	DDH-MX-S-160	peridotite	1267	35.90	0.04	174

GEOROC database	MU 033.241.21	gabbro norite	1267	23.70	0.04	174
GEOROC database	MU 033.252.76	gabbro norite	1267	22.90	0.04	174
GEOROC database	MU 033.252.76	gabbro norite	1267	22.92	0.04	178
GEOROC database	MU 033.252.76	gabbro norite	1267	22.98	0.04	179
GEOROC database	HDB-2001-MX5	gabbro norite	1267	22.42	0.05	209
GEOROC database	HDB-2001-MX5	gabbro norite	1267	22.45	0.05	210
GEOROC database	DDH-MX-S-156	dunite	1267	36.60	0.05	218
GEOROC database	DDH-MX-S-164	peridotite	1267	34.40	0.05	218
GEOROC database	HDB-2001-MX5	gabbro norite	1267	22.40	0.05	218
GEOROC database	66356	basalt	1267	8.60	0.06	262
GEOROC database	98-119A	picrite	1267	20.70	0.06	262
GEOROC database	98-119B	picrite	1267	21.50	0.06	262
GEOROC database	98-109	picrite	1267	21.10	0.06	262
GEOROC database	DDH-MX-N-18	gabbro	1267	9.35	0.06	262
GEOROC database	DDH-MX-N-54	websterite	1267	23.90	0.06	262
GEOROC database	71072	peridotite	1267	32.31	0.06	262
GEOROC database	DDH-MX-N-27	gabbro	1267	10.00	0.07	305
GEOROC database	DDH-MX-S-171	peridotite	1267	28.70	0.07	305
GEOROC database	DDH-MX-S-182	picrite	1267	27.30	0.07	305
GEOROC database	DDH-MX-S-192	gabbro	1267	12.10	0.07	305
GEOROC database	71082	gabbro norite	1267	20.61	0.07	305
GEOROC database	71116	peridotite	1267	31.29	0.07	305
GEOROC database	71122	peridotite	1267	30.23	0.07	305
GEOROC database	66994	basalt	1267	9.40	0.08	349
GEOROC database	66988	basalt	1267	11.40	0.08	349
GEOROC database	66997	basalt	1267	9.70	0.08	349
GEOROC database	DDH-MX-N-35	websterite	1267	11.70	0.08	349
GEOROC database	71078	peridotite	1267	29.41	0.08	349
GEOROC database	71084	gabbro norite	1267	19.03	0.08	349
GEOROC database	71115	peridotite	1267	31.16	0.08	349
GEOROC database	98-176	picrite	1267	12.90	0.09	392
GEOROC database	99-CM36	picrite	1267	9.97	0.09	392
GEOROC database	71076	peridotite	1267	26.49	0.09	392
GEOROC database	71106	peridotite	1267	33.08	0.09	392
GEOROC database	71128	peridotite	1267	25.24	0.09	392
GEOROC database	61037	basalt	1267	6.90	0.10	436
GEOROC database	66346	basalt	1267	8.40	0.10	436
GEOROC database	66981	basalt	1267	9.00	0.10	436
GEOROC database	661022	basalt	1267	9.20	0.10	436
GEOROC database	661087	basalt	1267	10.50	0.10	436
GEOROC database	661101	basalt	1267	9.90	0.10	436
GEOROC database	661116	basalt	1267	10.50	0.10	436
GEOROC database	99CM35B	picrite	1267	8.92	0.10	436
GEOROC database	71064	peridotite	1267	30.67	0.10	436
GEOROC database	60990	basalt	1267	9.80	0.11	480
GEOROC database	66976	basalt	1267	10.50	0.11	480
GEOROC database	661017	basalt	1267	6.80	0.11	480
GEOROC database	661051	basalt	1267	9.00	0.11	480
GEOROC database	661105	basalt	1267	10.70	0.11	480
GEOROC database	661081	basalt	1267	9.00	0.11	480
GEOROC database	99CM19B	andesite	1267	5.08	0.11	480
GEOROC database	98-125	basalt	1267	9.87	0.11	480
GEOROC database	71138	gabbro norite	1267	15.00	0.11	480
GEOROC database	66345	basalt	1267	8.50	0.12	523
GEOROC database	66980	basalt	1267	8.30	0.12	523
GEOROC database	66970	basalt	1267	10.40	0.12	523
GEOROC database	661006	basalt	1267	8.90	0.12	523
GEOROC database	661004	basalt	1267	5.50	0.12	523
GEOROC database	661058	basalt	1267	3.70	0.12	523

GEOROC database	661079	basalt	1267	5.50	0.12	523
GEOROC database	661122	basalt	1267	6.90	0.12	523
GEOROC database	98-94	basalt	1267	10.10	0.12	523
GEOROC database	99CM19B	andesite	1267	4.93	0.12	523
GEOROC database	98-130A	basalt	1267	7.95	0.12	523
GEOROC database	98-127	basalt	1267	9.15	0.12	523
GEOROC database	71121	peridotite	1267	30.71	0.12	523
GEOROC database	66343	basalt	1267	6.70	0.13	567
GEOROC database	66989	basalt	1267	8.10	0.13	567
GEOROC database	661047	basalt	1267	8.40	0.13	567
GEOROC database	661091	basalt	1267	8.30	0.13	567
GEOROC database	661082	basalt	1267	7.30	0.13	567
GEOROC database	661077	basalt	1267	7.70	0.13	567
GEOROC database	61076	basalt	1267	5.20	0.14	610
GEOROC database	66342	basalt	1267	7.20	0.14	610
GEOROC database	66341	basalt	1267	7.40	0.14	610
GEOROC database	66972	basalt	1267	7.40	0.14	610
GEOROC database	66983	basalt	1267	8.20	0.14	610
GEOROC database	661003	basalt	1267	10.20	0.14	610
GEOROC database	661109	basalt	1267	5.50	0.14	610
GEOROC database	661099	basalt	1267	7.60	0.14	610
GEOROC database	661076	basalt	1267	5.10	0.14	610
GEOROC database	661078	basalt	1267	8.00	0.14	610
GEOROC database	661092	basalt	1267	6.30	0.14	610
GEOROC database	661075	basalt	1267	7.10	0.14	610
GEOROC database	98-87	basalt	1267	8.33	0.14	610
GEOROC database	DDH-MX-N-11	gabbro	1267	7.62	0.14	610
GEOROC database	66351	basalt	1267	10.10	0.15	654
GEOROC database	66335	basalt	1267	7.40	0.15	654
GEOROC database	66977	basalt	1267	7.40	0.15	654
GEOROC database	66998	basalt	1267	7.70	0.15	654
GEOROC database	661048	basalt	1267	9.90	0.15	654
GEOROC database	661110	basalt	1267	6.40	0.15	654
GEOROC database	661088	basalt	1267	6.90	0.15	654
GEOROC database	661120	basalt	1267	5.70	0.15	654
GEOROC database	71133	gabbro norite	1267	21.66	0.15	654
GEOROC database	61133	basalt	1267	11.20	0.16	698
GEOROC database	66355	basalt	1267	9.20	0.16	698
GEOROC database	66361	basalt	1267	7.80	0.16	698
GEOROC database	66979	basalt	1267	8.60	0.16	698
GEOROC database	661027	basalt	1267	7.50	0.16	698
GEOROC database	661033	basalt	1267	6.60	0.16	698
GEOROC database	661002	basalt	1267	7.40	0.16	698
GEOROC database	661014	basalt	1267	7.00	0.16	698
GEOROC database	66986	basalt	1267	5.30	0.16	698
GEOROC database	66992	basalt	1267	1.60	0.16	698
GEOROC database	661010	basalt	1267	5.90	0.16	698
GEOROC database	66993	basalt	1267	6.10	0.16	698
GEOROC database	661065	basalt	1267	7.80	0.16	698
GEOROC database	661083	basalt	1267	7.30	0.16	698
GEOROC database	98-91	basalt	1267	8.47	0.16	698
GEOROC database	98-170	basalt	1267	8.43	0.16	698
GEOROC database	66336	basalt	1267	7.00	0.17	741
GEOROC database	66362	basalt	1267	7.40	0.17	741
GEOROC database	661005	basalt	1267	5.40	0.17	741
GEOROC database	66996	basalt	1267	6.90	0.17	741
GEOROC database	661073	basalt	1267	8.80	0.17	741
GEOROC database	661114	basalt	1267	6.90	0.17	741
GEOROC database	661093	basalt	1267	6.60	0.17	741

GEOROC database	661094	basalt	1267	6.70	0.17	741
GEOROC database	661123	basalt	1267	4.70	0.17	741
GEOROC database	661128	basalt	1267	6.10	0.17	741
GEOROC database	Mar-66	basalt	1267	6.84	0.17	741
GEOROC database	157-66	basalt	1267	8.37	0.17	741
GEOROC database	98-90B	basalt	1267	7.88	0.17	741
GEOROC database	DDH-MX-N-14	websterite	1267	23.00	0.17	741
GEOROC database	61112	basalt	1267	7.10	0.18	785
GEOROC database	61093	basalt	1267	6.90	0.18	785
GEOROC database	66357	basalt	1267	7.50	0.18	785
GEOROC database	66968	basalt	1267	5.10	0.18	785
GEOROC database	66978	basalt	1267	6.80	0.18	785
GEOROC database	661039	basalt	1267	5.60	0.18	785
GEOROC database	661040	basalt	1267	1.80	0.18	785
GEOROC database	661016	basalt	1267	6.40	0.18	785
GEOROC database	661050	basalt	1267	6.50	0.18	785
GEOROC database	661070	basalt	1267	8.50	0.18	785
GEOROC database	661059	basalt	1267	6.00	0.18	785
GEOROC database	661113	basalt	1267	6.10	0.18	785
GEOROC database	661112	basalt	1267	7.00	0.18	785
GEOROC database	61074	basalt	1267	4.70	0.19	828
GEOROC database	61130	basalt	1267	9.60	0.19	828
GEOROC database	661060	basalt	1267	6.00	0.19	828
GEOROC database	661106	basalt	1267	7.30	0.19	828
GEOROC database	661074	basalt	1267	4.70	0.19	828
GEOROC database	661080	basalt	1267	7.40	0.19	828
GEOROC database	661115	basalt	1267	6.90	0.19	828
GEOROC database	98-55	basalt	1267	5.31	0.19	828
GEOROC database	98-126	basalt	1267	8.65	0.19	828
GEOROC database	61132	basalt	1267	6.70	0.20	872
GEOROC database	66353	basalt	1267	12.00	0.20	872
GEOROC database	66347	basalt	1267	6.70	0.20	872
GEOROC database	66340	basalt	1267	5.60	0.20	872
GEOROC database	66973	basalt	1267	5.80	0.20	872
GEOROC database	66985	basalt	1267	5.90	0.20	872
GEOROC database	661042	basalt	1267	5.20	0.20	872
GEOROC database	661064	basalt	1267	5.80	0.20	872
GEOROC database	661056	basalt	1267	5.80	0.20	872
GEOROC database	661053	basalt	1267	5.50	0.20	872
GEOROC database	661111	basalt	1267	10.30	0.20	872
GEOROC database	661086	basalt	1267	5.80	0.20	872
GEOROC database	661089	basalt	1267	5.40	0.20	872
GEOROC database	661084	basalt	1267	6.90	0.20	872
GEOROC database	661119	basalt	1267	7.00	0.20	872
GEOROC database	66352	basalt	1267	5.60	0.21	916
GEOROC database	66322	basalt	1267	7.20	0.21	916
GEOROC database	66363	basalt	1267	7.10	0.21	916
GEOROC database	66995	basalt	1267	5.70	0.21	916
GEOROC database	661041	basalt	1267	7.70	0.21	916
GEOROC database	661062	basalt	1267	5.80	0.21	916
GEOROC database	661063	basalt	1267	5.60	0.21	916
GEOROC database	661107	basalt	1267	9.00	0.21	916
GEOROC database	661121	basalt	1267	5.80	0.21	916
GEOROC database	661117	basalt	1267	5.50	0.21	916
GEOROC database	661127	basalt	1267	6.30	0.21	916
GEOROC database	98-51	basalt	1267	5.45	0.21	916
GEOROC database	61131	basalt	1267	5.90	0.22	959
GEOROC database	66321	basalt	1267	6.70	0.22	959
GEOROC database	66339	basalt	1267	9.70	0.22	959

GEOROC database	66348	basalt	1267	7.10	0.22	959
GEOROC database	661055	basalt	1267	5.70	0.22	959
GEOROC database	661069	basalt	1267	5.70	0.22	959
GEOROC database	661044	basalt	1267	8.10	0.22	959
GEOROC database	661100	basalt	1267	5.50	0.22	959
GEOROC database	661102	basalt	1267	6.60	0.22	959
GEOROC database	661124	basalt	1267	6.70	0.22	959
GEOROC database	661118	basalt	1267	5.50	0.22	959
GEOROC database	66974	basalt	1267	4.80	0.23	1003
GEOROC database	661029	basalt	1267	5.10	0.23	1003
GEOROC database	661043	basalt	1267	5.90	0.23	1003
GEOROC database	661104	basalt	1267	5.80	0.23	1003
GEOROC database	661126	basalt	1267	3.80	0.23	1003
GEOROC database	661125	basalt	1267	3.60	0.23	1003
GEOROC database	25263	basalt	1267	5.95	0.23	1003
GEOROC database	98-82	basalt	1267	7.15	0.23	1003
GEOROC database	661036	basalt	1267	7.80	0.24	1046
GEOROC database	661032	basalt	1267	6.60	0.24	1046
GEOROC database	661090	basalt	1267	6.40	0.24	1046
GEOROC database	31-69	basalt	1267	5.56	0.24	1046
GEOROC database	66359	basalt	1267	5.60	0.25	1090
GEOROC database	66344	basalt	1267	11.70	0.25	1090
GEOROC database	661038	basalt	1267	5.90	0.25	1090
GEOROC database	661025	basalt	1267	8.20	0.25	1090
GEOROC database	661046	basalt	1267	4.00	0.25	1090
GEOROC database	661098	basalt	1267	7.80	0.25	1090
GEOROC database	661095	basalt	1267	6.00	0.25	1090
GEOROC database	24-66	tholeiite	1267	8.96	0.25	1090
GEOROC database	98-60	basalt	1267	6.08	0.25	1090
GEOROC database	66338	basalt	1267	6.20	0.26	1134
GEOROC database	66360	basalt	1267	7.70	0.26	1134
GEOROC database	66982	basalt	1267	5.50	0.26	1134
GEOROC database	66999	basalt	1267	6.70	0.26	1134
GEOROC database	661030	basalt	1267	6.50	0.26	1134
GEOROC database	661045	basalt	1267	4.50	0.26	1134
GEOROC database	661061	basalt	1267	6.00	0.26	1134
GEOROC database	661052	basalt	1267	5.70	0.26	1134
GEOROC database	661108	basalt	1267	6.60	0.26	1134
GEOROC database	661097	basalt	1267	6.10	0.26	1134
GEOROC database	98-124	basalt	1267	6.44	0.26	1134
GEOROC database	66320	basalt	1267	4.30	0.27	1177
GEOROC database	66349	basalt	1267	6.70	0.27	1177
GEOROC database	98-89A	basalt	1267	7.97	0.27	1177
GEOROC database	66337	basalt	1267	7.10	0.28	1221
GEOROC database	66328	basalt	1267	6.20	0.28	1221
GEOROC database	66971	basalt	1267	5.50	0.28	1221
GEOROC database	661035	basalt	1267	5.40	0.28	1221
GEOROC database	661018	basalt	1267	4.60	0.28	1221
GEOROC database	661072	basalt	1267	5.20	0.28	1221
GEOROC database	66334	basalt	1267	5.80	0.29	1264
GEOROC database	66364	basalt	1267	6.70	0.29	1264
GEOROC database	98-61B	basalt	1267	6.25	0.29	1264
GEOROC database	661024	basalt	1267	6.20	0.30	1308
GEOROC database	66991	basalt	1267	5.70	0.30	1308
GEOROC database	661068	basalt	1267	5.10	0.30	1308
GEOROC database	661096	basalt	1267	4.90	0.30	1308
GEOROC database	661085	basalt	1267	7.90	0.30	1308
GEOROC database	661066	basalt	1267	4.20	0.31	1352
GEOROC database	98-75	basalt	1267	5.40	0.31	1352

GEOROC database	66330	basalt	1267		6.50	0.32	1395
GEOROC database	66332	basalt	1267		5.60	0.32	1395
GEOROC database	66333	basalt	1267		5.20	0.33	1439
GEOROC database	661013	basalt	1267		4.70	0.33	1439
GEOROC database	66358	basalt	1267		8.20	0.34	1482
GEOROC database	66326	basalt	1267		5.00	0.34	1482
GEOROC database	661001	basalt	1267		5.10	0.34	1482
GEOROC database	661103	basalt	1267		7.10	0.34	1482
GEOROC database	716	dolerite	1267		3.40	0.34	1482
GEOROC database	DDH-MX-N-3	gabbro	1267		4.01	0.34	1482
GEOROC database	66327	basalt	1267		5.60	0.35	1526
GEOROC database	66975	basalt	1267		5.20	0.35	1526
GEOROC database	661054	basalt	1267		5.00	0.35	1526
GEOROC database	17-69	basalt	1267		5.23	0.35	1526
GEOROC database	661015	basalt	1267		4.80	0.36	1570
GEOROC database	661011	basalt	1267		5.30	0.36	1570
GEOROC database	29-69	basalt	1267		5.74	0.37	1613
GEOROC database	661020	basalt	1267		4.70	0.38	1657
GEOROC database	661007	basalt	1267		4.80	0.39	1700
GEOROC database	115-66	basalt	1267		4.83	0.39	1700
GEOROC database	98-70	basalt	1267		5.17	0.39	1700
GEOROC database	661023	basalt	1267		4.90	0.41	1788
GEOROC database	661067	basalt	1267		4.90	0.41	1788
GEOROC database	661071	basalt	1267		5.90	0.41	1788
GEOROC database	13-69	basalt	1267		5.30	0.42	1831
GEOROC database	66324	basalt	1267		4.30	0.43	1875
GEOROC database	718	dolerite	1267		2.72	0.43	1875
GEOROC database	66325	basalt	1267		4.90	0.45	1962
GEOROC database	98-64	basalt	1267		4.98	0.45	1962
GEOROC database	661049	basalt	1267		4.50	0.47	2049
GEOROC database	661129	basalt	1267		5.10	0.47	2049
GEOROC database	661031	basalt	1267		5.30	0.49	2136
GEOROC database	42-66	tholeiite	1267		4.64	0.49	2136
GEOROC database	66329	basalt	1267		5.60	0.51	2224
GEOROC database	661008	basalt	1267		5.20	0.51	2224
GEOROC database	66331	basalt	1267		5.90	0.52	2267
GEOROC database	66354	basalt	1267		8.60	0.60	2616
GEOROC database	661057	basalt	1267		3.40	0.62	2703
		n =	**316**			**Average =**	**780**
						Median =	**741**
Glen Doe (~870 Ma)							
Miller (1999)	D32	metagabbro	873	6	5.17	0.29	1264
Miller (1999)	D69	metagabbro	873	6	4.38	0.4	1744
Miller (1999)	D49	metagabbro	873	6	5.79	0.35	1526
Miller (1999)	D87	metagabbro	873	6	5.64	0.29	1264
Miller (1999)	D86	metagabbro	873	6	4.61	0.08	349
Miller (1999)	D85	metagabbro	873	6	4.83	0.25	1090
Miller (1999)	D88	metagabbro	873	6	4.91	0.48	2093
Miller (1999)	D68	metagabbro	873	6	4.48	0.52	2267
Miller (1999)	D47	metagabbro	873	6	5.29	0.4	1744
Miller (1999)	D41	metagabbro	873	6	4.09	0.34	1482
Miller (1999)	D93	metagabbro	873	6	5.19	0.43	1875
Miller (1999)	D81	metagabbro	873	6	8.26	0.12	523
Miller (1999)	D4	metagabbro	873	6	8.02	0.15	654
Miller (1999)	D33	metagabbro	873	6	7.29	0.12	523
Miller (1999)	D37	metagabbro	873	6	7.58	0.16	698
		n =	**15**			**Average =**	**1273**
						Median =	**1264**

Willouran-Gairdner (~800 Ma)

Ling et al. (2003)	KW-19	gabbro	~820		6.61	0.21	916
Ling et al. (2003)	KW-20	gabbro	~820		7.72	0.15	654
Ling et al. (2003)	KW-21	gabbro	~820		7.93	0.25	1090
Ling et al. (2003)	KW-22	gabbro	~820		9.34	0.03	131
Ling et al. (2003)	KW-23	gabbro	~820		6.92	0.16	698
Ling et al. (2003)	KW-24	gabbro	~820		8.22	0.15	654
Ling et al. (2003)	KW-25	gabbro	~820		9.12	0.32	1395
Ling et al. (2003)	KW-26	gabbro	~820		8.96	0.32	1395
Ling et al. (2003)	KW-27	gabbro	~820		7.34	0.15	654
Ling et al. (2003)	KW-28	gabbro	~820		6.62	0.1	436
Ling et al. (2003)	KW-29	gabbro	~820		8.96	0.05	218
Ling et al. (2003)	KW-30	gabbro	~820		6.94	0.19	828
Ling et al. (2003)	KW-31	gabbro	~820		6.51	0.07	305
Ling et al. (2003)	KW-32	gabbro	~820		9.14	0.04	174
Ling et al. (2003)	KW-34	gabbro	~820		6.82	0.09	392
Ling et al. (2003)	WJS-1	gabbro	~820		5.16	0.37	1613
Ling et al. (2003)	WJS-2	gabbro	~820		6.88	0.06	262
Ling et al. (2003)	WJS-3	gabbro	~820		6.07	0.09	392
Ling et al. (2003)	WJS-4	gabbro	~820		8.07	0.3	1308
Ling et al. (2003)	WJS-6	gabbro	~820		5.81	0.11	480
Ling et al. (2003)	4007	basalt	817	5	7.63	0.16	698
Ling et al. (2003)	4008	basalt	817	5	6.63	0.18	785
Ling et al. (2003)	4009	dacite	817	5	1.83	0.52	2267
Ling et al. (2003)	4010	basalt	817	5	2.84	0.63	2747
Ling et al. (2003)	4012	dacite	817	5	0.13	0.06	262
Ling et al. (2003)	4014	trachytic dacite	817	5	0.10	0.05	218
Ling et al. (2003)	XG-03	trachytic dacite	817	5	0.33	0.06	262
Ling et al. (2003)	XG-04	basalt	817	5	2.89	0.75	3270
Ling et al. (2003)	XG-05	basalt	817	5	3.31	0.41	1788
Ling et al. (2003)	XG-06	basalt	817	5	6.37	0.2	872
Ling et al. (2003)	XG-07	basalt	817	5	8.10	0.13	567
Ling et al. (2003)	XG-08	basalt	817	5	5.93	0.19	828
Ling et al. (2003)	XG-09	basalt	817	5	5.67	0.21	916
Ling et al. (2003)	XG-10	basalt	817	5	6.67	0.19	828
Ling et al. (2003)	XG-11	basalt	817	5	6.77	0.18	785
Ling et al. (2003)	XG-12	basalt	817	5	2.92	0.93	4055
Ling et al. (2003)	XG-13	basalt	817	5	5.44	0.42	1831
Ling et al. (2003)	XG-14	trachytic dacite	817	5	1.06	0.25	1090
Wang et al. (2008)	05BK22	basalt	821	7	5.4	0.24	1046
Wang et al. (2008)	05BK43	basalt	821	7	6.13	0.13	567
Wang et al. (2008)	05BK44	basalt	821	7	6.38	0.13	567
Wang et al. (2008)	05BK45	basalt	821	7	6.44	0.12	523
Wang et al. (2008)	05BK57	basalt	821	7	6.61	0.26	1134
Wang et al. (2008)	05BK59	basalt	821	7	7.31	0.31	1352
Wang et al. (2008)	05BK61	basalt	821	7	12.7	0.33	1439
Wang et al. (2008)	05BK62	basalt	821	7	11.7	0.31	1352
Wang et al. (2008)	05BK64	basalt	821	7	1.81	0.36	1570
Wang et al. (2008)	05BK65	basalt	821	7	6.85	0.33	1439
Wang et al. (2008)	05BK68	basalt	821	7	5.94	0.11	480
Wang et al. (2008)	05BK74	basalt	821	7	4.39	0.86	3750
Wang et al. (2008)	05BK75	basalt	821	7	7.99	0.39	1700
Wang et al. (2008)	05BK79	basalt	821	7	3.19	0.29	1264
Wang et al. (2008)	05BK81	basalt	811	12	10	0.11	480
Wang et al. (2008)	05BK83	basalt	811	12	7.46	0.31	1352
Wang et al. (2008)	05BK85	basalt	811	12	5.9	0.27	1177
Wang et al. (2008)	05BK88	basalt	811	12	7	0.15	654
Wang et al. (2008)	05BK89	basalt	811	12	8.66	0.33	1439
Wang et al. (2008)	05BK90	basalt	811	12	7.98	0.12	523

Wang et al. (2008)	05BK94	basalt	811	12	6.82	0.2	872
Wang et al. (2008)	05BK95	basalt	811	12	6.47	0.14	610
Wang et al. (2008)	05BK96	basalt	811	12	7.12	0.14	610
Wang et al. (2008)	05BK98	basalt	811	12	7.54	0.25	1090
Wang et al. (2008)	05BK99	basalt	811	12	6.36	0.28	1221
Wang et al. (2008)	05BK102A	basalt	811	12	3.27	0.16	698
Wang et al. (2008)	05BK102B	basalt	811	12	7.15	0.14	610
Wang et al. (2008)	05BK104	basalt	811	12	6.23	0.11	480
Wang et al. (2008)	05BK106	basalt	811	12	4.42	0.12	523
Wang et al. (2008)	05BK107	basalt	811	12	6.18	0.12	523
Wang et al. (2008)	05BK108	basalt	811	12	6.12	0.13	567
Wang et al. (2008)	05BK111	basalt	811	12	4.18	0.35	1526
Wang et al. (2008)	05BK113	basalt	811	12	6.96	0.16	698
Wang et al. (2008)	05BK115	basalt	811	12	2.37	0.22	959
Wang et al. (2008)	05BK117	basalt	811	12	4.78	0.15	654
Wang et al. (2008)	05BK122	basalt	811	12	2.5	0.08	349
Wang et al. (2008)	05BK128	basalt	811	12	5.59	0.42	1831
Wang et al. (2008)	05BK130	basalt	811	12	6	0.13	567
Wang et al. (2010)	AG04	basalt	823	10	11.7	0.11	480
Wang et al. (2010)	AG06	basalt	823	10	9.81	0.15	654
Wang et al. (2010)	AG07	basalt	823	10	12.5	0.09	392
Wang et al. (2010)	AG08	basalt	823	10	9.32	0.09	392
Wang et al. (2010)	AG09	basalt	823	10	12.2	0.13	567
Wang et al. (2010)	AG11	basalt	823	10	12.9	0.25	1090
Wang et al. (2010)	AG15	basalt	823	10	11.4	0.09	392
Wang et al. (2010)	AG16	basalt	823	10	8.62	0.1	436
Wang et al. (2010)	AG17	basalt	823	10	8.67	0.09	392
Wang et al. (2010)	AG18	basalt	823	10	9.43	0.1	436
Wang et al. (2010)	AG19	basalt	823	10	9.51	0.09	392
Wang et al. (2010)	AG20	basalt	823	10	10	0.09	392
Wang et al. (2010)	AG23	basalt	823	10	10	0.1	436
Wang et al. (2010)	AG27	basalt	823	10	7.57	0.15	654
Wang et al. (2010)	AG29	basalt	823	10	8.98	0.11	480
Wang et al. (2010)	AG30	basalt	823	10	9.83	0.13	567
Wang et al. (2010)	AG31	basalt	823	10	5.25	0.14	610
Wang et al. (2010)	AG33	basalt	823	10	8.22	0.12	523
Wang et al. (2010)	AG36	basalt	823	10	8.52	0.13	567
Wang et al. (2010)	AG37	basalt	823	10	8.64	0.11	480
Zhao et al. (1994)	91-563	mafic dike	~800		7.55	0.23	1003
Zhao et al. (1994)	91-564	mafic dike	~800		7	0.18	785
Zhao et al. (1994)	91-565	mafic dike	~800		4.58	0.21	916
Zhao et al. (1994)	87-497	mafic dike	~800		6.9	0.14	610
Zhao et al. (1994)	87-504	mafic dike	~800		6.76	0.15	654
Zhao et al. (1994)	91-562	mafic dike	~800		7.32	0.14	610
Zhao et al. (1994)	91-555	mafic dike	~800		7.16	0.12	523
Zhao et al. (1994)	91-566	mafic dike	~800		6.17	0.13	567
Zhao et al. (1994)	91-567	mafic dike	~800		7.57	0.15	654
Zhao et al. (1994)	91-568	mafic dike	~800		9.12	0.13	567
Zhao et al. (1994)	RS27	mafic dike	~800		7.95	0.1	436
Zhao et al. (1994)	W6	mafic dike	~800		8.16	0.14	610
Zhao et al. (1994)	5483	mafic dike	~800		7.07	0.14	610
Zhao et al. (1994)	5479	mafic dike	~800		6.92	0.14	610
Zhao et al. (1994)	5282	mafic dike	~800		9.59	0.14	610
Zhao et al. (1994)	5345	mafic dike	~800		6.43	0.17	741
Li et al. (2002)	98KD78-1	basaltic andesite	803	12	0.85	0.65	2834
Li et al. (2002)	98KD78-2	basaltic	803	12	0.95	0.71	3096
Li et al. (2002)	99KD21-1	alkali basalt	803	12	5.47	0.71	3096
Li et al. (2002)	99KD22-1	alkali basalt	803	12	9.3	0.34	1482
Li et al. (2002)	99KD22-2	alkali basalt	803	12	9.16	0.43	1875

Li et al. (2002)	99KD22-3	alkali basalt	803	12	10.97	0.44	1918
Li et al. (2002)	99KD22-4	alkali basalt	803	12	10.08	0.52	2267
Li et al. (2002)	99KD22-5	alkali basalt	803	12	11.96	0.54	2354
Li et al. (2002)	99KD22-6	alkali basalt	803	12	8.27	0.38	1657
Li et al. (2002)	99KD22-7	alkali basalt	803	12	7.03	0.35	1526
Li et al. (2002)	99KD22-8	alkali basalt	803	12	7.24	0.31	1352
Li et al. (2008)	S1.6-1	diabase	794	9	1.94	0.91	3968
Li et al. (2008)	S1.6-2	diabase	794	9	3.23	0.85	3706
Li et al. (2008)	S1.6-3	diabase	794	9	5.30	0.93	4055
Li et al. (2008)	02SC49.2	diabase	794	9	5.02	0.39	1700
Li et al. (2008)	02SC49.3	diabase	794	9	6.35	0.45	1962
Li et al. (2008)	02SC51.1	diabase	794	9	3.19	0.85	3706
Li et al. (2008)	02SC50.2	diabase	794	9	6.04	0.45	1962
Li et al. (2008)	99SC73.1	basalt	792	5	5.52	0.36	1570
Li et al. (2008)	99SC73.2	basalt	792	5	4.19	0.33	1439
Li et al. (2008)	99SC73.3	basalt	792	5	7.57	0.25	1090
Li et al. (2008)	99SC73.4	basalt	792	5	2.48	0.27	1177
Li et al. (2008)	99SC73.5	basalt	792	5	7.11	0.38	1657
Li et al. (2008)	99SC73.6	basalt	792	5	5.62	0.3	1308
Li et al. (2008)	99SC75	basalt	792	5	5.42	0.21	916
Zhu et al. (2008)	04HS-09	mafic dike	792	13	8.67	0.25	1090
Zhu et al. (2008)	HT-01	mafic dike	792	13	6.780	0.29	1264
Zhu et al. (2008)	HT-02	mafic dike	792	13	8.53	0.32	1395
Zhu et al. (2008)	HT-03	mafic dike	792	13	7.21	0.39	1700
Zhu et al. (2008)	HT-04	mafic dike	792	13	8.72	0.31	1352
Zhu et al. (2008)	HT-05	mafic dike	792	13	8.83	0.26	1134
Zhu et al. (2008)	DW-01	mafic dike	792	13	10.09	0.23	1003
Zhu et al. (2008)	07DW-01	mafic dike	792	13	8.8	0.28	1221
		n =	**109**			**Average =**	**1110**
						Median =	**828**
Gunbarrel (~780 Ma)							
Dudás and Lustwerk (1997)	19-4	basalt	779	2	5.05	0.23	1003
Dudás and Lustwerk (1997)	43A	basalt	779	2	4.83	0.23	1003
Dudás and Lustwerk (1997)	47	basalt	779	2	4.86	0.24	1046
Dudás and Lustwerk (1997)	R490	basalt	779	2	5.10	0.33	1439
Dudás and Lustwerk (1997)	R496	basalt	779	2	4.07	0.36	1570
Dudás and Lustwerk (1997)	TC1-2	basalt	779	2	3.49	0.28	1221
Dudás and Lustwerk (1997)	TC3-2	basalt	779	2	5.11	0.15	654
Dudás and Lustwerk (1997)	XBA-12	basalt	779	2	5.65	0.23	1003
Dudás and Lustwerk (1997)	XBA-15B	basalt	779	2	5.61	0.23	1003
Dudás and Lustwerk (1997)	XBA-19A	basalt	779	2	6.31	0.24	1046
Dudás and Lustwerk (1997)	XBA-20B	basalt	779	2	7.44	0.2	872
Dudás and Lustwerk (1997)	XBA-25	basalt	779	2	5.76	0.21	916
Dudás and Lustwerk (1997)	R419	basalt	779	2	6.73	0.14	610
Dudás and Lustwerk (1997)	R420	basalt	779	2	6.07	0.13	567
Burtis et al. (2007)	Ale 01	basalt	777.5	3	4.98	0.224	977
Burtis et al. (2007)	Ale 02	basalt	777.5	3	6.95	0.21	916
Burtis et al. (2007)	KF 01	basalt	777.5	3	4.09	0.514	2241
Burtis et al. (2007)	KF 02	basalt	777.5	3	4.55	0.471	2054
Burtis et al. (2007)	KF03	basalt	777.5	3	4.29	0.531	2315
Burtis et al. (2007)	MR 01	basalt	777.5	3	5.00	0.256	1116
Burtis et al. (2007)	MR 02	basalt	777.5	3	5.50	0.225	981
Burtis et al. (2007)	RPE 04	basalt	777.5	3	4.85	0.252	1099
Burtis et al. (2007)	RPE 21	basalt	777.5	3	5.82	0.212	924
Burtis et al. (2007)	RPM 01	basalt	777.5	3	4.89	0.255	1112
Burtis et al. (2007)	RPM 02	basalt	777.5	3	4.85	0.252	1099
Zhang et al. (2014)	KP-3	basalt	783.7	2.3	4.76	0.63	2747
Zhang et al. (2014)	KP-4	basalt	783.7	2.3	5.98	0.59	2572
Zhang et al. (2014)	KP-5	basalt	783.7	2.3	4.93	0.5	2180

Zhang et al. (2014)	KP-6	basalt		783.7	2.3	5.57	0.52	2267
Zhang et al. (2014)	KP-8	basalt		783.7	2.3	5.63	0.55	2398
Zhang et al. (2014)	KP-11	basalt		783.7	2.3	5.27	0.59	2572
Zhang et al. (2014)	KP-13	basalt		783.7	2.3	5.14	0.53	2311
Zhang et al. (2014)	KP-14	basalt		783.7	2.3	5.03	0.57	2485
Zhang et al. (2014)	KP-15	basalt		783.7	2.3	5.42	0.53	2311
Zhang et al. (2014)	KP-16	basalt		783.7	2.3	5.75	0.58	2529
Zhang et al. (2014)	KP-17	basalt		783.7	2.3	5.7	0.57	2485
Zhang et al. (2014)	KP-19	basalt		783.7	2.3	5.72	0.6	2616
Zhang et al. (2014)	KP-20	basalt		783.7	2.3	5.68	0.62	2703
Zhang et al. (2014)	KP-21	basalt		783.7	2.3	6.09	0.58	2529
Zhang et al. (2014)	DKP-4	basalt		783.7	2.3	5.09	0.67	2921
Zhang et al. (2014)	DKP-6	basalt		783.7	2.3	5.76	0.61	2660
Zhang et al. (2014)	DKP-7	basalt		783.7	2.3	5.5	0.56	2442
Zhang et al. (2014)	DKP-8	basalt		783.7	2.3	5.1	0.69	3008
Zhang et al. (2014)	DKP-9	basalt		783.7	2.3	5.44	0.67	2921
Zhang et al. (2014)	DKP-10	basalt		783.7	2.3	5.64	0.56	2442
Zhang et al. (2014)	DKP-11	basalt		783.7	2.3	5.34	0.72	3139
Zhang et al. (2014)	DKP-12	basalt		783.7	2.3	5.23	0.62	2703
Zhang et al. (2014)	DKP-13	basalt		783.7	2.3	5.28	0.63	2747
Zhang et al. (2014)	DKP-14	basalt		783.7	2.3	4.88	0.61	2660
Zhang et al. (2014)	DKP-15	basalt		783.7	2.3	5.07	0.64	2790
			n =	**50**			**Average =**	**1685**
							Median =	**2254**
Mundine Well (~755 Ma)								
Li et al. (2006)	EDMH2.2	dolerite		755	3	7.67	0.04	174
Li et al. (2006)	EDMB7.2	dolerite		755	3	6.77	0.18	785
Li et al. (2006)	EDMC	dolerite		755	3	3.35	0.31	1352
Li et al. (2006)	EDMC4.3	dolerite		755	3	6.3	0.24	1046
Li et al. (2006)	EDMD15.2	dolerite		755	3	5.82	0.06	262
Li et al. (2006)	EDME16.2	dolerite		755	3	6.48	0.1	436
Li et al. (2006)	B6	dolerite		755	3	11.95	0.08	349
Li et al. (2006)	B6.1	dolerite		755	3	5.03	0.1	436
Li et al. (2006)	EDMI1.1	dolerite		755	3	6.8	0.08	349
Li et al. (2006)	EDMI4.1	dolerite		755	3	6.6	0.09	392
Li et al. (2006)	B7	dolerite		755	3	7.32	0.09	392
Li et al. (2006)	EDMG	dolerite		755	3	5.07	0.21	916
Li et al. (2006)	EDME3.2	dolerite		755	3	5.63	0.23	1003
Li et al. (2006)	EDMH1.2	dolerite		755	3	7.11	0.08	349
Li et al. (2006)	EDMF	dolerite		755	3	4.69	0.49	2136
Li et al. (2006)	EDMF1.2	dolerite		755	3	5.58	0.4	1744
Zhu et al. (2008)	XF-01	mafic dike		761	14	3.75	0.26	1134
Zhu et al. (2008)	XF-03	mafic dike		761	14	3.91	0.26	1134
Zhu et al. (2008)	XF-04	mafic dike		761	14	7.75	0.36	1570
Zhu et al. (2008)	XF-06	mafic dike		761	14	6.97	0.36	1570
Zhu et al. (2008)	TJ-01	mafic dike		761	14	6.98	0.2	872
Zhu et al. (2008)	TJ-03	mafic dike		761	14	7.27	0.22	959
Zhu et al. (2008)	TJ-04	mafic dike		761	14	7.06	0.22	959
Zhu et al. (2008)	TJ-05	mafic dike		761	14	9.48	0.16	698
Zhu et al. (2008)	TJ-07	mafic dike		761	14	7.24	0.22	959
Zhu et al. (2008)	DW-02	mafic dike		761	14	6.67	0.2	872
Zhu et al. (2008)	HL-01	mafic dike		761	14	7.97	0.2	872
Zhu et al. (2008)	HL-03	mafic dike		761	14	7.23	0.26	1134
Zhu et al. (2008)	HS-04	mafic dike		761	14	7.44	0.2	872
Zhu et al. (2008)	HS-08	mafic dike		761	14	7.53	0.19	828
Zhu et al. (2008)	HT-06	mafic dike		761	14	5.32	0.29	1264
Zhu et al. (2008)	HT-07	mafic dike		761	14	5.14	0.3	1308
Zhu et al. (2008)	HS-06	mafic dike		761	14	6.3	0.24	1046
Zhu et al. (2008)	HS-07	mafic dike		761	14	6.85	0.23	1003

Zhu et al. (2008)	04HS-01	mafic dike		761	14	7.36	0.19	828
Zhu et al. (2008)	04HS-04	mafic dike		761	14	6.5	0.27	1177
Zhu et al. (2008)	04HS-05	mafic dike		761	14	7.75	0.17	741
Zhu et al. (2008)	04HS-06	mafic dike		761	14	8.69	0.14	610
Zhu et al. (2008)	04HS-07	mafic dike		761	14	7.33	0.17	741
Zhu et al. (2008)	04HS-08	mafic dike		761	14	7.25	0.17	741
Zhu et al. (2008)	04HS-10	mafic dike		761	14	7.33	0.19	828
Zhu et al. (2008)	04HS-11	mafic dike		761	14	7.36	0.17	741
			n =	**42**			**Average =**	**895**
							Median =	**872**
Franklin (~720 Ma)								
Dostal et al. (1986)	7169	basalt		723	3	7.8	0.18	785
Dostal et al. (1986)	7170	basalt		723	3	7.48	0.22	959
Dostal et al. (1986)	7171	basalt		723	3	6.84	0.16	698
Dostal et al. (1986)	7172	basalt		723	3	6.88	0.16	698
Dostal et al. (1986)	7173	basalt		723	3	6.72	0.18	785
Dostal et al. (1986)	7174	basalt		723	3	4.59	0.22	959
Dostal et al. (1986)	7175	basalt		723	3	6.19	0.17	741
Dostal et al. (1986)	7176	basalt		723	3	6.59	0.17	741
Dostal et al. (1986)	7177	basalt		723	3	7.67	0.15	654
Dostal et al. (1986)	7178	basalt		723	3	6.94	0.14	610
Dostal et al. (1986)	7180	basalt		723	3	7.67	0.14	610
Dostal et al. (1986)	7181	basalt		723	3	7.86	0.17	741
Dostal et al. (1986)	7182	basalt		723	3	7.96	0.14	610
Dostal et al. (1986)	7183	basalt		723	3	6.36	0.18	785
Dostal et al. (1986)	7184	basalt		723	3	5.52	0.17	741
Dostal et al. (1986)	7185	basalt		723	3	3.38	0.32	1395
Dostal et al. (1986)	7186	basalt		723	3	10	0.13	567
Dostal et al. (1986)	7189	basalt		723	3	8.94	0.16	698
			n =	**18**			**Average =**	**765**
							Median =	**741**

Appendix References

Aleinikoff, J.N., Schenck, W.S., Srogi, L., Fanning, C.M., Kamo, S.L., Bosbyshell, H., (2006), Deciphering igneous and metamorphic events in high-grade rocks of the Wilmington Complex, Delaware: Morphology, cathodoluminescence and backscatter electron zoning, and SHRIMP U-Pb geochronology of zircon and monazite, *GSA Bulletin*, **118**, 39–64.

Bossi, J. et al. (1993), Early Proterozoic dike swarms from western Uruguay: geochemistry, Sr- Nd isotopes and petrogenesis, *Chemical Geology*, **106**(3), 263–277.

Burtis, E. W., J. W. Sears, and K. R. Chamberlain (2006), Age and petrology of Neoproterozoic intrusions in the northern Rocky Mountains, USA: Correlation with the Gunbarrel magmatic event, *SPECIAL PUBLICATION-SEPM*, **86**, 175.

Cornell, D. H., S. S. Schütte, and B. L. Eglington (1996), The Ongeluk basaltic andesite formation in Griqualand West, South Africa: submarine alteration in a 2222 Ma Proterozoic sea*, Precambrian Research*, **79**(1), 101–123.

Crow, C., and K. C. Condie (1988), Geochemistry and origin of late Archean volcanics from the Ventersdorp Supergroup, South Africa, *Precambrian Research*, **42**(1), 19–37.

Dostal, J., W. R. A. Baragar, and C. Dupuy (1986), Petrogenesis of the Natkusiak continental basalts, Victoria Island, Northwest Territories, Canada, *Canadian Journal of Earth Sciences*, **23**(5), 622–632.

Dudás, F. Ö., and R. L. Lustwerk (1997), Geochemistry of the Little Dal basalts: continental tholeiites from the Mackenzie mountains, Northwest Territories, Canada, *Canadian Journal of Earth Sciences*, **34**(1), 50–58.

French, J. E., and L. M. Heaman (2010), Precise U–Pb dating of Paleoproterozoic mafic dyke swarms of the Dharwar craton, India: implications for the existence of the Neoarchean supercraton Sclavia, *Precambrian Research*, **183**(3), 416–441.

Fryer, B. J., and G. A. Jenner (1978), Geochemistry and origin of the Archean Prince Albert group volcanics, western Melville Peninsula, Northwest territories, Canada, *Geochimica et Cosmochimica Acta*, **42**(11), 1645–1654.

Geochemistry of Rocks of the Oceans and Continents (GEOROC) database, available at <http://georoc.mpch-mainz.gwdg.de/georoc/>. Precompiled Continental Flood Basalt File for MacKenzie Large Igneous Province downloaded January 2015.

Hanson, R. E., W. A. Gose, J. L. Crowley, J. Ramezani, S. A. Bowring, D. S. Bullen, R. P. Hall, J. A. Pancake, and J. Mukwakwami (2004), Paleoproterozoic intraplate magmatism and basin development on the Kaapvaal Craton: Age, paleomagnetism and geochemistry of ~1.93 to ~1.87 Ga post-Waterberg dolerites, *South African Journal of Geology*, **107**(1–2), 233–254.

Hartlaub, R. P., L. M. Heaman, K. E. Ashton, and T. Chacko (2004), The Archean Murmac Bay Group: evidence for a giant archean rift in the Rae Province, Canada, *Precambrian Research*, **131**(3), 345–372.

Höy, T. (1989), The age, chemistry, and tectonic setting of the Middle Proterozoic Moyie sills, Purcell Supergroup, southeastern British Columbia, *Canadian Journal of Earth Sciences*, **26**(11), 2305–2317.

Jahn, B., G. Gruau, and A. Y. Glikson (1982), Komatiites of the Onverwacht Group, S. Africa: REE geochemistry, Sm/Nd age and mantle evolution, *Contributions to Mineralogy and Petrology*, **80**(1), 25–40.

Kuiper, K.F., Deino, A., Hilgen, F.J., Krijgsman, W., Renne, P.R., and Wijbrans, J.R. (2008), Synchronizing rock clocks of Earth history, *Science*, **320**(5875), 500–504.

Kullerud, K. are, K. P. Skjerlie, F. Corfu, and D. Jesús (2006), The 2.40 Ga Ringvassøy mafic dykes, West Troms Basement Complex, Norway: the concluding act of early Palaeoproterozoic continental breakup, *Precambrian Research*, **150**(3), 183–200.

Kumar, A., M. A. Hamilton, and H. C. Halls (2012), A Paleoproterozoic giant radiating dyke swarm in the Dharwar Craton, southern India, *Geochemistry, Geophysics, Geosystems*, **13**(2), Q02011.

Kylander-Clark, A.R., Hacker, B.R., and Cottle, J.M. (2013), Laser-ablation split-stream ICP petrochronology, *Chemical Geology,* **345**, 99–112.

Li, X., Z.-X. Li, H. Zhou, Y. Liu, and P. D. Kinny (2002), U–Pb zircon geochronology, geochemistry and Nd isotopic study of Neoproterozoic bimodal volcanic rocks in the Kangdian Rift of South China: implications for the initial rifting of Rodinia, *Precambrian Research*, **113**(1), 135–154.

Li, X.-H., W.-X. Li, Z.-X. Li, and Y. Liu (2008), 850–790 Ma bimodal volcanic and intrusive rocks in northern Zhejiang, South China: a major episode of continental rift magmatism during the breakup of Rodinia, *Lithos*, **102**(1), 341–357.

Li, X.-H., Z.-X. Li, M. T. Wingate, S.-L. Chung, Y. Liu, G.-C. Lin, and W.-X. Li (2006), Geochemistry of the 755Ma Mundine Well dyke swarm, northwestern Australia: part of a Neoproterozoic mantle superplume beneath Rodinia? *Precambrian Research*, **146**(1), 1–15.

Ling, W., S. Gao, B. Zhang, H. Li, Y. Liu, and J. Cheng (2003), Neoproterozoic tectonic evolution of the northwestern Yangtze craton, South China: implications for amalgamation and break-up of the Rodinia Supercontinent, *Precambrian Research*, **122**(1), 111–140.

Manyeruke, T. D., T. G. Blenkinsop, P. Buchholz, D. Love, T. Oberthür, U. K. Vetter, and D. W. Davis (2004), The age and petrology of the Chimbadzi Hill Intrusion, NW Zimbabwe: first evidence for early Paleoproterozoic magmatism in Zimbabwe, *Journal of African Earth Sciences*, **40**(5), 281–292.

Miller, I. L. (1999), Neoproterozoic extensional basic magmatism associated with emplacement of the West Highland granite gneiss in the Moine Supergroup of NW Scotland, *Journal of the Geological Society, London*, **156**, 1153–62.

Parrish, R.R. (1990), U-Pb dating of monazite and its application to geological problems, *Canadian Journal of Earth Sciences*, **27**, 1431–1450.

Paton, C., Woodhead, J.D., Hellstrom, J.C., Hergt, J.M., Greig, A., and Maas, R. (2010), Improved laser ablation U-Pb zircon geochronology through robust down-hole fractionation correction, *Geochemistry, Geophysics, Geosystems*, **11**(3), Q0AA06.

Reis, N. J., W. Teixeira, M. A. Hamilton, F. Bispo-Santos, M. E. Almeida, and M. S. D'Agrella-Filho (2013), Avanavero mafic magmatism, a late Paleoproterozoic LIP in the Guiana Shield, Amazonian Craton: U–Pb ID-TIMS baddeleyite, geochemical and paleomagnetic evidence, *Lithos*, **174**, 175–195.

Schärer, U. (1984), The effect of initial ^{230}Th disequilibrium on young UPb ages: the Makalu case, Himalaya, *Earth and Planetary Science Letters*, **67**(2), 191–204.

Schweitzer, J., and A. Kröner (1985), Geochemistry and petrogenesis of early Proterozoic intracratonic volcanic rocks of the Ventersdorp Supergroup, South Africa, *Chemical Geology*, **51**(3), 265–288.

Upton, B. G. J., O. T. Rämö, L. M. Heaman, J. Blichert-Toft, F. Kalsbeek, T. L. Barry, and H. F. Jepsen (2005), The Mesoproterozoic Zig-Zag Dal basalts and associated intrusions of eastern North Greenland: mantle plume–lithosphere interaction, *Contributions to Mineralogy and Petrology*, **149**(1), 40–56.

Wang, X.-C., X.-H. Li, W.-X. Li, Z.-X. Li, Y. Liu, Y.-H. Yang, X.-R. Liang, and X.-L. Tu (2008), The Bikou basalts in the northwestern Yangtze block, South China: Remnants of 820–810 Ma continental flood basalts? *Geological Society of America Bulletin*, **120**(11–12), 1478–1492.

Wang, X.-C., X.-H. Li, Z.-X. Li, Y. Liu, and Y.-H. Yang (2010), The Willouran basic province of South Australia: its relation to the Guibei large igneous province in South China and the breakup of Rodinia, *Lithos*, **119**(3), 569–584.

Zhang, Z., J. Kang, T. Kusky, M. Santosh, H. Huang, D. Zhang, and J. Zhu (2012), Geochronology, geochemistry and petrogenesis of Neoproterozoic basalts from Sugetbrak, northwest Tarim block, China: implications for the onset of Rodinia supercontinent breakup, *Precambrian Research*, **220**, 158–176.

Zhao, J., M. T. McCulloch, and R. J. Korsch (1994), Characterisation of a plume-related 800 Ma magmatic event and its implications for basin formation in central-southern Australia, *Earth and Planetary Science Letters*, **121**(3), 349–367.

Zhu, W.-G., H. Zhong, X.-H. Li, H.-L. Deng, D.-F. He, K.-W. Wu, and Z.-J. Bai (2008), SHRIMP zircon U–Pb geochronology, elemental, and Nd isotopic geochemistry of the Neoproterozoic mafic dykes in the Yanbian area, SW China, *Precambrian Research*, **164**(1), 66–85.